Direct Recycling of Spent Layered Cathode Materials for Lithium-ion Batteries

Zur Erlangung des akademischen Grades eines
DOKTORS DER NATURWISSENSCHAFTEN
(Dr. rer. nat.)

von der KIT-Fakultät für Chemie und Biowissenschaften
des Karlsruher Instituts für Technologie (KIT)
genehmigte

DISSERTATION

von
M. Sc. Shuaiwei Liu
aus Jiangxi, China

KIT-Dekan: Prof. Dr. Martin Bastmeyer
Referent: Prof. Dr. Helmut Ehrenberg
Korreferent: Prof. Dr. Daria Mikhailova
Tag der mündlichen Prüfung: 15.12.2025

Contents

Symbols and Abbreviations

ΔG_0	Standard Gibbs free energy
l	Orbital momentum quantum number
λ	Wavelength
d	Interplanar spacing of the crystal planes
hkl	Miller indices of a crystal plane
K_α	Characteristic X-ray line (L → K transition)
K_β	Characteristic X-ray line (M → K transition)
h	Planck's constant
FT	Fourier transform
LUMO	Lowest Unoccupied Molecular Orbital
HCP	Hexagonally close-packed
CCP	Cubic close-packed
ESCA	Electron Spectroscopy for Chemical Analysis
SOC	State of charge
eV	Electron volts
KE	Kinetic energy
BE	Binding energy
UHV	Ultra-high vacuum
RT	Room Temperature
ICP-OES	Inductively Coupled Plasma Optical Emission Spectrometry
CGHE	Carrier gas hot extraction
NMR	Nuclear magnetic resonance
XAS	X-ray absorption spectroscopy
XANES	X-ray absorption near edge structure
EXAFS	Extended X-Ray absorption fine structure
XPS	X-ray photoelectron spectroscopy
XRD	X-ray Diffraction
SRD	Synchrotron Radiation Diffraction
SEM	Scanning electron microscopy
EDX	Energy Dispersive X-ray spectroscopy
TEM	Transmission Electron Microscopy

PVDF	Polyvinylidene fluoride
CMC	Sodium carboxymethylcellulose
SBR	Styrene-butadiene rubber latex
NMP	N-methyl-2-pyrrolidone
DMF	N, N-Dimethylformamide
DMAC	N, N-Dimethylacetamide
EC	Ethylene carbonate
DEC	Diethyl carbonate
DMC	Dimethyl carbonate
VC	Vinylene Carbonate
CC-PET	Polyethylene terephthalate fabric
LIBs	Lithium-ion batteries
LFP	Lithium iron phosphate ($LiFePO_4$)
LMO	Lithium manganese oxide ($LiMn_2O_4$)
LNO	Lithium nickel oxide ($LiNiO_2$)
NCM	Lithium nickel-cobalt-manganese-oxide ($LiNi_xCo_yMn_zO_2$)
NCA	Lithium nickel-cobalt-aluminum oxide ($LiNi_xCo_yAl_zO_2$)
CAM	Cathode active material
SEI	Solid electrolyte interphase
RS	Rock-salt phase
TM	Transition metal

List of Figures

Appendix

List of Tables

Appendix

Abstract

Direct recycling represents a sustainable approach to the recovery of spent lithium-ion batteries. Currently, the direct recycling of cathode active material (CAM) has garnered most attention due to their high intrinsic value compared with other cell components. This process seeks to preserve the original structural framework and electrochemical functionality of the CAM while repairing degradation accumulated during cycling. It typically involves disassembling discharged cells, separating the cathode composite from the current collector, and restoring the active material through re-lithiation. By retaining the original structure of CAM, direct recycling significantly reduces energy consumption, minimizes environmental impact, and lowers operational cost, rendering it an attractive alternative to conventional pyrometallurgical and hydrometallurgical approaches.

Despite its potential, direct recycling of CAM remains at the pilot-scale stage, with critical technical and operational barriers impeding large-scale implementation. Advancing the technology requires a deeper understanding of the underlying processes. This thesis focuses on $LiNi_xCo_yMn_zO_2$ (NCM) cathode material and two key steps: thermal pretreatment enabled separation, and subsequent solid-state regeneration, with particular emphasis on the influence of impurities during regeneration.

(1) Thermal pre-treatment of LIB electrodes

The effects of thermal pretreatment under different atmospheres and temperatures on the separation of cathode (NCM622) and anode (graphite) materials from current collectors were systematically studied. It was found that air/oxygen atmospheres facilitate efficient separation of CAM from Al foil at relatively low temperatures, with minimal structural degradation, while graphite anodes demonstrate good thermal stability in inert or reducing atmospheres. However, the cycled anode electrode exhibits interfacial adhesion that hinders effective separation.

(2) Structural repair of spent NCM materials

The structural repair of spent NCM622 cathode powder was investigated using multiscale characterization techniques. Results show that degradation present in spent material is primarily associated with Ni occupying Li sites, leading to cation disorder and local cubic domain formation. The regeneration process involves re-lithiation, oxygen uptake, and transition-metal migration, strongly influenced by temperature and lithium compensation ratio. Decreasing transition-metal occupancy in the Li layer was found to closely correlate with

improved capacity recovery, offering an atomic-level understanding of degradation and repair mechanisms beyond conventional phase-transition perspectives.

(3) Effect of impurity on Structural repair of Spent NCM Material

The effect of impurities in spent NCM622 material on its regeneration was systematically elucidated. The analysis identified Al_2O_3, $AlPO_4$, AlF_3, Li_3PO_4, LiF, $Li_xPF_yO_4$, and Li_2CO_3 as main impurities in the spent material, accompanied by Al-inclusion likely induced by thermal pretreatment. Among these, Al- and F-containing species play dominant roles in the regeneration process, leading to Al- and F-inclusion in the regenerated material. Specifically, F-inclusion occurs via substitution of lattice oxygen, causing lattice distortion and reduced transition-metal oxidation states, while Al-inclusion promotes crystal growth along specific planes. Both contaminants, when accumulated, impair electrochemical performance and structural integrity, underscoring the necessity of impurity control prior to regeneration to ensure long-term cycling stability in direct recycling.

Overall, this thesis clarifies the mechanisms of thermal pretreatment, regeneration, and impurity effect, deepens the understanding of material-level processes in direct recycling, and provides practical insights into optimizing recycling protocols.

Zusammenfassung

Die direkte Wiederverwertung stellt einen nachhaltigen Ansatz zur Rückgewinnung von verbrauchten Lithium-Ionen-Batterien dar. Derzeit gilt das Hauptaugenmerk der direkten Wiederverwertung des Kathodenaktivmaterials (CAM), da dieses im Vergleich zu anderen Zellkomponenten einen höheren intrinsischen Wert besitzt. Ziel dieses Prozesses ist es, das ursprüngliche Strukturgerüst und die elektrochemische Funktionalität des CAM zu bewahren und gleichzeitig die während des Zyklierens entstandenen Degradationen zu reparieren. Typischerweise umfasst der Prozess das Zerlegen entladener Zellen, das Abtrennen des Kathodenverbunds vom Stromableiter sowie die Wiederherstellung des Aktivmaterials durch Relithiierung. Durch den Erhalt der ursprünglichen Struktur der CAMs reduziert das direkte Recycling den Energieverbrauch erheblich, minimiert die Umweltbelastung und senkt die Betriebskosten, wodurch es zu einer attraktiven Alternative gegenüber konventionellen pyro- und hydrometallurgischen Verfahren wird.

Trotz ihres Potenzials befindet sich die direkte Wiederverwertung von CAM noch im Pilotstadium, da wesentliche technische und betriebliche Hürden eine großtechnische Umsetzung behindern. Der Fortschritt dieser Technologie erfordert ein tieferes Verständnis der zugrunde liegenden Prozesse. Diese Dissertation konzentriert sich auf $LiNi_xCo_yMn_zO_2$ (NCM) Kathodenmaterialien und zwei zentrale Schritte: die durch thermische Vorbehandlung ermöglichte Trennung sowie die anschließende Festkörperregeneration, mit besonderem Augenmerk auf den Einfluss von Verunreinigungen während der Regeneration.

(1) Thermische Vorbehandlung LIB-Elektroden

Die Auswirkungen einer thermischen Vorbehandlung unter verschiedenen Atmosphären und Temperaturen auf die Trennung von Kathodenmaterialien (NCM622) und Anodenmaterialien (Graphit) von Stromableitern wurden systematisch untersucht. Es wurde festgestellt, dass Luft- oder Sauerstoffatmosphären eine effiziente Trennung des Kathodenmaterials von der Aluminiumfolie bereits bei relativ niedrigen Temperaturen ermöglichen, wobei die strukturelle Degradation minimal bleibt. Graphitanoden hingegen zeigen in inerten oder reduzierenden Atmosphären eine gute thermische Stabilität. Allerdings weisen bereits zyklierte Anoden eine Grenzflächenhaftung auf, die eine effektive Trennung behindert.

(2) Strukturelle Regeneration verbrauchter NCM-Materialien

Die strukturelle Reparatur von gebrauchten NCM622-Kathodenpulvern wurde mittels multiskaliger Charakterisierungstechniken untersucht. Die Ergebnisse zeigen, dass die im gebrauchten Material beobachtete Degradation hauptsächlich mit Ni-Atomen in Li-Positionen zusammenhängt, was zu Kationenunordnungen und lokalen kubischen Domänen führt. Der Regenerationsprozess umfasst Re-Lithiierung, Sauerstoffaufnahme und Migration der Übergangsmetalle, wobei dieser stark von der Temperatur und dem Lithium-Ausgleichsverhältnis beeinflusst wird. Es wurde festgestellt, dass eine Abnahme der Übergangsmetallbesetzung in der Li-Schicht eng mit einer verbesserten Kapazitätsrückgewinnung korreliert, wodurch ein atomarer Einblick in Degradations- und Reparaturmechanismen jenseits konventioneller Phasenübergangsbetrachtungen ermöglicht wird.

(3) Einfluss von Verunreinigungen auf die strukturelle Regeneration verbrauchter NCM-Materialien

Die Auswirkungen von Verunreinigungen im verbrauchten NCM622-Material auf dessen Regeneration wurden systematisch aufgeklärt. Die Analyse identifizierte Al_2O_3, $AlPO_4$, AlF_3, Li_3PO_4, LiF, $Li_xPF_yO_4$, und Li_2CO_3 als Hauptverunreinigungen im verbrauchten Material, begleitet von einer Aluminium-Einlagerung, die vermutlich durch eine thermische Vorbehandlung verursacht wurde. Unter diesen spielen aluminium- und fluorhaltige Spezies eine dominierende Rolle im Regenerationsprozess und führen zu Al- und F-Einlagerungen im regenerierten Material. Konkret erfolgt die F-Einlagerung durch Substitution von Gitter-Sauerstoff, was zu Gitterverzerrungen und reduzierten Oxidationszuständen der Übergangsmetalle führt, während die Al-Einlagerung das Kristallwachstum entlang spezifischer Ebenen fördert. Beide Kontaminanten beeinträchtigen bei Anreicherung die elektrochemische Leistung und strukturelle Integrität, was die Notwendigkeit einer Kontrolle der Verunreinigungen vor der Regeneration unterstreicht, um eine langfristige Zyklenstabilität beim direkten Recycling zu gewährleisten.

Insgesamt klärt diese Arbeit die Mechanismen der thermischen Vorbehandlung, der Regeneration und der Wirkung von Verunreinigungen, vertieft das Verständnis der materialbezogenen Prozesse beim direkten Recycling und liefert praxisrelevante Erkenntnisse zur Optimierung von Recyclingprotokollen.

1. Background

1.1 Lithium-ion batteries

Electrochemical energy storage systems, such as batteries, have a rapidly expanding role in contemporary society. Since commercial inception in 1991, rechargeable Li-ion battery (LIB) technology has enabled the widespread deployment of portable electronic devices, such as mobile phones and portable computers, that are now a ubiquitous part of modern life. With the global effort to limit CO_2 gas emissions, LIBs are poised to have an even greater impact on society through green transformation of electricity delivery and transportation systems.

The fundamental structure of a LIB consists of a cathode and an anode separated by a separator and an electrolyte. As shown in **Fig. 1.1**, its operational mechanism is governed by the intercalation and deintercalation of Li^+ between the anode and cathode, with energy being stored and released as a result of electrochemical reactions [1, 2]. Specifically, during charging, lithium ions migrate from the cathode (typically a lithium metal oxide) to the anode (usually graphite), where they are intercalated, while electrons travel through an external circuit. During discharge, the process reverses, allowing energy release. The electrolyte, often a lithium salt in an organic solvent, facilitates ion transport while a separator prevents short circuits.

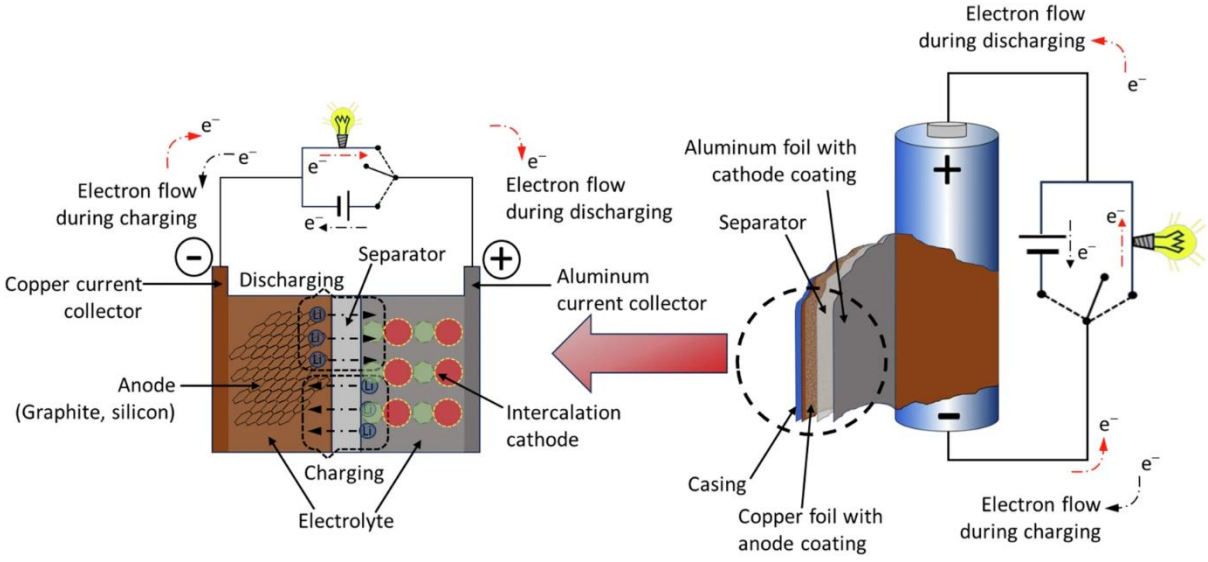

Fig. 1.1. Schematic illustration of the Li-ion battery. Adapted from reference [2].

1.2 Cathode materials for lithium-ion batteries

Cathode materials for LIBs play a crucial role in determining the battery's energy capacity, stability, and overall performance. These materials can be broadly categorized into three main

types based on their structural characteristics: olivine-type, spinel-type, and layered cathodes.

1.2.1 Olivine-type cathode materials

Since John Goodenough discovered the olivine phase's electrochemical characteristics in 1997 [3], lithium metal phosphates with ordered structures, $LiMPO_4$ (M=Co, Ni, Mn, Fe, Cu) [4-6], have gained significant attention as promising cathode materials for rechargeable lithium batteries. The olivine-structured $LiMPO_4$ (**Fig. 1.2a**) exhibits an orthorhombic lattice (space group: *Pnma*) with a slightly distorted hexagonally close-packed (HCP) oxygen arrangement. In this structure, oxygen ions form strong covalent bonds with P^{5+}, creating PO_4^{3-} tetrahedral polyanions and stabilize the entire three-dimensional framework. This structural feature ensures stable battery operation at elevated temperatures and provides exceptional safety under extreme conditions [7], which greatly enhances the appeal of olivine-type cathodes. However, the PO_4 tetrahedral unit shares the corners with metal ions and edges with Li ions at octahedral positions, forming a linear chain running along the *b* axis. As a result, there is no continuous network of MO_6 edge-sharing octahedra in $LiMPO_4$ materials, distinguishing it notably from spinel and layered cathodes. This leads to a confined lithium-ion transport through one-dimensional channels, resulting in inherently low electronic conductivity (**Fig. 1.2b**).

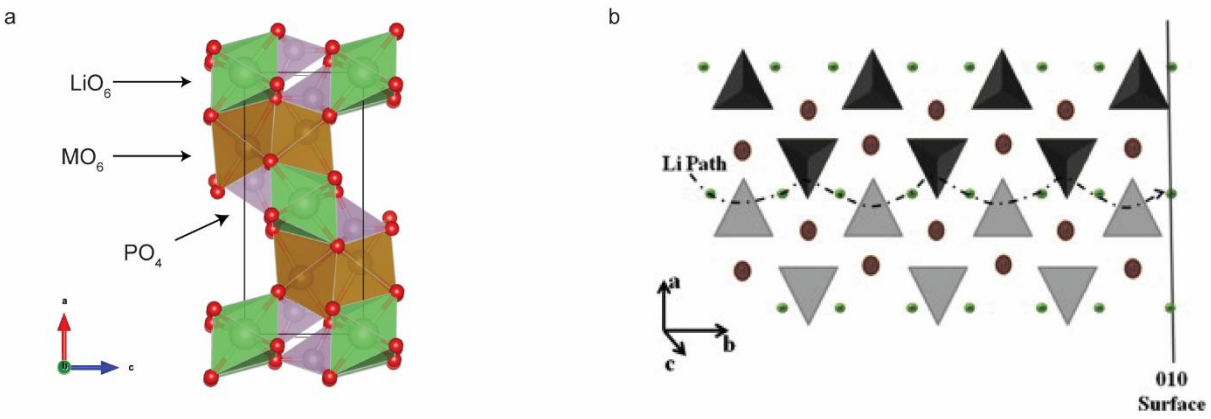

Fig. 1.2**.** (a) Schematic illustration of the $LMPO_4$ crystal structure. (b) Li diffusion along (010) direction in $LiMPO_4$ olivine Adapted from references [8].

Nonetheless, $LiFePO_4$ (LFP) has emerged a leading cathode material over the past decade [9-11]. It has a theoretical capacity of 170 mAh g^{-1}, with its electrochemical properties characterized by a flat voltage plateau at approximately 3.45 V in the galvanostatic profile (**Fig. 1.3**). This plateau corresponds to Li^+ (de)intercalation in the two-phase $LiFePO_4/FePO_4$ system, which plays a critical role in cell performance. However, early electrochemical studies indicated a limited extraction of ~0.6 Li per formula unit, yielding a capacity of only ~110 mAh g^{-1}

capacity [3]. The primary obstacle to achieving the full theoretical capacity of LFP is its inherently low electronic conductivity. To address this limitation, several strategies have been explored, including reducing particle size to shorten Li-ion diffusion paths and improve charge transport [12], coating particles with carbon or synthesizing carbon-composite materials to enhance electronic conductivity [13, 14], tailoring particle morphology and texture [15], and selective cation doping to increase intrinsic conductivity [16]. These strategies have significantly improved the practical capacity of commercial LFP, bringing it closer to its theoretical value and contributing to its widespread commercial success.

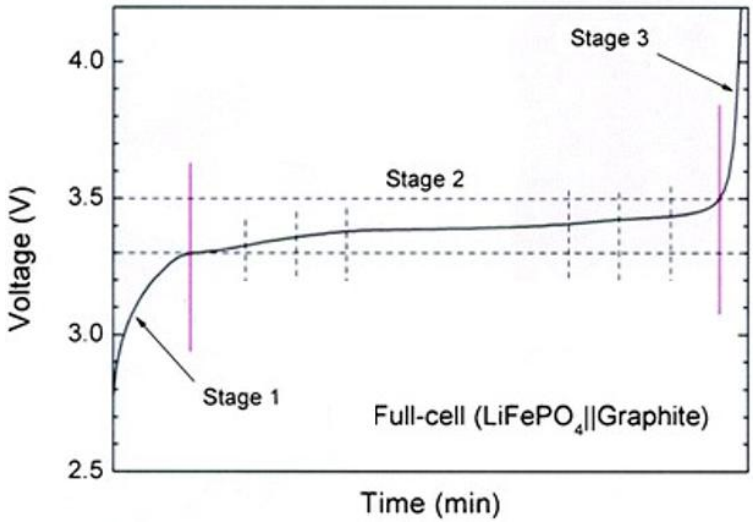

Fig. 1.3. Typical charge profiles for LFP-based full-cell. Adapted from reference [17].

1.2.2 Spinel-type cathode materials

Spinel-type cathode material, $LiMn_2O_4$ (LMO), was first studied in 1950s [18], introduced as cathode material at the University of Oxford in 1983 [19]. LMO crystallizes in a cubic close-packed (CCP) oxygen array (*Fd-3m*), where Li^+ occupies the 8a tetrahedral site, while Mn^{3+} or Mn^{4+} (in equal amounts) occupy the 16d octahedral site (**Fig. 1.4a**). The formula for LMO can be written as $[Li^+]_{8a}[Mn^{3+}Mn^{4+}]_{16d}[\square]_{16c}[O_4]_{32e}$ (where $\square$ represents the vacancy). This structural arrangement forms a stable three-dimensional $[Mn_2]_{16d}[\square]_{16c}[O_4]_{32e}$ framework, which facilitates fast Li-ion diffusion through edge-sharing 8a tetrahedral sites and adjacent face-sharing vacant 16c octahedral sites.

On the basis of these two Li-ion diffusion pathways, two redox couples contribute to its electrochemical capacity: $Mn^{4+}/Mn^{3.5+}$ (3–4.3 V vs. Li^+/Li) and $Mn^{3.5+}/Mn^{3+}$ (~3 V vs. Li^+/Li). As depicted in **Fig. 1.4b**, during charge (de-lithiation), LMO ($Mn^{3.5+}$) undergoes the following

reaction in the 4 V region (3.0-4.3 V): $2\mathrm{Li}M\mathrm{n}_2O_4 \rightarrow Li_{0.5}M\mathrm{n}_2O_4 + M\mathrm{n}_2O_4 + 1.5Li^+$, delivering a theoretical charge capacity of 148.2 mAh g^{-1}, resulting from the Li deintercalation from 8a site [20]. During discharge (lithiation), the reverse reaction occurs (4.0 V region). Further lithium insertion transforms $LiMn_2O_4$ ($Mn^{3.5+}$) into over-lithiated $Li_2Mn_2O_4$ (Mn^{3+}), producing an additional voltage plateau below 3 V, which is ascribed to the Li migration into the 16c octahedral site.

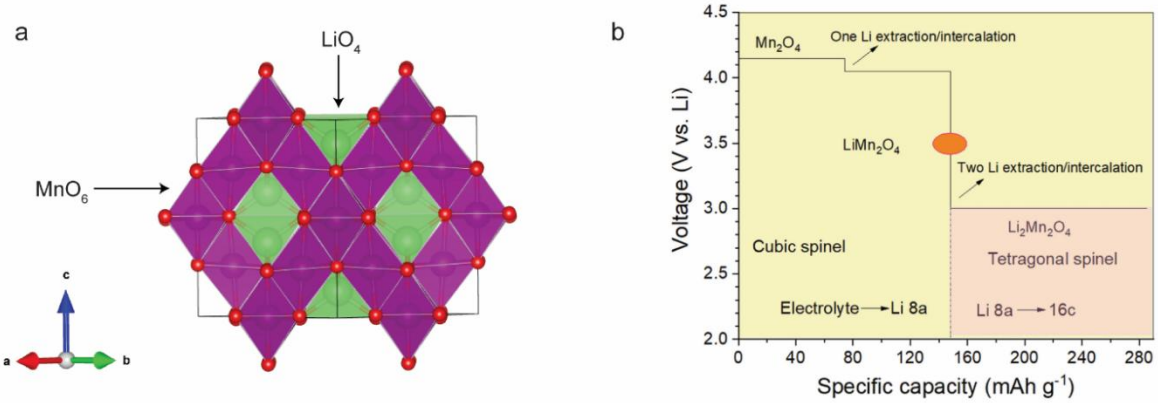

Fig. 1.4. (a) Schematic illustration of the LMO crystal structure. (b) Ideal voltage curves for Li^+ insertion process, where 4 V region showing two plateaus while 3 V region exhibiting a plateau ($Mn^{3.5+}/Mn^{3+}$), which is ascribed to inserting of Li^+ at 8a tetrahedron site to the empty 16c octahedral sites. Adapted from reference [18].

The second lithium intercalation doubles the theoretical capacity of LMO to 285.5 mAh g^{-1} [21]. Meanwhile, the Jahn–Teller effect of high-spin Mn^{3+} ($3d^4$, $t_{2g}^3 e_g^1$), causes a phase transition from cubic spinel to tetragonal spinel ($Li_2Mn_2O_4$), leading to rapid capacity fading. Hence, the use of this cathode is limited by a particular voltage range. Additionally, when the electrolyte includes $LiPF_6$ salt with trace amounts of HF, Mn^{3+} undergoes a disproportionation reaction: $2M\mathrm{n}^{3+} \rightarrow M\mathrm{n}^{2+} + M\mathrm{n}^{4+}$. This results in Mn^{2+} dissolution into the electrolyte during cycling, further degrading the cathode's long-term stability.

So far, tremendous efforts have been made to address these challenges. Key strategies include: (1) bulk doping to increase the average Mn valence and thus inhibiting the disproportionation mechanism of Mn ions [22, 23]; (2) surface coating to suppress the side reaction and Mn dissolution [24]; (3) morphology engineering to optimize the particle size and shape, improving the stress relief and damage tolerance of materials [25]. Such modification techniques have significantly improved the LMO's performance, making it a more viable candidate for broader adoption in energy storage systems.

1.2.3 Layered cathode materials

The concept of layered cathode material was first demonstrated in the early 1970s by Whittingham employing metal dichalcogenides (e.g. TiS_2) as an intercalation compound [26, 27]. In the early 1980s, Mizushima, Goodenough, and colleagues introduced Li_xCoO_2 (LCO) with an ordered rock-salt structure as a new cathode material for batteries in the early 1980s [28]. The widespread adoption of LCO followed the successful commercialization of the LCO/Graphite cell by Sony in 1991 [29]. The LCO cathode offers several advantages, including high energy density, excellent electrical conductivity, high open-circuit voltage (~4.0 V), and low self-discharge [10, 30, 31]. Structurally, LCO features an α-$NaFeO_2$-type layered structure (*R-3m*) in which oxygen atoms form a CCP arrangement (**Fig. 1.5a**). The Li and Co ions occupy the octahedral 3a and 3b sites, respectively, creating alternative cationic slabs along the *c* axis. The theoretical capacity of LCO is 274 mAh g^{-1}, when one mole of Li is deintercalated. However, in practical application, only about 140 mAh g^{-1}, roughly half of the theoretical capacity, can be utilized practically, because of the physical and chemical instabilities stemming from band overlapping between $Co^{3+/4+}$: t_{2g} and O^{2-}: 2*p* in the energy diagram (**Fig. 1.5b**). At high voltage range, the oxidation state changes from Co^{3+} into Co^{4+}, followed by the removal of electrons from the O^{2-}: 2*p* band, which in turn causes some phase transitions in the crystal structure and rapid capacity fading [32]. Several attempts have been made to replace Co with different transition metal (TM) elements that minimize the overlap with the O^{2-}: 2*p* band, and offer ecological and economic advantages.

$LiNiO_2$ (LNO) is known to be isostructural with LCO, which is generally denoted as the O3-structure based on Delmas notation [33]. As implied in the energy diagram (**Fig. 1.5b**), during the Li deintercalation, LNO only involves the e_g band, which lies well above the O^{2-}: 2*p* band. Therefore, the single electron in the redox active e_g band can be extracted during charging, giving rise to its significantly high theoretical capacity of 270 mAh g^{-1} and a practical capacity of over 200 mAh g^{-1} [34]. However, LNO is not a very promising cathode material as it suffers from critical drawbacks. It is challenging to synthesize a stoichiometric LNO with pure Ni^{3+} element at high temperatures, because of the instability of Ni^{3+} above 250 °C [35]. As a result, the presence of Ni^{2+} in the lithium 3a-site is generally unavoidable, resulting in poor rate capability. It has also been found that LNO undergoes a series of phase transitions at different intercalation states [36-38]. Such phase transitions can lead to severe capacity fading upon cycling.

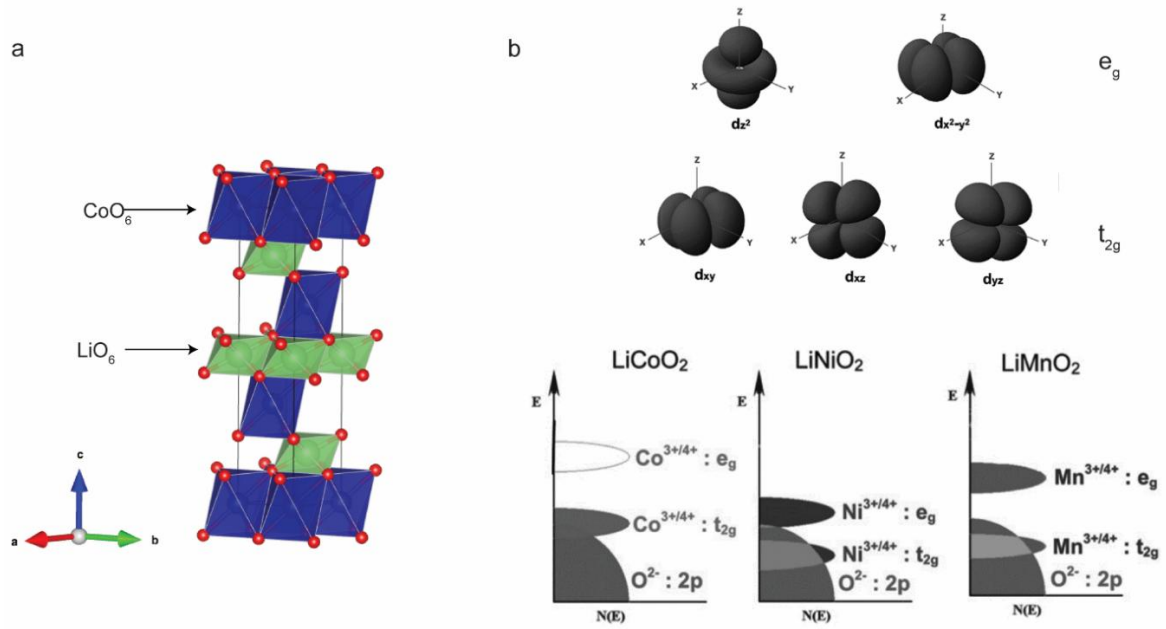

Fig. 1.5. (a) Schematic illustration of the LCO crystal structure. (b) The energy vs. density of states with the relative Fermi level and redox couples of $Co^{4+/3+}$, $Ni^{4+/3+}$, and $Mn^{4+/3+}$ for $LiCoO_2$, $LiNiO_2$, and $LiMnO_2$, respectively. Adapted from reference [10].

The $LiMnO_2$ has also been explored as an alternative layered cathode material, offering a potential replacement for LCO due to its high theoretical capacity of 285 mAh g^{-1} and higher energy density. Moreover, it is inexpensive, and it is environmentally benign compared to LCO and LNO. Although the chemical formula of $LiMnO_2$ is similar to that of LCO and LNO, the structure is not identical to the layered O3-structure as it crystallizes in an orthorhombic phase (*Pmmm*) [39]. The $LiMnO_2$ with a layered structure is not thermodynamically stable. It has been reported that an ion exchange method between Na^+ and Li^+ in layered $NaMnO_2$ yields a layered structure of $LiMnO_2$, but it undergoes a phase transition from the layered structure to a spinel structure ($LiMn_2O_4$), resulting in a poor cycle life on charge and discharge [40].

The $LiNi_xCo_yMn_zO_2$ (NCM-*xyz*) layered cathode materials, firstly introduced by Liu et al in 1999 [41], have garnered significant attention in recent years due to their synergistic advantages over cathodes based on a single transition metal. These mixed-transition-metal cathodes, which incorporate Ni, Co, and Mn in an α-$NaFeO_2$-type layered structure, are commonly referred to as NCM cathodes. They combine the high charge capacity of $LiNiO_2$, and the rate capability of $LiCoO_2$, and demonstrate the structural stability due to Mn^{4+} in the lattice. Although NCM111 has been widely studied, the demand for NCM cathodes with reduced cobalt content has grown to address sustainability concerns and mitigate the cost implications associated with critical material supply risks. This has led to the development of low-cobalt formulations such

as NCM442, NCM523, NCM622, and NCM811, which reduce raw material costs. Additionally, the increased nickel concentration enhances capacity, with NCM811 showing an improved specific capacity of 200 mAh g^{-1} when compared to NCM111 (160 mAh g^{-1}, both 4.3 V vs Li^+/Li) [42, 43]. However, higher nickel content also increases cathode reactivity due to the instability of Ni ions, which is one of the reasons resulting in severe capacity fading.

Alongside NCM-type cathodes, NCA cathodes ($LiNi_xCo_yAl_zO_2$) have emerged as frontrunners in the automotive industry [44]. The optimized NCA composition, with 5 wt% Al (NCA-80, $LiNi_{0.8}Co_{0.15}Al_{0.05}O_2$), offers a specific capacity comparable to that of NCM811 (200 mAh g^{-1}, 4.3 V vs Li^+/Li). Unlike NCM cathodes, NCA materials (e.g., NCA-80, NCA-81, NCA-82) exclude Mn, which eliminates manganese ion dissolution and contributes to improved capacity retention. Additionally, aluminum incorporation enhances thermal stability. As a result, NCA cathodes are frequently chosen for "long-range" electric vehicles [45-47], such as those produced by Tesla, which achieve driving ranges exceeding 500 km.

Overall, each type of cathode material has its specific applications. For instance, LCO is widely used in portable electronics for its high energy density [48], while LMO finds applications in power tools and hybrid vehicles owing to its thermal stability and high-rate capability [49]. As the global shift toward electrified transportation accelerates to meet decarbonization targets, the cathode material market continues to evolve, driven by cost, performance, and policy considerations. Currently, NCM materials still dominate globally, accounting for roughly 45–60% of total demand depending on the year [50, 51]. Within this category, high-nickel variants (e.g., NCM811 and above) prevail in premium electric vehicles due to their superior energy density. NCA, once a major competitor to high-nickel NCM, has seen its share decline but remains strategically important in long-range and performance-oriented platforms [52]. Meanwhile, mid-nickel, high-voltage formulations are gaining momentum as a balanced option between cost, safety and performance [53], while low-nickel grades are losing competitiveness due to their relatively low energy density and high cobalt content [54].

1.3 Cathode degradation in NCM cathode-based LIBs

High- and mid-nickel NCM, widely used in EVs, typically have a service life of approximately 6–10 years depending on the use scenario [55, 56]. Cathode degradation is a primary factor resulting in this limited longevity. The primary degradation mechanism for NCM materials includes: TM dissolution as the consequence of HF attack, intragranular and intergranular

cracks formed at high state of charge (SOC) and intensive cycling, and structural degradation mainly occurring at the material's surface induced by layered-spinel-rock-salt phase transition combined with oxygen release.

1.3.1 Transition Metal Dissolution

The dissolution of TM ions from the cathode into the electrolyte often occurs, during battery cycling, resulting in capacity degradation because of the loss of Li-ion insertion sites in the host structure. This phenomenon is mostly the result of the corrosion caused by electrolyte decomposition by-products, such as HF, and is further accelerated at elevated temperatures and high operating voltages. It is widely accepted that the electrolyte solvents might contain trace amounts of water introduced during manufacturing, which react with lithium salts (e.g., $LiPF_6$, $LiPF_6 + H_2O \rightarrow LiF + 2HF + POF_3$) [57], yielding acidic species that contribute to cathode degradation. Alternatively, HF can also be generated through reactions between organic solvents and PF_6^-, such as the one-electron oxidation of EC. In addition, TM dissolution can result from the formation of low-valence metal ions due to lattice oxygen loss during cycling. The lower-valence metal ions are more soluble in the electrolyte than their higher-valence counterparts, further accelerating degradation.

1.3.2 Intragranular and Intergranular Cracks

Mechanical failure of NCM cathode particles, caused by the generation and development of cracks, has been widely considered a significant factor influencing battery degradation [58]. Cracks have been observed in both intragranular regions (within the single crystal primary grains and particles) and intergranular spaces (along grain boundaries and between primary particles), as illustrated in the **Fig. 1.6**.

High cut-off voltage cycling induces a high density of intragranular cracks in NCM cathode particles, as follows from the post-mortem analysis. This occurs because the significant strain associated with extensive de-lithiation/lithiation cannot be effectively accommodated by the densely packed primary particles. Consequently, inhomogeneous mechanical stress applied to each primary grain is relieved through the formation of dislocations. To reduce the accumulated strain in the dislocation cores, Li and O are released from the affected area [59]. With further cycling, these dislocation cores gradually develop into premature cracks. Notably, with increasing cycles, the length of the intragranular crack along the (003) plane can reach around

440 nm, ultimately leading to complete cracks that cause fragmentation and dissociation of cathode grains [60, 61].

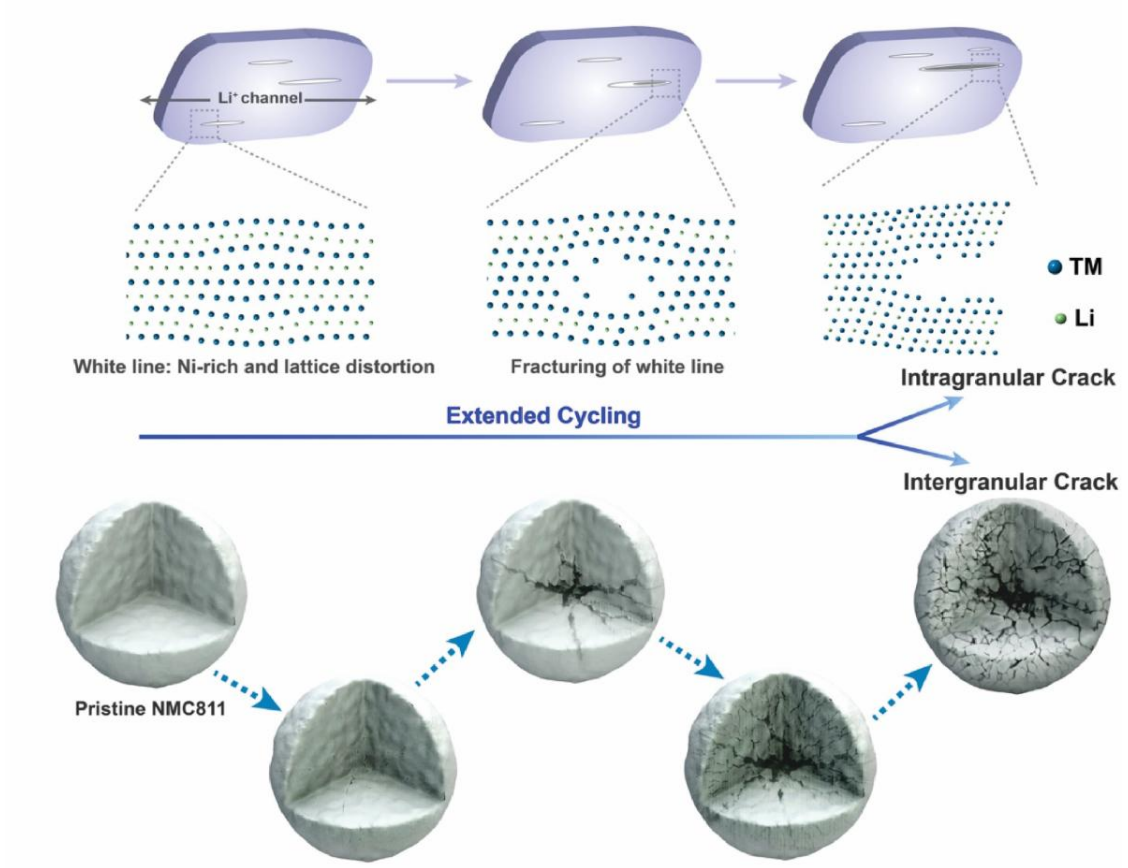

Fig. 1.6. Schematic illustration of the microstructural features of the intragranular and intergranular crack of NCM cathode. Adapted from reference [62].

In addition, intergranular cracking also arises from inhomogeneous lattice contraction and expansion during repeated cycling at high cut-off voltages[63]. This cyclic contraction and expansion within primary particles lead to grain disintegration and the loss of electrical contact between active material particles. Furthermore, phase transformations and oxygen release reactions, triggered by high-temperature exposure, can accumulate stress at grain boundaries, further promoting intergranular cracking [64, 65]. Overall, the crack phenomenon has been frequently discussed in the literature and represents a combined effect of intra- and intergranular cracks. The severity of cracking becomes more pronounced with higher Ni content, increasing cycling number, and higher SOC.

1.3.3 Structural degradation

Structural degradation in NCM cathodes is related to a phase transition from the layered phase to rock-salt or spinel phases, mostly at the material's surface [66]. It is well-known that the

rhombohedral (*R-3m*), spinel (*Fd-3m*), and rock-salt (*Fm-3m*) structures all rely on a cubic-closed framework packing of oxygen atoms, with cations occupying either tetrahedral or octahedral sites. As such, the origin of the structural degradation is fundamentally linked to the cation migration (**Fig. 1.7**). The migration of TMs from their octahedral sites into the alternating Li octahedral site, driven by excessive Li deintercalation (increased formation of Li vacancies), is considered an initial step in this degradation process [67]. Such atomic migration triggers a phase transition from the original layered structure to a $LiMn_2O_4$-type spinel phase and is accompanied by an oxygen release reaction.

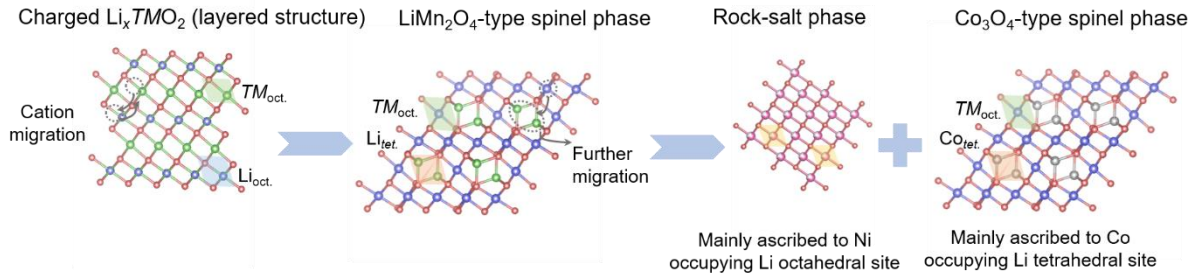

Fig. 1.7. Schematic illustration of the structural degradation in NCM cathode.

The studies using transmission Electron Microscopy (TEM) and X-ray absorption (XAS) on charged NCM cathodes reveal that Ni is the first cation to migrate into the Li layer and thus has a large contribution on the structural instability of NCM cathodes [68-70]. Moreover, the migration pathways of Ni and Co into Li octahedral sites differ. The Co ions pass through neighboring tetrahedral sites before occupying the octahedral Li sites, whereas the Ni ions migrate directly from the transition metal layers to Li sites, bypassing the tetrahedral positions due to their instability in tetrahedral coordination [71].

While both migration pathways lead to the $LiMn_2O_4$-type spinel phase, prolonged migration of Ni ions leads to the formation of the NiO-type rock-salt (*Fm-3m*) phase. On the other hand, Co atoms tend to migrate into Li tetrahedral site, forming a Co_3O_4-type spinel phase, which retains a higher oxygen content compared to the CoO-type rock-salt phase [72]. As such, the degraded phases in NCM cathodes likely include three types: (1) NiO-type rock-salt phase; (2) Co_3O_4-type spinel phase; (3) $LiMn_2O_4$-type spinel phase. The existence and content of such degraded phases depend on the relative fraction of Ni, Mn and Co in the NCM materials and the material's degradation level.

1.4 Recycling technologies for spent NCM cathode-based LIBs

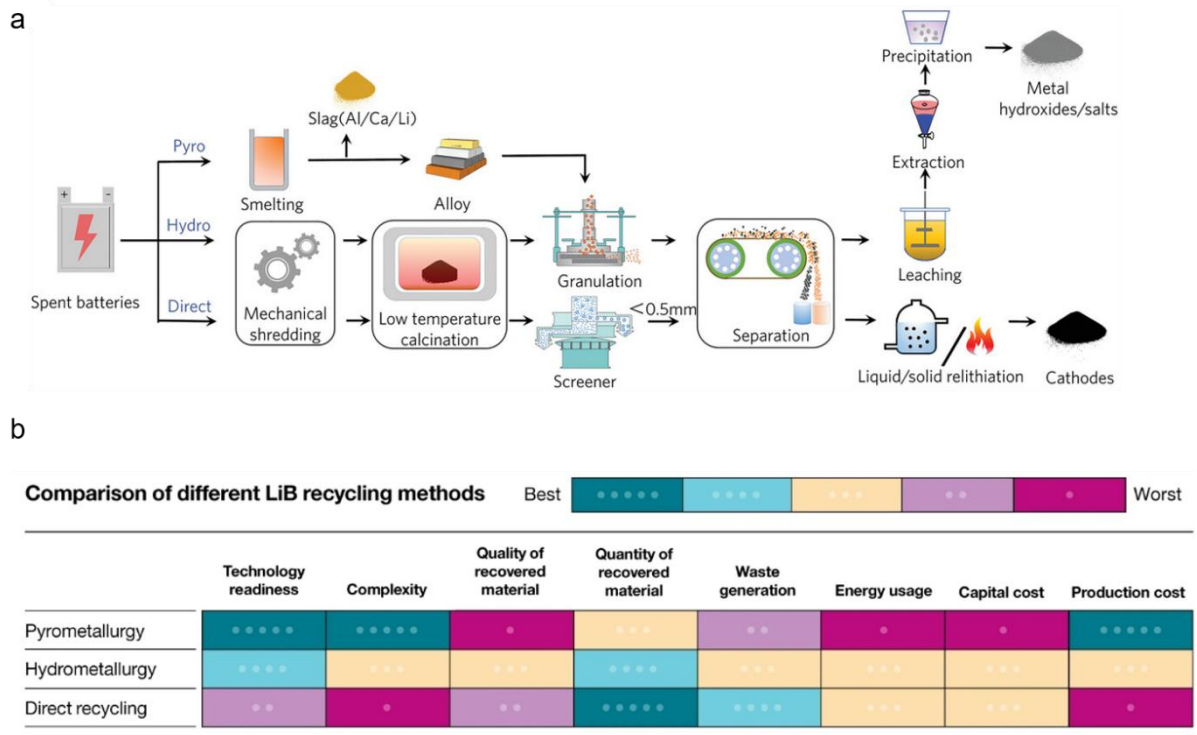

Fig. 1.8. (a) Schematic diagram of pyrometallurgical, hydrometallurgical and direct recycling processes. Adapted from reference [73]. (b) Comparison of different recycling methods. Adapted from reference [74].

Battery demand in the energy sector, encompassing both EVs and stationary storage applications, reached a historic milestone of 1 TWh in 2024 [51]. This growth was predominantly driven by EV sales, with demand for EV batteries exceeding 950 GWh, representing a 25% increase compared to 2023 [51]. Forecasts suggest that EV battery demand will surpass 3 TWh by 2030 [51, 75]. As a result, ensuring a sustainable and resilient supply of battery materials has become an urgent priority [55]. At the same time, NCM-based batteries, which have dominated EV applications in previous years, are now approaching retirement, posing significant environmental challenges [54]. In this context, the development and implementation of efficient recycling strategies are essential to safeguard resources and mitigate environmental impact [76]. Currently, the recycling technologies for spent NCM cathode materials primarily focus on three main approaches: hydrometallurgy, pyrometallurgy, and direct recycling (**Fig. 1.8a**) [73]. Each of these methods has its own advantages and limitations, making the choice of recycling strategy highly dependent on factors such as economic viability, environmental impact, and the specific composition of the cathode material (**Fig. 1.8b**). As the EV industry continues to expand, optimizing these recycling technologies will be crucial for ensuring the sustainable recovery of valuable metals and minimizing the environmental footprint of battery waste.

1.4.1 Hydrometallurgy

The hydrometallurgical processes, combined with mechanical pre-treatment, offer a viable method for processing spent LIBs and recovering valuable metals, as well as other battery components such as graphite and Al [77]. These processes have been successfully commercialized, particularly for recycling spent NCM cathode-based LIBs. Notably, China is home to two of the largest LIB recycling companies, GEM High-Tech Co. and Brunp Co. [78, 79], which employ closed-loop hydrometallurgical processes to re-synthesize cathode materials, demonstrating the feasibility and scalability of this approach.

The mechanical pre-treatment involves shredding, sieving, and physically separating the components of spent LIBs. However, due to the explosive and flammable nature of charged LIBs, safety measures such as deactivation (e.g., discharging or cryogenic treatment) or conducting the process in a strictly inert environment are essential. Cryogenic treatment and the use of inert gases like CO_2 or argon can be energy-intensive [80, 81], adding to the operational costs. Additionally, the yield of valuable fine electrode materials after mechanical treatment is often limited, with laboratory experiments, such as those by Diekmann et al. [82], reporting recovery rates of around 75%.

The recovered fine electrode materials, often called black mass, which consists primarily of cathode and anode particles, then undergo a leaching process. This involves leaching them in acidic solutions to dissolve both lithium and other metals. However, the efficiency of this process is constrained by the kinetics of leaching and the solubility of metal compounds. A low solid-to-liquid ratio in the leaching process can result in large volumes of waste solution. Subsequently, metals are recovered as metal compounds or pure metals through precipitation, solvent extraction, and electrolysis. For closed-loop cathode production, achieving extremely high purity in the separated metals is critical. Notably, for spent NCM-based LIBs, the metal recovery process is primarily related to a co-precipitation process to generate NCM cathode precursors, thus avoiding the need for separation among Ni, Co and Mn.

The complexity of LIBs and the wide range of used materials make the complete separation of battery components challenging [83]. As a result, the economic viability of these processes heavily depends on the yields of high-value metals like cobalt and nickel, which are necessary to offset operational costs. Without sufficient recovery of these metals, the lower market value of most LIB materials often fails to cover the expenses of the recycling process. In addition,

the large volumes of waste solution generated pose significant environmental concerns, creating a further barrier to the broader application of this technology.

1.4.2 Pyrometallurgy

The primary objective of pyrometallurgical routes is to produce cobalt- or nickel-bearing alloys. One of the key advantages of pyrometallurgical processes is their ability to process LIBs alongside ores, other types of batteries, or industrial wastes simultaneously. In certain processes, such as those employed by Umicore [84], pre-treatment of LIB packs is unnecessary, and charged batteries can be directly fed into the reactor. However, further refining steps, typically still involving leaching and solvent extraction, are required to separate Co, Ni, and Cu. Additionally, the furnace necessitates off-gas treatment to mitigate the release of toxic emissions, such as dioxins and furans [85]. Volatile metals like Zn and Cd can be recovered through distillation. Most Li and Al are lost to the slag and are generally not recovered. While it is possible to recover Li from flue dust and slag as Li_2CO_3 through leaching and precipitation after grinding the slag into fine particles (e.g., 100 μm) [86], this additional recovery step is only economically viable when lithium prices are sufficiently high to offset the operating costs. Organic components, graphite and Al, are utilized as energy sources or reductants during the smelting process.

The economic feasibility of pyrometallurgical processes heavily depends on the recovery yields and market prices of Co, Ni, and Cu [87]. However, the ongoing trend in LIB chemistry toward reducing cobalt and nickel content poses a challenge to the sustainability of pyrometallurgy as a primary recycling method for LIBs. Despite this, pyrometallurgical processes remain effective for recycling LIBs as a secondary feed material alongside other industrial metal source. This approach ensures that pyrometallurgy continues to play a complementary role in the broader LIB recycling ecosystem.

1.4.3 Direct recycling

Direct recycling represents a sustainable approach to the recovery of spent LIBs. Currently, the direct recycling of CAM has garnered most attention due to their high intrinsic value compared with other cell components. This process seeks to preserve the original structural framework and electrochemical functionality of the CAM while repairing degradation accumulated during cycling. It typically involves disassembling discharged cells, separating the cathode composite from the current collector, and restoring the active material through re-lithiation. By retaining

the original structure of CAM, direct recycling significantly reduces energy consumption, minimizes environmental impact, and lowers operational cost, rendering it an attractive alternative to conventional pyrometallurgical and hydrometallurgical approaches.

However, despite its promising potential, direct recycling is still in the pilot-scale development stage, with several technical and operational challenges hindering its further commercialization. A key challenge lies in ensuring the quality and consistency of the refreshed materials. For instance, variations in the degradation mechanisms of spent LIBs might lead to non-uniform restoration of the CAM. Therefore, achieving precise control over re-lithiation processes is critical to restoring the material's electrochemical performance, including capacity, cycle life, and rate capability, to levels comparable to those of virgin materials. Additionally, the scalability of direct recycling processes requires advancements in efficient separation techniques, cost-effective re-lithiation methods, and robust quality assessment protocols. Addressing these challenges will be essential to realizing the full potential of direct recycling as a sustainable and economically viable solution for LIB waste management, contributing to the development of a circular economy in the battery industry.

1.5 Motivation and objectives of the thesis

With the rapid expansion of the electric vehicle industry, the recycling of spent lithium-ion batteries has become increasingly critical, driven by environmental concerns and the need for sustainable resource utilization. Among various recycling strategies, direct recycling has emerged as a promising next-generation technology due to its potential to retain material value and reduce processing costs. While significant progress has been made in this field, several critical challenges remain insufficiently addressed. This thesis aims to investigate these often-overlooked aspects, with a particular focus on the separation, structural repair, and impurity treatment during the direct recycling of CAM. By developing a deeper understanding of these key processes, this work seeks to contribute to the advancement of more efficient and sustainable battery recycling technologies. The research work is organized into three parts, as briefly illustrated in **Fig. 1.9**:

(1) **Separation of electrode active materials from Al/Cu current collector**. This study investigates the thermal treatment of NCM622 (cathode) and graphite (anode) electrodes to separate them from Al and Cu current collectors. It establishes the relationship between separation efficiency and temperature under various atmospheres and highlights the effects of

thermal conditions on the structural degradation of electrode materials during pretreatment.

(2) **Mechanisms behind structural repair in spent layered cathodes**. Using XRD, XAS and ^{6}Li solid-state NMR, this part explores the mechanisms of structural degradation and repair in spent NCM622. It identifies the degraded structures in the spent material and tracks long- and short-range structural evolution during regeneration, providing atomic-level insights that go beyond traditional phase-transition models.

(3) **Impurity effect on direct recycling of spent layered cathodes**. Given that impurities might be introduced in the spent material during pretreatment, this study focuses on identifying the specific impurity species and their influence on the regeneration. The findings shed light on the roles and mechanisms of various impurities during regeneration, contributing to more effective recovery of high-quality cathode materials and promoting circularity in the lithium-ion battery lifecycle.

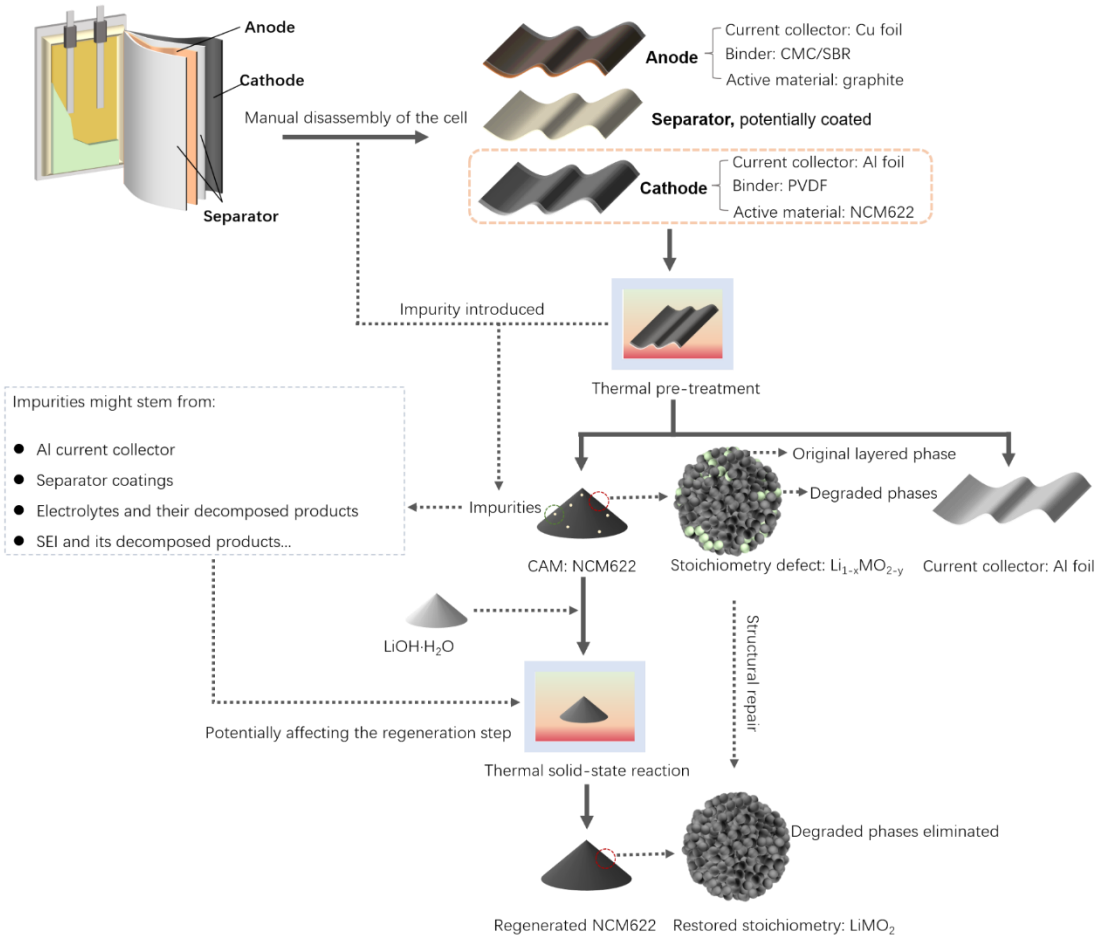

Fig. 1.9. Schematic illustration of the direct recycling processes in this thesis

2. X-ray techniques

Since the discovery of X-rays by Wilhelm Conrad Roentgen at the end of the 19th century and the pioneering work on X-ray diffraction by crystals by Max von Laue and the Braggs (William Henry Bragg and William Lawrence Bragg) [88, 89], X-ray-based techniques have undergone tremendous advancements, becoming indispensable tools for material characterization. Over the century, these methods have evolved from fundamental scientific discoveries to state-of-the-art analytical techniques, enabling detailed insights into the structural, chemical, and electronic properties of materials. In the field of materials science and engineering, X-ray techniques have been widely adopted to study a diverse range of materials, from metals and ceramics to polymers and nanomaterials, driving innovation and technological progress. This chapter provides a brief introduction to the X-ray techniques employed in this thesis for material characterization.

2.1 Generation of X-ray radiation

X-rays are high-energy electromagnetic waves with a wavelength between 10^{-3} and10^{1} nm [90]. They are typically generated using sealed tubes, rotating anodes, or synchrotron radiation sources. In sealed tubes and rotating anodes, electrons emitted from a heated tungsten filament in a vacuum are accelerated by a high-voltage field and directed onto a target. X-rays are then generated via two mechanisms: (1) Bremsstrahlung [91], in which decelerating electrons emit a continuous spectrum of X-ray photons, and (2) characteristic radiation [91], in which inner-shell electrons are ejected and vacancies are filled by outer-shell electrons, releasing photons with energies characteristic of the target material.. Therefore, the radiation coming out of a sealed tube or a rotating anode is a superimposition of a continuous spectrum and of characteristic radiations as presented schematically in **Fig. 2.1** [91, 92]. Notably, XRD characterization primarily use the most intense characteristic radiation, K_α, filtering out other wavelengths using materials with absorption edges tailored to suppress unwanted radiation, such as K_β and the continuous spectrum. The K_α emission itself consists of two closely spaced components, $K_{\alpha 1}$ and $K_{\alpha 2}$, corresponding to electronic transitions from $2p_{3/2}$ to 1s, and $2p_{1/2}$ to 1s, respectively. A list of the common target materials with the wavelength of their characteristic radiations K_α and K_β, together with the minimum excitation potential and the required filters is given in **Table 2.1**.

Synchrotron radiation, on the other hand, is produced by relativistic electrons or positrons circulating at near-light speeds. High-energy electrons, produced by a high-power electron gun,

are injected into a booster ring for acceleration and then transferred to a storage ring, where the radiation is emitted. Modern storage rings are typically polygonal, with dipole magnets guiding the electron beam between straight sections [93]. In third-generation synchrotrons, wigglers or undulators are generally used, which consist of a periodic arrangement of magnets. The electrons are then forced to follow a sinusoidal path in the orbital plane of the ring leading to the emission of photons. In simple terms, the emitted photon energy spans a broad spectrum from the infrared to γ-rays [93]. Synchrotron radiation offers significant advantages, including a wide energy range (up to 500 keV or more), enabling measurements through thick samples, and at exceptionally high brilliance, making it ideal for high-quality, time-resolved, and in situ studies. However, access to synchrotron facilities requires beam time applications, limiting the number of experiments that can be performed. This makes synchrotron radiation a powerful but specialized tool for advanced material characterization.

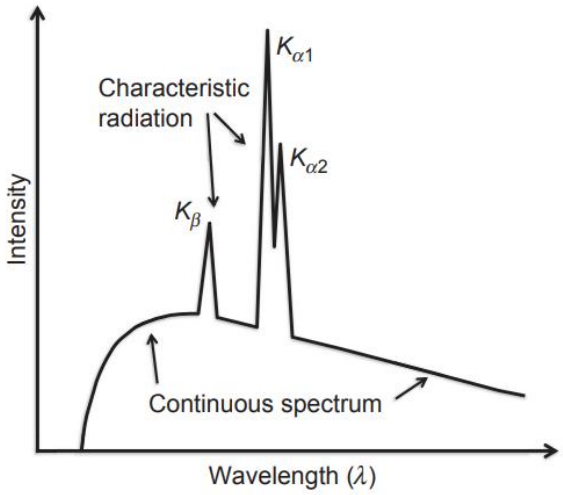

Fig. 2.1. Intensity over wavelength distribution of the X-ray radiation produced by a sealed-tube showing the continuous and the characteristic spectrum. Adapted from reference [92].

Table 2.1. List of several common target materials and corresponding wavelength of K_{α} and K_{β} radiation in nanometer together with the minimum excitation potential in kV and the appropriate filter material [92, 94, 95].

Target	$K_{\alpha 1}$ (nm)	$K_{\alpha 2}$ (nm)	$K_{\alpha\ mean}$ (nm)	K_{β} (nm)	Excitation Potential (kV)	Filter
Cr	0.22897263	0.22936513	0.22910346	0.20848881	5.98	V
Mn	0.21018543	0.21058223	0.21031770	0.19102164	6.54	Cr
Fe	0.19360413	0.19399733	0.19373520	0.17566055	7.11	Mn
Co	0.17889961	0.17928351	0.17902758	0.16208263	7.71	Fe
Ni	0.16579301	0.16617561	0.16592054	0.15001523	8.33	Co
Cu	0.15405929	0.15444274	0.15418711	0.13922346	8.98	Ni
Mo	0.07093000	0.07135900	0.07107300	0.06322880	20.0	Zr

2.2 X-ray Diffraction

The powder X-ray diffraction (XRD) is a powerful analytical technique used to study the long-range structure of crystalline materials. It is based on the diffraction of X-rays by periodic atomic planes and the angle- or energy-resolved detection of the diffracted signal.

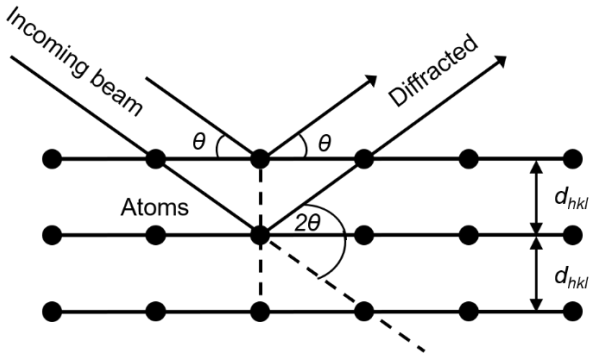

Fig. 2.2. Geometrical condition for diffraction from lattice planes.

The interpretation of the XRD phenomenon (constructive interferences) has been given by W.L. Bragg [96]. **Fig. 2.2** gives the details about the geometrical condition for diffraction and the determination of Bragg's law. Bragg's law is given in **Eq. 2.1**.

$$n\lambda = 2d_{hkl}\sin(\theta) \quad \text{(Eq. 2.1)}$$

In this equation, n is the order of diffraction, λ the wavelength of the incident beam in nm, d_{hkl} the lattice spacing in nm and θ the angle of the diffracted beam in degree. In a polycrystalline, untextured material with fine grains, diffraction occurs for each lattice plane and direction that satisfies the Bragg's law in the case of constructive interferences. This results in the occurrence of diffraction cones appearing in the form of so-called Debye rings or diffraction rings if detected by a plane detector.

The total intensity diffracted by a unit cell is determined by summing the contributions from individual atoms [91]. The diffracted intensity $I_{(hkl)}$ is proportional to the square of the crystallographic structure factor $F_{(hkl)}$, a complex quantity defined as **Eq. 2.2** [97]:

$$F_{(hkl)} = \sum_{j=1}^{N} f_j e^{2\pi i(hx_j+ky_j+lz_j)} \quad \text{(Eq. 2.2)}$$

In this equation, f_j is the atomic scattering factor of atom j, (x_j, y_j, z_j) the relative atomic positions in the unit cell, and hkl the Miller indices of the diffracting planes. The summation j runs over all atoms in one-unit cell [97].

The total diffracted intensity for a family of lattice planes $I_{(hkl)}$ depends on several factors, combined as follows (**Eq. 2.3**):

$$I_{hkl} \propto |F(hkl)|^2 \cdot L(\theta) \cdot P(\theta) \cdot A \cdot T(\theta) \quad \text{(Eq. 2.3)}$$

where $L(\theta)$ is Lorentz Factor accounting for the geometric effects of diffraction and given by $1/\sin(2\theta)$, $P(\theta)$ the Polarization Factor considering the effect of X-ray polarization on the diffracted intensity which is equal to $(1+\cos^2(2\theta))/2$, A the Absorption Factor. $T(\theta)$ is the Temperature Factor, also known as the Debye-Waller factor, accounts for the effect of atomic thermal vibrations on the diffraction intensity, and expressed as $f_a e^{-B\cdot sin^2(\theta)/\lambda^2}$ [90-92].

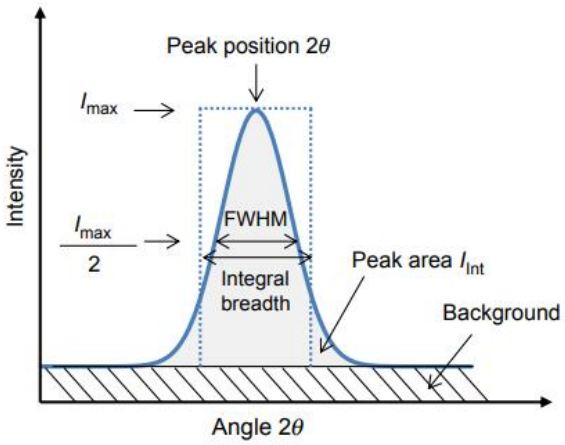

Fig. 2.3. Diffraction peak and information content that can be extracted. Adapt from reference [92].

As real materials inevitably contain imperfections, the intensity distribution of the signal diffracted by considered family of *hkl* planes can be affected. The shape of the diffracted signal is influenced by different factors, and the resulting signal is then a convolution of the following contributions [98]:

- The instrumental broadening which depends on the X-ray source, primary and secondary optics, detector, etc.;
- Composition heterogeneity within the analyzed crystallites (leading to a distribution of lattice constants and so to a possible broadening);
- The size of the coherently diffracting domains (also called crystallite size);
- Crystal defects like dislocations, stacking faults, twins, etc.;
- Inhomogeneous strains and macrostrains.

In general, diffraction data are represented as intensity distribution as a function of the 2θ angle.

The information content that can be extracted is represented in **Fig. 2.3**.

2.3 X-ray absorption spectroscopy

X-ray absorption spectra (XAS) of any material being it atomic or molecular in nature are characterized by sharp increases in absorption at specific X-ray photon energies, which are characteristic of the absorbing element. These sudden increases in absorption are called absorption edges, which correspond to the energy required to eject a core electron into the LUMO (Lowest Unoccupied Molecular Orbital) or to the continuum thus producing a photoelectron. The absorption discontinuity is known as the K-edge, when the photoelectron originates from a 1s core level, and an L-edge when the ionization is from a 2s or 2p electron. **Fig. 2.4** shows a typical energy level diagram. The following content mainly focuses on K-edge spectroscopy.

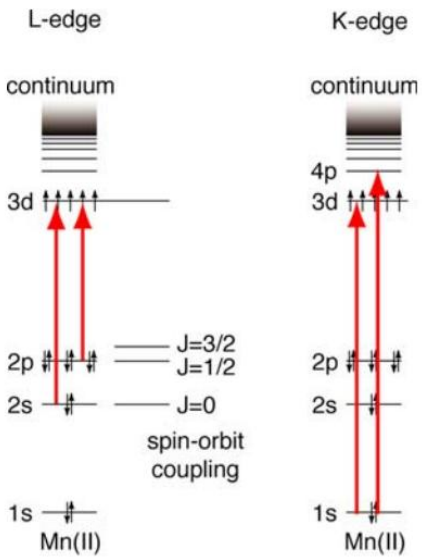

Fig. 2.4. The energy level diagram for L-edge (L_I, L_{II}, and L_{III}) transitions (2s and 2p to 3d) and K-edge transitions (1s to 3d and 4p) for Mn (II). The energy levels are not drawn to scale. Adapted from reference [99].

2.3.1 X-ray absorption near-edge structure

X-ray absorption near-edge structure (XANES) spectra provide detailed information about the oxidation state and coordination environment of the metal atoms (**Fig. 2.5**). The K-edge absorption edge energy increases with increasing oxidation state. In general, the rising edge position shifts when the effective number of positive charges (in a simplified view, oxidation state) changes resulting from 1s core hole shielding effects [100]. In an atom with one electron, for example, the electron experiences the full charge of the positive nucleus. However, in an

atom with many electrons, the outer electrons are simultaneously attracted to the positive nucleus and repelled by the negatively charged electrons. The higher the oxidation state of the metal, the more positive the overall charge of the atom, and therefore more energy is required to excite an electron from an orbital. Conversely, the XANES spectrum shifts to a lower energy when there is more negative charge on the metal.

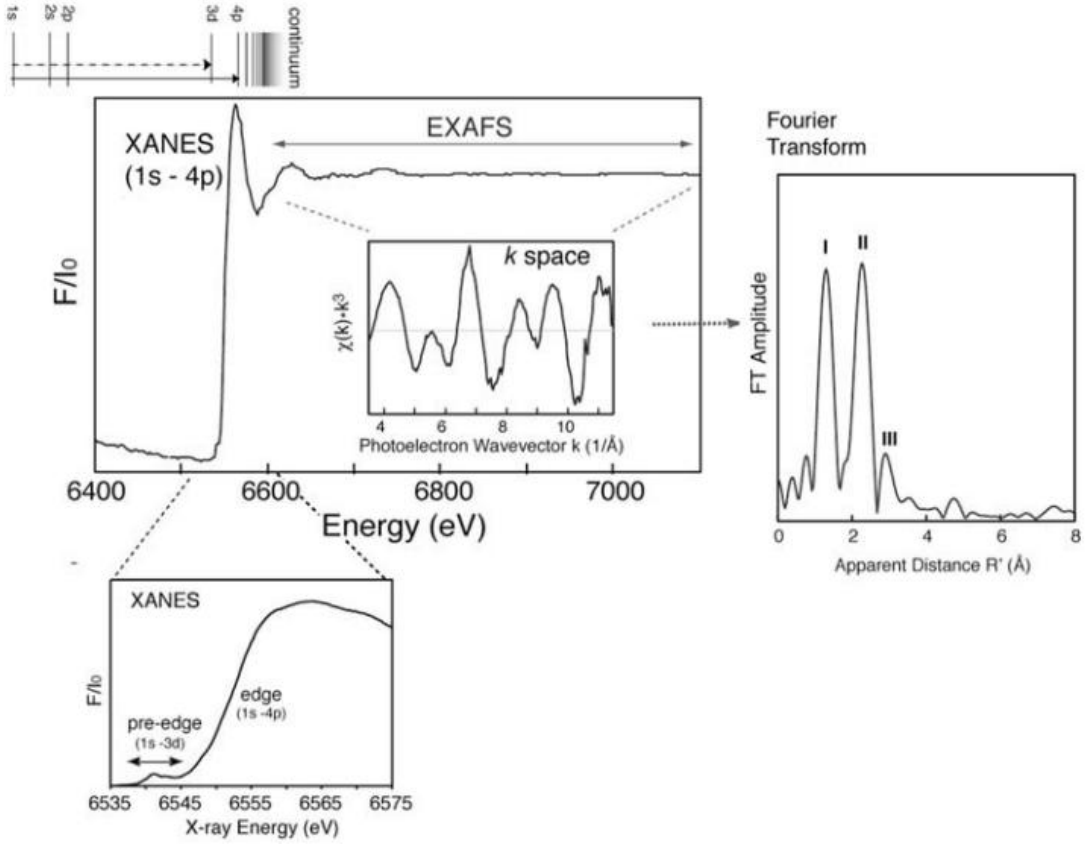

Fig. 2.5. The example of Mn K-edge XANES and EXAFS spectra. Adapted from reference [99].

The dominant contribution to the K-edge spectrum comes from 1s → np transitions, where n*p* represents the lowest unoccupied *p* orbital of the absorbing atom. This transition, with $\Delta l = 1$ (*l* is the orbital momentum quantum number), is quantum mechanically allowed and is typically intense. For transition metals with partially occupied *d* orbitals, additional insights can be gained by examination of pre-edge features that result from 1s to (n −1)d transitions. These are relatively weak in intensity ($\Delta l = 2$; hence, formally forbidden or dipole-forbidden), but they can be detected as they occur at energies slightly less than that of the main absorption edge [99]. The pre-edge peak intensity increases when the ligand environment is perturbed from octahedral symmetry [99].

2.3.2 Extended X-ray absorption fine structure

At energies somewhat greater than the LUMO level, the absorption of an X-ray provides sufficient energy to cause the absorbing atom to release the electron (ionize). Any excess energy is converted into the translational kinetic energy, which can also be described in terms of the wavelength associated with the electron's wave-like nature. The Extended X-ray Absorption Fine Structure (EXAFS) modulations, shown in **Fig. 2.5**, are a direct consequence of the wave nature of the photoelectron with the velocity *v* imparted to the photoelectron by the energy of the absorbed X-ray photon, which is in excess of the binding or threshold energy for the electron. The kinetic energy of the photoelectron is given by the following relation (**Eq. 2.4**) [99, 101]:

$$(\mathrm{E} - \mathrm{E}_0) = \frac{1}{2} m_e v^2 \qquad \text{(Eq. 2.4)}$$

where E is the X-ray photon energy, E_0 is the ionization or threshold energy for the electron, and m_e is the electron mass. The EXAFS modulations are better expressed as a function of the photoelectron wave vector k ($k = 2\pi/\lambda$, where λ is the wavelength given by the de Broglie relation, $\lambda = h/m_e \cdot v$, h is Planck's constant), which is expressed as follows (**Eq. 2.5**) [99, 101]:

$$k = \frac{2\pi}{h}[2m_e(E - E_0]^{1/2} = 0.512(E - E_0)^{1/2} \qquad \text{(Eq. 2.5)}$$

where E and E_0 are expressed in electron volts (eV) and k has the units of inverse angstroms ($Å^{-1}$).

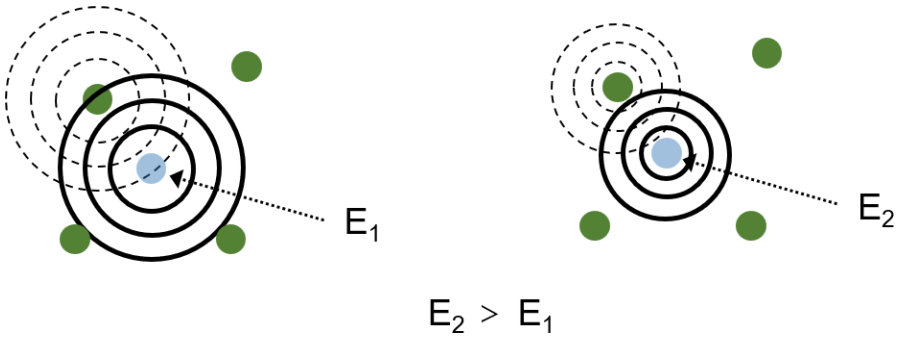

Fig. 2.6. A schematic of the outgoing and backscattered photoelectron wave, which illustrates the concept of interference in EXAFS.

The wave nature of the emitted electron leads to interference effects due to scattering from nearby atoms. Thus, the EXAFS oscillations result from the interference between the outgoing photoelectron wave and the backscattered waves from neighboring atoms in the material. These

oscillations begin immediately after the absorption edge and extend up to about 1 keV above the edge. The EXAFS phenomenon χ(k), which represents the oscillatory part of the absorption coefficient, is defined as the difference between the observed absorption coefficient μ(k) and the free-atom absorption coefficient μ_0(k), normalized by the free-atom contribution (**Eq. 2.6**) [99, 101]:

$$\chi(k) = \frac{\mu(k) - \mu_0(k)}{\mu_0(k)} \quad \text{(Eq. 2.6)}$$

One can envision the EXAFS phenomena by the help of a schematic of the outgoing and backscattered waves as shown in **Fig. 2.6**. In this figure, E_1 and E_2 are the energy of the incident X-ray photon ($E_2 > E_1$, and the wavelength of the photo-electron is shorter at E_2 compared to E_1). The central atom (blue) is the absorbing atom and the photoelectron is backscattered from the surrounding atoms (green). The backscattered wave from the surrounding atoms (dashed blue circular lines) is in phase with the outgoing wave (solid blue circular lines).

At a specific energy E_1, the outgoing and the backscattered waves are in phase and constructively interfere, thus increasing the probability of X-ray absorption or, in other words, increase the absorption coefficient. At a different energy E_2, the outgoing and backscattered waves are out-of-phase and destructively interfere, decreasing the absorption coefficient. This modulation of the absorption coefficient by the backscattered wave from neighboring atoms is essentially the basic phenomenon of EXAFS. And, Fourier transform (FT) of the modulation provides distance information describing the vector(s) between the absorbing atom and atoms to which it is bound—typically within a range limit of 4 – 5 Å [99, 101, 102].

2.4 X-ray photoelectron spectroscopy

X-ray photoelectron spectroscopy (XPS) is widely regarded as one of the main techniques for the surface characterization and chemical analysis of biomedical polymers. Also known as Electron Spectroscopy for Chemical Analysis (ESCA), XPS provides comprehensive elemental analysis, excluding hydrogen and helium, of the outermost ~10 nm of any solid surface that is vacuum-stable or can be stabilized under vacuum by cooling. In addition to elemental composition, XPS also offers valuable information on chemical bonding.

XPS operates under ultra-high vacuum (UHV) conditions. The sample is irradiated with X-rays, causing the emission of photoelectrons from various atomic energy levels at the surface. These photoelectrons are detected by a hemispherical analyzer, which measures their kinetic

energy (KE). A change in the binding energy (BE) of an electron, relative to the Fermi level, can occur due to variations in oxidation state or changes in the electron density around the nucleus—commonly referred to as a chemical shift. These shifts provide insight into the chemical environment and bonding of the atom. The BE of an energy level can be determined from the measured KE of the photoelectron derived from the particular level following Koopman's theorem, resulting from Hartree-Fock calculation, by the following relation (**Eq. 2.7**) [103]:

$$E_B = hv - E_K - \varphi \qquad \text{(Eq. 2.7)}$$

Where E_K is the kinetic energy, E_B is the binding energy, h is the Plank's constant, v is the frequency of X-ray photon and φ is the work function of the spectrometer, both are constant for a given spectrometer. A schematic of the process is shown in **Fig. 2.7**.

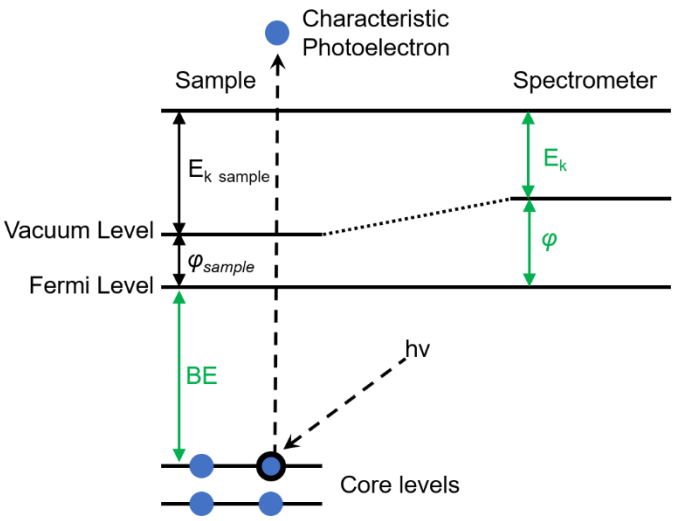

Fig. 2.7. Schematic illustration of the principle behind XPS.

According to this theorem, the electron energy levels are approximated as 'frozen orbitals', where these levels are identical in both the initial (atomic ground state before the photoelectron emission) and final (ionic excited state after the photoelectron emission) states. However, the experimentally measured EB values differ from the theoretical values by a few eV, which is known as 'relaxation energy' (ER), due to the rearrangement of the electrons and their energy levels during the process of photoemission. The relaxation process is accompanied by the emission of Auger electrons as the excited ion returns to the ground state. The dependence of EB, for an atom in a solid-state material, on various factors/parameters can be represented as **Eq. 2.8** [103, 104]:

$$E_B = -E_{HF} + V_{MP} + V_{VC} - E_{IA} - E_{EA} - \varphi \quad \text{(Eq. 2.8)}$$

where E_{HF} is the Hartree-Fock orbital energy for a free atom in vacuum, V_{MP} is the shift in E_{HF} due to Madelung potential when the free atoms condense to form a solid, V_{VC} is the shift in E_{HF} due to valence charge, E_{IA} is the intra-atomic relaxation energy and E_{EA} is the extra atomic relaxation energy. It means that E_B is not only dependent on the atom itself but also on the environment / neighboring atoms and hence a variation in the environment or bonding of the atom alters the E_B. The change in E_B is called the 'chemical shift'.

In XPS, the penetration depth of X-rays (~ 1-3 keV) in solid materials is on the order of several microns and varies significantly (~ 1-100 μm) depending on the material, the energy of the X-ray used and its angle of incidence. However, the surface sensitivity of XPS is due to the photoelectrons generated only within the top ~ 10 nm thickness of the material surface as they have a considerable probability to eject out of the surface without inelastic scattering and to get detected [104]. The other photoelectrons produced within the subsurface / bulk would be reabsorbed by the material as the electrons lose energy by inelastic scattering with the material lattice atoms / ions [104].

3. Thermal pre-treatment of LIB electrodes

3.1 Introduction

The delamination of cathode active material is a crucial step in direct recycling, which can be categorized into three main stages: mechanical separation, dissolution, and thermal treatment. The mechanical separation includes processes such as crushing, sieving, magnetic separation, and flotation [105]. It is widely adopted in industrial applications due to its scalability. However, maintaining impurity levels within an acceptable range in obtained active material remains a major challenge, bringing significant difficulties for subsequent regeneration. The dissolution technique utilizes solvents to dissolve the binder, thus effectively separating the active material from the current collector. Common solvents include N-methyl pyrrolidone (NMP) [106], dimethyl formamide (DMF) [107], and dimethylacetamide (DMAC) [108], all of which effectively dissolve polyvinylidene fluoride (PVDF), the most commonly used binder. While this method minimizes impurities, the dissolution kinetics is hindered by the deteriorated interface between active material and current collector [109], resulting in low efficiency. Additionally, the high cost and toxicity of most organic solvents present major challenges for large-scale implementation. The thermal treatment involves heating of the material to decompose the binder, enabling the separation of cathode or anode active materials[110, 111]. It is a simple and effective process that also allows for impurity control. From the perspective of direct recycling, thermal treatment could be a promising approach for recovering high-purity active material.

In this chapter, thermal treatment is employed to separate the cathode and anode active materials from Al and Cu current collectors (NCM622 and graphite, respectively), establishing the relationship between separation efficiency and temperature under different atmospheres. Additionally, XRD analysis is utilized to examine structural changes in the materials after thermal treatment. Rietveld refinement provides detailed structural information, enabling the identification of optimal condition that maximize separation efficiency while minimizing structural degradation.

3.2 Methods

3.2.1 Materials

Battery electrodes were provided by the KIT Battery Technology Center (KIT-BATEC) [112] . The cathodes in this study were composed of NCM622 ($LiNi_{0.6}Co_{0.2}Mn_{0.2}O_2$), PVDF binder, and conductive carbon additive in a weight ratio of 96.0:2.0:2.0. The anodes for this study were

composed of graphite, binder consisting of sodium carboxymethylcellulose and styrene-butadiene rubber latex (CMC/SBR) and conductive additive carbon black in a weight ratio of 96.0:2.8:1.2. The current collectors of cathode and anode are Al and Cu foil respectively. Fresh cathodes and anodes along with ceramic coated polyethylene terephthalate fabric (CC-PET) as a separator, were assembled using 1 mol L^{-1} $LiPF_6$ in EC, DMC and VC as additives in the electrolyte to build multi-layer pouch cells, resulting in a nominal capacity of 12 Ah. The cells underwent about 2100 cycles at a 1 C charge and discharge rate within the voltage range of 3.0-4.2 V until their capacity reached approximately 81 % of their initial level, indicating the end of their useful life. Subsequently, the LIBs were deeply discharged to 0 V, short-circuited, and disassembled to extract the cycled cathodes and anodes for further analysis.

3.2.2 Delamination process

The fresh and cycled electrodes were cut into round pieces with a diameter of 18 mm. These samples were then placed in the center of a gas flow furnace to undergo thermal treatment at various temperatures and atmospheres. A gas flow rate of 55 $L \cdot min^{-1}$ was maintained for experiments in argon, nitrogen and hydrogen atmospheres. The heating and cooling rates were set at 5 °C min^{-1}, and the samples were held at the target temperature for 2 h. After the thermal treatment process, the fresh and cycled electrodes were immersed in 15 mL of solvent (water for cathode, and acetone for anode) and subjected to sonication for 10 seconds. After sonication, the obtained active materials, as well as the Al and Cu foils, were dried overnight in an oven set at a temperature of 80 °C. This ensured the complete removal of any remaining solvent and moisture from the samples, preparing them for further analysis and characterization.

The electrode weight was measured before ($\mathbf{M_1}$) and after ($\mathbf{M_2}$) the complete peeling-off process, which removed all active materials (including CAM, Al foil, binder, and conductive carbon). The difference ($\mathbf{M_0 = M_1 - M_2}$) represents the total mass of detachable material, corresponding to 100% delamination efficiency. Then, the electrodes before ($\mathbf{M_{x1}}$) and after ($\mathbf{M_{x2}}$) subjecting the electrodes to thermal treatment, sonication, and drying processes, were measured. The corresponding mass difference was defined as: $\mathbf{M_x = M_{x1} - M_{x2}}$. The separation efficiency ($\boldsymbol{\eta}$) was then determined by normalizing the measured mass loss ($\mathbf{M_x}$) to the total removable mass ($\mathbf{M_0}$) according to the following equation:

$$\eta\ (\%) = \frac{M_x}{M_0} \times 100$$

3.2.3 Materials characterization

The characterization of crystal structure was carried out using XRD on a STOE Stadi P powder diffractometer with monochromatic Cu-Kα_1 radiation (λ = 1.54056 Å) in transmission geometry. The XRD measurements were performed at room temperature with a 0.015° 2θ step between 10 and 70 degrees of 2θ. The Kapton film's presence visibly adds amorphous-like background in the XRD patterns at $10° < 2\theta < 17°$.

The obtained diffraction patterns were subjected to Rietveld refinement performed in the FullProf software package [113]. The background of all the diffraction patterns was fitted using linear interpolation between selected data points in regions with no reflections present. The Thompson-Cox-Hastings pseudo-Voigt function was used for the reflection profile shape description. The scale factor, lattice parameter, fractional coordinates of atoms, their overall isotropic displacement (temperature) parameter, zero angular shift, profile shape parameters, and half-width (Caglioti) parameters were allowed to vary during fitting.

3.3 Separation efficiency

3.3.1 Cathode

The separation efficiency for cathode active material (NCM622) from Al foil under different temperatures (heated to a certain temperature and then cooled down to RT) and atmospheres is shown in **Fig. 3.1a-j and 3.2a-j**. For fresh cathode, the separation begins at 400 °C under argon, reaching 100% at 500 °C (**Fig. 3.1a and f**). Under nitrogen, the results are similar, with 100% efficiency at 500 °C, indicating that nitrogen, like argon, simply provides an inert environment (**Fig. 3.1b and g**). In this case, the separation can be ascribed to the decomposition of PVDF.

Prior studies have shown that the decomposition of PVDF generally initiate at ~400 °C under an inert atmosphere, undergoing a gradual decomposition process [114-116]. This process leads to a gas release, and only about 20−25 wt% of carbon from PVDF is left in the treated material. The volatile pyrolysis products mainly include HF gas and fluorocarbon chain fragments, resulting from the cleavage of the polymer chain and hydrogen transfer. As such, the observed increase in separation efficiency at 400 °C, further increase in 450 °C, and 100% efficiency at 500 °C under inert atmosphere can be understood as the onset, continuous progression, and complete decomposition of PVDF. Furthermore, the separation efficiency reaches 100% at 400 °C in air and 350 °C in oxygen, both lower than the temperatures required under argon and

nitrogen (**Fig. 3.1d-e and h-i**). This can be ascribed to the promoted decomposition of PVDF by oxygen through forming oxygenated carbon compounds, which enhance reactivity [117].

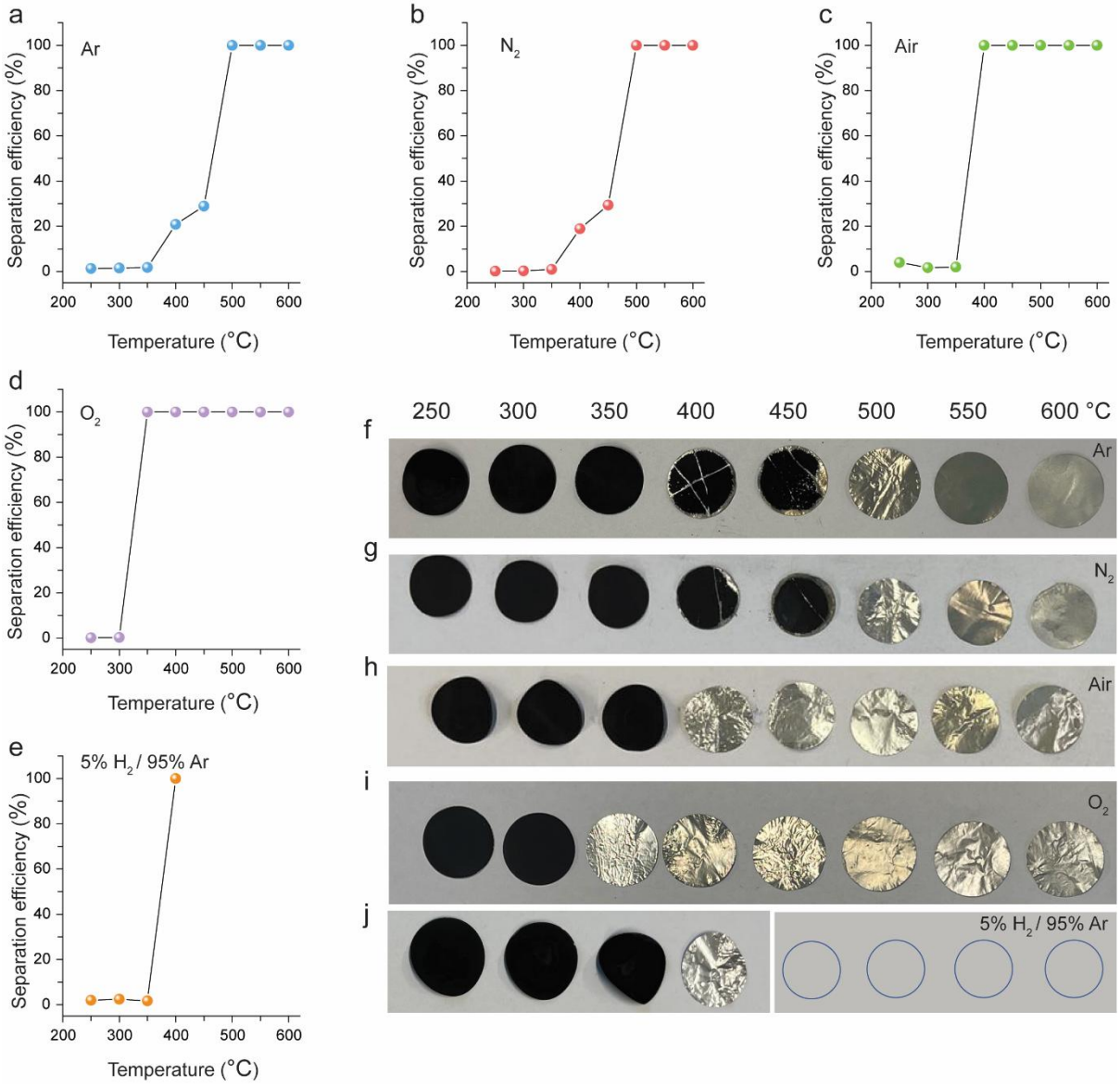

Fig. 3.1. Separation efficiency of active material through thermal treatment at different temperatures under (a) Ar, (b) N_2, (c) Air, (d) O_2 and (e) 5% H_2 / 95% Ar for fresh cathode. Electrode state of fresh cathode after thermal treatment with different temperatures under (f) Ar, (g) N_2, (h) air, (i) O_2 and (j) 5% H_2 / 95% Ar (empty circles represent that the electrodes have been transformed into powder after sonication).

An interesting phenomenon is observed in a hydrogen atmosphere (5% H_2 / 95% Ar). Although hydrogen does not promote the decomposition of PVDF and may even inhibit it to some extent, 100% separation efficiency is achieved at 400 °C (**Fig. 3.1e and j**). This suggests that factors beyond the decomposition of PVDF influence the separation process in hydrogen. This additional factor can be attributed to significant volume changes within the NCM lattice due to structural changes. This structural change weakens the bonds between active material, PVDF,

and Al, thus promoting separation. Besides, temperatures above 400 ℃ lead to the brittleness of Al. This brittleness can arise from the phase transformation of TM oxide into TM alloy, causing the Al foil to turn into powder during the sonication process. The more detailed explanation for these findings will be provided in the *Structural Degradation Study* section.

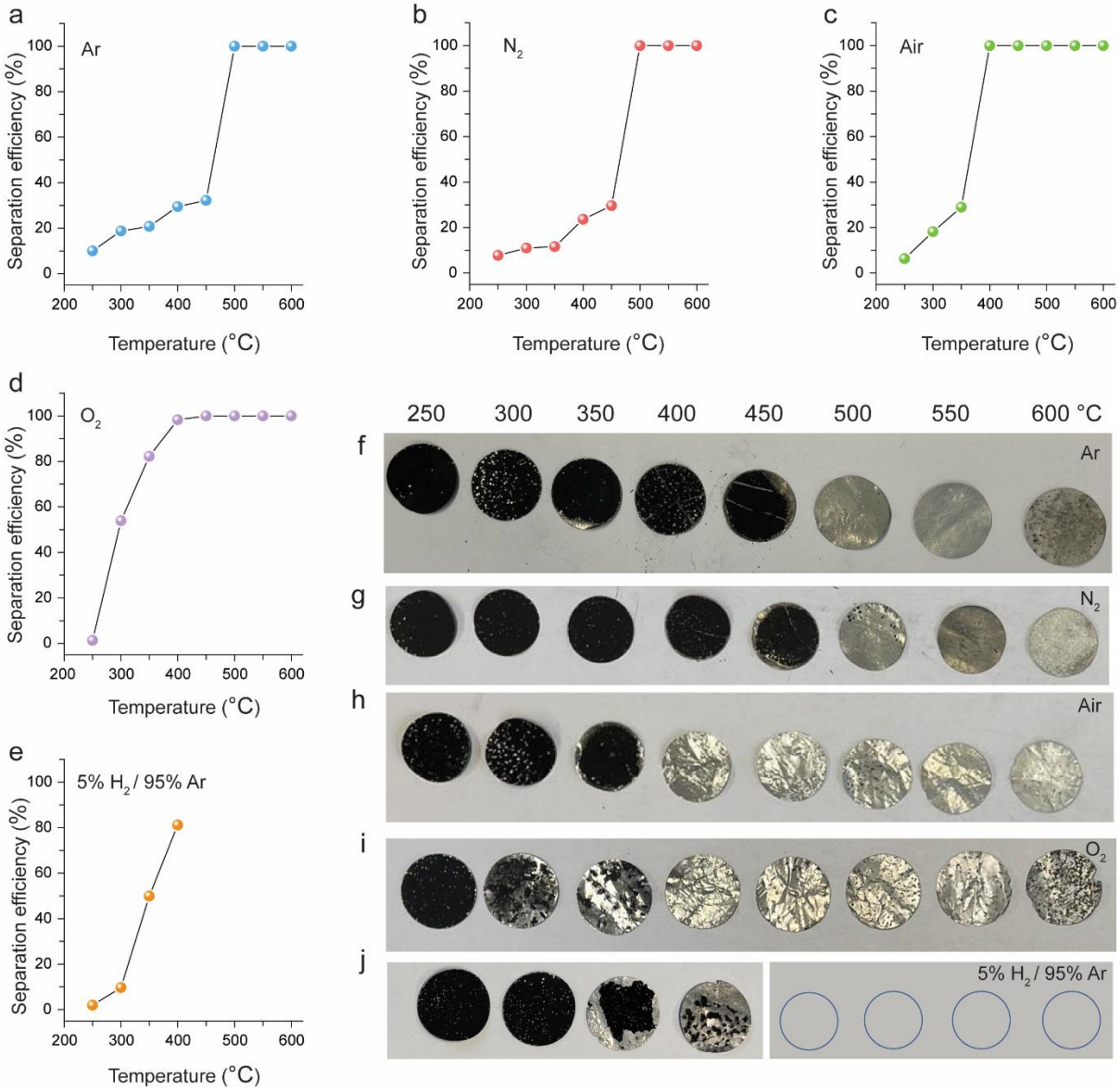

Fig. 3.2. Separation efficiency of active material through thermal treatment at different temperatures under (a) Ar, (b) N_2, (c) Air, (d) O_2 and (e) 5% H_2 / 95% Ar for cycled cathode. Electrode state of cycled cathode after thermal treatment with different temperatures under (f) Ar, (g) N_2, (h) air, (i) O_2 and (j) 5% H_2 / 95% Ar (empty circles represent that the electrodes have been transformed into powder after sonication).

For cycled cathode, the separation efficiency reaches 100 % at 500 ℃ under argon and nitrogen (**Fig. 3.2a-b and f-g**), and 100 % at 400 ℃ under air (**Fig. 3.2c and h**), similar to the case of fresh electrodes. However, in an oxygen atmosphere, the separation efficiency at 350 ℃ is ~80%, which differs from the 100% of fresh cathode (**Fig. 3.2d and i**). This discrepancy is

likely attributed to the corrosion of current collector and the deteriorated interface between the active material and Al due to cycling. As observed, the Al-foil of cycled cathodes shows more pronounced corrosion compared to the fresh cathode once active materials are removed. Moreover, at 300 °C under oxygen, cycled cathodes demonstrate higher separation efficiency than the fresh cathodes. Similar trends are observed at 300 and 350 °C under air. These increases in separation efficiency are likely linked to the local degradation of PVDF, caused by long-term cycling. Previous studies have indicated that the degradation of PVDF during cycling involves processes such as de-hydro-fluorination and the formation of carbon-carbon double bonds [118, 119]. These reactions can be described as:

$$Li^{+} - [CH_2 - CF_2] - \rightarrow -[CH = CF] - \ + LiF + \frac{1}{2}H_2 \quad (3\text{-}1)$$

$$-[CH_2 - CF_2] - \rightarrow -[CH = CF] - \ + HF \quad (3\text{-}2)$$

Literature on the thermal stability of PVDF indicates that its stability is primarily provided by C–F bonds, whereas thermal degradation is driven by the formation of carbon–carbon double bonds [120, 121]. Consequently, PVDF degradation increases the susceptibility of carbon bonds to oxidation, enhancing separation efficiency at lower temperatures under air or oxygen. In contrast, under inert atmospheres like argon and nitrogen, the decomposition of PVDF predominantly occurs through a gradual self-lysis process. Therefore, the temperature required for complete separation remains consistent, and there is no significant increase in separation efficiency at lower temperatures compared to air and oxygen.

Under hydrogen (5% H_2 / 95% Ar), the separation efficiency of cycled cathodes does not reach 100% within the temperature range, displaying a slightly lower efficiency at 400 °C when compared to fresh cathodes (**Fig. 3.2e and j**). This most likely arises from the deteriorated interface between the active material and Al foil as well.

Moreover, at lower temperatures under all atmospheres, cycled cathodes exhibit separation efficiencies of 8%–20%, whereas fresh cathodes remain close to zero. It is well-known that solid electrolyte interphase (SEI) is generally formed on the surface of cathode particles during cycling, composed of various chemical compounds due to the reaction between the electrolyte and the cathode material [122]. The higher separation efficiency observed for cycled cathodes at the lower temperatures is therefore attributed to the decomposition of the SEI on the cathode particle surface.

3.3.2 Anode

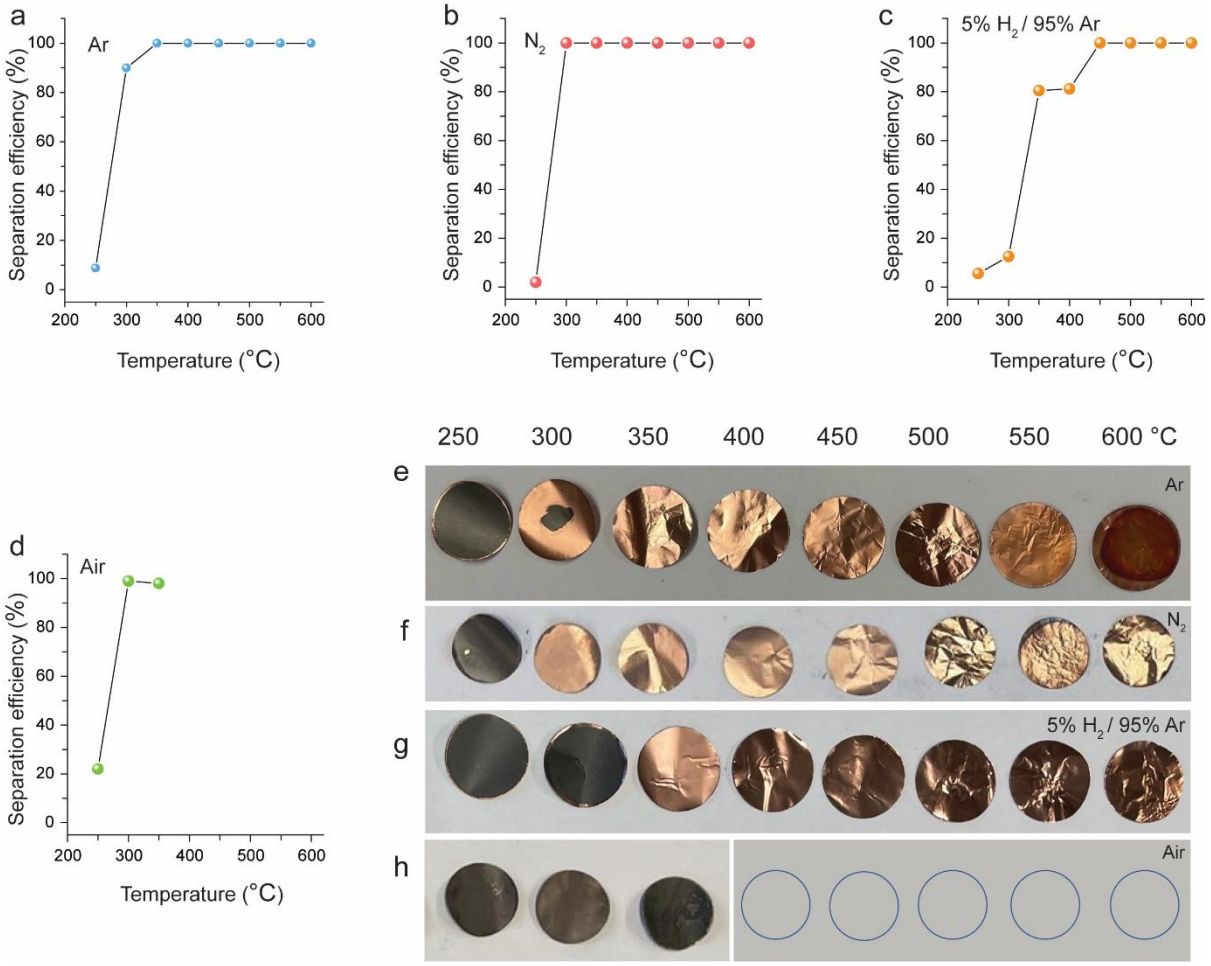

Fig. 3.3. Separation efficiency of active material through thermal treatment at different temperatures under (a) Ar, (b) N_2, (c) 5% H_2 / 95% Ar and (d) air for fresh anode. Electrode state of fresh anode after thermal treatment with different temperatures under (e) Ar, (f) N_2, (g) 5% H_2 / 95% Ar and (h) air (empty circles represent that the electrodes have been transformed into powder after sonication).

Fig. 3.3a-h and 3.4a-h display the separation efficiency of anode active material (graphite) from Cu foil under different temperatures and atmospheres. Unlike the cathode material, graphite does not undergo drastic lattice changes or phase transition during heating, as will be elucidated later. In this case, the separation of graphite from Cu foil is mainly realized by the decomposition of the binder, composed of CMC and SBR (that both decompose at around 300 °C [123, 124]). Consequently, under argon and nitrogen atmospheres with a holding time of 2 h, the detachment of active material from the Cu foil begins at 300 °C for fresh anode (**Fig. 3.3a-b and e-f**), where the separation efficiency can be already close to100%. However, when exposed to a hydrogen atmosphere (5% H_2 / 95% Ar), the separation efficiency at 300 °C is around 15% and the full separation takes place at 350 °C (**Fig. 3.3c and g**), suggesting that the reducing atmosphere inhibits the decomposition of CMC/SBR to some extent. When heated in

air, although the separation efficiencies of the fresh anode are close to 100 % at 300 and 350 °C, the Cu foil undergo substantial oxidation, which becomes more pronounced with increasing temperature (**Fig. 3.3d and h**). This oxidation eventually leads to foil embrittlement, causing it to break into powder during the sonication process.

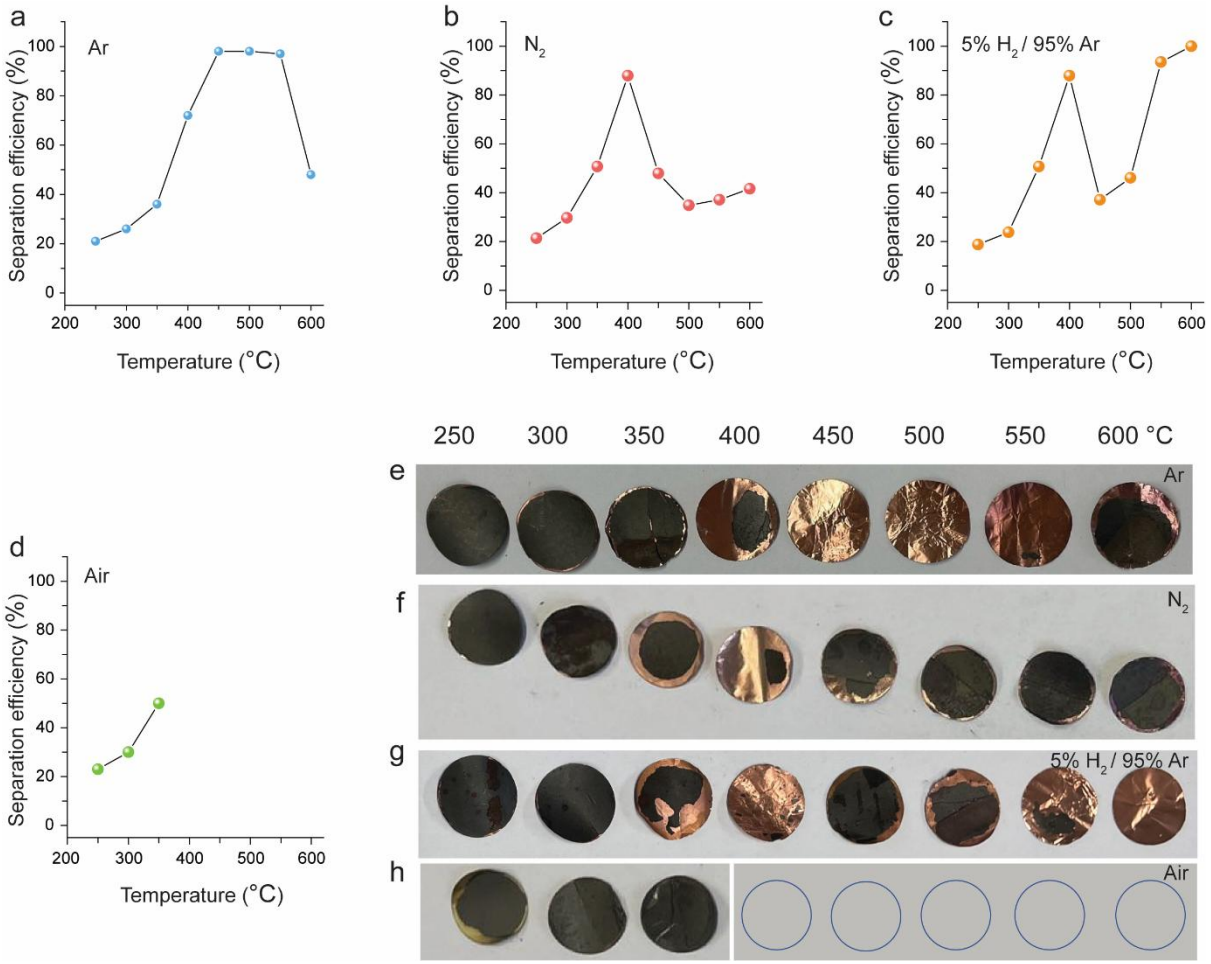

Fig. 3.4. Separation efficiency of active material through thermal treatment at different temperatures under (a) Ar, (b) N_2, (c) 5% H_2 / 95% Ar and (d) air for cycled anode. Electrode state of cycled anode after thermal treatment with different temperatures under (e) Ar, (f) N_2, (g) 5% H_2 / 95% Ar and (h) air (empty circles represent that the electrodes have been transformed into powder after sonication).

Similarly, for the cycled anodes, significant oxidation and embrittlement is observed for the Cu-foil under air, but with lower separation efficiency at 300°C and 350 °C compared to fresh anodes (**Fig. 3.4d and h**). In addition, under argon, nitrogen and the hydrogen atmospheres, in some cases, the separation efficiency of cycled anodes at high temperatures (500-600 °C) is lower than that of fresh anodes (**Fig. 3.4a-c and e-g**). For instance, despite the displayed separation efficiency being close to 100% under argon from 450 to 550 °C, further experiments suggest that structural changes, material degradation, and binder issues can lead to reduced separation efficiency in cycled anode **(Fig. 3.5a-f)**. In other words, due to the varied states of

cycled anode, different separation efficiencies were observed at the same temperatures. Similar to cathode, anode particles form a SEI layer on their surface during cycling as well [125]. The interface degradation at the interface between anode active material and Cu-foil also occurs upon cycling. Therefore, the difference in separation efficiency at the same temperatures is attributed to the decomposition of SEI and the CMC/SBR binder upon thermal treatment. Such decomposition induces chemical alterations at the interface contact, reinforcing the adhesion between the graphite and Cu-foil.

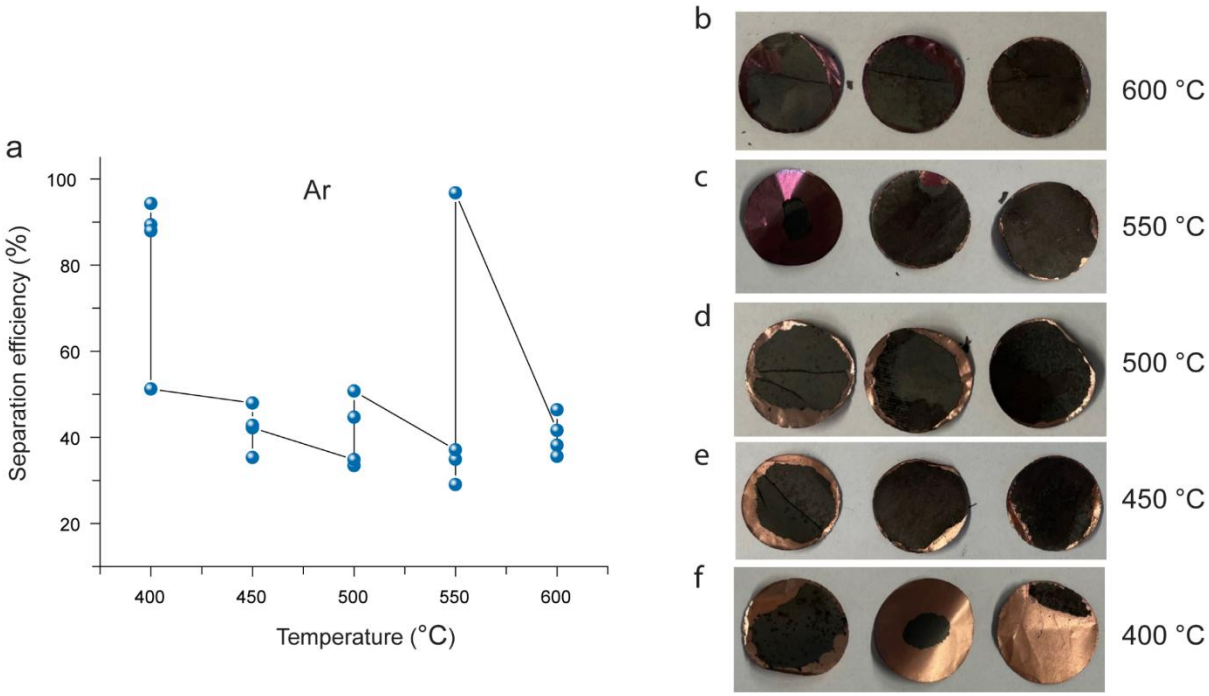

Fig. 3.5. (a) Separation efficiency of active material through thermal treatment under argon from 400 to 600 °C for cycled anode. Electrode state after thermal treatment at (b) 600, (c) 550, (d) 500, (e) 450 and (f) 400 °C.

3.4 Structural degradation study

Previous works highlighted that thermal treatment could induce further structural degradation of active materials, in addition to the degradation that occurred during cycling in the full-cell battery, which brings difficulties in the subsequent structure repair process [126-128]. Yet, an investigation that systematically reveals the potential structural changes after thermal treatment is still absent. As such, the following study focuses on the structural changes in materials after thermal treatment through XRD and Rietveld refinement.

3.4.1 Cathode material

Fig. 3.6a shows the corresponding XRD results of the fresh cathode materials, heated under argon and then cooled down to RT. As observed, the samples after 250-550 °C show a typical

diffraction pattern of α-$NaFeO_2$ layered structure (*R-3m*). The 006/102 and 108/110 doublets separate clearly from 250 to 500 ℃, suggesting ordered layer structure, but at 550 ℃, the spacing between 006/102 and 108/110 doublets decrease and even tend to merge, which indicates the degradation of layered structure. The phase degradation after 550 ℃ can be ascribed to Li/O release and the reduction of TM driven by inert atmosphere and high temperature [129]. In addition, a more significant phase degradation occurs after 600 ℃, where the layered structure undergoes a transformation into a phase consisting of rock-salt type phase (RS) with a cubic structure (NiO- or CoO-type structure, *Fm-3m*), along with the formation of Ni or Co metal phase also exhibiting a cubic structure (*Fm-3m*). This phase transformation is associated with carbothermal reduction triggered by the conductive carbon additive and the decomposition products of PVDF [130, 131].

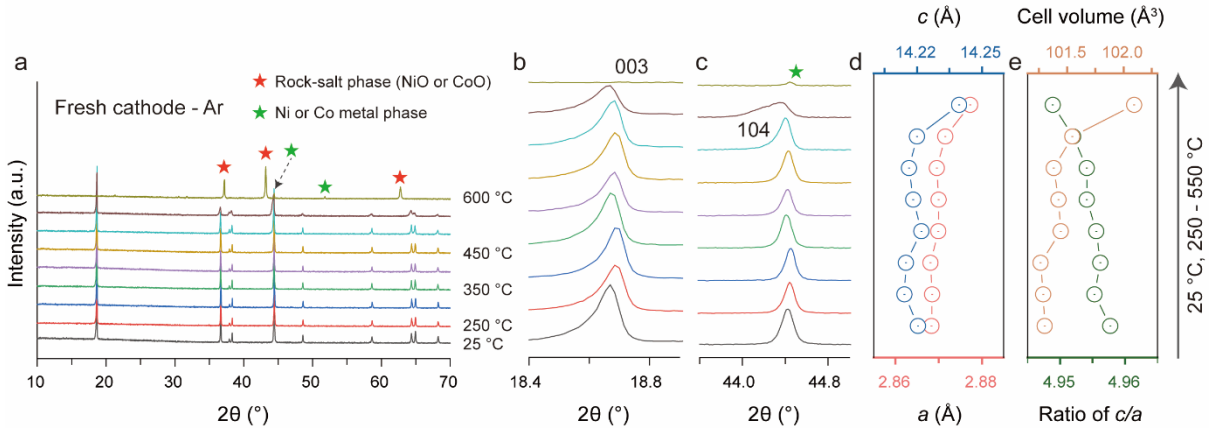

Fig. 3.6. (a) XRD pattern of fresh cathode under argon from 25 to 600 ℃, and its area of (b) 18.4-19.0°, (c) 43.8-45.0°. The corresponding (d) *a* and *c*, (e) ratio of *c/a* and cell volume from 25 to 550 ℃.

The expanded regions of the XRD pattern (**Fig. 3.6b-c**) were analyzed to further understand the structural changes. The positions of 003 and 104 reflections after 250-550 ℃ fluctuate in a small range. In general, the shift of the 003 reflection signifies variations in the lattice parameter *c*, while the displacement of the 104 reflection indicates changes in the lattice parameter *a*. To better comprehend these phenomena, the cell parameters were obtained through Rietveld refinement (**Fig. 3.6d-e**). The *a* parameter and cell volume consistently increase with the temperature rising, while parameter *c* exhibits an irregular variation. These changes could be ascribed to the oxygen release, the reduction of TM, and the corrosion by HF after the decomposition of PVDF.

Although illustrating the precise mechanism behind the parameter variation remains challenging, the *c/a* ratio can offer valuable insights into the cation order of the layered

structure. In the case of a perfect cubic rock-salt phase, exemplified by NiO, the cubic lattice can be represented in a hexagonal lattice with parameters $a_H = a_c/\sqrt{2}$ and $c_H = 2\sqrt{3}a_c$ resulting in a *c/a* ratio of $2\sqrt{6} = 4.899$. In *R-3m* layered TM oxides, the *c/a* ratio is expected to exceed 4.899 due to weak interlayer forces, causing a subtle separation of the TM layers along the *c*-axis. Literatures on well-ordered layer structures of NMC622 materials suggest a *c/a* ratio of approximately 4.96 [129, 132, 133]. In our study, the initially fresh NCM622 material exhibits a *c/a* ratio of 4.958, assumed to be the optimal value for our NCM622 materials, indicating an ideal layer structure ordering. Consequently, the assessment of structural degradation after thermal treatment involves comparing the calculated *c/a* ratio with the reference value of 4.958.

As shown in **Fig. 3.6e**, the *c/a* ratio for the fresh cathode under argon gradually decreases as the temperature rises, and is gradually deviating from the reference value of 4.958, indicating that the layer structure undergoes continuous structural degradation.

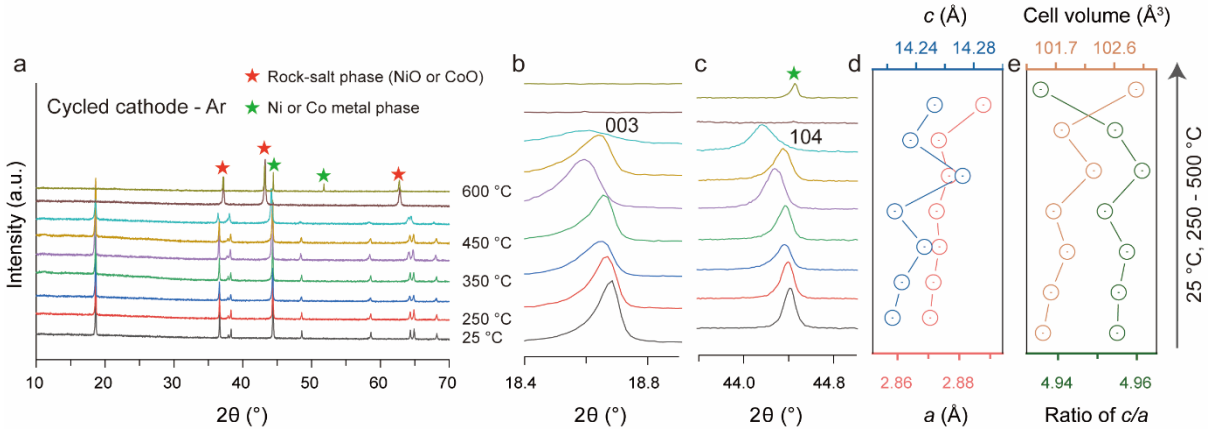

Fig. 3.7. (a) XRD pattern of cycled cathode under argon from 25 to 600 °C, and its enlarged area of (b) 18.4-19.0°, (c) 43.8-45.0°. The corresponding (d) *a* and *c*, (e) ratio of *c/a* and cell volume from 25 to 500 °C.

For the cycled cathode material, the layered structure is preserved only after heating to 250-500 °C (**Fig. 3.7a**). The significant degradation of the layered structure occurs after 500 °C, which is 50 °C lower than for the fresh cathodes, as indicated by the separation of 006/102 and 108/110 doublets. After 550 °C, the layered phase transforms to NiO or CoO-type RS phase, with a small presence of Ni or Co metal phase. After 600° C, this transformation becomes more pronounced, resulting in a higher proportion of the Ni or Co metal phase. In addition, the 003 and 104 reflections exhibit a larger angle shift in comparison to the fresh cathode (**Fig. 3.7b-c**). This observation can be further explained by considering the variations in the cell parameters (**Fig. 3.7d**). The cell parameters show that, after 500 °C, the *a*, *c*, and cell volume of the obtained material expand by 0.600%, 0.203%, and 1.412%, respectively, compared to

the original material, which is higher than the 0.112%, 0.003% and 0.243% of fresh cathodes, treated at the same temperature, indicating a more obvious structure change in the cycled cathodes. Additionally, the *c/a* ratio for fresh cathodes after 500 ℃ is 4.955, while for cycled cathodes after the same temperature, it is 4.936 (**Fig. 3.7e**). These findings indicate that the degradation of the layered structure upon thermal treatment is more pronounced in cycled cathodes, most likely due to the degraded structural stability resulting from the cycling. Moreover, the ratio of *c/a* exhibits an increase after 400 and 450 ℃, approaching the value of 4.958. This change is mainly attributed to the expansion of the material structure along the *c*-axis, given that *a* shows no significant change. The expansion of *c* is likely caused by a weakened interlayer force; however, it remains unclear whether this behavior is associated with a more ordered or disordered structure.

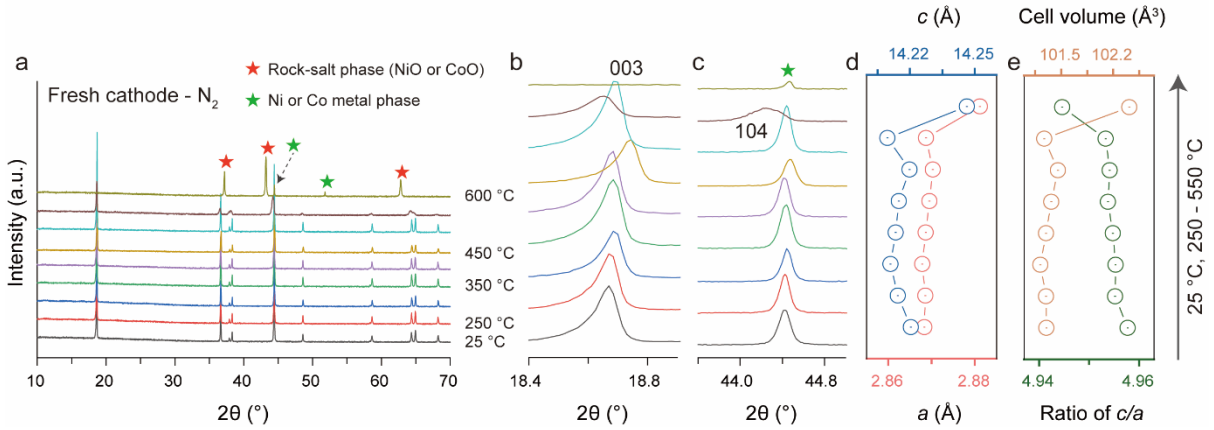

Fig. 3.8. (a) XRD pattern of fresh cathode under nitrogen from 25 to 600 ℃, and its enlarged area of (b) 18.4-19.0°, (c) 43.8-45.0°. The corresponding (d) *a* and *c*, (e) ratio of *c/a* and cell volume from 25 to 550 ℃.

Fig. 3.8a-j and 3.9a-j present the XRD results of the samples after thermal treatment under a nitrogen atmosphere, which exhibit similar behavior to the results obtained under argon. In the case of fresh cathode, the peaks observed after heating 250-550 ℃ can be indexed to the layered structure (**Fig. 3.8a**). However, after 550 ℃, a noticeable degradation of the layer structure is observed, as evidenced by the separation of the 006/102 and 108/110 doublets. After 600 ℃, the layer structure transforms to NiO or CoO-type RS phase and Ni or Co metal phase. The shift of the 003 and 104 reflections remains small from 250 to 500 ℃ (**Fig. 3.8b-c**). The obtained cell parameters reveal a consistent increase in *a* and cell volume (**Fig. 3.8d-e**), while the variation of *c* does not exhibit a clear regularity as the temperature increases. The continuous decrease of the ratio of *c/a* indicates a gradual degradation of the layer structure.

In the case of cycled cathodes, after heating to 250-450 ℃, the material maintains a well-

ordered layer structure (**Fig. 3.9a**). However, a significant degradation occurs after 500 °C, leading to transformation into NiO or CoO-type RS phase, and Ni or Co metal phase after 550 °C. Further heating to 600 °C results in an increased proportion of the metal phase. The shift of 003 and 104 reflections towards higher diffraction angles was observed in the cycled cathode compared to the fresh cathode (**Fig. 3.9b-c**). The obtained cell parameters show that *a* continuously increases with the temperature increase, while *c* and the cell volume constantly rise after 250-450°C but decrease after 500 °C (**Fig. 3.9d-e**). The ratio of *c/a* increases after 400-450 °C, similar to the results observed under argon, and then decreases to 4.948 after 500 °C.

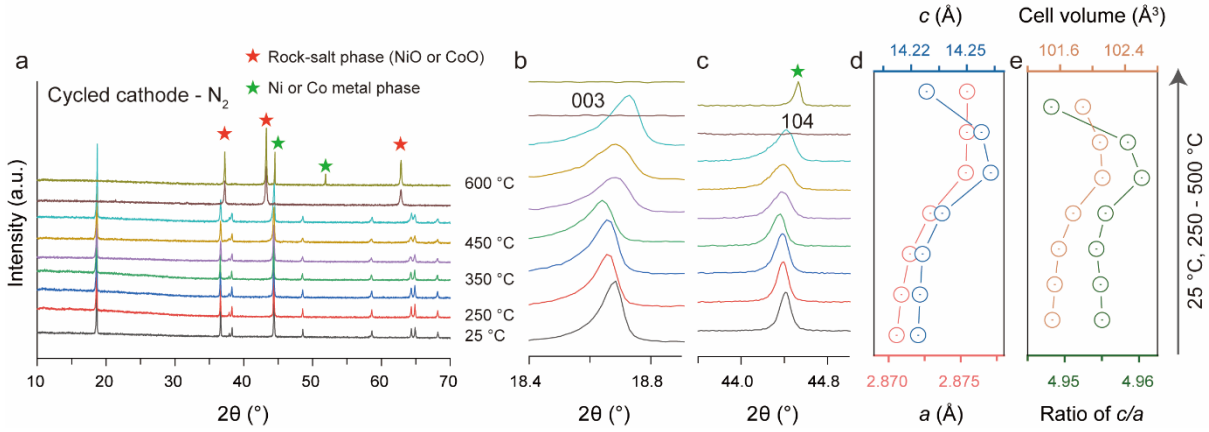

Fig. 3.9. (a) XRD pattern of cycled cathode under nitrogen from 25 to 600 °C, and its enlarged area of (b) 18.4-19.0°, (c) 43.8-45.0°. The corresponding (d) *a* and *c*, (e) ratio of *c/a* and cell volume from 25 to 500 °C.

Fig. 3.10a-j and Fig. 3.11a-j present the XRD results for the samples from hydrogen atmosphere (5% H_2 / 95% Ar). For the fresh cathode, the samples exhibit the layered structure after heating to 250-350 °C (**Fig. 3.10a**). Notably, the 006/102 and 108/110 doublets, after 300 °C, exhibit a tendency to merge, indicating a characteristic sign of structural degradation. After 400 °C, the layered structure undergoes a transformation into NiO or CoO-type RS phase. Simultaneously, a metal phase of Ni or Co emerges, resembling the phase observed in fresh cathode under argon and nitrogen after 550 °C. After 450 °C, the phase observed after 400 °C undergoes additional transformation. The RS phase tends to fully convert into Ni or Co metal phase, resulting in Al becoming brittle and ultimately breaking into powder during the sonication process. This transformation is also accompanied by the formation of a Mn_3O_4-type structure (*Fd-3m*). After heating above 500 °C, Mn_3O_4-type structure transforms into MnO-type structure (*Fm-3m*). Therefore, under a hydrogen atmosphere, the materials undergo substantial structural changes compared to argon and nitrogen.

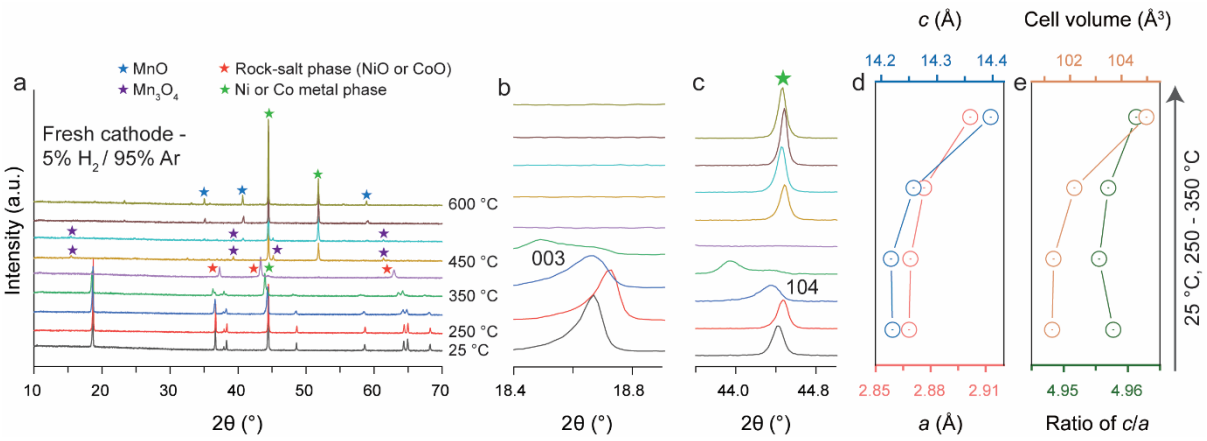

Fig. 3.10. (a) XRD pattern of fresh cathode under hydrogen (5% H_2 / 95% Ar) from 25 to 600 °C, and its area of (b) 18.4-19.0°, (c) 43.8-45.0°; The corresponding (d) *a* and *c*, (e) ratio of *c/a* and cell volume from 25 to 350°C.

According to the separation experiments, the fresh cathode achieves 100% separation efficiency after 400 °C under hydrogen, whereas the same efficiency is attained after 500 °C under argon and nitrogen. The lower temperature requirement under hydrogen can be ascribed to the significant phase transformation of TM oxide. This transformation contributes to the disruption of bonds between Al-foil and active material, thereby facilitating the separation process. Additionally, **Fig. 3.10b-e** depict expanded sections of the XRD patterns and the calculated cell parameters after heating to 25-350 °C. It is evident that, while maintaining the layered structure, the samples exhibit an increase in *a*, *c*, and cell volume with rising temperature (**Fig. 3.10d-e**). The *c/a* ratio also follows a similar pattern. This increase is attributed to the over-expansion of the lattice along the *c*-axis, most likely stemming from reduction reactions induced by hydrogen.

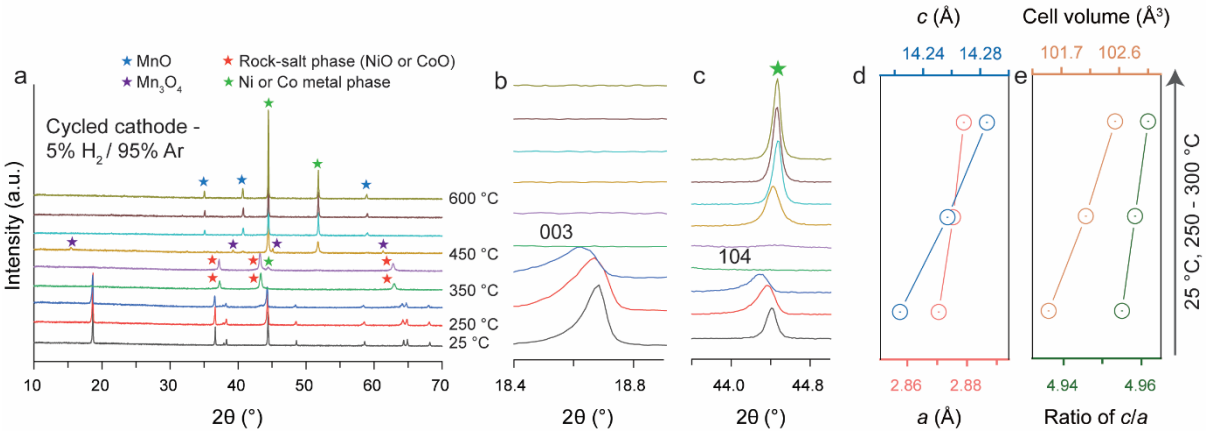

Fig. 3.11. (a) XRD pattern of cycled cathode under hydrogen (5% H_2 / 95% Ar) from 25 to 600 °C, and its enlarged area of (b) 18.4-19.0°, (c) 42.8-45.0°; The corresponding (d) *a* and *c*, (e) ratio of *c/a* and cell volume from 25 to 300 °C.

For cycled cathodes, similarly to those heated under argon and nitrogen, the phase

transformation occurs after a lower temperature when compared to fresh cathodes. As depicted in **Fig. 3.11a**, the layered structure is maintained only up to 250-300 ℃. Above this range, a phase transition to NiO or CoO-type RS phase occurs after 350 ℃. Moreover, after 400 ℃, a subtle metal phase of nickel or cobalt emerges alongside the RS phase. Similar to fresh cathode under hydrogen, the Mn_3O_4-type phase appears after 450 ℃ and the RS phase totally transforms into a metal phase. Above 500 ℃, MnO-type and metal phases coexist in the obtained materials. In the separation experiment, the cycled cathode exhibits an almost 100% separation efficiency after 400 ℃, and have a remarkably higher separation efficiency than the fresh cathode under hydrogen after 350 ℃. This highlights the significant influences of the phase transition of TM oxides on separation efficiency. Furthermore, the expanded segments of the XRD pattern and the calculated cell parameters after heating to 25-300 ℃ are shown in **Fig. 3.11b-e.** These variations correspond to the observed regularities seen in the fresh cathode.

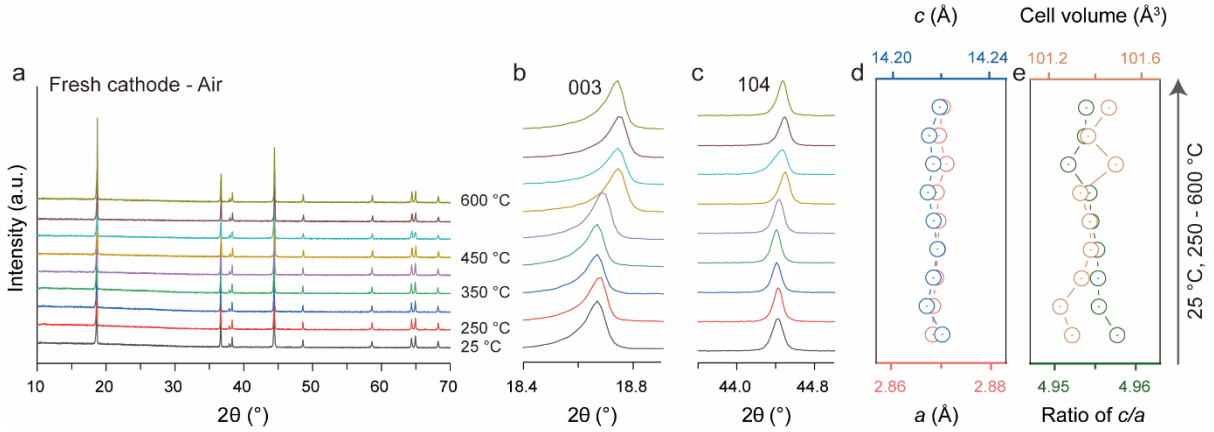

Fig. 3.12. (a) XRD pattern of fresh cathode under air from 25 to 600 ℃, and its enlarged area of (b) 18.4-19.0°, (c) 43.8-45.0°. The corresponding (d) *a* and *c*, and (e) ratio of *c/a* and cell volume.

Fig. 3.12a-e and Fig. 3.13a-e exhibit the XRD results for the samples treated in air. For fresh cathodes, the samples retain the layered structure after heating to 250-600 ℃ (**Fig. 3.12a**). The separation of the 006/102 and 108/110 doublets indicate an ordered layer structure for all samples. The shifts of the 003 and 104 reflections reflect the changes in the layered structure (**Fig. 3.12b-c**), which can be further explained by the obtained cell parameters (**Fig. 3.12d-e**). The variations of *a*, *c*, and cell volume is relatively small. The ratio of *c/a* decreases gradually with increasing temperature, but it remains higher than 4.95. Besides, these values are closer to 4.958 compared to results obtained under argon and nitrogen atmospheres at the same temperatures. These results suggest that the air atmosphere favors maintaining the initial structure upon thermal treatment. The structural stability is favored by the abundancy of oxygen in the air, which contributes to inhibiting the Li/O release from the bulk phase, enabling

a much slighter structure degradation.

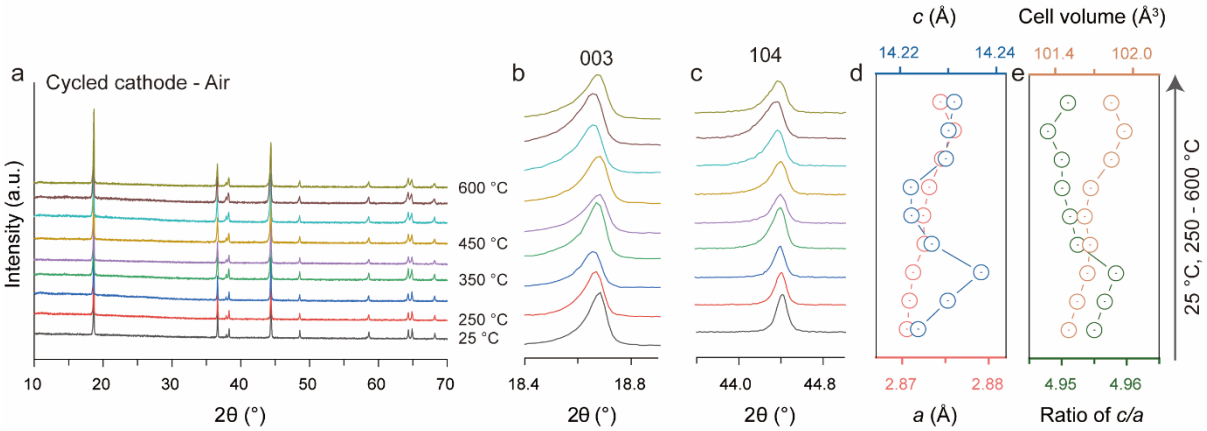

Fig. 3.13. (a) XRD pattern of cycled cathode under air from 25 to 600 ℃, and its enlarged area of (b) 18.4-19.0°, (c) 43.8-45.0°. The corresponding (d) *a* and *c*, and (e) ratio of *c/a* and cell volume from 25 to 600 ℃.

Similarly, for the cycled cathode, the layered structure is observed when heating to 250-600 ℃, and the spacing of the 006/102 and 108/110 doublets suggests a good cation ordering (**Fig. 3.13a**). The shifts of 003 and 104 reflections and the variations of cell parameters are shown in **Fig. 3.13b-c**. The 104 reflection continuously shifts towards a lower angle after 250-550 ℃ and then towards a higher angle after 600 ℃, which is consistent with the variation of *a* (**Fig. 3.13d**). The shift of the 003 reflection and the changes in *c* and cell volume exhibit a more irregular pattern in the cycled cathode. Meanwhile, the *c/a* ratio shows a decreasing trend with increasing temperature, and these ratios are all lower than those of the fresh cathode under the same conditions (**Fig. 3.13e**). Therefore, the cycled cathode experiences a more pronounced degradation of crystal structure, which is consistent with the results obtained under other atmospheres.

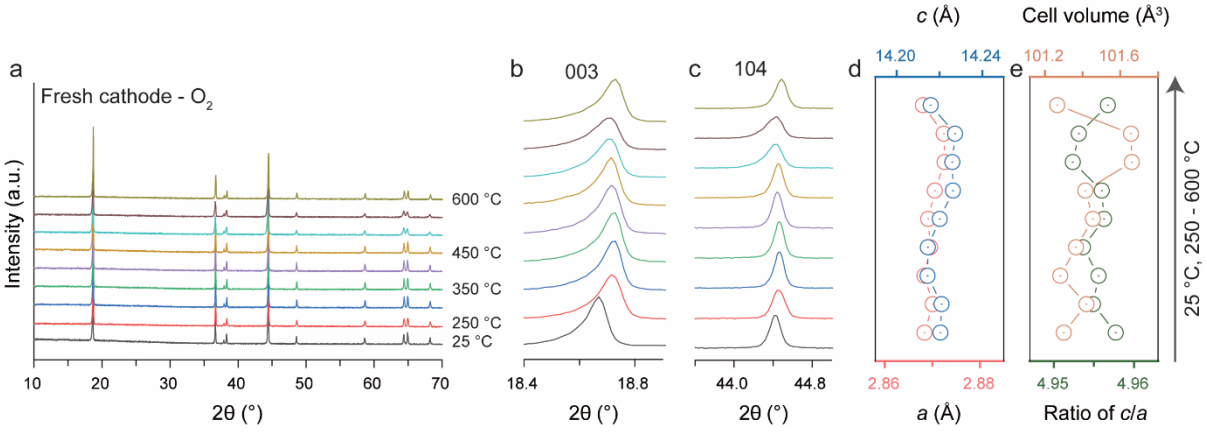

Fig. 3.14. (a) XRD pattern of fresh cathode under oxygen from 25 to 600 ℃, and its enlarged area of (b) 18.4-19.0°, (c) 43.8-45.0°. The corresponding (d) *a* and *c*, and (e) ratio of *c/a* and cell volume.

Fig. 3.14a-e and Fig. 3.15a-e exhibit the XRD results of the cathode samples treated under oxygen. Similar to the finding under air, the samples retain the layered structure, exhibiting good structural ordering after 250-600 ℃ (**Fig. 3.14a**). A comparison with the air atmosphere reveals that the 003 and 104 reflections under oxygen experience a smaller shift (**Fig. 3.14b-c**). This corresponds to a slight alteration in *a*, *c*, and cell volume, as illustrated in **Fig. 3.14d-e**. Furthermore, the *c/a* ratio consistently remains above 4.95, with values approaching 4.958 in contrast to the air atmosphere. These results suggest a superior degree of structural order for samples treated under oxygen.

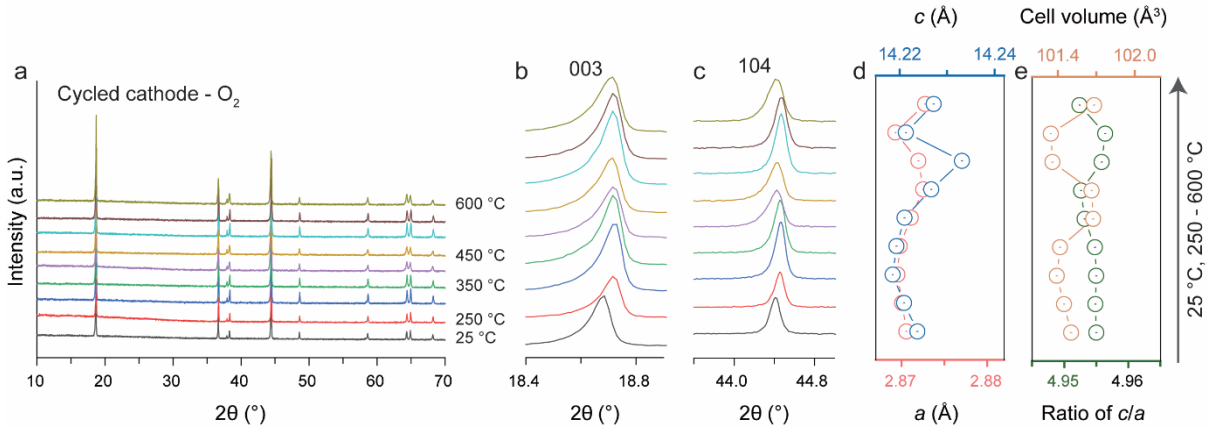

Fig. 3.15. (a) XRD pattern of cycled cathode under oxygen from 25 to 600 ℃, and its enlarged area of (b) 18.4-19.0°, (c) 43.8-45.0°. The corresponding (d) *a* and *c*, and (e) ratio of *c/a* and cell volume from 25 to 600 ℃.

For cycled cathodes, the samples maintain a well-ordered layer structure after heating to 250-600 ℃ (**Fig. 3.15a**), accompanied by a smaller shift in the 003 and 104 reflections (**Fig. 3.15b-c**) and slight variations in *a*, *c*, and cell volume (**Fig. 3.15d-e**). The *c/a* ratios in this temperature range hover around 4.955. These results further demonstrate that the presence of an oxygen atmosphere can effectively impede the structural degradation.

Table 3.1. Variation rate of cell parameters for fresh and cycled cathode compared with original material, while the ratio of *c/a* is compared with reference value of 4.958. The values highlighted in bold indicate the suitable conditions for thermal treatment, ensuring the highest separation efficiency while minimizing structural degradation.

	Atmosphere	Temperature (℃)	Normalized rate of cell parameters (%)			*c/a* (%)
			a	*c*	volume	
Fresh cathode	Ar	500	0.112	-0.003	0.243	-0.061
		550	0.313	0.134	0.783	-0.443
	N_2	500	0.013	-0.076	-0.030	-0.100

		550	0.447	0.182	1.101	-0.262
	5% H_2 / 95% Ar	400	/	/	/	/
	Air	**400**	**0.039**	**-0.025**	**0.075**	**-0.061**
		450	**0.028**	**-0.042**	**0.035**	**-0.081**
		500	0.096	-0.026	0.186	-0.121
		550	0.043	-0.038	0.068	-0.081
		600	0.071	-0.007	0.156	-0.081
	O_2	**350**	**0.041**	**-0.041**	**0.063**	**-0.081**
		400	**0.028**	**-0.002**	**0.152**	**-0.040**
		450	**0.076**	**0.041**	**0.113**	**-0.040**
		500	0.147	0.039	0.355	-0.101
		550	0.141	0.048	0.351	-0.101
		600	-0.012	-0.032	-0.035	-0.020
Cycled cathode	Ar	500	0.600	0.206	1.412	-0.444
	N_2	500	0.170	0.032	0.371	-0.202
	5% H_2 / 95% Ar	400	/	/	/	/
	Air	**400**	**0.066**	**-0.010**	**0.121**	**-0.141**
		450	**0.090**	**-0.011**	**0.167**	**-0.161**
		500	0.142	0.040	0.324	-0.161
		550	0.189	0.044	0.423	-0.202
		600	0.135	0.053	0.323	-0.141
	Oxygen	**350**	**-0.020**	**-0.045**	**-0.055**	**-0.088**
		400	**-0.033**	**-0.006**	**0.034**	**-0.035**
		450	**0.015**	**0.037**	**-0.006**	**-0.041**
		500	0.086	0.036	0.237	-0.114
		550	0.080	0.045	0.233	-0.098
		600	-0.073	-0.035	-0.153	-0.025

Finally, the normalized variation of cell parameters and *c/a* ratio for fresh and cycled cathodes at temperatures that can achieve 100% separation efficiency while maintaining the layered structure is summarized in **Table 3.1**. The results indicate that both air and oxygen atmosphere contribute to achieving 100% separation efficiency while minimizing structural degradation. Specifically, under an air atmosphere, the suitable temperature range is determined to be from

400 to 450 ℃. Conversely, under an oxygen atmosphere, the recommended temperature range shifts slightly lower, spanning from 350 to 450 ℃.

3.4.2 Potential application of thermal treatment for cycled cathode

From the perspective of direct recycling, treating cycled cathodes in an inert or reducing atmosphere could be undesirable due to the severe structural degradation, which significantly challenges the subsequent regeneration of the material. However, this structural degradation may benefit hydrometallurgical processes. Typically accompanied by the release of lithium and oxygen, such degradation facilitates the selective extraction of lithium in water-leaching processes and enhances the dissolution of TM oxides in acid-leaching processes due to their reduced oxidation states.

Conversely, a direct recycling process may benefit from treating cycled cathodes in the air or oxygen atmospheres. Although the separation efficiency of the cycled cathode at 350 °C in oxygen is noticeably higher than in air, it does not reach 100%. This outcome suggests that both air and oxygen atmospheres exhibit similar temperature thresholds for maximizing separation efficiency. Given this, an air atmosphere could be economically favorable. From an energy consumption standpoint, 400 °C is preferable to higher temperatures. However, carbon additives in cycled cathodes typically decompose completely at ~600 °C under air [116]. Therefore, it may be necessary to increase the temperature or extend the holding time to reduce the proportion of these carbon additives in the recovered active material.

3.4.3 Anode material

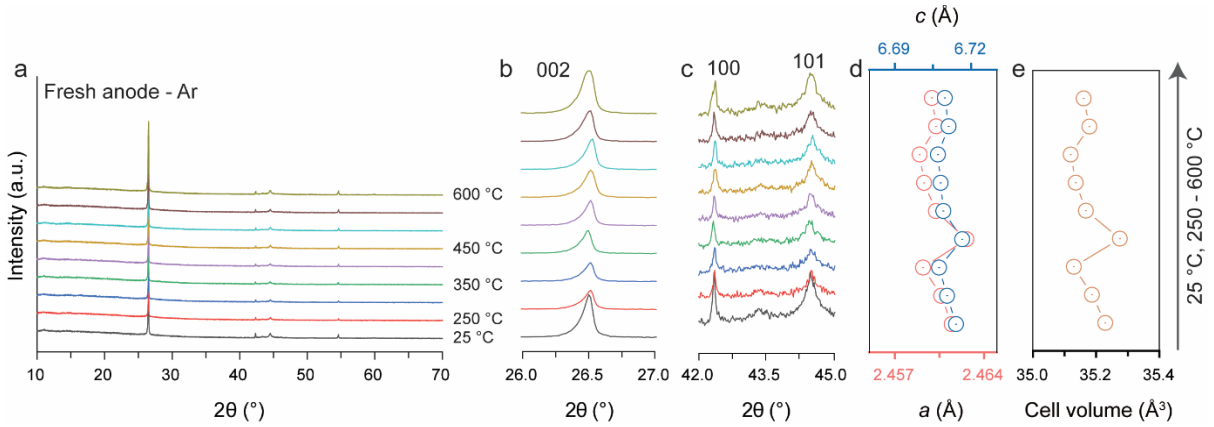

Fig. 3.16. (a) XRD pattern of fresh anode under argon from 25 to 600 °C, and its enlarged area of (b) 26.0-27.0°, (c) 42.0-45.0°. The corresponding (d) *a* and *c*, and (e) cell volume.

The XRD results for the fresh and cycled anodes after thermal treatment under argon atmosphere are displayed in **Fig. 3.16a-e and Fig. 3.17a-e**. The powders obtained from the fresh anodes after 250-600 °C are indexed with a hexagonal layer structure of *P6₃/mmc* space group (**Fig. 3.16a**). The shift of 002 reflection represents the change of interlayer distance and lattice parameter *c*, while the shift of 100 and 101 reflections corresponds to the variation of parameter *a*. As seen in **Fig. 3.16b-c**, there is only a small shift for the 002, 100, and 101 reflections after 250-600 °C, corresponding to a slight variation of cell parameters (**Fig. 3.16d-e)**, reflecting good structure stability of graphite at these conditions.

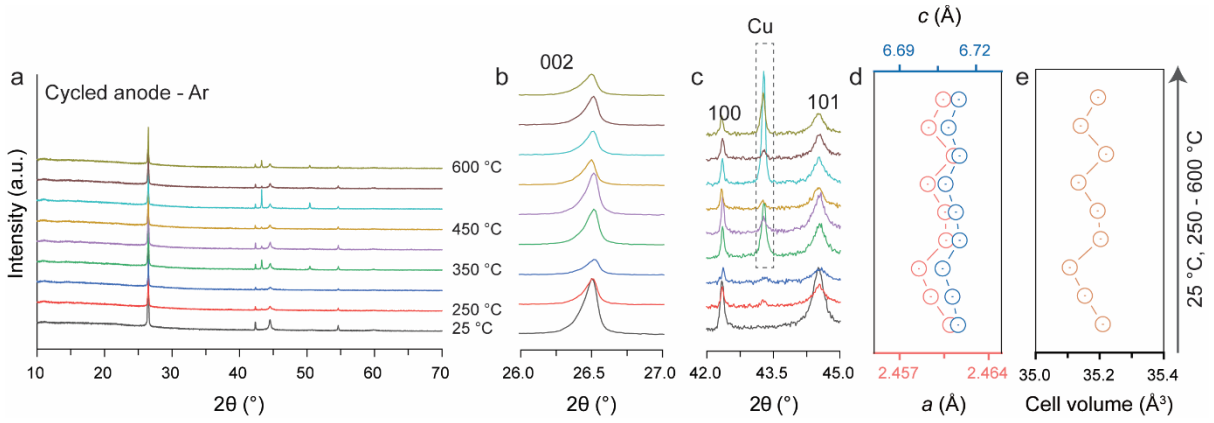

Fig. 3.17. (a) XRD pattern of cycled anode under argon from 25 to 600 °C, and its enlarged area of (b) 26.0-27.0°, (c) 42.0-45.0°. The corresponding (d) *a* and *c*, and (e) cell volume.

The materials obtained after 250-600 °C for the cycled anodes also maintain the layer structure (**Fig. 3.17a**). The observed slight shift in reflection position and the variation in cell parameters (**Fig. 3.17b-e**) suggest that the cycled materials also possess good structural stability when exposed to high temperatures. Notably, reflections attributed to Cu are observed after 350-

600 °C. Their presence can be attributed to chemical changes occurring at the interface contact between graphite and Cu-foil during thermal treatment. These changes result in the inclusion of Cu impurity in graphite after the scraping process.

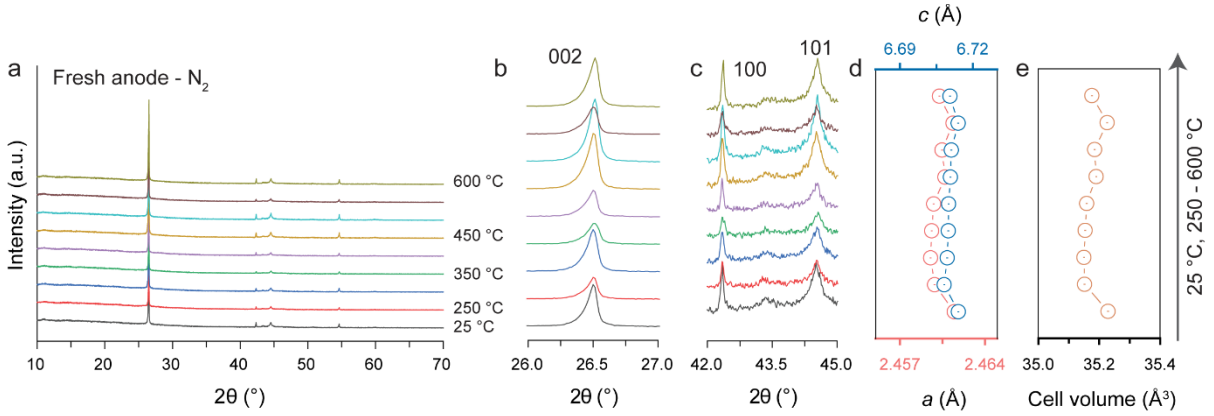

Fig. 3.18. (a) XRD pattern of fresh anode under nitrogen from 25 to 600 °C, and its enlarged area of (b) 26.0-27.0°, (c) 42.0-45.0°. The corresponding (d) *a* and *c*, and (e) cell volume.

Fig. 3.18a-e and Fig. 3.19a-e show the XRD results for the fresh and cycled anode after thermal treatment under a nitrogen atmosphere. For the fresh anode, the material exhibits the layered structure after heating to 250-600 °C, which is similar to the results obtained under an argon atmosphere. The shifts of 002, 100, and 101 reflections at these temperatures are not noticeable (**Fig. 3.18b-c**). Correspondingly, the cell parameters have only slight variation (**Fig. 3.18d-e**), which implies good structure stability of graphite in this temperature range.

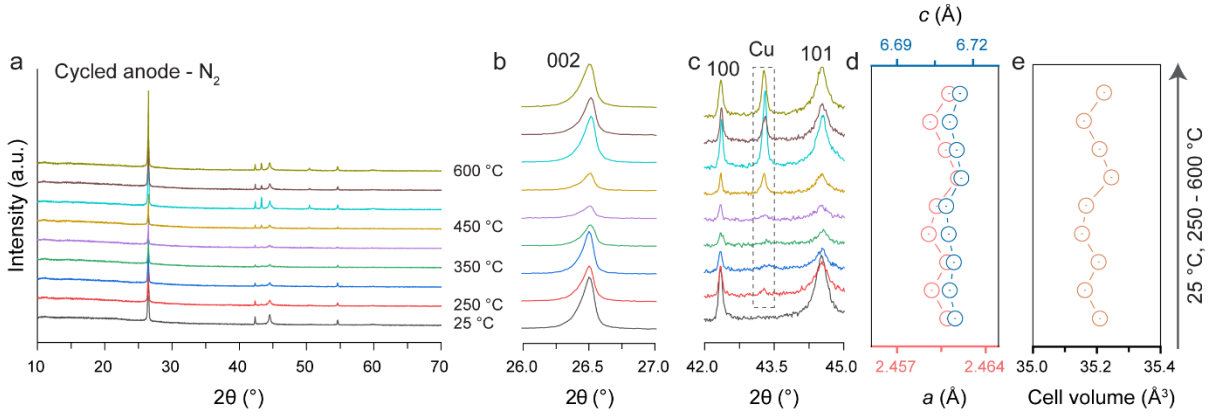

Fig. 3.19. (a) XRD spectrum of cycled anode under nitrogen from 25 to 600 °C, and its enlarged pattern of (b) 26.0-27.0°, (c) 42.0-45.0°. The corresponding (d) *a* and *c*, and (e) cell volume.

For the cycled anode, the material obtained after 250-600 °C retains the layered graphite structure (**Fig. 3.19a**). The shifts of 002, 100, and 101 reflections are also very minor (**Fig. 3.19b-c**), corresponding to the slight fluctuation of the cell parameters (**Fig. 3.19d-e**), indicating that the thermal treatment at this temperature range does not have a significant

impact on the graphite. Yet, the distinct reflections of Cu are also observed after 400-600 °C, resembling the results observed for cycled anodes treated under the argon atmosphere.

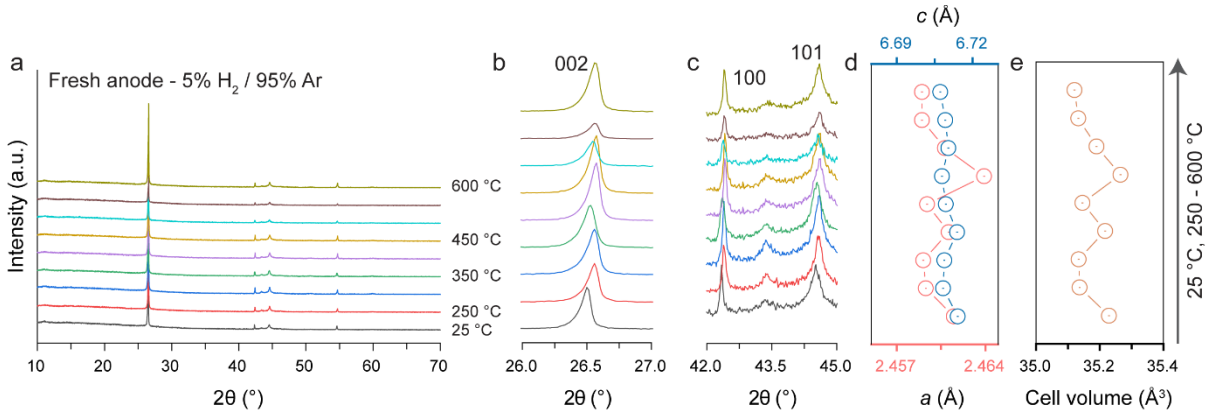

Fig. 3.20. (a) XRD pattern of fresh anode under hydrogen (5% H_2 / 95% Ar) from 25 to 600 °C, and its partial enlarged area of (b) 26.0-27.0°, (c) 42.0-45.0°. The corresponding (d) *a* and *c*, and (e) cell volume.

Fig. 3.20a-e and Fig. 3.21a-e show the XRD results for the fresh and cycled anode after thermal treatment under a hydrogen atmosphere (5% H_2 / 95% Ar). In the case of the fresh anode, the material exhibits a layered structure after heating to 250-600 °C, mirroring the outcomes observed under argon and nitrogen atmospheres (**Fig. 3.20a**). Notably, there are no discernible shifts in the 002, 100, and 101 reflections at these temperatures (**Fig. 3.20b-c**). Correspondingly, there is only a slight variation in cell parameters (**Fig. 3.20d-e**), indicating the robust structural stability of graphite within this temperature range.

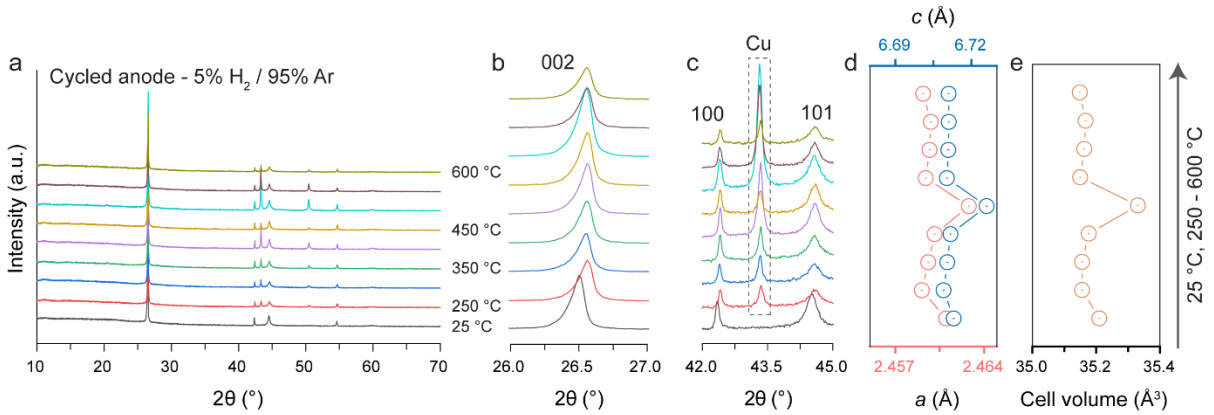

Fig. 3.21. (a) XRD pattern of cycled anode under hydrogen (5% H_2 / 95% Ar) from 25 to 600 °C. and its partial enlarged area of (b) 26.0-27.0°, (c) 42.0-45.0°. The corresponding (d) *a* and *c*, and (e) cell volume.

For the cycled anode, the material maintains the graphite structure after 250-600 °C (**Fig. 3.21a**). The shifts in 002, 100, and 101 reflections are also minimal (**Fig. 3.21b-c**), corresponding to slight fluctuations in cell parameters (**Fig. 3.21d-e**). This implies, under the hydrogen atmosphere, that thermal treatment within this temperature range has a negligible

impact on the graphite structure, akin to the effects observed under argon and nitrogen atmospheres. Besides, more distinct reflections of Cu are observed after 400-600 ℃, resembling the results observed in cycled anode under argon and nitrogen atmosphere.

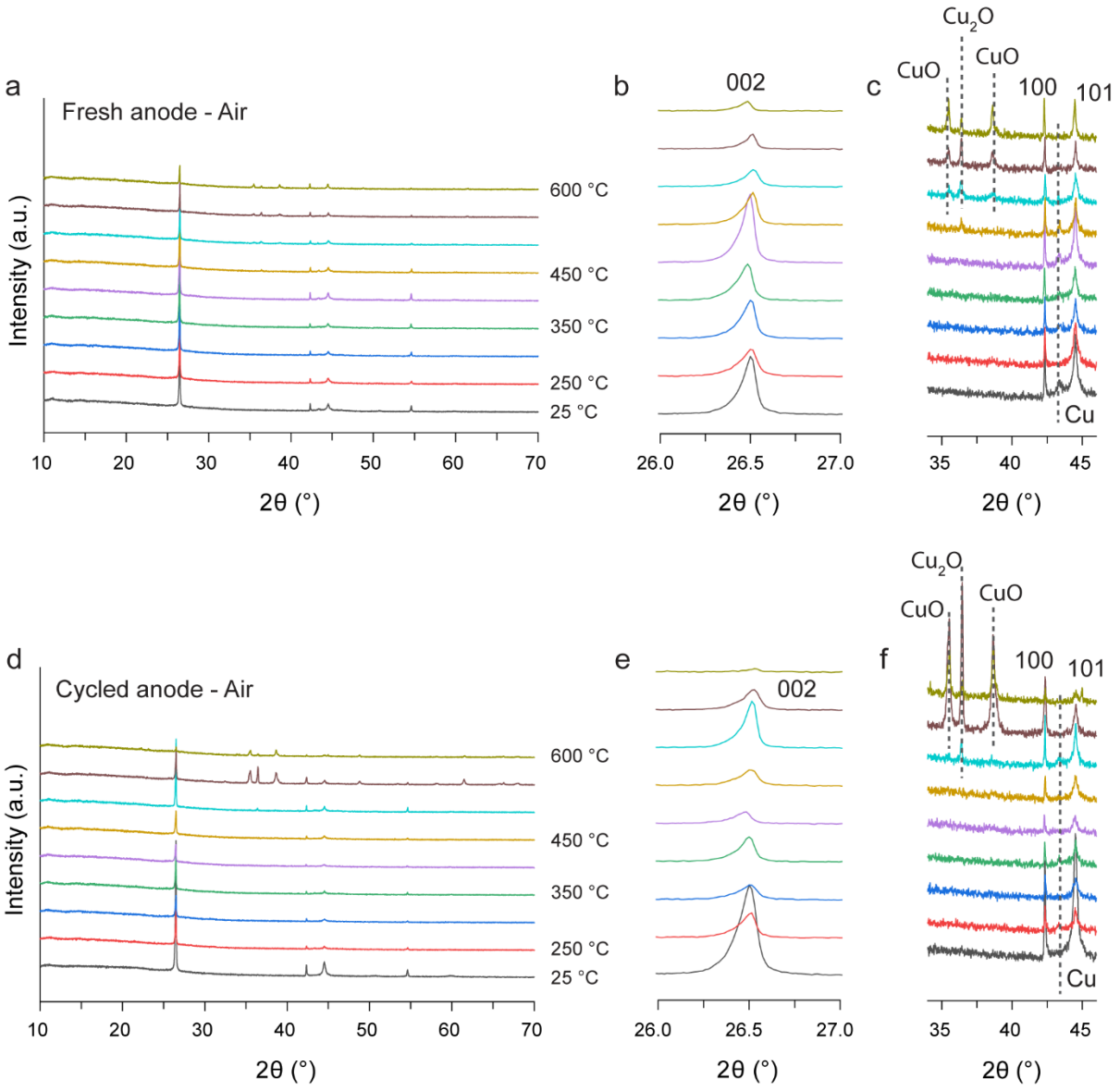

Fig. 3.22. (a) XRD pattern of fresh anode under air from 25 to 600 ℃, and its partial enlarged area of (b) 26.0-27.0°, (c) 34.0-46.0°. (d) XRD pattern of cycled anode under air from 25 to 600 ℃, and its partial enlarged area of (e) 26.0-27.0°, (f) 34.0-46.0°.

Finally, **Fig. 3.22a-f** exhibits the XRD results of the cycled and fresh anodes after the thermal treatment in air. In this case, the calculation of cell parameters is omitted due to a pronounced oxidation of graphite and incomplete separation from the Cu-foil. Consequently, the study on the cell parameters of graphite is considered less appealing. Nevertheless, the structure variation can still be determined based on shifts and intensity of reflections. The fresh anodes maintain the layered graphite structure after 250-600 ℃ (**Fig. 3.22a**). There is no significant

shift of 002, 100, and 101 reflections. The reflection intensity of graphite notably decreases after 450-600 ℃, indicating the oxidation process. Additionally, certain reflections attributed to CuO and Cu_2O are observed after the same temperatures (**Fig. 3.22b-c**), which further confirms the oxidation of Cu-foil. By combining the XRD analysis with the separation results, it is evident that the oxidation of Cu occurs after 250 ℃. Notably, before reaching 350 °C, the oxidation of copper is relatively minor and primarily affects the surface. Therefore, even after the decomposition of the binder, the active material can still be peeled off from the Cu-foil. Above 350 ℃, the oxidation of copper becomes more pronounced, resulting in the embrittlement of the copper, which poses significant challenges for the separation process.

The layered structure of the cycled graphite anodes remains intact after 250-550 ℃ (**Fig. 3.22d**). After 600 ℃, substantial oxidation of graphite is evident based on the very low intensity of graphite reflections. The shift of the 002, 100, 101, and 004 reflections remain very low after 250 -550 ℃ (**Fig. 3.22e-f**). Additionally, reflections corresponding to CuO and Cu_2O are observed after 500 to 600 ℃, indicating the oxidation of the Cu-foil.

3.4.4 Potential application of thermal treatment for cycled anode

Thermal treatment of graphite under argon, nitrogen, and hydrogen (5% H_2 / 95% Ar) atmospheres effectively preserves its desired layered structure. However, a significant challenge arises in the separation process, where achieving a complete delamination of active materials is hindered by the deterioration of the interface between graphite and Cu-foil. Such degradation complicates the separation process, as it obstructs the efficient and thorough detachment of graphite. Furthermore, within the temperature range of 350 to 600 °C, incomplete delamination exacerbates the issue, making the simultaneous handling of cycled cathode and anode problematic. This leads to an unavoidable mixing of cathode and anode materials. Given these complications, relying solely on thermal treatment for separating graphite from copper foil is not advisable. Instead, a potentially more efficient approach may involve combining thermal treatment with solvent-assisted direct recycling techniques.

3.5 Conclusion

In summary, this chapter provides a comprehensive understanding of the separation efficiency and structural degradation resulting from the thermal treatment under different atmospheres and temperatures for both fresh and cycled cathodes and anodes.

The results reveal that the use of air/oxygen atmosphere allows for achieving 100% separation efficiency of active cathode material at a lower temperature compared to argon, nitrogen and hydrogen (5% H_2 / 95% Ar). Under inert environments, the layered structure undergoes gradual degradation as the temperature increases. In contrast, using air and oxygen atmosphere effectively inhibits such transformation and minimizes the degradation process. The structural changes observed under air and oxygen conditions are desirable for direct recycling. Moreover, the cycled cathode material experiences more pronounced phase degradation compared to fresh materials treated under the same conditions. This is primarily attributed to the degraded structural stability due to cycling.

Complete separation of graphite from fresh anodes can be achieved under argon and nitrogen atmosphere at 300 ℃, and under hydrogen (5% H_2 / 95% Ar) at 350 ℃. However, achieving such separation for cycled anodes is challenging due to enhanced interface adhesion between the Cu-foil and graphite caused by the decomposition of residual compounds on the surface. Nevertheless, graphite exhibits excellent thermal stability under argon, nitrogen and hydrogen, maintaining the layered structure after 250-600 ℃. Yet, air atmosphere induces the oxidation of graphite and copper foil, which affects the separation efficiency and material purity.

Finally, it should be mentioned that a treatment condition of 450 °C for 4 h under air for spent cathodes was considered as a suitable balance between separation efficiency and structural preservation, and the resulting NCM622 powders were used as the basis for subsequent regeneration studies.

4. Structural repair of spent NCM material

4.1 Introduction

Among the various steps during direct recycling, the regeneration is garnering most attention, as it is pivotal in determining the properties of the regenerated materials. The regeneration is essentially a structural repair process, involving a local phase transformation from degraded phases (rock-salt/spinel phases) back to original phase (layered phase), driven by re-lithiation [134]. It is well known that rhombohedral (*R-3m*), spinel (*Fd-3m*), and rock-salt (*Fm-3m*) structures all rely on a CCP oxygen framework, with cations occupying tetrahedral or octahedral sites. Consequently, the repair process is fundamentally governed by the kinetics of cation migration and diffusion. Currently, thermal solid-state reaction is the most commonly employed method to enhance these kinetic processes and drive the reformation of the layered phase [135-137].

Understanding how degraded phases transform back to the original structure is essential for designing effective regeneration strategies for such spent layered cathode materials. However, due to the similarity in the cubic-close-packed oxygen framework in the degraded and layered phases, as well as the localized formation of degraded phases in spent materials, differentiating between these phases can be challenging. While transmission electron microscopy (TEM) along with Fast Fourier Transform (FFT) analyses are commonly used to evaluate the success of structural repair [54, 56, 138], these methods often fail to fully capture the detailed structural and chemical evolution occurring throughout the repair process. As a result, the specific mechanisms involving cation migration and differences in migration behavior among the three TMs (Ni, Co, and Mn) remain largely unexplored. Investigating these aspects could provide crucial insights into optimizing repair conditions and improving the effectiveness of direct recycling for NCM materials.

In this chapter, the structural repair of spent NCM622 using thermal solid-state reaction is investigated, focusing specifically on how lithium compensation ratio and reaction temperature affect regeneration. To gain a comprehensive understanding of structural and chemical changes throughout the repair process, multiscale characterization techniques are employed, including diffraction, absorption spectroscopy, and nuclear magnetic resonance to illustrate the structural degradation in spent NCM622, and to reveal both long- and short-range structural evolution upon the repair process. Moreover, the recovery of the electrochemical capacity is evaluated

for cathode materials regenerated under different reaction conditions, revealing a correlation between capacity recovery and structural order. Finally, a possible thermal solid-state reaction mechanism for the structural repair, involving re-lithiation, oxygen capture, TM oxidation and migration, is proposed. These findings provide essential insights into structural repair mechanisms and contribute to advancing sustainable battery recycling technologies.

4.2 Methods

4.2.1 Direct regeneration of cathode active material

The used cycled pouch cells were the same as those mentioned in *Chapter 3*. The cathode sheets extracted from the pouch cells were cut into small pieces, and heated at 450 °C for 4 hours under an air atmosphere to decompose the PVDF binder, thereby facilitating the delamination of CAM from Al foil. After that, CAM was collected by manually shaking the cathode sheets, yielding approximately 65 g spent NCM622 powder.

The spent NCM622 powder was regenerated by a thermal solid-state reaction with a subsequent washing step, and a second heating process to remove the residual lithium salts on the surface. Specifically, the powder was mixed homogeneously in a mortar with $LiOH{\cdot}H_2O$ (Sigma Aldrich, >98 %) in different lithium compensation/TM molar ratios of 0.1/1.0, 0.2/1.0, and 0.3/1.0. The obtained mixture was heated under an air atmosphere in a muffle furnace (100-900 °C for 12 h, heating rate 5 °C min^{-1} and passive cool down to room temperature). During the second thermal treatment after washing, materials regenerated below 650 °C underwent heating to the same temperature as the initial heating, with a holding time of 6 h. In contrast, materials regenerated above 650 °C were subjected to a heating at 650 °C, also with a 6 h holding time.

4.2.2 Electrode Preparation

The electrodes were fabricated by thoroughly blending the cathode active material, Super-C65 conductive carbon black (MTI Co., Ltd.), and polyvinylidene fluoride (PVDF, Sigma-Aldrich) in an 8:1:1 mass ratio using a mortar. N-methyl-2-pyrrolidone (NMP) with a moisture content below 0.1% (VMR) served as the solvent. The mixture was homogenized using a planetary mixer (THINKY ARV-310) at 2000 rpm for 10 minutes in an air atmosphere. The resulting slurry was uniformly applied onto 15 μm thick Al foil (Häberle LABORTECHNIK GmbH & Co.KG) using a ZUA 2000 Universal applicator at a speed of 25.0 mm/s, achieving a coating thickness of 150 μm. The coated Al foil was dried at 80 °C in ambient conditions for 6 h to

remove the NMP solvent. After drying, the electrode material was punched into 12 mm diameter disks (with an approximate active material loading of 3 mg/cm²) using a handheld punch (NOGAMIGIKEN Co., Ltd.). A final drying step was performed in a Büchi glass oven (B-585) under vacuum at 120 °C for 12 hours to ensure complete solvent removal.

4.2.3 Cell Assembly and Electrochemical Characterization

To assess the electrochemical performance, CR2032-type coin cells were assembled. Each cell consisted of a lithium metal anode (14 mm diameter, 0.25 mm thickness, PI-KEM), a WHATMAN GF/C membrane (WHATMAN INT. LTD, Chro.) serving as the separator, and 100 µL of electrolyte. The electrolyte (Sigma-Aldrich) comprised 1 mol L^{-1} $LiPF_6$ dissolved in a 1:1:1 volume ratio of ethylene carbonate (EC), diethyl carbonate (DEC), and dimethyl carbonate (DMC), with the moisture content maintained below 10 ppm. The assembly process was conducted in an argon-filled glovebox with O_2 and H_2O levels kept below 0.1 ppm. The electrochemical cycling and rate tests were performed at a constant temperature of 25 °C using a Biologic VMP3 multichannel battery testing system, operating within a voltage window of 3.0–4.3 V. To ensure reproducibility, all electrochemical experiments were conducted using a minimum of two-coin cells per test. The current density for each cell was determined based on the mass of the active material in the electrode, ensuring accurate and consistent comparisons across measurements.

4.2.4 Material characterization

The elements except oxygen of the materials were analyzed by Inductively Coupled Plasma Optical Emission Spectrometry (ICP-OES), and oxygen was analyzed by Carrier Gas Hot Extraction (CGHE).

The ex-situ X-ray Diffraction (XRD) experiments were conducted on a STOE Stadi P powder diffractometer with monochromatic Cu-$K\alpha_1$ radiation (λ = 1.54056 Å) in transmission geometry. The measurements were performed at room temperature with a 0.015° 2θ step between 10 and 70 degrees of 2θ. The Kapton film's presence visibly adds an amorphous-like background in the XRD patterns at $10° < 2\theta < 17°$.

The in-situ high-temperature XRD experiments were conducted on a STOE Stadi P powder diffractometer with monochromatic Mo-$K\alpha_1$ radiation (λ = 0.7093 Å). The samples were loaded into quartz capillaries with an outer diameter of 0.5 mm. The tests started at room

temperature, followed by a 1-hour dwell at every 50 °C increment. XRD data collection was performed during the dwell period, taking approximately 40 minutes.

The Synchrotron Radiation Diffraction (SRD, λ = 0.9542 Å) data was sequentially collected alongside Hard X-ray absorption Spectroscopy (XAS) at BL16 (NOTOS) at ALBA (Spain) with a synchrotron radiation energy of 13 keV. Specifically, the XAS data was acquired first, with each edge requiring approximately 5 minutes. Subsequently, the system switched to SRD mode, where SRD data collection was completed in approximately 30 seconds. Similar to *Chapter 3*, the Rietveld refinement based on the obtained XRD and SRD patterns was performed in the FullProf software package [139].

The ex-situ Hard X-ray Absorption Spectroscopy (XAS) experiments, focusing on collecting Extended X-ray Absorption Fine Structure (EXAFS) spectra, were performed at beamline P64 Advanced X-ray Absorption Spectroscopy at PETRA III (Germany). The obtained XAS data was processed using ATHENA software [140]. The corresponding $k^2\chi(k)$ data is presented in **Fig. A1-3**, with k-ranges for Fourier transformation selected as 3-11, 3-10.3 and 3-10.5 $Å^{-1}$ for Ni, Co and Mn K-edge, respectively. During Fourier transformation processing in ATHENA, phase correction was applied, resulting in an ~3 Å shift.

Solid-state nuclear magnetic resonance (NMR) spectroscopy was conducted on Bruker Avance 200 MHz spectrometer at a magnetic field of 4.7 T. The spectra were acquired with 1.3 mm rotors at a spinning speed of 60 kHz. The recycle delay was set to 1 s, and the Larmor frequency was 29.5 MHz for ^{6}Li. The ^{6}Li NMR spectra were measured using a rotor-synchronized Hahn-echo pulse sequence (90°−τ–180°−τ–acquisition) with a 90° pulse length of 0.95 μs. The ^{6}Li NMR shifts were referenced using an aqueous 1 M ^{6}LiCl solution (0 ppm). All spectra were normalized with respect to sample mass and number of scans. The temperature of the rotors during spinning were investigated using the shift of ^{207}Pb in $Pb(NO_3)_2$ [141, 142].

4.3 Results and discussions

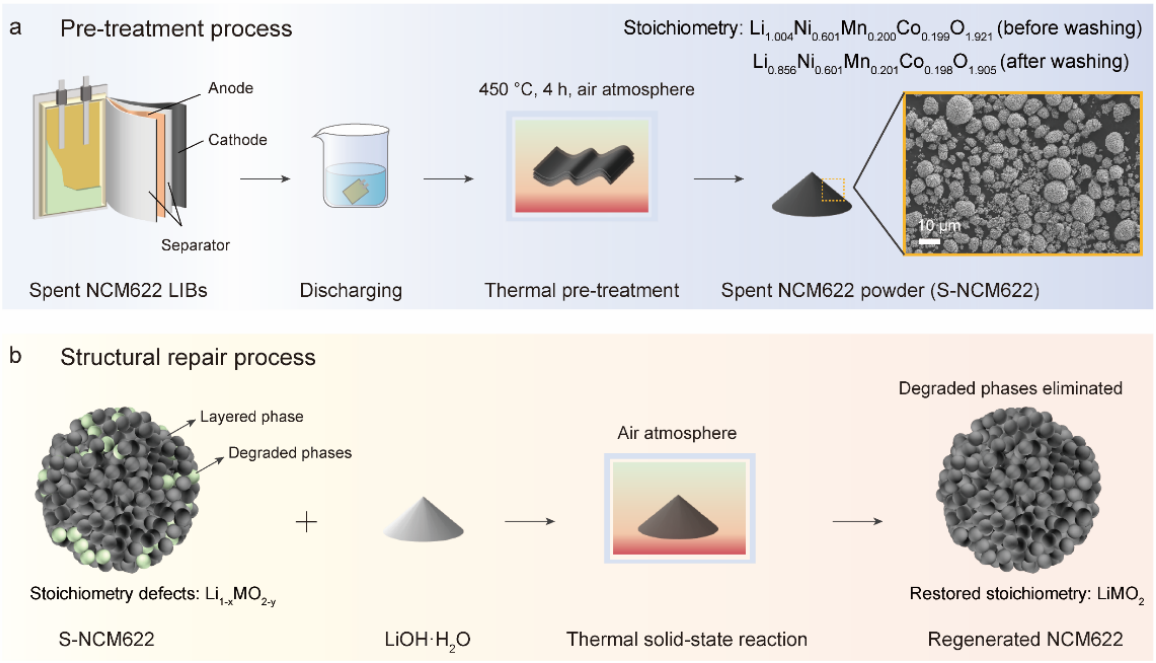

Fig. 4.1. Schematic illustration for a (a) pre-treatment process and (b) subsequent structural repair process used in the present work.

In the present chapter**,** the spent NCM622 powder (denoted as S-NCM622) was obtained from an end-of-life pouch cell (retired after thousands of cycles with a capacity retention of 81%) via thermal treatment at 450 °C for 4 h in air atmosphere (**Fig. 4.1a**), as mentioned in *Chapter 3*. S-NCM622 exhibits a typical polycrystalline morphology but with cracked particles**,** likely arising from the long-term cycling[143, 144]. Its stoichiometry is confirmed as $Li_{1.004}Ni_{0.601}Mn_{0.200}Co_{0.199}O_{1.921}$ (see **Table 4.1**, the result of sample without washing) through ICP-OES and CGHE. After a water-washing process to remove the potentially residual lithium salts (e.g., LiOH, Li_2CO_3 and Li_3PO_4) from the surface, this stoichiometry shifts to $Li_{0.856}Ni_{0.601}Mn_{0.201}Co_{0.198}O_{1.905}$ (see **Table 4.1**, the result of sample with washing), suggesting lithium and oxygen loss from the structure. It is important to note that the unwashed material is primarily used for analysis and regeneration in this study. Besides, no significant stoichiometry changes are observed for the TM elements.

To better understand the structural and chemical changes in S-NCM622, pristine NCM622 (denoted as P-NCM622), commercially purchased, is employed as a reference. Its stoichiometry is found to be $Li_{1.046}Ni_{0.602}Mn_{0.200}Co_{0.198}O_{2.036}$ (**Table 4.2**), aligning well with standard stoichiometry of NCM622. Electrochemical studies on P-NCM622 using a half-cell configuration reveal a discharge capacity of 170.1 mAh g^{-1} at its initial 0.1 C (1 C = 160 mA g^{-}

[1]) cycle over 3.0-4.3 V, and a capacity retention of 96% after 100 cycles at 1 C charge/discharge within the same voltage range, as illustrated in **Fig. 4.2a-b**.

Table 4.1. Elemental composition analysis from ICP-OES and CGHE of the obtained active material after thermal treatment under air at 450°C with and without water washing. (Avg: Average; SD: Standard deviation.)

Samples	Weight percent (%)									
	Ni		Co		Mn		**Li**		O	
	Avg	SD	Avg	SD	Avg	SD	**Avg**	**SD**	Avg	SD
Without washing	31.0	1.0	11.8	0.3	11.1	0.2	**6.83**	**0.12**	35.6	0.7
With washing	31.8	0.7	12.2	0.1	11.5	0.1	**6.02**	**0.06**	36.8	0.3

Table 4.2. Elemental composition analysis from ICP-OES and CGHE of pristine NCM622 (P-NCM622). (Avg: Average; SD: Standard deviation.)

Sample	Weight percent (%)									
	Ni		Co		Mn		Li		O	
	Avg	SD	Avg	SD	Avg	SD	Avg	SD	Avg	SD
P-NCM622	34.5	0.5	11.4	0.2	10.7	0.1	6.88	0.07	31.8	0.4

The structural repair process of S-NCM622 was realized by a thermal solid-sate reaction, as depicted in **Fig. 4.1b**. Specifically, S-NCM622 was homogeneously mixed with $LiOH{\cdot}H_2O$, and then was heated under an air atmosphere in a muffle furnace to restore its structure and stoichiometry.

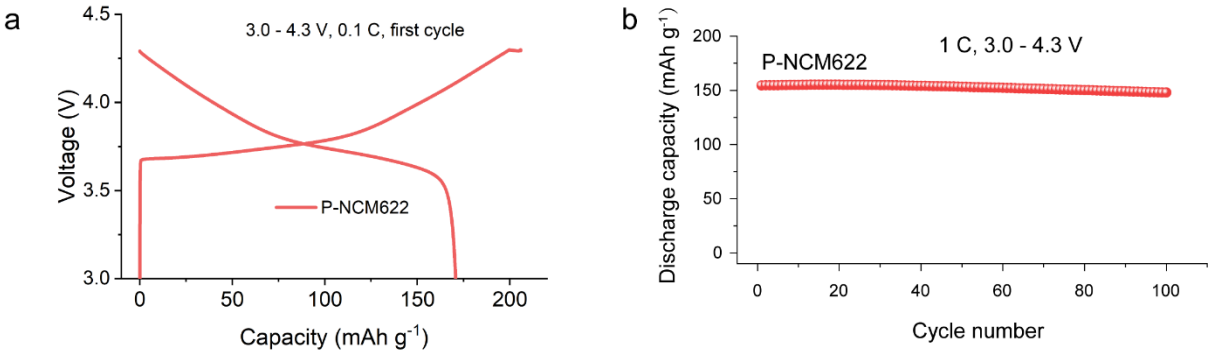

Fig. 4.2. (a) Initial charge/discharge capacities at 0.1 C (1 C = 160 mA g^{-1}), over 3.0-4.3 V and (b) cycling performance at charge-discharge rate of 1 C within the same voltage range for P-NCM622.

4.3.1 Structural degradation in Spent NCM622 cathode material

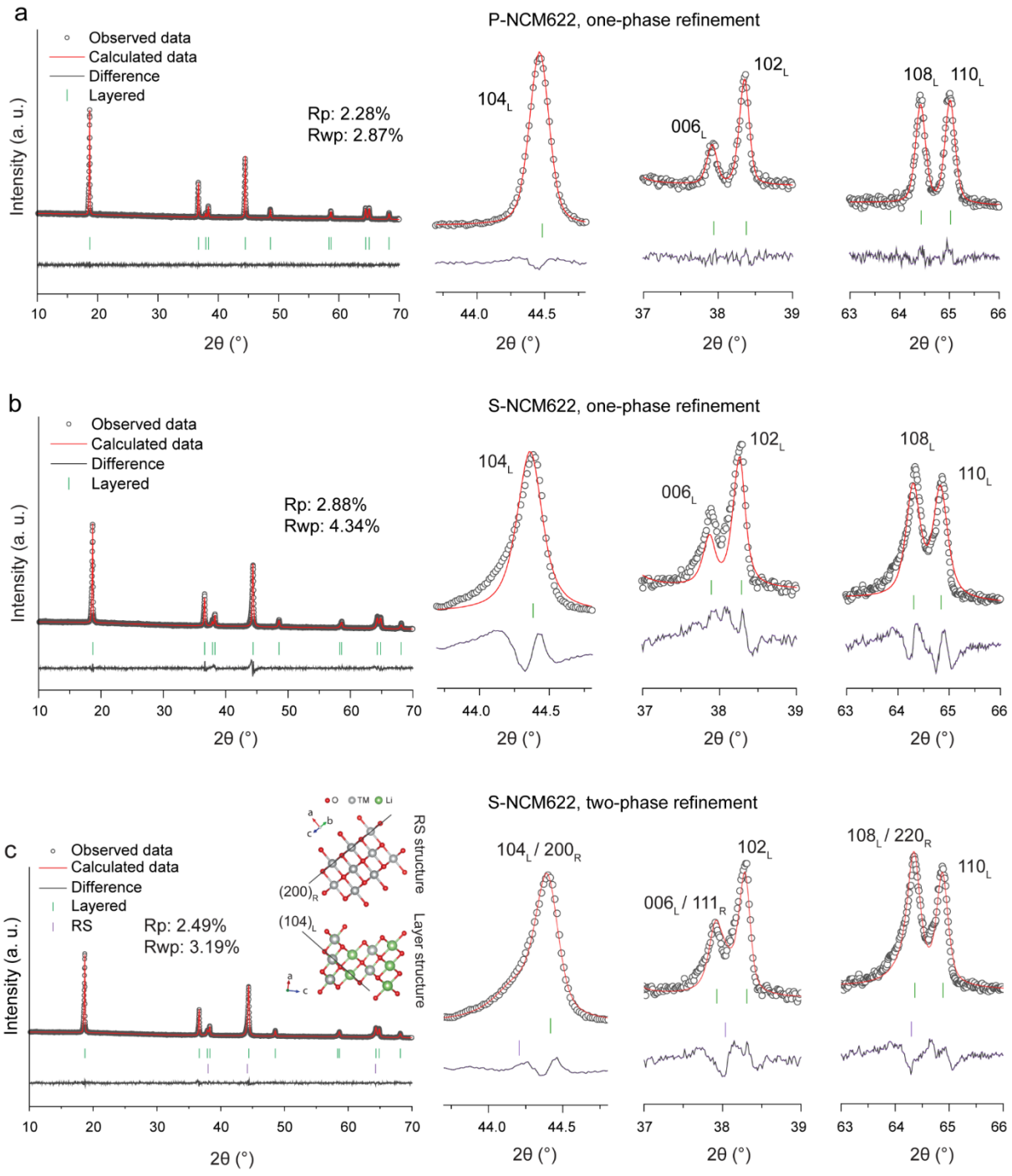

Fig. 4.3. XRD patterns (Cu-Kα_1 radiation, $\lambda = 1.54056$ Å) and corresponding one-phase Rietveld refinement result for (a) pristine NCM622 (P-NCM622), and (b) one-phase and (c) two-phase Rietveld refinement results for spent NCM622 (S-NCM622).

To clarify the structural repair process, it is crucial to first understand the structural degradation occurring in S-NCM622. To investigate the structural degradation, XRD analysis was initially conducted on both P-NCM622 and S-NCM622. The resulting patterns and Rietveld refinement are presented in **Fig. 4.3a-c**. As displayed in **Fig. 4.3a**, P-NCM622 exhibits the characteristic

rhombohedral structure (*R-3m*) with well-defined reflections, indicating a highly ordered layered structure. In S-NCM622, the observed reflections suggest that it retains the layered structure. Nonetheless, the application of a one-phase (layered phase, *R-3m*) Rietveld refinement results in a suboptimal fit to the observed peaks. This poor fit can be attributed to profile anomalies in certain reflections (**Fig. 4.3b**), particularly at the 104_L reflection, which represents local destruction of the crystal's rhombohedral symmetry. Importantly, these anomalies are primarily located at positions corresponding to reflections associated with rock-salt structure (RS, *Fm-3m*, **Fig. A4**). This suggests that the profile anomalies most likely arise from contributions by domains exhibiting cubic symmetry in the spent material. To further illustrate this, a two-phase refinement was then performed (layered and RS). The inclusion of RS improves the fit to the observed peaks, as evidenced by changes in the R_p and R_{wp} values from their initial values of 2.88% and 4.34%, to improved values of 2.49 % and 3.19 %, respectively (**Fig. 4.3b-c**). This indicates that the profile anomalies can be ascribed to overlapping contributions from both phases (layered and RS) with varying degrees of cation ordering. That is to say, RS-type domains resulting from cation disorder are formed in S-NCM622. This conclusion is supported by SRD results as well (**Fig. A5**).

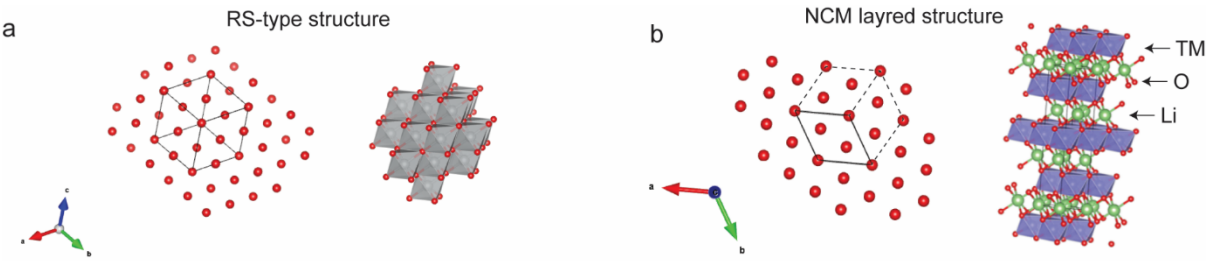

Fig. 4.4. Schematic illustration for (a) RS-type structure and (b) NCM layered structure.

Generally, the RS structure can be characterized by cation occupying edge-sharing octahedra in a cubic-close-packed (CCP) oxygen framework (**Fig. 4.4a**)[57, 145, 146]. While layered NCM materials with rhombohedral symmetry, as shown in **Fig. 4.4b**, feature alternating Li and TM ions occupying edge-sharing octahedra along $(104)_L$ plane, also in an CCP oxygen framework, but with slight distortion that locally disrupts the CCP symmetry (due to the Jahn-Teller effect of Ni^{3+}: $3d^7$, particularly pronounced in high-nickel materials)[147, 148]. As such, the formation of RS-type domains in S-NCM622 can be fundamentally understood as TM migration and occupying the Li octahedral site, coupled with Li and O loss (as evidenced by ICP-OES and CGHE results), possibly along with an intensified or alleviated CCP oxygen framework distortion in NCM622.

Moreover, such migration is typically accompanied by a reduction in TM oxidation states[67, 149]. Based on this characteristic, chemical valence study using XAS with focus on XANES was conducted, to further understand the formation of RS-type domains in S-NCM622 and the potential migration differences among Ni, Co and Mn. The XANES results for both P-NCM622 and S-NCM622 in **Fig. A6** were sequentially collected alongside SRD (as shown in **Fig. A5**). The corresponding Ni, Co, and Mn K-edge XANES spectra reveal that S-NCM622 exhibits edge shifts toward lower energy across all three edges compared to P-NCM622, suggesting decreased average oxidation states of TMs in S-NCM622[69, 150]. Notably, the Ni K-edge exhibits more significant edge shifts than that in Co and Mn K-edge, most likely indicating that the formation of RS-type domains in S-NCM622 resulting from TM migration are largely induced by Ni.

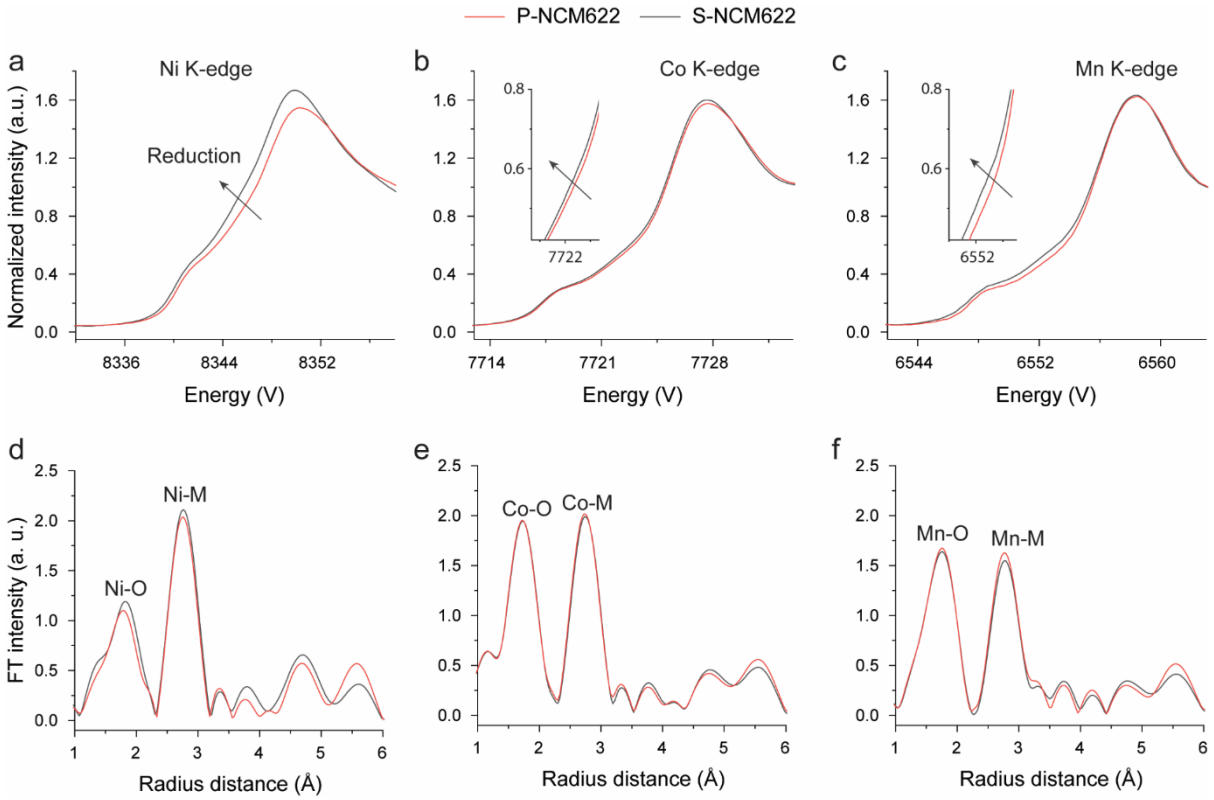

Fig. 4.5. Normalized XANES spectra of (a) Ni, (b) Co, and (c) Mn K-edges for P-NCM622 and S-NCM622. EXAFS results of (d) Ni, (e) Co and (f) Mn K-edges for P-NCM622 and S-NCM622.

The XANES results for P-NCM622 and S-NMC622 measured at PETRA III P64 show consistent trends (**Fig. 4.5a-c**). To obtain atomic-level insights into the coordination environment changes of Ni, Co, and Mn during RS-type domain formation, the corresponding EXAFS analysis (Fourier transformation $k^2|\chi(k)|$) was performed. As shown in **Fig. 4.5d-f**, both samples display two dominant peaks in the radial distribution function for each metal edge at

~1.8 and ~2.8 Å, assigned to metal-oxygen (M-O) and metal-metal (M-M) bonds, respectively[68, 151]. As observed, the Ni-O peak of S-NCM622 displays a substantial magnitude increase relative to P-NCM622, while the Co/Mn-O peak shows only minor differences. These findings suggest that RS-type domain formation involves changes in the NiO_6 octahedral coordination environment, while leaving the Co and Mn local structures relatively unaffected. It is therefore inferred that the structural changes of NiO_6 octahedra could be related to the transition of Ni^{3+}-O_6 to a more symmetric Ni^{2+}-O_6 (Jahn−Teller free)[151, 152], with subsequent local accumulation of Ni^{2+} in specific regions by cation diffusion along *a*/*b*-axis. This accumulation is most likely responsible for the emergence of cubic-symmetry domains, while simultaneously inducing locally symmetry changes in the CCP oxygen framework of NCM622 material. In contrast, Co and Mn are believed to exhibit slight variations in their local environments only, largely due to their limited migration and the inherent stability of Co^{3+}-O_6 and Mn^{4+}-O_6 octahedra within the TM layer[70]. In other words, these observations further suggest that the Ni ions occupying the Li octahedral site, accompanied by local geometric changes in Ni and O coordination environment, serves as the dominant mechanism driving the RS-type domain formation in S-NCM622.

In addition, the increased magnitude observed at ~3.8 Å from the Ni-edge spectra for S-NCM622, a peak generally associated with 180° Ni–O–Ni correlations, provides further evidence for Ni occupying Li octahedral sites, reinforcing the proposed Ni migration mechanism[153-155]. Two more distant peaks observed at ~4.7 and ~5.5 Å, correspond to combined single M–M and multiple M–M–M scattering between or within TM planes[152, 153], offering insights into longer-range structural changes. These peaks, show similar trends in S-NCM622 compared to P-NCM622 across all radial distributions for Ni, Co, and Mn elements, as seen in the corresponding absorption edge spectra. The magnitude variations for S-NCM622 in these two peaks may be attributed to enhanced interlayer backscattering induced by TM ions in the Li layer (~4.7 Å), and reduced intralayer backscattering due to Li ions when TM absorbers are located in the Li layer (~5.5 Å), respectively. As a result, these changes most likely further indicate an overall increase in amounts of TM ions within the Li layer in S-NCM622 [155].

Overall, the migration of TM ions, particularly Ni, from the TM layer to the Li layer, coupled with lithium and oxygen loss, reduction in TM oxidation states, results in local destruction of crystal's rhombohedral symmetry and the formation of RS-type domains. This is identified as

the primary driving force for structural degradation in S-NCM622. Based on previous studies, the RS-type domains are believed to be near the material's surface to achieve a low-energy state[66, 68, 156]. In the following sections, we will explore how this structural degradation can be repaired. The long- and short-range structural evolution during this repair process is examined, and the impact of structural reordering on the recovery of battery capacity of the repaired cathode is discussed.

4.3.2 Electrochemical performance evaluation

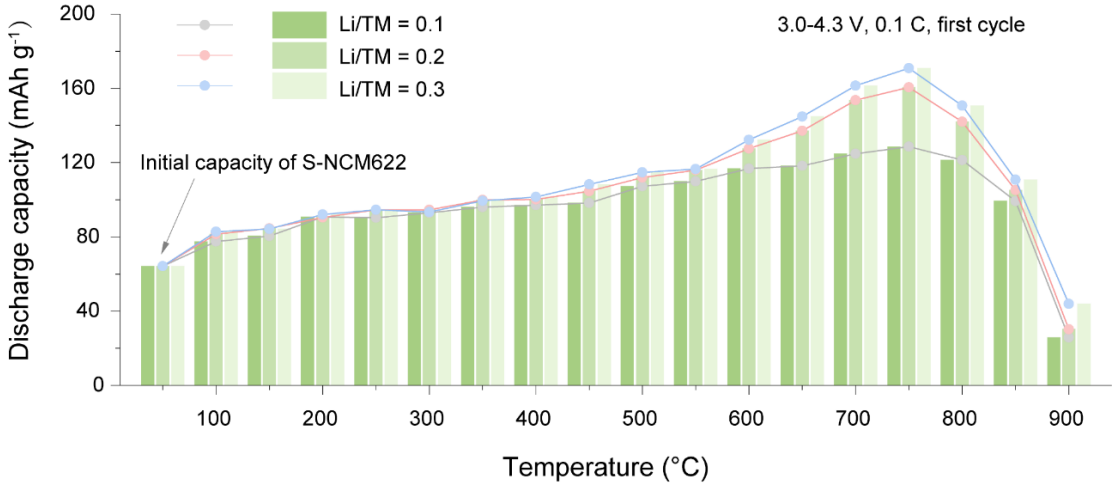

Fig. 4.6. Initial discharge capacities at 0.1 C (1 C = 160 mA g^{-1}), over 3.0-4.3 V for materials regenerated at various temperatures and Li/TM molar ratios (Li/TM refers to lithium compensation/TM molar ratio).

To illustrate the mechanisms behind the structural repair, the restoration of electrochemical performance was first evaluated by measuring the initial discharge capacities at a charge-discharge rate of 0.1 C (1 C = 160 mA g^{-1}) over a voltage range of 3.0-4.3 V. This was performed for materials regenerated at various temperatures (100-900 °C, in 50 °C intervals) and with different lithium compensation/TM molar ratios (denoted as Li/TM = 0.1, 0.2 and 0.3, using $LiOH{\cdot}H_2O$ as the lithium source) in a half-cell configuration.

As seen in **Fig. 4.6**, S-NCM622 delivers a discharge capacity of 64.2 mAh g^{-1} in its first cycle at 0.1 C. This low capacity is likely attributed to impurities and further structural degradation introduced during the pre-treatment process(water washing through centrifuge), in addition to the degradation that occurred during cycling in the initial full-cell battery. After undergoing the structural repair process, the materials exhibit different levels of capacity recovery. It should be noted that the capacity increases below 200 °C is believed to stem from the removal of certain impurities during the washing process following regeneration (**Fig. 4.7a**). The majority of the capacity recovery occurs when the materials are treated between 600 and 750 °C,

with higher Li/TM ratios further enhancing the recovery. However, after 750 °C, the capacity recovery begins to decline. Among the regenerated samples, the material regenerated at 750 °C and Li/TM ratio of 0.3 (denoted as R-NCM622) shows the highest capacity, achieving 170.8 mAh g^{-1}, comparable to that of P-NCM622 (**Fig. 4.7b).** Further investigation into higher Li/TM ratios (0.4, 0.5, and 0.6) at 750 °C reveals that increasing the Li/M ratio beyond 0.3 does not further improve the capacity (**Fig. 4.8a**). These findings suggest that the optimal condition for achieving maximum capacity recovery in this structural repair process should be at 750 °C with a Li/TM ratio of 0.3.

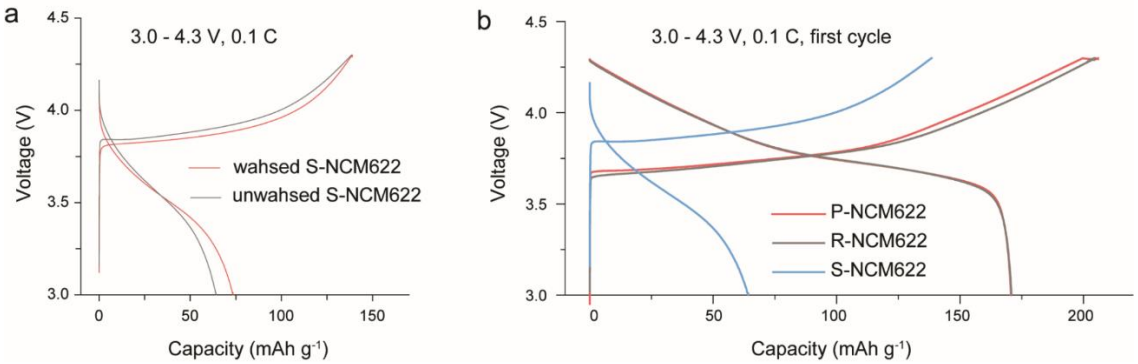

Fig. 4.7. (a) Initial charge/discharge capacities at 0.1 C, over 3.0-4.3 V for S-NCM622 with and without washing, (b) Initial charge/discharge capacities at 0.1 C, over 3.0-4.3 V for S-NCM622, P-NCM622 and R-NCM622 (regenerated under 750 °C with a Li/TM ratio of 0.3).

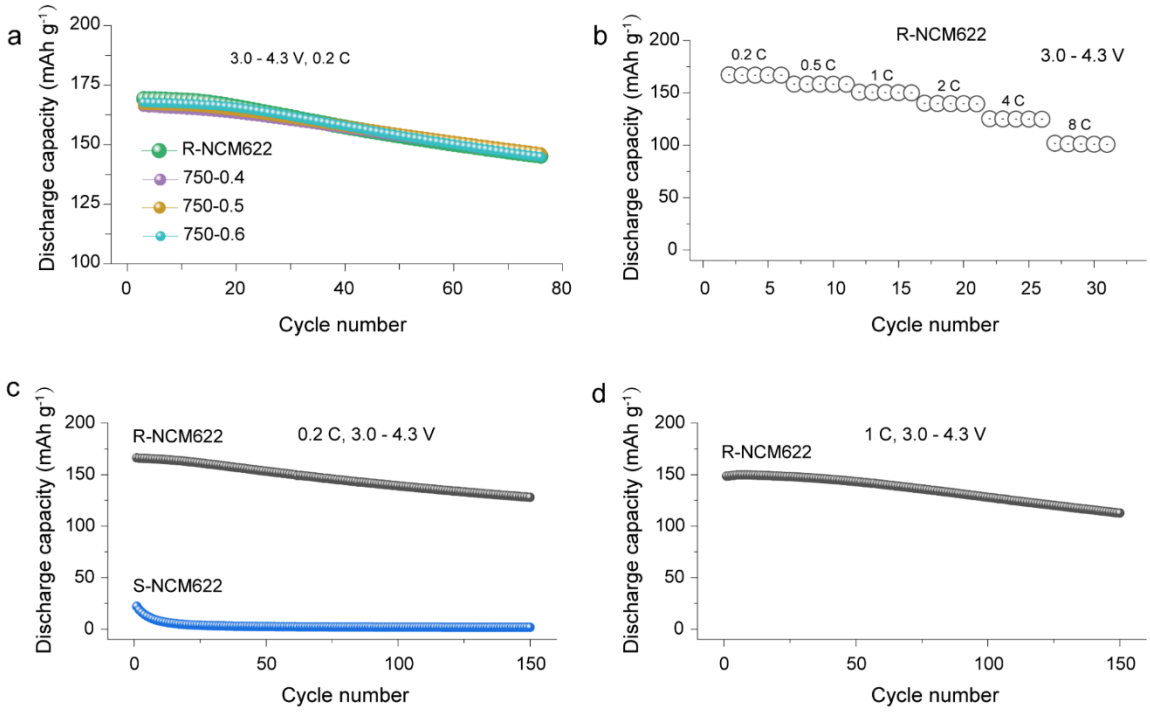

Fig. 4.8. (a) Cycling performance for materials regenerated at 750 °C with different Li/TM ratios (Li/TM = 0.3, 04, 0.5 and 0.6, the corresponding samples are denoted as 750-0.3, 750-0.4, 750-0.5 and 750-0.6, respectively) at charge-discharge rate of 0.2 C, over 3.0-4.3 V. (b) Rate performance of R-NCM622. (c) Cycling performance of

R-NCM622 and S-NCM622 at charge-discharge rate of 0.2 C, over 3.0-4.3 V. (d) Cycling performance of R-NCM622 at charge-discharge rate of 1 C, over 3.0-4.3 V.

To further evaluate the restoration of electrochemical properties, the rate and cycling abilities of R-NCM622 were studied. **Fig. 4.8b** shows that R-NCM622 delivers initial discharge capacities of 167.2, 158.4, 150.6, 140.0, 125.3 and 102.0 mAh g^{-1} at 0.2, 0.5, 1, 2, 4 and 8 C with a cut-off voltage of 4.3 V, respectively. **Fig. 4.8c-d** exhibit that R-NCM622 retains 77% of its initial capacity after 150 cycles at a charge/discharge rate of 0.2 C within the voltage range of 3.0-4.3 V, and 76% capacity retention after 150 cycles at 1 C within the same voltage range. These results further demonstrate the successful restoration of electrochemical properties.

4.3.3 Analysis of the repair mechanism

With the understanding of the capacity recovery trend in the regenerated materials, a series of in-depth characterizations to uncover the underlying mechanisms behind the capacity recovery was conducted.

Structurally, the repair process can be understood as the reverse of structural degradation. This process generally involves re-lithiation, oxygen capture, an increase in TM oxidation states, and the TM migration from the Li layer back to the TM layer. This can be represented by the following reaction, where LiOH serves as the lithium source:

$$Li_{1-x}Ni_{0.6}Co_{0.2}Mn_{0.2}O_{2-y} + LiOH + O_2 \uparrow \rightarrow LiNi_{0.6}Co_{0.2}Mn_{0.2}O_2 + H_2O \uparrow \quad (4\text{-}1)$$

The structural evolution occurring during this reaction was initially studied by mixing S-NCM622 with different Li/TM ratios (0.1, 0.2, and 0.3) and analyzing it using in-situ high-temperature XRD over a temperature range from room temperature (RT) to 800 °C under an air atmosphere. As shown in **Fig. 4.8a-c**, reflections corresponding to $LiOH{\cdot}H_2O$ are detected below 150 °C, growing more prominent with increasing Li/M ratios. Around 150 °C, $LiOH{\cdot}H_2O$ loses water to form LiOH, which then melts around 450 °C, indicated by the shift of reflections and their disappearance. Throughout the tested temperature range and various Li/M ratios, the layered structure of S-NCM622 is maintained. However, a continuous shift towards lower angles is observed for 003_L and 104_L reflections as the temperature increases, implying changes in lattice parameters. Such shifts of reflections have been noted in prior studies on direct recycling of layered materials[157-159], though the mechanisms may not have been fully explored.

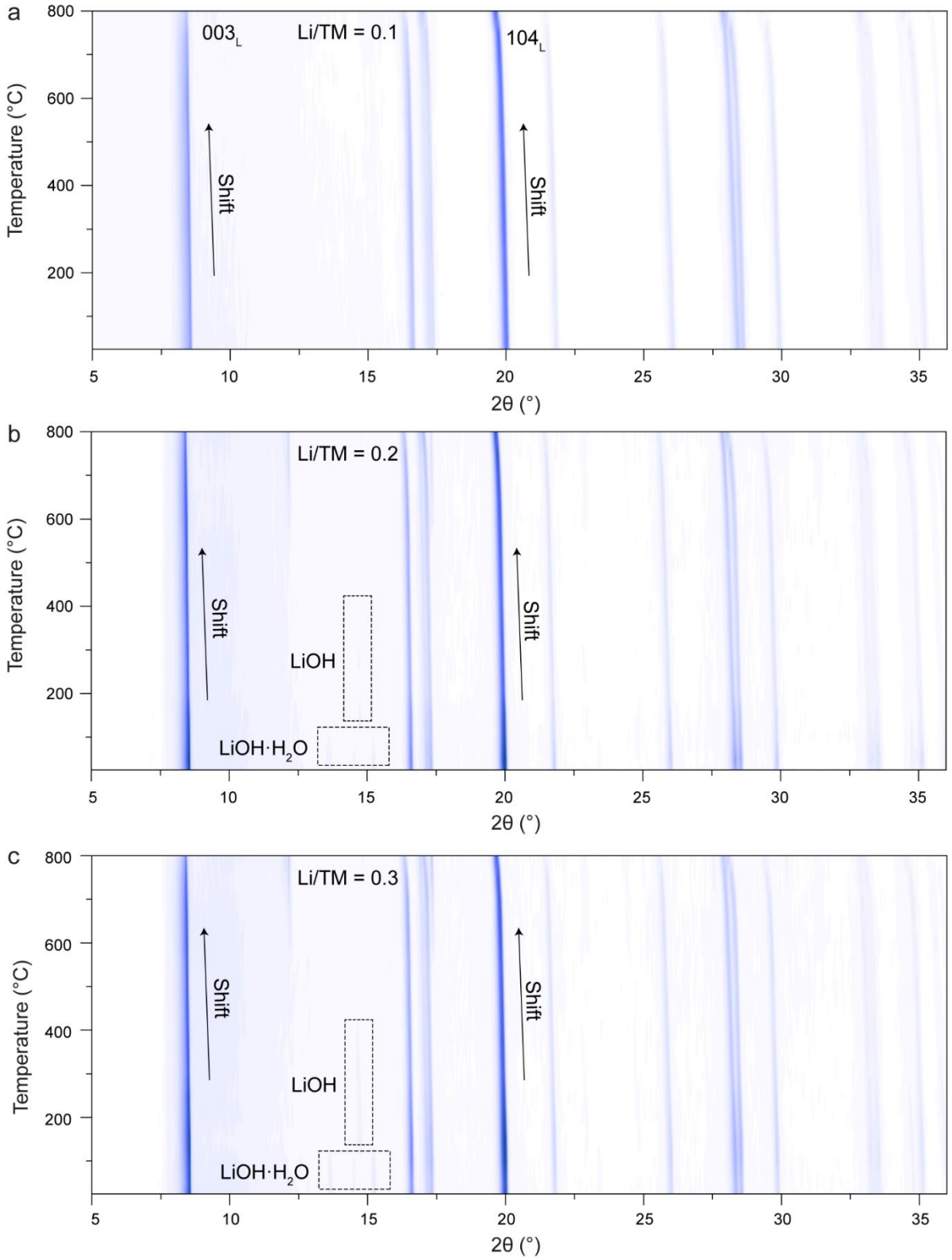

Fig. 4.9. In-situ high-temperature XRD patterns (Mo-Kα_1 radiation, λ = 0.7093 Å) for (a) Li/TM = 0.1, (b) Li/TM = 0.2 and (c) Li/TM = 0.3.

To comprehend this behavior, we further characterized both P-NCM622 and S-NCM622 across the same temperature range without adding an additional lithium source (**Fig. 4.9a-b**). Cell

parameters for all samples were then extracted using Rietveld refinement.

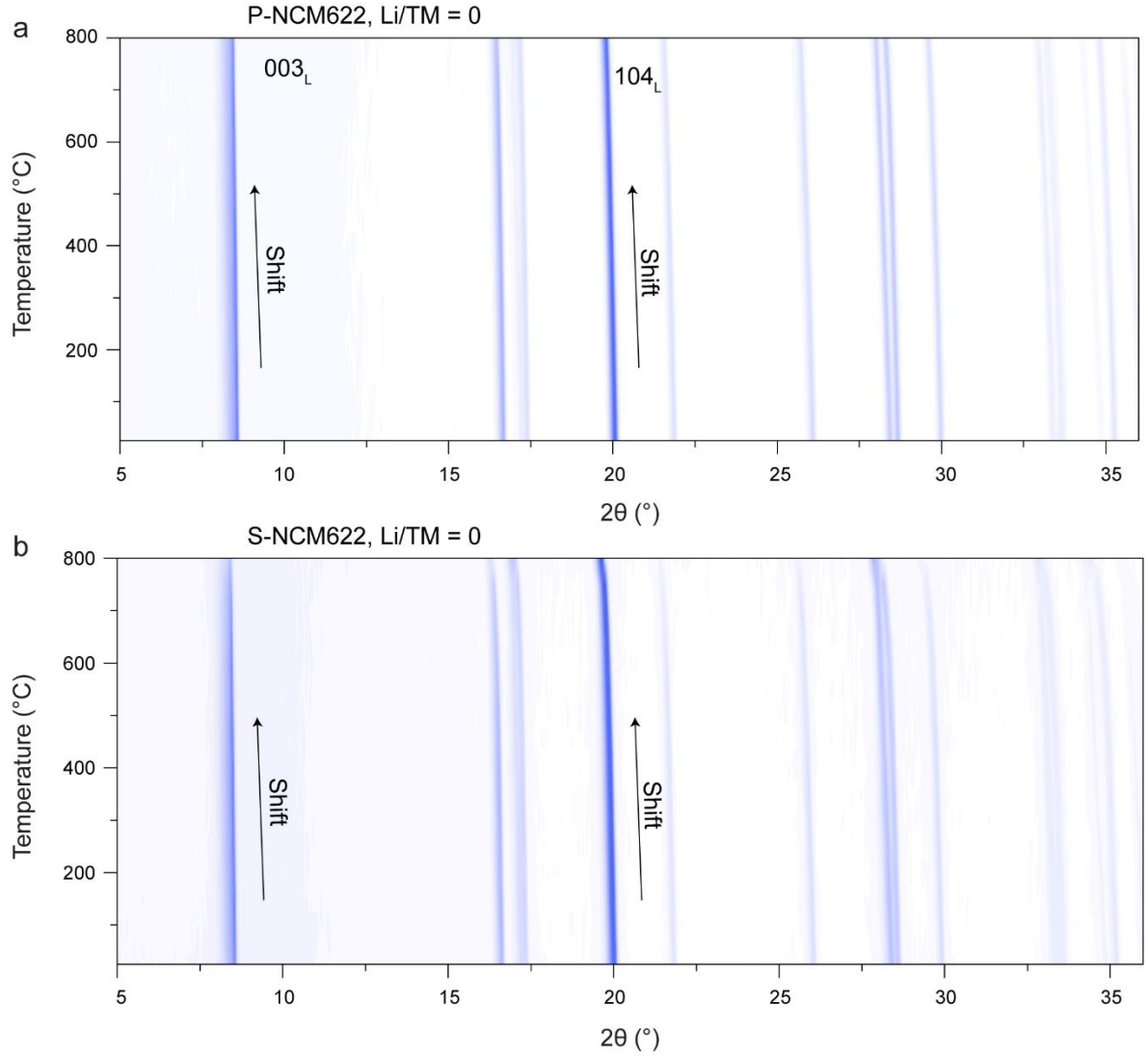

Fig. 4.10. In-situ high-temperature XRD patterns (Mo-Kα_1 radiation, λ = 0.7093 Å) for (a) P-NCM622 and (b) S-NCM622.

For P-NCM622, the *a* and *c* values also expand as the temperature increases (**Fig. 4.10a**). Notably, the expansion of *a* and *c* remains relatively constant over each 50 °C increment, suggesting that the expansions should be mainly ascribed to anharmonicities of lattice vibrations (thermal expansion). The differing thermal expansion of *a* and *c* can be explained by weaker interlayer forces (O-Li-O) than intralayer forces (O-TM-O). Yabuuchi et al.'s work on the thermal instability of cycled lithium-nickel-manganese oxides demonstrates similar conclusions[160]. In the case of S-NCM622, similar expansion trends in *a* and *c* are found (**Fig. 4.10b**). Nevertheless, there is an evident increase in the expansion rate of *a* at 650 °C, with gradual intensification as temperature further increases. The increases could indicate some

degree of structural degradation, resulting from inferior thermal stability. Since *a* is generally linked to TM-O bonding distance, the higher expansion of *a* likely reflects a reduction in the oxidation states of TMs[161, 162]. When lithium compensation is applied, the expansion behavior under Li/M=0.1 closely resembles that of untreated spent S-NCM622 (**Figure. 4.10c**). However, at higher lithium compensation ratios, the evident increase in the expansion rate of *a* is delayed to 700 °C, and the overall expansion is largely inhibited (**Figure. 4.10d-e**). This phenomenon might originate from the enhanced lithiation and structural repair promoted by higher lithium content, which results in improved thermal stability.

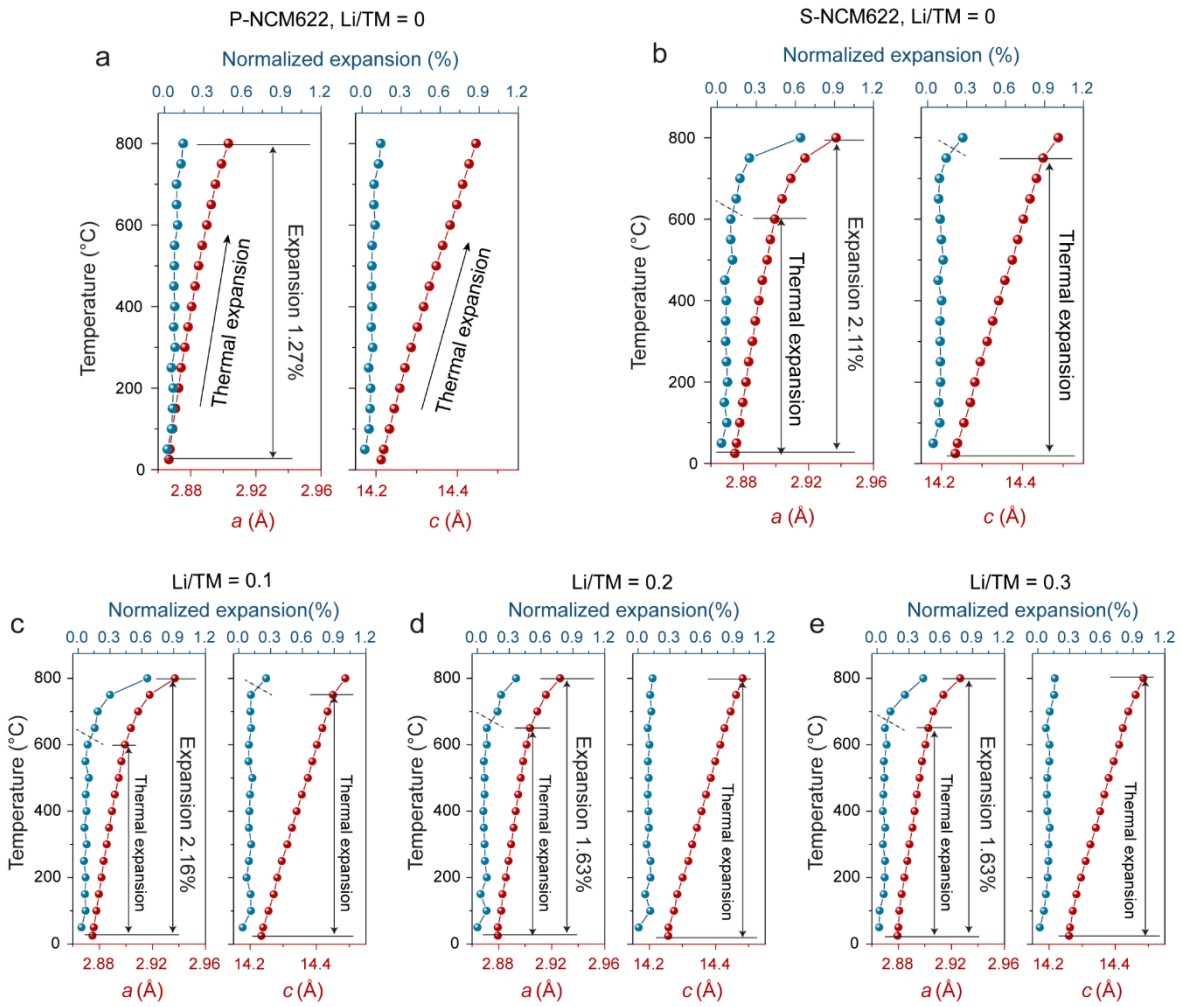

Fig. 4.11. Calculated *a* and *c* and their normalized expansion for (a) P-NCM622, (b) S-NCM622, (c) Li/TM = 0.1, (d) Li/TM = 0.2, and (e) Li/TM = 0.3 (the lattice expansion in the figures was normalized by calculating the growth of the lattice parameters over each 50 °C increment).

Due to the thermal expansion, it is challenging to fully understand the evolution of structural order during the repair process through in-situ XRD findings. **Fig. 4.12 and 4.13a-f** presents ex-situ XRD results to further elucidate the structural evolution, where the samples were heated to different temperatures (200, 400, 600, 750, and 900 °C) with various Li/TM ratios (0.1, 0.2,

and 0.3) and then cooled down to RT. Unlike the in-situ findings, the ex-situ results reveal that drastic lattice expansions are only observed at 900 °C (**Fig. 4.12**), as indicated by the notable reflection shifts, which are related to structural degradation.

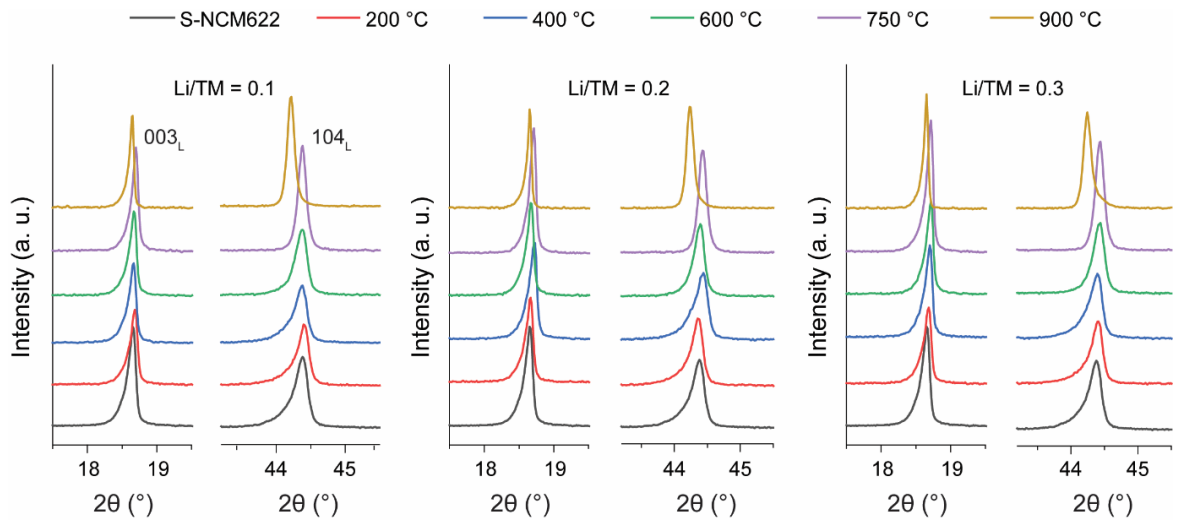

Fig. 4.12. Enlarged region of ex-situ XRD patterns for materials regenerated under different temperatures (200, 400, 600, 750 and 900 °C) and Li/TM ratio of 0.1, 0.2 and 0.3.

To better understand the changes below 750 °C, we conducted two-phase Rietveld refinement (layered and RS) on the in-situ data, focusing on the structural disorder. Here, the structural disorder is believed to originate primarily from two sources: (1) the random distribution and mixing of cations within a local region, which alters the local crystal's symmetry and is referred to as RS-type domain. In the XRD pattern such disorder is mainly reflected in profile anomalies in reflections. (2) the occupation of Li octahedral sites by TM ions, which does not necessarily change the symmetry but still contributes to disorder, known as cation mixing. In XRD pattern, this type of disorder is primarily reflected in the relative peak intensity.

For the materials regenerated below 600 °C, no significant reduction in structural disorder is observed compared to S-NCM622, as indicated by similar levels of RS and cation mixing (**Fig. 4.13a-d**). At 600 °C, however, the regenerated materials exhibit a noticeable alleviation in profile anomalies in reflections, corresponding to a significant decrease in RS content alongside a slight increase in cation mixing. These observations demonstrate an overall improvement in structural order. This transition from disorder to order, as illustrated in **Fig. 4.13e**, can be attributed to the restoration of rhombohedral symmetry, driven by the reduction of domains with disordered RS-type cation ordering. These findings account for the noticeable capacity recovery observed after 600 °C, which is ascribed to the obviously improved structural order.

As the temperature reaches 750 °C, the profile anomalies in reflections nearly disappear, indicating the restoration of rhombohedral symmetry (**Fig. 4.13f**).

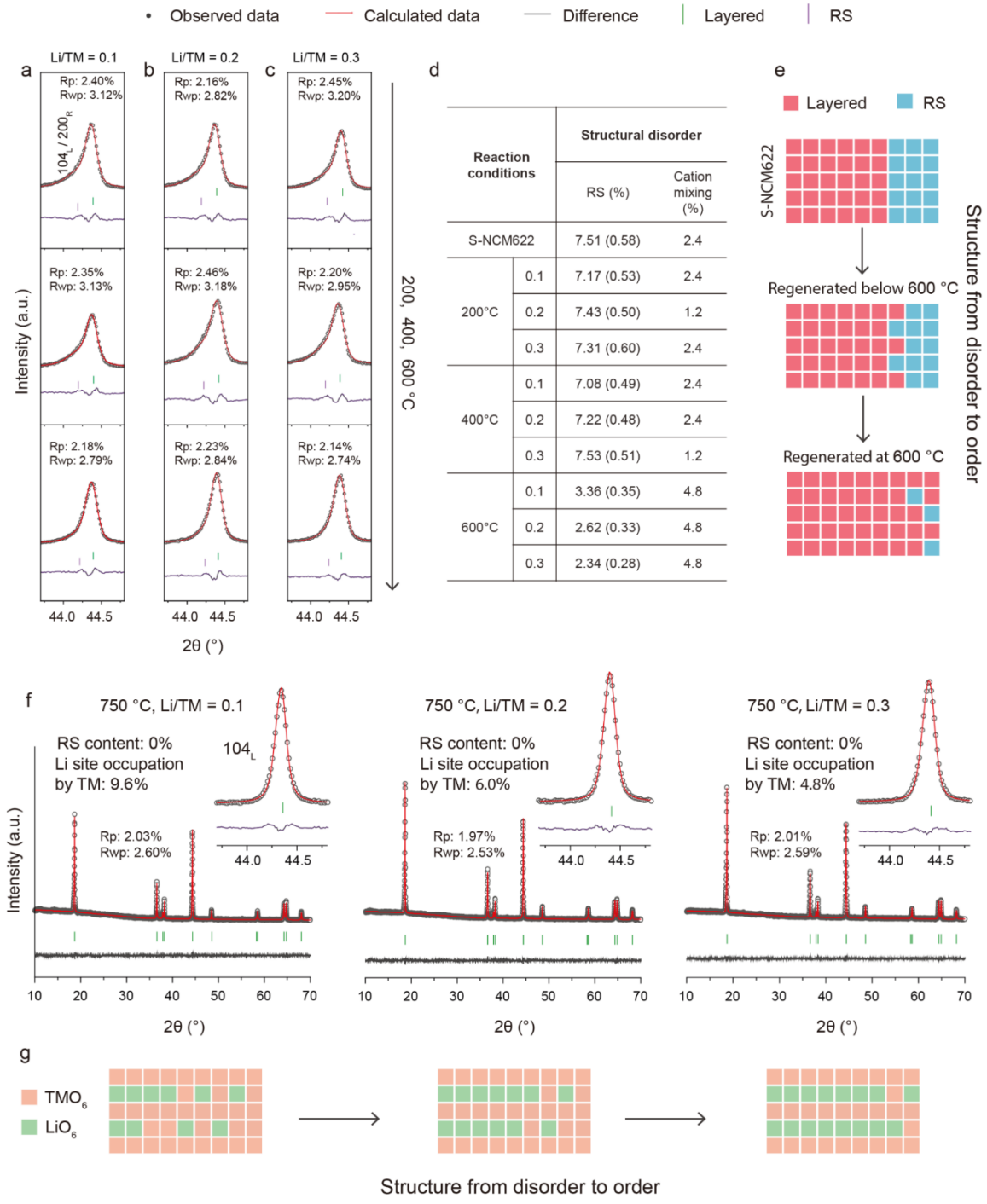

Fig. 4.13. Ex-situ XRD (Cu-Kα_1 radiation, λ = 1.54056 Å) and corresponding refinement results (focusing on 104_L reflection) for materials regenerated under different temperatures (200, 400 and 600 °C) with a Li/TM ratio of (a) 0.1, (b) 0.2 and (c) 0.3. (d) Corresponding calculated content of RS and cation mixing in these materials through Rietveld refinement. (e) Schematic illustration for the structure from disorder to order when materials regenerated ≤600 °C. (f) Ex-situ XRD patterns and corresponding refinement results for materials regenerated at 750 °C with Li/TM ratio of 0.1, 0.2 and 0.3, respectively. (g) Schematic illustration for the structure from disorder to order when materials regenerated at 750 °C with different Li/TM ratios.

However, despite this recovery, underlying disorder may still persist. This is evident in the varying degrees of TM occupation at Li octahedral sites among regenerated materials with different Li/TM ratios: 9.6%, 6.0%, and 4.8% for Li/TM ratios of 0.1, 0.2, and 0.3, respectively (calculated from Rietveld refinement). Notably, the material regenerated with a Li/TM ratio of 0.1 exhibits significantly increased cation mixing, suggesting that structural order remains poor despite the decrease of RS-type domains.

Therefore, it could be challenging to determine whether the structure of materials regenerated at 750 °C with low Li/TM ratios is more ordered than those regenerated at 600 °C with high Li/TM ratios, based solely on the ex-situ XRD results. However, it can be conclusively stated that at 750 °C, the structural order of regenerated materials is strongly influenced by the Li/TM ratio. This also explains the significant impact of the Li/TM ratio on capacity recovery at 750 °C. The structural evolution from a Li/TM ratio of 0.1 to 0.3 at this temperature, as shown in **Fig. 4.13g**, can be ascribed to the alleviation of the cation mixing, driven by the cation migration and rearrangement. This alleviation contributes to the improvement of capacity recovery. As such, R-NCM622 (750 °C, Li/TM = 0.3) achieves the highest capacity among all regenerated materials, corresponding to the optimal structural order.

Overall, the combined in-situ and ex-situ XRD findings provide preliminary insights into the long-range structural evolution during the repair process, highlighting a strong correlation between improved structural order and enhanced capacity recovery, driven by elevated temperature and Li/TM ratio.

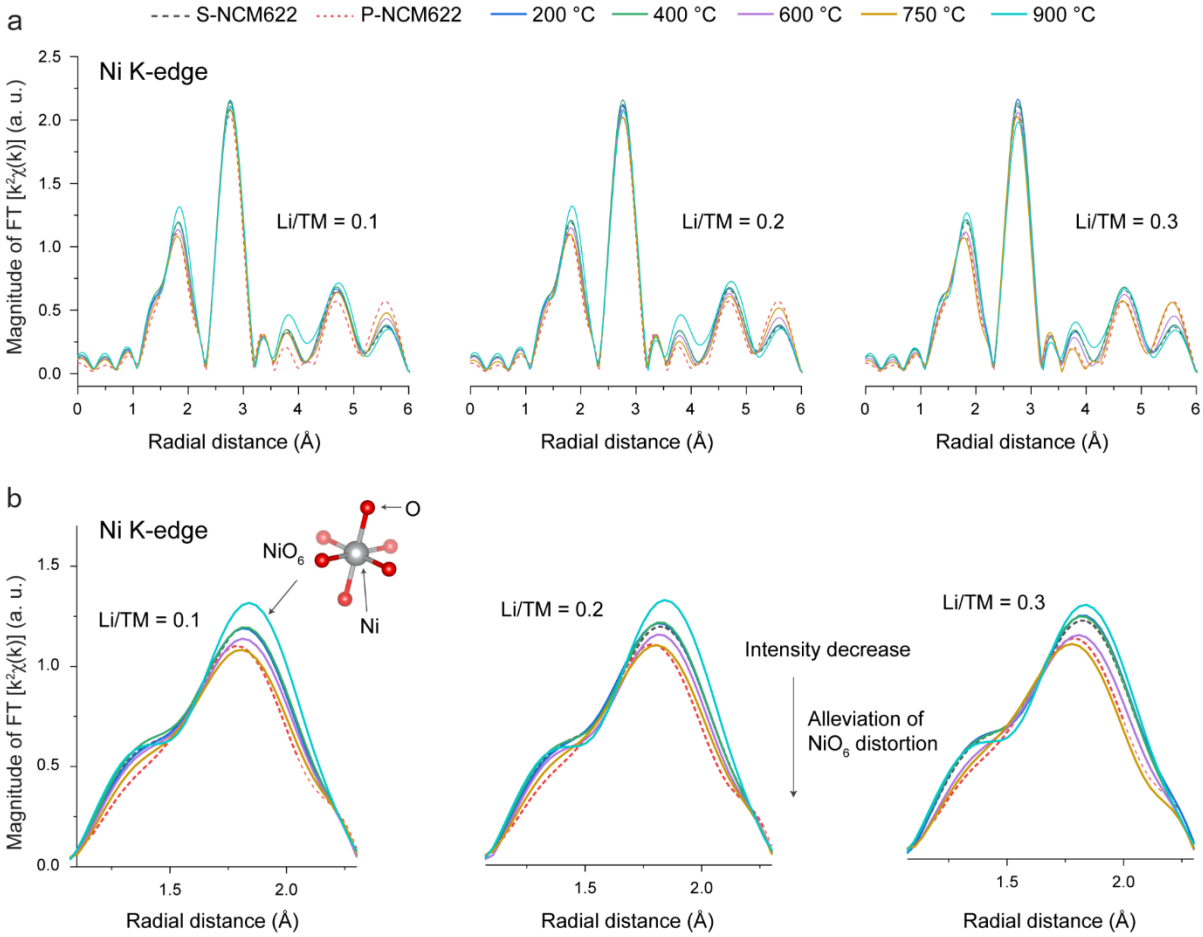

Fig. 4.14. (a) EXAFS results of Ni K-edge and (b) the corresponding enlarged ranges from 1.1 to 2.3 Å for materials regenerated under different temperatures (200, 400, 600, 750 and 900 °C) with various Li/TM ratios (0.1, 0.2 and 0.3).

To probe deeper insights into the structural evolution during the repair process, particularly in differentiating the local structural changes among Ni, Co, and Mn, EXAFS analysis was conducted on the ex-situ samples. In the Ni K-edge spectra (**Fig. 4.14a**), the magnitude of the Ni-O peak (~1.8 Å) exhibits a clear temperature-driven trend, largely independent of Li/TM ratios (**Fig. 4.14b**). Specifically, the FT magnitude of the Ni-O peak begins to decrease at 600 °C, reaches its minimum at 750 °C, and increases at 900 °C. This trend aligns well with the changes in profile anomalies in reflections observed in ex-situ XRD. While several factors, such as lattice distortions, static and thermal disorder, and interference from multiple scattering paths, can influence the FT magnitude, the observed decrease is believed to closely correlate with the recovery of rhombohedral symmetry, as supported by the consistency between ex-situ XRD and EXAFS results. More fundamentally, this decrease may stem from changes in the CCP oxygen framework of the NCM622 material, which results in reduced O backscattering to Ni. On the one hand, the reverse transition from Ni^{2+}-O_6 to Jahn-Teller active Ni^{3+}-O_6 could restore the oxygen framework closer to its original state. Alternatively, the more dispersed

distribution of Ni^{2+} within the Li layer, due to cation rearrangement, lithium intercalation, and TM migration from the Li layer back to the TM layer, might mitigate oxygen framework distortions induced by structural degradation and similarly contribute to restoring the oxygen framework to its original state.

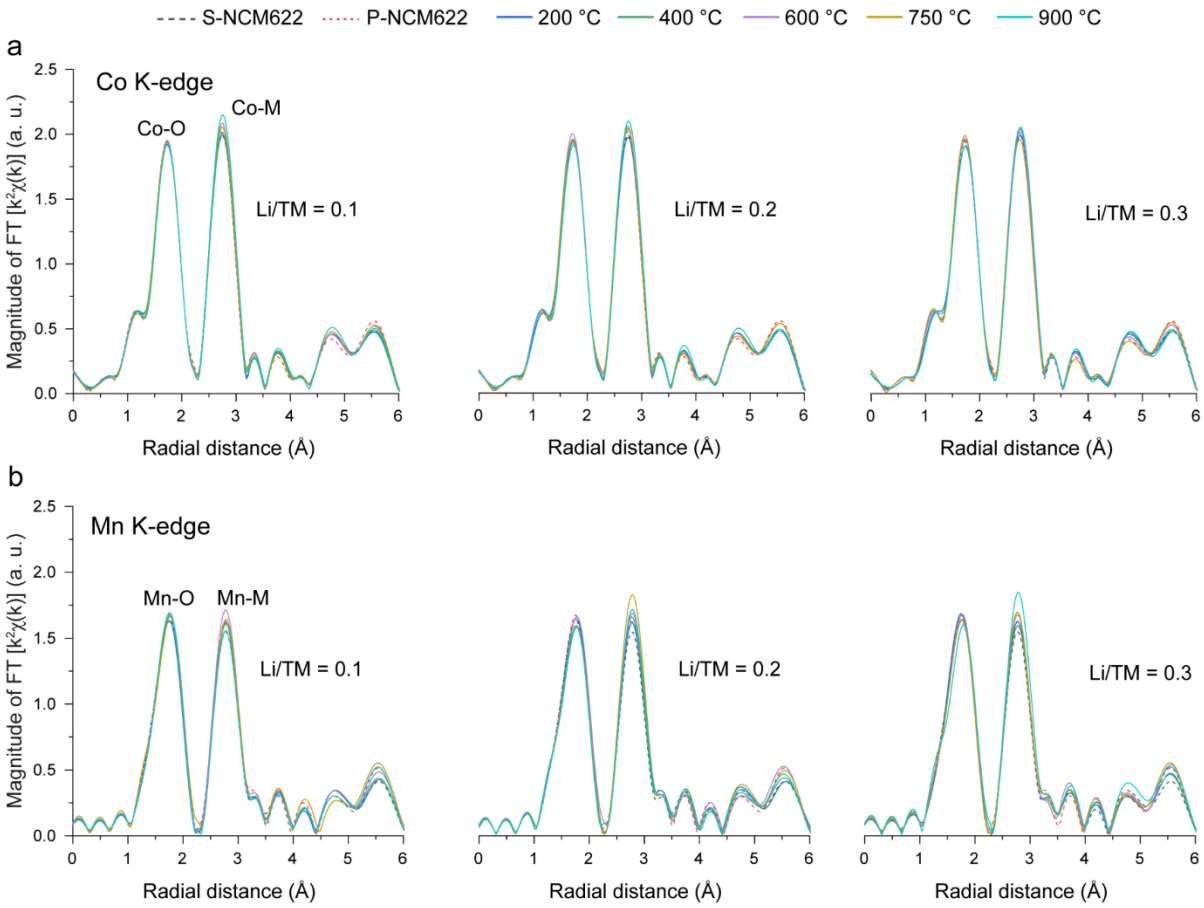

Fig. 4.15. EXAFS results of (a) Co and (b) Mn K-edges for materials regenerated under different temperatures (200, 400, 600, 750 and 900 °C) with various Li/TM ratios (0.1, 0.2 and 0.3).

In contrast, the Co and Mn K-edge spectra reveal much smaller changes in their Co/Mn-O peaks across different temperatures and Li/TM ratios (**Fig. 4.15a-b**). These observations indicate that the structural repair is associated with the recovery of rhombohedral lattice, which is mainly ascribed to the changes in NiO_6 octahedral structure. In other words, the migration of Ni from the Li layer back to the TM layer governs the structural repair.

Moreover, changes in FT magnitude at ~3.8, ~4.6, and ~5.5 Å in the Ni spectra, which reflect the longer-range structure, to some extent provide clearer view into the relative amounts of TM ions (mainly Ni) within the Li layer. As observed in **Fig. 4.16a**, evident FT magnitude changes begin at 600 °C, indicating a clear decrease in TM ions within the Li layer. This can correspond to an obvious improvement in the structural order, consistent with ex-situ XRD observations.

It should be mentioned that, as the number of TM ions within the Li layer changes, the FT magnitude variations at ~3.8 and ~4.6 Å, in some cases, are less pronounced than those at ~5.5 Å. This may be attributed to the greater complexity of interlayer coordination environments compared to those of intralayer. Additionally, the Li/TM ratio also plays a crucial role in influencing FT magnitude when temperatures are above 600 °C, particularly at 750 °C. This suggests that a higher Li/TM ratio can also enhance structural order by promoting the migration of TM ions back to the TM layer but mainly after 600 °C.

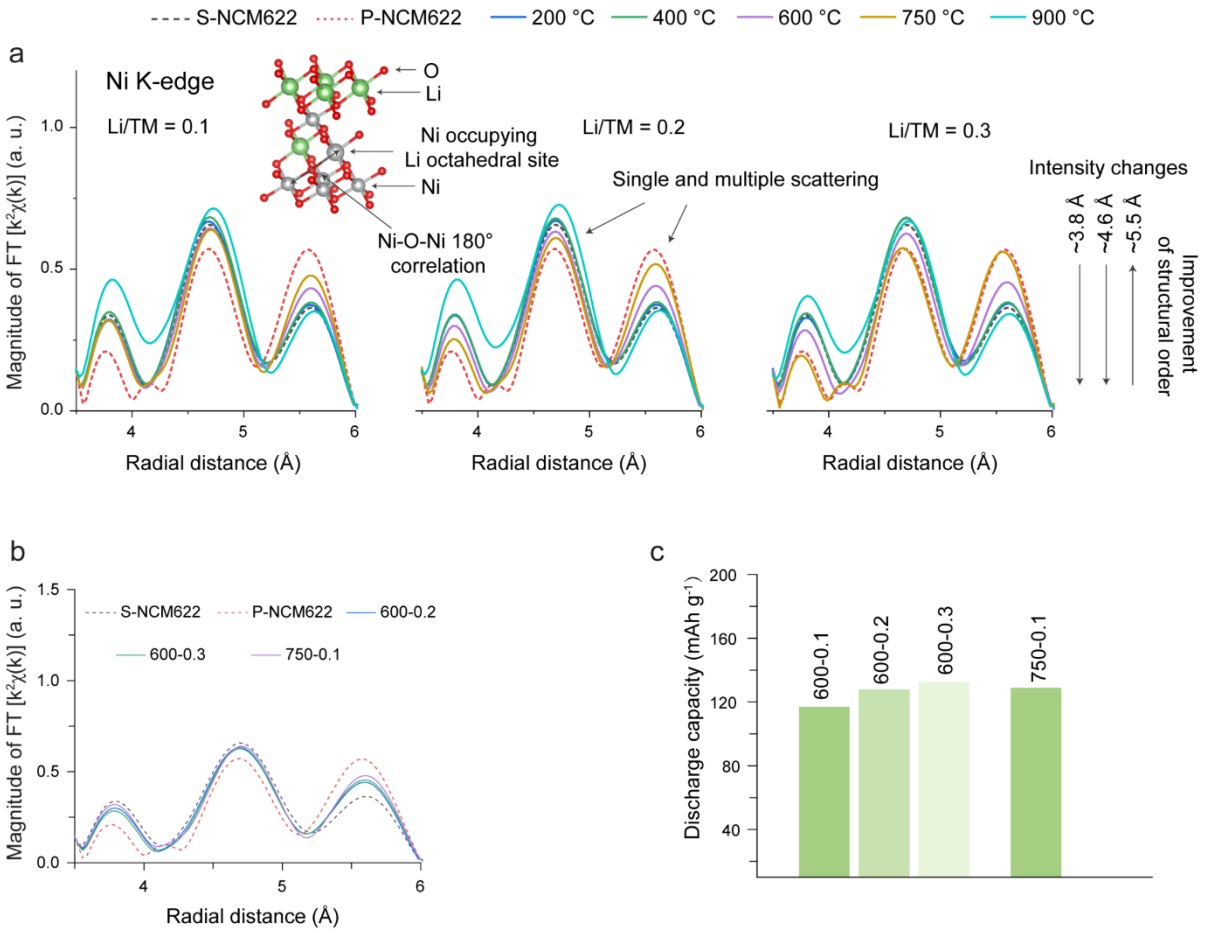

Fig. 4.16. (a) EXAFS results of Ni K-edge from 3.5 to 6.0 Å for materials regenerated under different temperatures (200, 400, 600, 750 and 900 °C) with various Li/TM ratios (0.1, 0.2 and 0.3). (b) Enlarged region of EXAFS of Ni K-edge, and (c) initial discharge capacities at 0.1 C, over 3.0-4.3 V for materials regenerated at 600 °C with the Li/TM ratios of 0.2 and 0.3, and under 750 °C with the Li/TM ratios of 0.1 (denoted as 600-0.2, 600-0.3, and 750 -0.1 respectively).

Although the ex-situ XRD results show incomplete recovery of rhombohedral symmetry in materials regenerated at 600 °C with Li/TM ratios of 0.2 and 0.3 (denoted as 600-0.2 and 600-0.3, respectively), compared to the material regenerated at 750 °C with a Li/TM ratio of 0.1 (denoted as 750-0.1), the EXAFS results likely indicate a similar amount of TM ions within the Li layer across these samples (**Fig. 4.16b**). Consequently, it is observed that their initial

capacities are quite comparable (**Fig. 4.16c**). These observations highlight that the improved capacity is more likely associated with the decrease in the amount of TM ions within the Li layer.

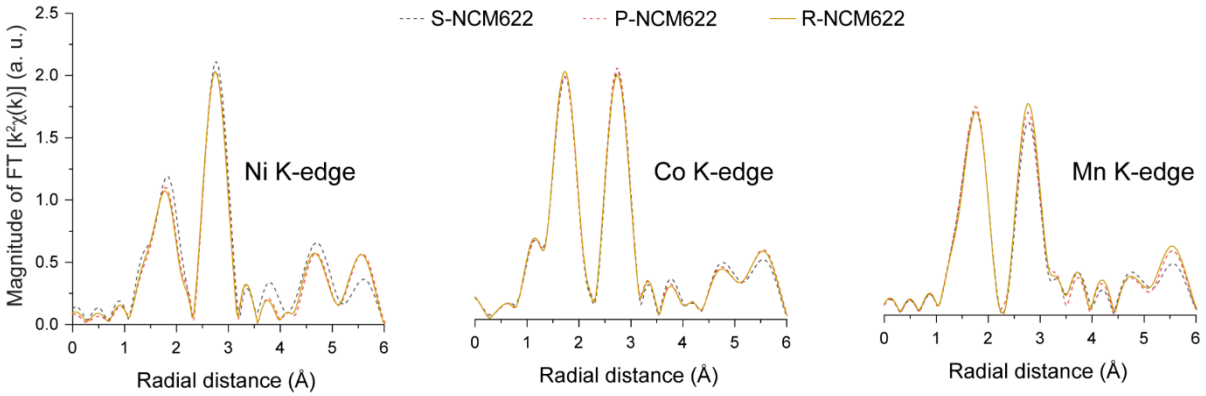

Fig. 4.17. EXAFS results of Ni, Co and Mn k-edges for S-NCM622, P-NCM622 and R-NCM622.

Lastly, all Ni, Co and Mn EXAFS results reveal that the peak shapes and intensities for R-NCM622 closely resemble those of P-NCM622 (**Fig. 4.17**), confirming the successful restoration of the layered structure.

Additionally, the TM migration from the Li layer back to the TM layer would highly rely on their oxidation. This is because the TM migration requires their oxidation to supply electrons to O_2, forming O^{2-} and realizing the expansion of CCP oxygen framework. This structural adjustment results in the formation of new octahedral sites, which is essential for Li insertion and TM migration. As such, the structural analysis was followed by the chemical-state analysis of TMs in the ex-situ samples using XANES results. In the Ni K-edge spectra (**Fig. 4.18a**), it is observed a notable edge shift toward higher energy beginning around 600 °C and peaking at 750 °C, indicative of Ni oxidation. Below 600 °C, the Ni oxidation remains relatively unaffected by the Li/TM ratios. Yet, as the temperature increases, differences in Li/TM ratios significantly affect the Ni oxidation, especially at 750 °C. At 900 °C, the edge shifts back toward lower energy, suggesting a reduction in the Ni oxidation state. These redox changes align closely with the magnitude variations observed at ~3.8, ~4.6, and ~5.5 Å in the Ni spectra, reinforcing the strong correlation between TM migration and their oxidation.

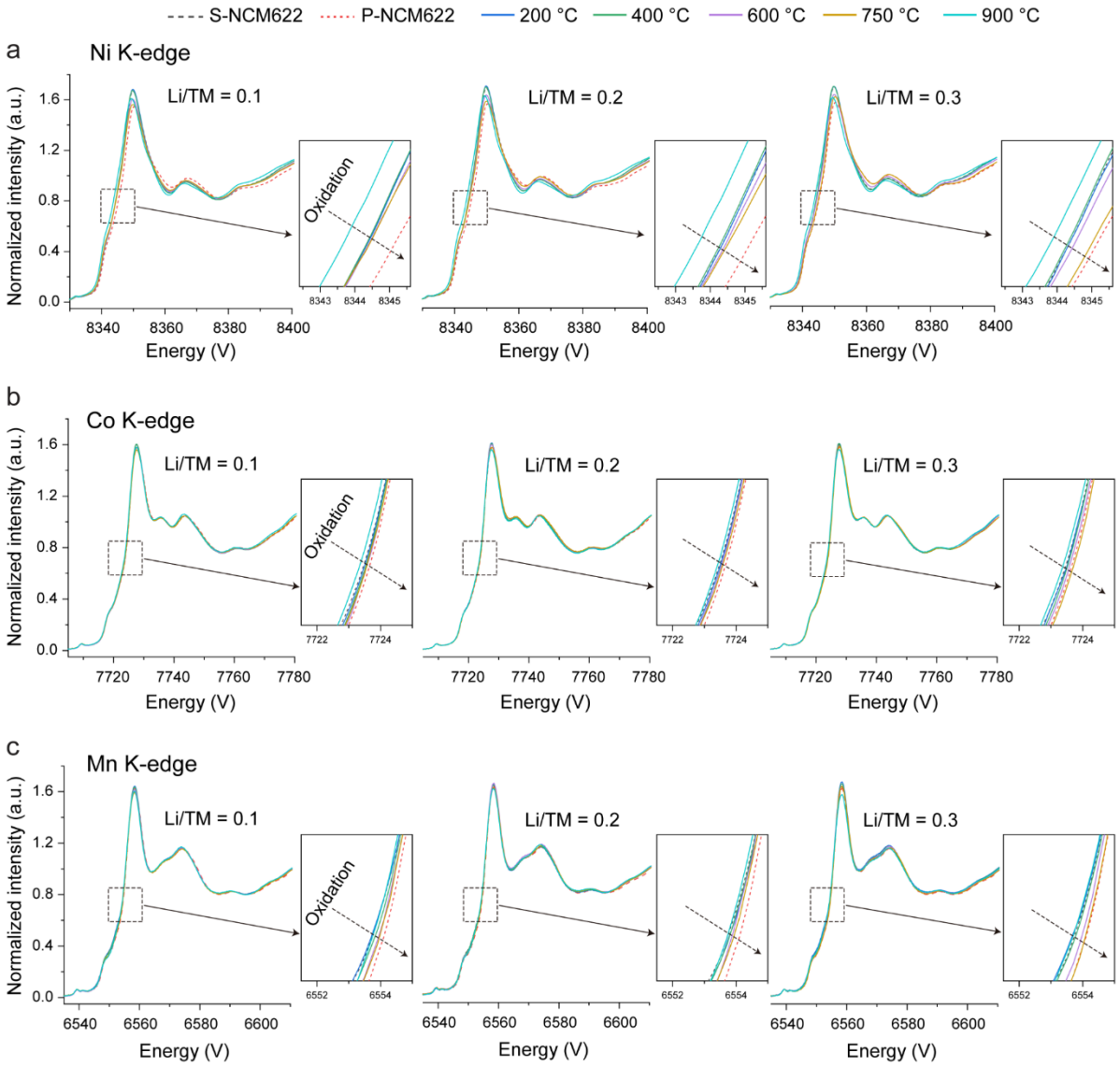

Fig. 4.18. Normalized XANES spectra of (a) N, (b) Co, and (c) Mn K-edges for materials regenerated under different temperatures (200, 400, 600, 750 and 900 °C) with various Li/TM ratios (0.1, 0.2 and 0.3).

For Co and Mn K-edges XANES spectra, more subtle edge shifts are observed following a similar trend as for Ni (**Fig. 4.18b-c**). Noteworthy, it is also observed that the Co and Mn edges shift towards higher energy at lower temperatures than Ni and they experience relatively smaller edge shifts at 900 °C. These trends likely suggest that Co and Mn undergo slight oxidation already at lower temperature and experience less reduction at elevated temperatures, compared to Ni. Overall, these observations suggest that the TM migration from the Li layer to the TM layer accompanied by their oxidation, and re-lithiation, would serve as the primary mechanism for structural repair.

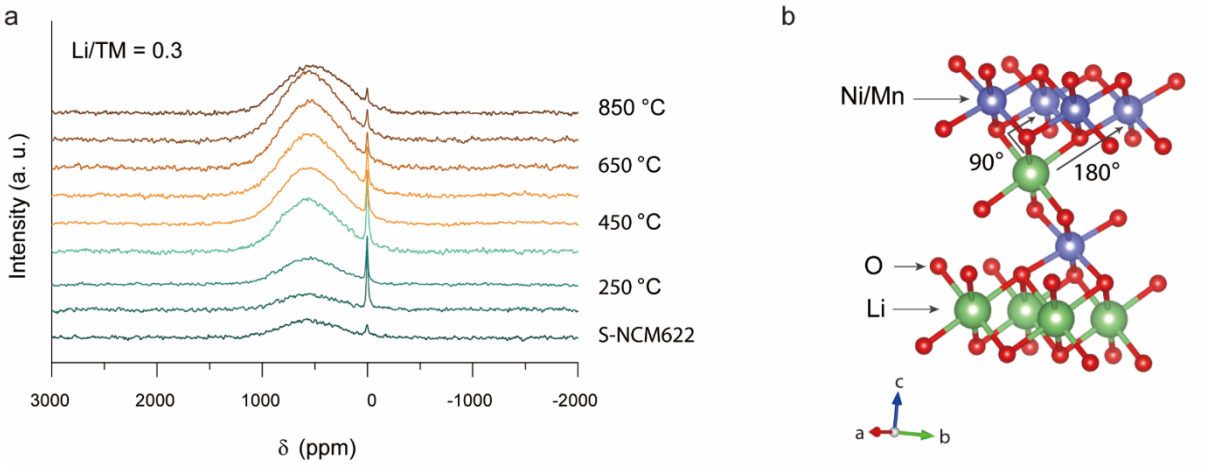

Fig. 4.19. (a) ^{6}Li solid-state NMR spectra for materials regenerated under different temperatures (150-850 °C, per 100 °C) with a Li/TM ratio of 0.3. (b) The local environment in the TM/Li layers that gives rise to the isotropic resonance at ~550 ppm is shown. The interactions occur via oxygen as intermediate atoms.

To fully elucidate the mechanisms underlying the structural repair, it is equally crucial to understand the coordination environment of re-intercalated lithium. **Fig. 4.19a** presents the ex-situ ^{6}Li solid-state NMR spectra of S-NCM622 mixed with $^{6}LiOH{\cdot}H_2O$ at a Li/TM ratio of 0.3, sintered at different temperatures (150-850 °C, per 100 °C) and then annealed to RT. The "S-NCM622" sample refers to spent material without added $^{6}LiOH{\cdot}H_2O$. Two major cluster groups of resonances are observed: one at ~550 ppm and one at ~0 ppm. The higher frequency resonances (~550 ppm) are assigned to Li local environments in Li layers, resulting from the interactions between the Li nucleus and unpaired electron spin density of Ni and Mn ions in the first and second cation coordination shell, as shown in **Fig. 4.19b** [163, 164]. The lower-frequency resonances (~0 ppm) are attributed to residual lithium salts on the surface.

Table 4.3. Elemental composition analysis from ICP-OES and CGHE for material regenerated at 750 and 800 °C with a Li/TM ratio of 0.3 (denoted as 750-0.3 and 800-0.3, respectively).

Sample	Weight percent (%)									
	Ni		Co		Mn		**Li**		O	
	Avg	SD	Avg	SD	Avg	SD	**Avg**	**SD**	Avg	SD
750-0.3	35.8	0.1	12.0	0.1	11.2	0.1	6.88	0.10	35.8	0.1
800-0.3	36.0	0.1	12.1	0.1	11.4	0.1	6.78	0.10	32.6	0.2

In the spectra, although S-NCM622 does not contain added ^{6}Li, there are still small contributions to the signal, corresponding to the natural isotope composition of Li (93% ^{7}Li, 7% ^{6}Li)[165]. The intensity of the high-frequency resonances begins to notably increase as the temperature reaches 250 °C, accompanied by a sharp decrease in the low-frequency resonances,

indicating the onset of lithiation. Besides, this phenomenon suggests that the lithiation initiates before the lithium salt transitions to a molten state. Between 250 and 750 °C, the high-frequency resonances progressively intensify and sharpen, while the low-frequency resonances decrease, reflecting ongoing lithiation (**Fig. A7**, offering a clearer view). The ICP-OES and CGHE results show that the stoichiometry of R-NCM622 is $Li_{1.003}Ni_{0.600}Co_{0.200}Mn_{0.200}O_{2.039}$ (**Table 4.2**), indicating a restoration of Li and O. Yet, at 850 °C, the high-frequency resonances exhibit a reversal, indicating lithium loss. According to ICP-OES and CGHE, the stoichiometry of the material regenerated at 800 °C with a Li/TM ratio of 0.3 is found to be $Li_{0.975}Ni_{0.596}Co_{0.201}Mn_{0.203}O_{1.982}$ (**Table 4.2**), suggesting lithium and oxygen loss after 750 °C, consistent with the NMR findings. In addition, no other significant resonances are detected during this process, suggesting that the intercalated Li predominantly occupies octahedral sites and exists within a Li local environment.

Based on the XRD, XAS and NMR findings, a clear relationship emerges among capacity recovery, phase transition, TM migration and oxidation, and re-lithiation. In essence, a lower concentration of TM ions (mainly Ni) in the Li layer corresponds to a higher TM oxidation state and a more ordered structure, and thus improved capacity recovery. Overall, this structural repair process can be mainly divided into three stages:

Stage I (below 600 °C): In this stage, the thermal energy is insufficient to significantly drive the oxidation state and interlayer migration of TMs, particularly for Ni, resulting in slow reaction kinetics. As evident from the ex-situ XRD data, the rhombohedral symmetry is not significantly recovered below 600 °C, and from the ex-situ EXAFS and XANES results, which indicate no obvious TM migration or oxidation. Accordingly, the capacity recovery of the regenerated materials during this stage remains limited.

Stage II (600-750 °C): This is the main stage for the transformation from RS to layered phase, where both temperature and lithium ratio play crucial roles in facilitating the cation migration and structural order. This is evidenced by the clear recovery of rhombohedral symmetry, along with noticeable TM migration and oxidation observed through XRD, EXAFS, and XANES analyses. As a result, the recovery of capacity occurs mostly during this stage.

Stage III (above 750 °C): At high temperatures, Li/O release from the material could be triggered, undermining the repair effects and even inducing further structural degradation. This

is also reflected in the XRD, XAS and NMR results. Consequently, there is a continuous decline in capacity beyond 750 °C.

4.3.4 Possible thermal solid-state reaction mechanism

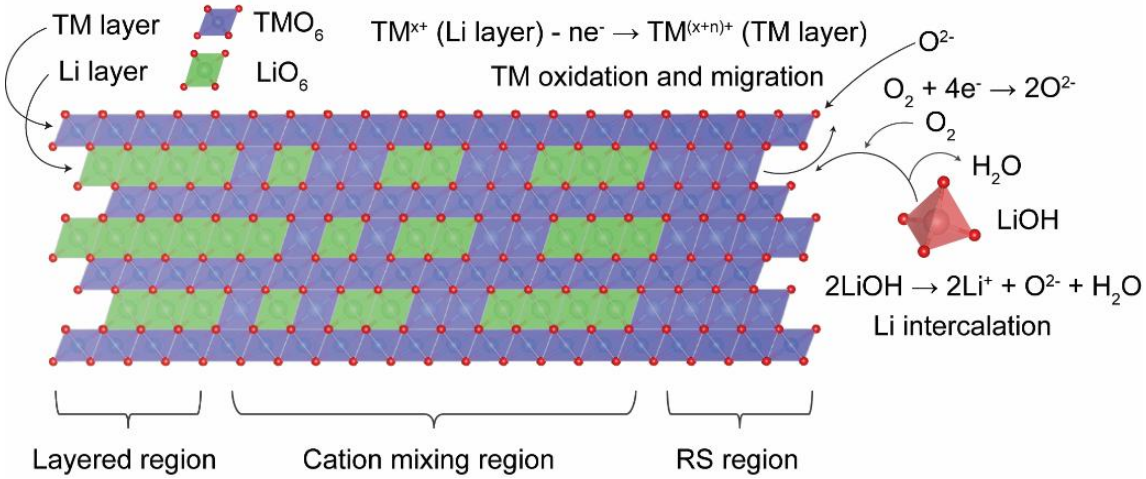

Fig. 4.20. Schematic illustration for a possible thermal solid-state reaction mechanism during the structural repair.

It is well established that the mechanism of a thermal solid-state reaction is driven by kinetic processes involving the cleavage and formation of chemical bonds[166]. The thermal treatment plays a crucial role by supplying the energy required to overcome activation barriers, thereby facilitating ionic diffusion within the solid state[167]. Based on the present findings, the solid-state reaction driving the structural repair process can be summarized as follows: With the gradual application of heat, the kinetic energy of ions increases, allowing the oxidation of TM ions within the Li layer. During this process, electrons from the TM ions are captured by O_2, forming O^{2-} and generating new octahedral sites in the TM layer. Subsequently, the oxidized TM ions migrate from the Li layer to the TM layer, while Li ions supplied by LiOH occupy the vacant octahedral sites in the Li layer, completing the insertion process. As TM ions continue to migrate and Li ions are inserted, the cation diffusion along the *a*/*b* axis takes place, accompanied by cation rearrangement. This leads to the formation of a lithium-ion concentration gradient in the Li layer along *a*/*b* axis within a localized region, which is schematically illustrated in **Fig. 4.20**.

During this reaction, heating is the most critical factor in overcoming the activation energy required for TM migration and oxidation. The EXAFS and XANES analyses indicate that Ni could possess the highest migration barrier from the Li layer to the TM layer among the three cations [168], as evidenced by its delayed oxidation relative to Co and Mn. Although Co and Mn

may exhibit an earlier onset of migration, the hindered Li insertion and diffusion, due to the significant presence of Ni within the Li layer, may still slow their migration. As a result, noticeable migration of Ni, Co, and Mn is observed mainly after 600 °C, once the Ni energy barrier is overcome. After that, the Li/TM ratio plays an increasingly pivotal role in facilitating TM migration and ionic diffusion within the solid state, further enhancing structural order. This influence is likely tied to the concentration of Li at the solid-contact surfaces and the resulting lithium-ion concentration gradient within the metal oxides. In other words, a higher Li/TM ratio might contribute to lower the TM energy barrier for the migration from the Li layer to the TM layer. While higher Li/TM ratios are beneficial for restoring the structural order, their effect has limitations. As observed, higher Li/TM ratios (e.g., 0.4, 0.5, and 0.6) at 750 °C do not lead to further improvements in electrochemical capacity (**Fig. 4.8a**). However, these elevated ratios aid in achieving optimal structural order at slightly lower temperatures, as supported by the data presented in **Fig. 4.21**.

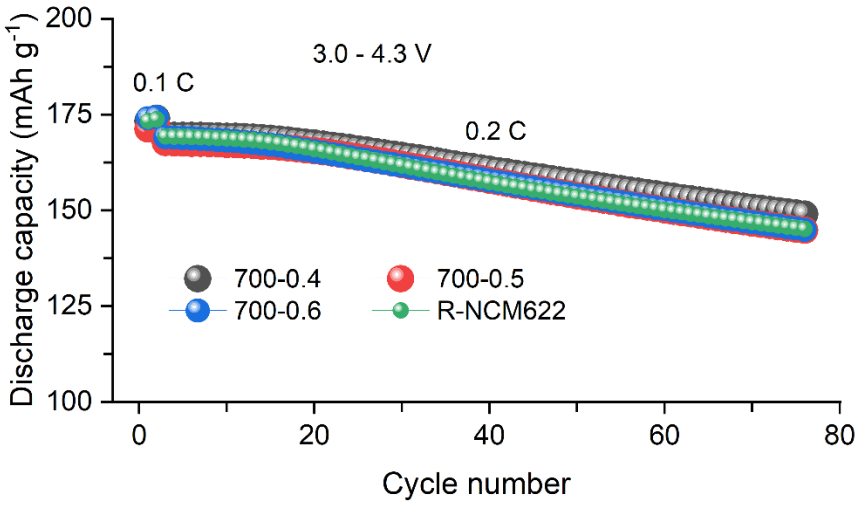

Fig. 4.21. Cycling performance for materials regenerated at 700 °C with different Li/TM ratios (Li/TM = 0.4, 0.5 and 0.6, the corresponding samples are denoted as 700-0.4, 700-0.5 and 700-0.6, respectively) at charge-discharge rate of 0.2 C, over 3.0-4.3 V, compared to R-NCM622.

4.3.5 Potential challenges for direct recycling

In this study, the structural repair of the spent NCM622 (retired after thousands of cycles with a capacity retention of 81%) is successfully accomplished, achieving structural order and restoring the capacity to the same level as for commercial NCM622.

By combining XRD, XAS, and NMR analyses, the phase transitions thoroughly investigated down to the atomic scale, provide valuable insights into cation migration and diffusion during

the repair process. Notably, the Ni migration from the Li layer back to the TM layer could be the greatest challenge in structural repair. Therefore, developing strategies to lower the energy barrier for Ni migration might contribute to enhance the electrochemical properties of regenerated material or reduce energy consumption during the repair process.

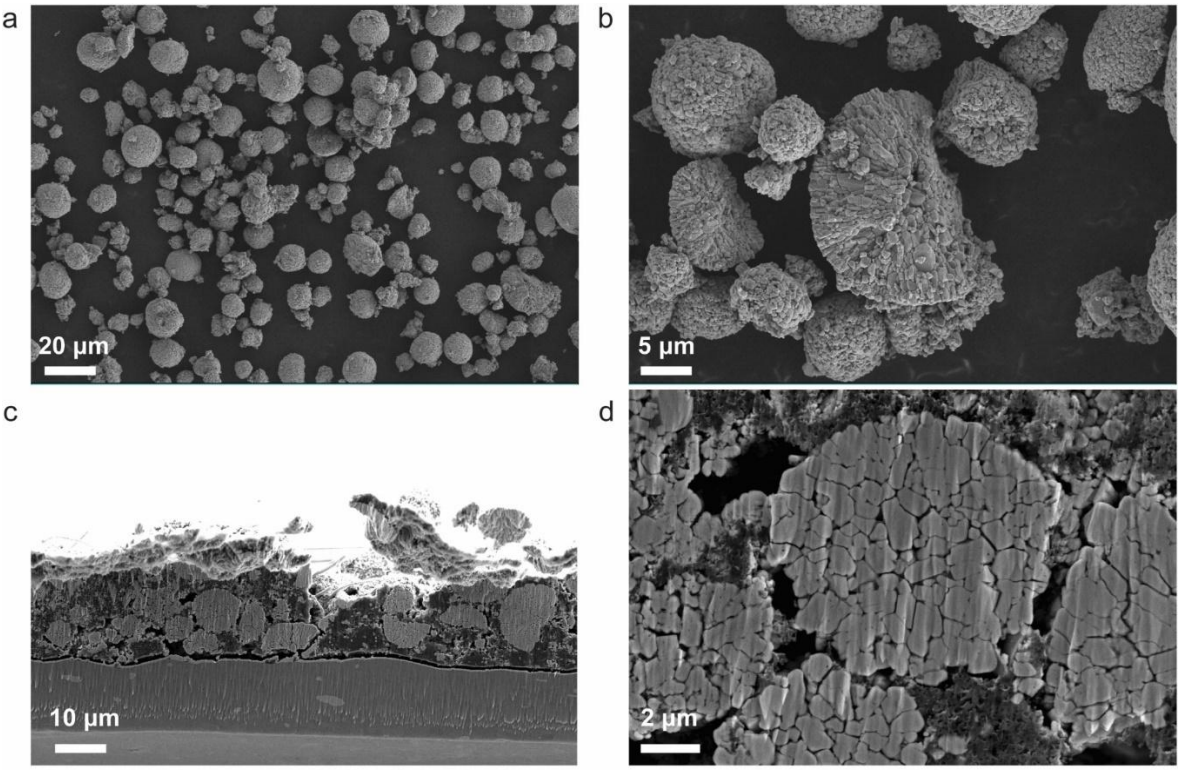

Fig. 4.22. SEM images of R-NCM622 (a-b) before and (c-d) after 200 cycles.

Moreover, it is observed that the regenerated material falls short of achieving satisfactory cycling performance when compared to commercial NCM622. This limitation may be attributed to the lack of additional modification strategies, such as element doping or surface coating. Alternatively, this limitation is likely due to potential impurities introduced during the pre-treatment process (e.g., Al, F, and P) and the presence of unrecovered particle cracks in the regenerated material (**Fig. 4.22**). Therefore, future research aimed at identifying the root causes of the poor cycling performance and developing strategies to address these challenges could be crucial for advancing sustainable battery recycling technologies.

4.4 Conclusion

In summary, this chapter systematically investigates the thermal solid-sate structural repair process of spent NCM622 cathode material. Through multiscale characterization techniques, including XRD, XAS, and ^{6}Li solid-state NMR, the structural degradation in spent NCM622,

and the long- and short-range structural changes during the repair process are thoroughly examined. The findings identify Ni migration from the TM layer to the Li layer along with lithium and oxygen loss, reductions in Ni oxidation states, and local destruction in rhombohedral symmetry, as the primary factors driving the structural degradation of NCM622.

During the repair process, both temperature and lithium compensation ratio are shown to play crucial roles in migration of TMs, particularly Ni, back to the TM layer and enhancing ionic diffusion within the solid state, thereby restoring the structural order in the spent material. Moreover, capacity recovery studies reveal a strong correlation between the restoration of structural order and the recovery of electrochemical performance. The regenerated material with optimal structural order (750 °C, Li/TM = 0.3) demonstrates a structural order and an initial capacity comparable to those of pristine NCM622, along with a 76% capacity retention after 150 cycles at 1 C charge/discharge over 3.0-4.3 V, validating the effectiveness of the repair process.

These findings highlight the potential of thermal solid-state repair as a viable strategy for restoring the functionality of spent cathode materials, offering insights for future advancements in battery recycling and sustainability.

5. Effect of impurity on Structural repair of Spent NCM Material

5.1 Introduction

Although manual disassembly and thermal pretreatment were employed to produce the spent NCM powder, some impurities are still unavoidably introduced and can potentially affect the structural repair process. These impurities may originate from several sources, including residual electrolytes and their decomposition products [169], binders [170, 171], conductive carbon [172], current collectors [173], and separator coatings [174]. Notably, some studies suggest that certain impurities, such as Al-, F- and Cu-containing species [175-179], may enhance electrochemical performances by doping of the regenerated materials. Yet, maintaining such impurities within an optimal concentration range remains technically challenging. While the impurity-induced doping may not compromise performance during the first regeneration process due to its trace level, or could even potentially enhance it, the accumulation of these elements in the crystal structure over multiple regeneration cycles must be carefully evaluated. Therefore, comprehensive identification of all potential impurities in spent material and a thorough understanding of their effect on the regeneration process are essential to improve the quality of recycled cathode materials.

The present chapter investigates the impurities present in the spent cathode material. Using synchrotron diffraction combined with X-ray photoelectron spectroscopy, Al_2O_3, $AlPO_4$, AlF_3, Li_3PO_4, LiF, $Li_xPF_yO_4$, and Li_2CO_3 impurities are identified, and Al-inclusion in the spent material likely induced by the thermal pretreatment is confirmed. The influence of these impurities on the subsequent regeneration step is systematically evaluated as well. The results reveal that Al- and F-containing impurities play dominant roles, leading to corresponding Al- and F-inclusion in the regenerated material. To elucidate the associated inclusion mechanisms and their effects on structural integrity, synchrotron-based diffraction and absorption spectroscopy techniques are employed. These findings provide critical insights into the role and behavior of impurities in direct recycling, supporting the development of high-performance regenerated cathode materials.

5.2 Methods

5.2.1 Direct regeneration of cathode active material

The spent active cathode material NCM622, which was used for experiments, was the same as that in *Chapter 4*. The spent NCM622 was regenerated by a thermal solid-state reaction with

or without a subsequent washing step. Specifically, the powder was mixed homogeneously in a mortar with $LiOH \cdot H_2O$ (Sigma Aldrich, >98 %) with a lithium compensation/TM molar ratio of 0.3/1.0. The obtained mixture was annealed at 750 °C for 12 h in air atmosphere using a muffle furnace, with a heating rate of 5 °C min^{-1} and passive cool down to room temperature. To study the impurities, LiF and Al_2O_3 were independently introduced at 3, 5, and 7 wt% relative to the spent NCM622 during the mixing step, and the mixtures were subjected to the same annealing conditions. For the washed samples, a second annealing step was conducted at 650 °C for 6 h to further remove residual surface lithium salts.

5.2.2 Water or NaOH washing process to decrease residual impurities

The washing with water was conducted during the centrifugation process. Approximately 0.3 g of material was dispersed in ~35 mL of deionized water and centrifuged at 8000 rpm for 1 min. This process was repeated three times. Subsequently, the material was dispersed in ~25 mL of ethanol and centrifuged under the same conditions three additional times to further remove residual water. Finally, the sample was dried in an oven at 80 °C.

In case of NaOH-washing, the spent NCM622 material was immersed in 2 mol L^{-1} NaOH solution at a solid-to-liquid ratio of 6 g L^{-1} and sonicated for 15 min. The NaOH solution was then removed by multiple rounds of centrifugation. Residual NaOH was further removed by sequential washing with deionized water and ethanol, following the same procedure as the water-washing process.

The procedures for **electrode preparation, cell assembly, and electrochemical characterization** are consistent with those described in *Chapter 4*.

5.2.3 Materials characterization

The elemental composition of the cathode material, except oxygen, was analyzed by Inductively Coupled Plasma Optical Emission Spectrometry (ICP-OES), and then oxygen was analyzed by Carrier gas hot extraction (CGHE).

The morphology of the samples was observed by a scanning electron microscope (SEM, Zeiss Merlin) with an acceleration voltage of 10 keV. The coupled energy-dispersive X-ray (EDX) analysis was conducted at a Quantax 400 system from Bruker.

The Synchrotron Radiation Diffraction (SRD) data was collected at BL04-MSPD at ALBA

(Spain). The Rietveld refinement based on the obtained SRD patterns was performed in the FullProf software package [139]. The background of all the diffraction patterns was fitted using linear interpolation between selected data points in regions with no reflections present. Thompson-Cox-Hastings pseudo-Voigt function was used for the reflection profile shape description. The scale factor, lattice parameter, fractional coordinates of atoms, their overall isotropic displacement (temperature) parameter, zero angular shift, profile shape parameters, and half-width (Caglioti) parameters were allowed to vary during fitting.

The X-ray photoelectron spectroscopy (XPS) was performed using a K-Alpha$^+$ instrument (Thermo Fisher Scientific) with a monochromatic Al-Kα X-ray source (1486.6 eV, 400 µm spot size). Thermo Avantage software was used to perform data acquisition and processing. The K-Alpha+ charge compensation system was employed during analysis, using electrons of 8 eV energy, and low-energy argon ions to prevent any localized charge build-up. The spectra were fitted with one or more Voigt profiles (BE uncertainty: ± 0.2 eV) and Scofield sensitivity factors were applied for quantification [180]. All spectra were referenced to the C 1s peak (C-C, C-H) at 285.0 eV binding energy controlled by means of the well-known photoelectron peaks of metallic Cu, Ag, and Au, respectively.

The ex-situ Hard X-ray Absorption Spectroscopy (XAS) experiments were performed at beamline P64 Advanced X-ray Absorption Spectroscopy at PETRA III (Germany). The obtained XAS data were processed using ATHENA software [140]. The corresponding $k^2\chi(k)$ data are presented in **Fig. A8**, with k-ranges for Fourier transformation selected as 3-11, 3-11 and 3-10.5 Å^{-1} for Ni, Co and Mn K-edge, respectively.

5.3 Results and Discussions

5.3.1 Impurity analysis

In this chapter of the thesis, the spent NCM622 powder, consistent with the previous chapters, is also denoted as S-NCM622. Due to manual disassembly of the cell, potential impurities originating from the anode or other components, such as Cu and Fe, were largely avoided. Therefore, the impurities in S-NCM622 primarily stem from Al current collector, separator coatings, residual electrolyte species (carbonates / $LiPF_6$) and their decomposition products, and solid electrolyte interphase (SEI) formed during cycling and its degradation products.

Due to the low content of impurities in the spent cathode materials, their detection and phase

identification present significant analytical challenges. Conventional techniques such as lab-scale XRD often lack sufficient sensitivity to detect the trace levels of materials. Therefore, SRD (λ = 0.413820 Å) is used as a more powerful analytical tool, leveraging its enhanced sensitivity for identification of potential impurity phases in the spent material. The corresponding result combined with Rietveld refinement is shown in **Fig. 5.1a**. The S-NCM622 powder exhibits a characteristic rhombohedral layered structure (*R-3m*), but accompanied by a significant presence of cation-disordered domains [181]. Such domains lead to profile anomalies, which are mainly responsible for the relatively high value of R_p and R_{wp}. Notably, in range I ($5.5° < 2\theta < 9.1°$), reflections corresponding to several impurity phases are observed, yet their relative intensities are rather too low to quantify their relative content through Rietveld refinement. As illustrated in **Fig. 5.1b**, these reflections are assigned to Li_3PO_4 (*Pmnb*), $AlPO_4$ ($P3_121$), Li_2CO_3 (*C12/c1*) and Al_2O_3 (*R-3c*). Furthermore, the $AlPO_4$ impurity appears to be distributed inhomogeneously. As shown in **Fig. A9**, a particle containing Al and P is observed and is presumed to be $AlPO_4$. In contrast, a different region (**Fig. A10**) reveals only Ni, Co, Mn, and O as the primary elements, indicating an inhomogeneous distribution of $AlPO_4$ in S-NCM622. Other impurity elements are not detectable, most likely due to the limited sensitivity of the SEM-EDX technique.

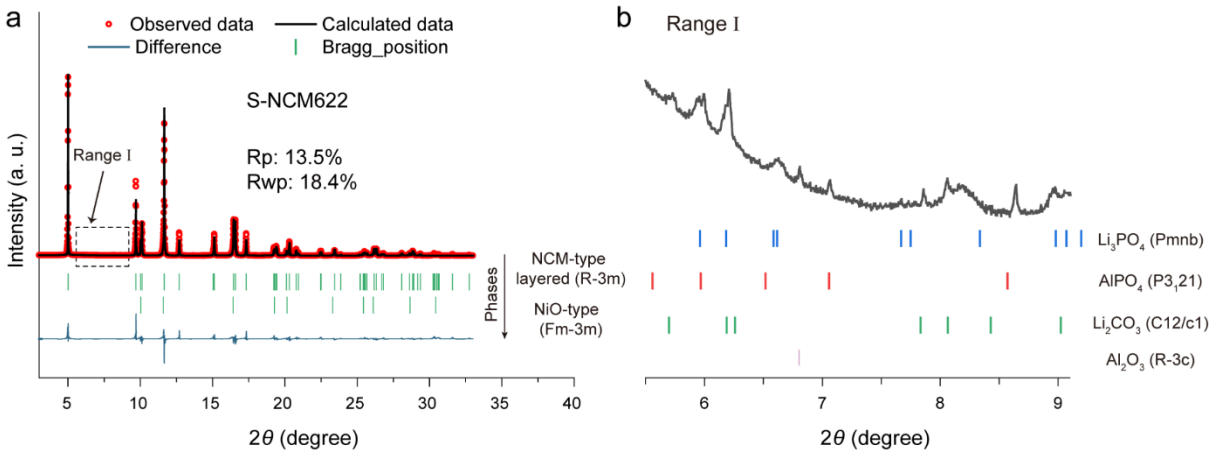

Fig. 5.1. SRD pattern (λ = 0.413820 Å) and corresponding Rietveld refinement results for spent NCM622 (S-NCM622). (b) Corresponding enlarged view of range I.

The Li_2CO_3 impurity likely originates after the cell dismantling from the decomposition of carbonate-based solvents, particularly ethylene carbonate (EC). The Al_2O_3 impurity can result from the Al current collector or the separator coatings. The formation of Li_3PO_4 and $AlPO_4$ is related to the decomposition of $LiPF_6$, and the subsequent erosion of the Al current collector by its degradation products, according to the following reactions [109, 182]:

$$LiPF_6 \rightarrow LiF + PF_5 \quad (5\text{-}1)$$

$$PF_5 + H_2O \rightarrow POF_3 + 2HF \quad (5\text{-}2)$$

$$POF_3 + 3H_2O \rightarrow H_3PO_4 + 3HF \quad (5\text{-}3)$$

$$2POF_3 + 6Li_2CO_3 \rightarrow 2Li_3PO_4 + 6LiF + 6CO_2\uparrow \quad (5\text{-}4)$$

$$4Al(s) + 4H_3PO_4 + 3O_2\uparrow \rightarrow 4AlPO_4 + 6H_2O \quad (5\text{-}5)$$

$$4Al(s) + 12HF + 3O_2\uparrow \rightarrow 4AlF_3 + 6H_2O \quad (5\text{-}6)$$

Based on the potential reaction pathways, the formation of P-containing compounds should be accompanied by the generation of F-containing species, particularly LiF. However, the detection of LiF via SRD remains challenging, as it typically crystallizes in the *Fm-3m* space group, with reflections that might overlap with those of the *R-3m* layered structure. Similarly, AlF_3 generally adopts the *R-3c* space group, which is also characteristic of Al_2O_3. As a result, it is difficult to distinguish the contributions of these compounds from the diffractogram.

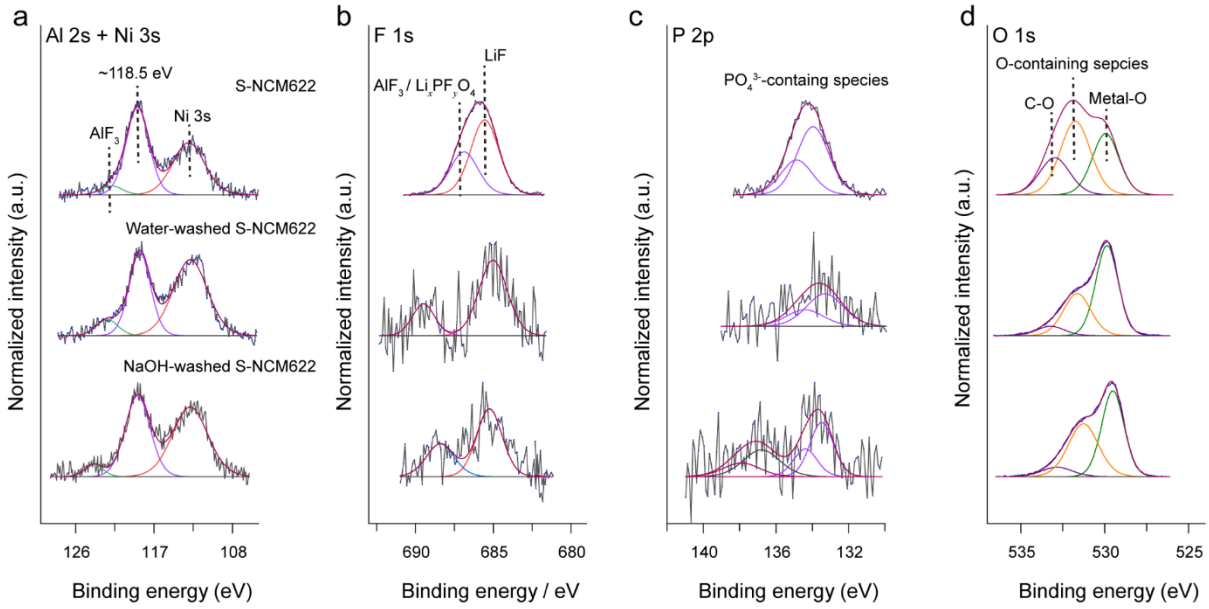

Fig. 5.2. XPS spectra of (a) Al 2s, (b) F 1s, (c) P 2p, and (d) O 1s (from top to bottom, they are respectively S-NCM622, water-washed NCM622 and NaOH-washed NCM622).

To identify the presence of F-containing impurities in S-NCM622, XPS measurements were conducted. The corresponding XPS results confirm the presence of Al, F, and P elements in S-NCM622 in addition to the primary elements Li, Ni, Co, Mn and O elements, as shown in **Fig. 5.2a-d**. The Al 2s (**Fig. 5.2a**) shows two peaks at ~118.5 eV and ~122.5 eV, given that the signal at ~112.5 eV is attributed to Ni 3s appearing in the same range of binding energy like Al 2s. The peak at ~118.5 eV corresponds to Al in oxygen environments, which may include

Al_2O_3 [183, 184], $AlPO_4$ [185, 186] or Al incorporated into the lattice of NCM material [187]. The highest-energy Al 2s peak (~122.5 eV) with low intensity can be ascribed to AlF_3 [188-190], indicating the presence of AlF_3 in S-NCM622.

In the F 1s spectra (**Fig. 5.2b**), two peaks are observed, one at ~685.3 and another between 687.0-689.0 eV. The lower-energy peak (~685.3 eV) can be attributed to LiF [191], indicating the presence of this impurity in the spent material. The second one can be assigned to $Li_xPF_yO_4$ species [187, 191], and could also include contributions from AlF_3, which typically appears around 687.5 eV in F 1s spectra [190, 192]. In the P 2p spectra (**Fig. 5.2c**), two peaks at ~133.5 and ~134.4 eV are identified, corresponding to the spin–orbit splitting of the P 2p orbital [193]. These P 2p peaks are attributed to PO_4^{3-}-containing species, possibly including $Li_xPF_yO_4$ [191], Li_3PO_4 [194] and $AlPO_4$ [185, 186]. The O 1s spectra (**Fig. 5.2d**) exhibit three peaks at ~529.8, ~531.7 and ~533.1 eV. The lowest-energy peak (~529.8 eV) corresponds to lattice oxygen in the material [191]. The intermediate peak (~531.7 eV) is associated with the oxygen-containing species on the material's surface, such as Li_2CO_3, LiOH and Li_3PO_4 [187, 195]. The highest-energy peak (~533.1 eV) can be ascribed to C-O bonds [196], which is likely related to the residual organic electrolyte species and their decomposition products. These assignments are further supported by the C 1s spectra, which also reveal features linked to CO_3^{2-} and C–O bonds in S-NCM622 (**Fig. 5.3**) [103, 195].

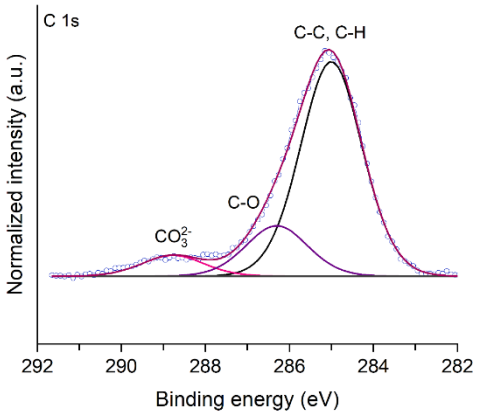

Fig. 5.3. XPS spectra of C 1s for S-NCM622

It is important to note that the ~118.5 eV Al 2s feature may arise from Al_2O_3, $AlPO_4$ or lattice-incorporated Al. Similarly, the F 1s signal near ~685.5 eV could reflect not only LiF but also substitutional fluorine incorporated into the lattice, forming transition-metal–fluorine (TM–F) bonds. In transition-metal fluorides such as NiF_2 and MnF_2, where each metal center is

octahedrally coordinated by F atoms, TM–F bonds give rise to F 1s binding energies near ~685.5 eV, which might overlap with the LiF peak.[197, 198]. Therefore, it is crucial to determine whether the detected signals in the Al 2s and F 1s spectra stem entirely from impurities or partially from Al and F structurally incorporated into S-NCM622.

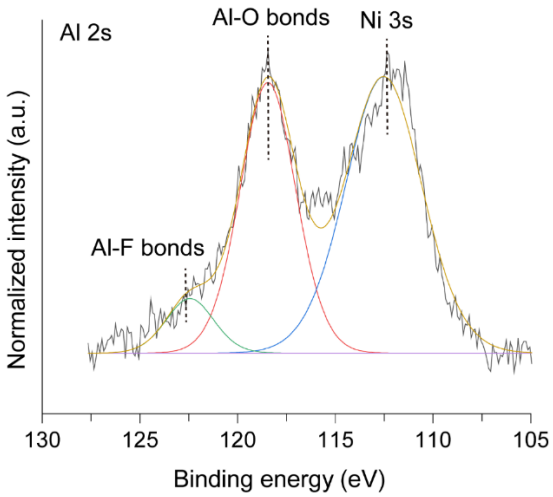

Fig. 5.4. XPS spectra of Al 2s for S-NCM622

Considering the low content of impurities, and the solubility of LiF in water and that of Al_2O_3 and $AlPO_4$ in concentrated NaOH solution, washing treatments using deionized water and 1 mol L^{-1} NaOH were conducted on S-NCM622 to investigate the possible inclusion of Al and F into the crystal structure. The washing process was mainly performed by centrifugation, while NaOH washing was further assisted by sonication to enhance the dissolution of Al-containing impurities. The XPS results for water- and NaOH-washed spent material are also shown in **Fig. 5.2a-d**. In the Al 2s spectra, the characteristic Al_2O_3 peak at around 118.5 eV is still observed in both the water- and NaOH-washed samples. To further study this phenomenon, washing with a higher concentration NaOH solution (2 mol L^{-1}) was conducted. Nevertheless, the resulting material still exhibits a peak at ~118.5 eV in the Al 2s spectra (**Fig. 5.4**). These results suggest that the observed Al 2s peak at ~118.5 eV primarily originates from Al incorporated into the lattice, indicating Al-inclusion in S-NCM622. This inclusion might occur at the interface between the Al foil current collector and the cathode active material during the thermal pretreatment (450 °C, air atmosphere), where Al ions incorporate into the NCM layered structure, facilitated by surface Li_2CO_3. A more detailed Al-inclusion mechanism will be elucidated in the *Influence of Al impurity on structural repair* section. In contrast, the intensity of the F 1s peak shows a substantial decrease after washing (nearly disappears), demonstrating that the observed signals primarily originate from surface LiF impurities. In addition, the

intensities of the P 2p and O 1s peaks also decrease, attributed to the removal of surface impurities such as $Li_xPF_yO_4$, Li_3PO_4, and Li_2CO_3. These observations are also indicated by the changes in Li and O stoichiometries before and after water washing, as determined by Inductively Coupled Plasma Optical Emission Spectrometry (ICP-OES) and Carrier Gas Hot Extraction (CGHE). Specifically, the stoichiometry shifts from $Li_{1.004}Ni_{0.601}Mn_{0.200}Co_{0.199}O_{1.921}$ (**Table 4.1**) to $Li_{0.856}Ni_{0.601}Mn_{0.201}Co_{0.198}O_{1.905}$ (**Table 4.2**) following the water-washing treatment.

Based on the above results, the impurity elements in S-NCM622 are identified to be Al, F, and P. The corresponding species include Al_2O_3, $AlPO_4$, AlF_3, Li_3PO_4, LiF, $Li_xPF_yO_4$, and Li_2CO_3. In addition, some degree of Al-inclusion may have already occurred in the spent material, likely due to thermal pretreatment.

5.3.2 Effect of impurity on direct regeneration

Understanding whether impurities in spent cathode materials influence the regeneration process is important in determining the necessity of a purification step prior to regeneration. It should be noted that, $AlPO_4$ and AlF_3, tend to transform into Al_2O_3, Li_3PO_4 and LiF during regeneration due to the presence of LiOH, according to the following reactions:

$$2AlPO_4 + 6LiOH \rightarrow Al_2O_3 + 2Li_3PO_4 + 3H_2O \quad (5\text{-}7)$$

$$2AlF_3 + 6LiOH \rightarrow Al_2O_3 + 6LiF + 3H_2O \quad (5\text{-}8)$$

The standard Gibbs free energy changes (ΔG^0) for reaction (5.7) and (5.8) are -23 and -1416 kJ mol^{-1} (**Table A1**, adapted from NIST Chemistry Webbook and reference [199]), respectively, indicating that both reactions are thermodynamically favorable under typical regeneration conditions. Meanwhile, $Li_xPF_yO_4$ will decompose into Li_3PO_4 and LiF. This reveals that the main impurities influencing the regeneration are Al_2O_3, Li_3PO_4, LiF and Li_2CO_3.

The regeneration was performed by mixing the unwashed S-NCM622 powder with $LiOH{\cdot}H_2O$ at a molar ratio of 1:0.3, followed by annealing at 750 °C. After calcination, the material was washed with deionized water to remove residual lithium salts and then subjected to an additional heat treatment at 650 °C to further eliminate any remaining lithium compounds. The regenerated material is denoted as R-NCM622, consistent with that in *Chapter 4*.

The XPS analysis was performed on R-NCM622 to study the potential effect of impurities in the spent material. In the Al 2s spectra (**Fig. 5.5a**), a peak at around 118.2 eV is observed, similar to that observed in the washed S-NCM622 samples. This feature is indicative of Al-inclusion in the regenerated material. Furthermore, the observed peak at ~122.4 eV can be attributed to Al-F bonds, likely indicating concurrent F-inclusion in the regenerated material. In the F *1s* spectra (**Fig. 5.5b**), a clear peak at ~685.8 eV is present, with significantly higher intensity compared to the washed spent samples. This observation further suggests that F^-, derived from LiF impurities, dissolve into the layered structure during the regeneration process.

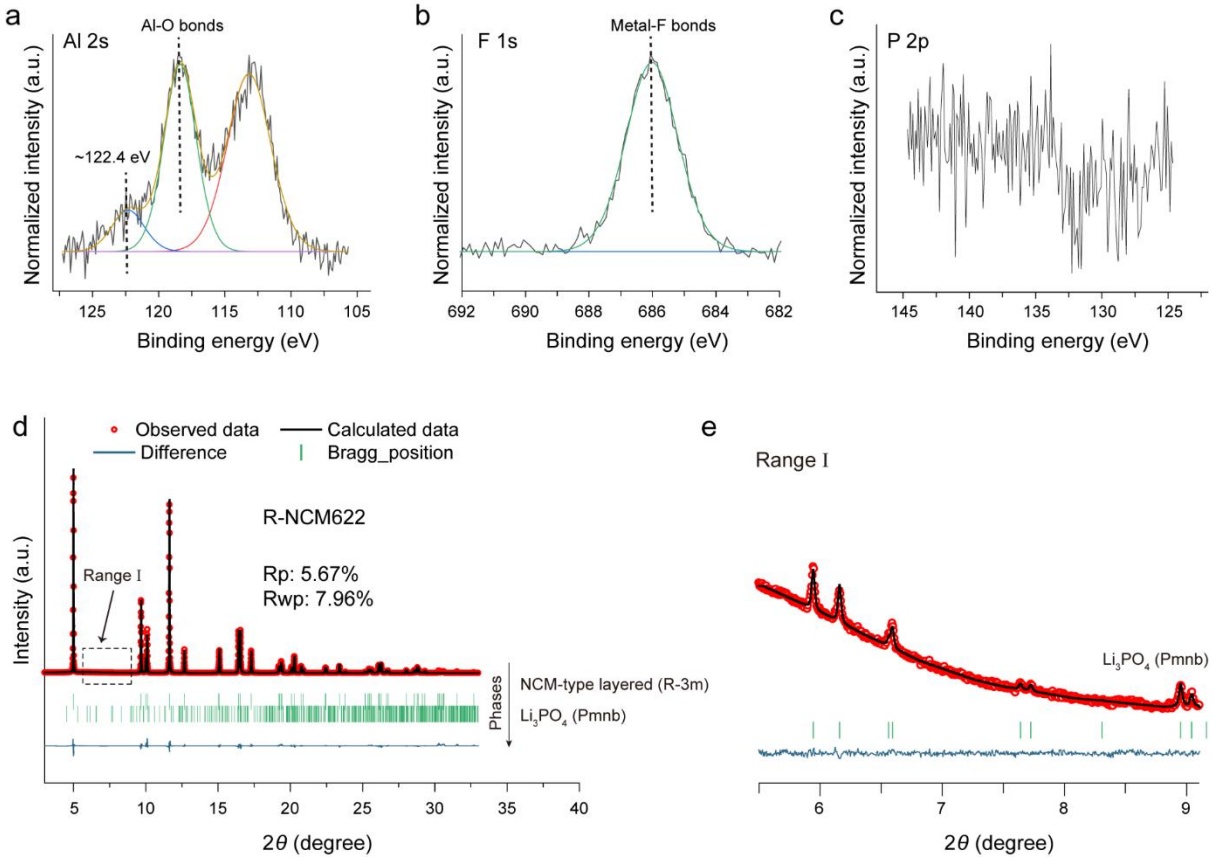

Fig. 5.5. XPS spectra of (a) Al 2s, (b) F 1s, and (c) P 2p for regenerated NCM622 (R-NCM622). (d) SRD pattern and corresponding Rietveld refinement results for regenerated NCM622 (R-NCM622). (e) Corresponding enlarged view of range I.

In the P *2p* spectra (**Fig. 5.5c**), as with the washed S-NCM622 samples, no distinct peaks are observed, indicating phosphorus species do not incorporate into the crystal structure during regeneration and might be removed through post-regeneration washing. Yet, the SRD analysis of R-NCM622 reveals that a small amount of Li_3PO_4 impurity remains, with its content quantified to be approximately 0.19 wt% via Rietveld refinement, as shown in **Fig. 5.5d-e**. For comparison, the Li_3PO_4 content in regenerated material without washing is around 0.40 wt%,

as discussed in later sections. This residual presence is likely due to the partial infiltration of impurities into the interparticle voids between primary grains [200], making their complete removal difficult. Since XPS is a surface-sensitive technique, it may not detect such embedded impurities, and such impurities would become more difficult to remove. Additionally, as shown in **Fig. 5.5e**, no residual Li_2CO_3 and other impurities are detected in R-NCM622.

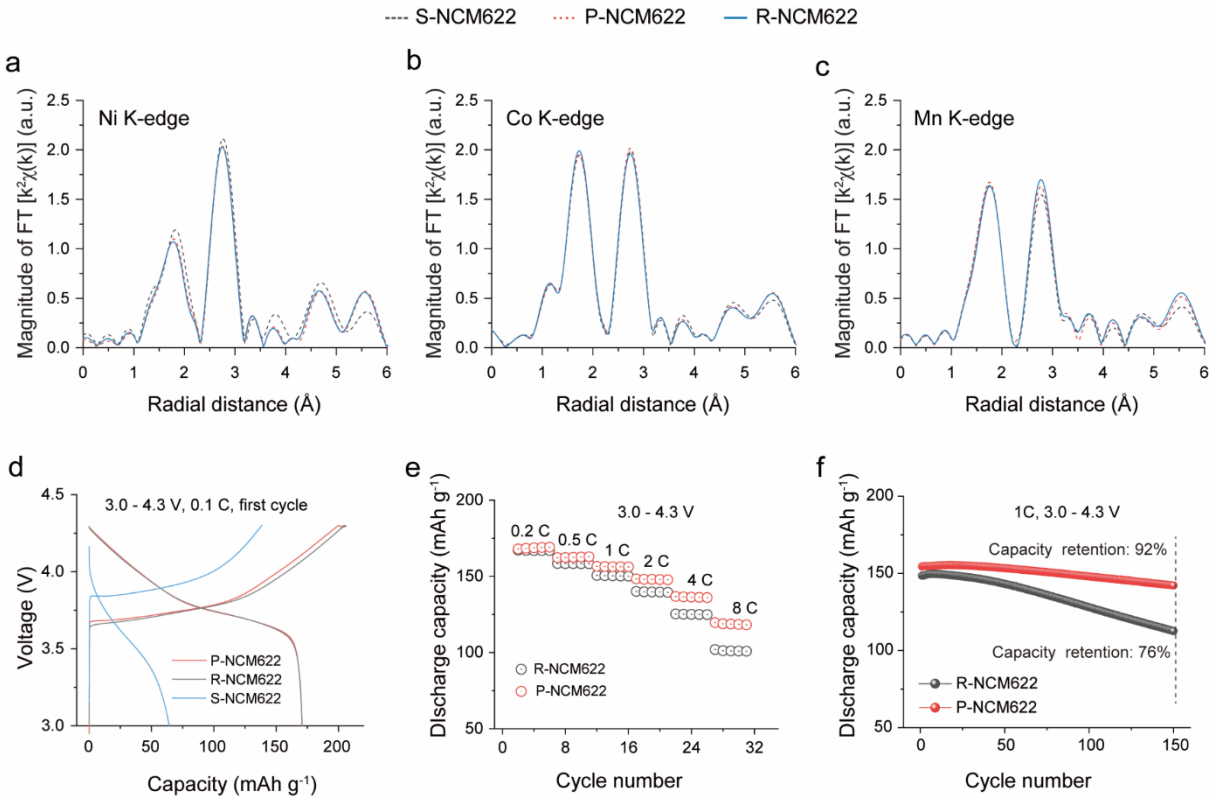

Fig. 5.6. EXAFS results of (a) Ni, (b) Co and (c) Mn K-edges for R-NCM622. (d) Initial charge/discharge capacities at 0.1 C (1 C = 160 mAh g^{-1}), over 3.0-4.3 V for R-NCM622 and pristine NCM622 (P-NCM622). (e) Rate performances of R-NCM622 and P-NCM622 over 3.0-4.3 V. The cells were charged to 4.3 V at the specified current rate and then discharged at the same rate. (f) Cycling performance of R-NCM622 and P-NCM622 at charge-discharge rate of 1 C, over 3.0-4.3 V.

Based on the above results, it is evident that the regeneration process is primarily influenced by Al- and F-containing impurities, which lead to Al- and F-inclusion in the regenerated material. To elucidate the structural and chemical changes induced by such inclusions in R-NCM622, commercially purchased pristine NCM622 (P-NCM622) was employed as a reference, which is also consistent with that in *Chapter 4*. EXAFS analysis at the Ni, Co, and Mn K-edges, were conducted on both regenerated and pristine samples to probe potential differences in their local structures. As observed in **Fig. 5.6a-c**, no obvious differences in the local structures between the two materials are observed. This is likely due to the low inclusion content, resulting from the relatively low levels of impurities present in the spent material.

Electrochemical testing at a charge–discharge rate of 0.1 C (1 C = 160 mA g^{-1}) over a voltage range of 3.0-4.3 V (**Fig. 5.7d**) further reveals that the initial discharge capacity of R-NCM622 (170.8 mAh g^{-1}) is comparable to that of P-NCM622 (170.1 mAh g^{-1}), indicating good structural reversibility of R-NCM622. This can be ascribed to the minimal local structural differences due to the low inclusion levels. However, at higher rates, R-NCM622 exhibits significantly lower capacities than P-NCM622 (**Fig. 5.7e**), likely due to Al- and F-inclusion impeding Li^+ diffusion within the structure despite their low contents [201]. Nevertheless, whether such low-level impurity inclusion affects long-term cycling stability remains uncertain. The inferior cycling performance of R-NCM622 compared with P-NCM622 (**Fig. 5.7f**) may be ascribed not only to potential effects of residual impurities but also to unrecovered particle cracks persisting after regeneration [60, 61], or the absence of protective surface coatings.

5.3.3 Influence of F impurity on structural repair

To gain deeper insight into the roles of Al- and F-containing impurities in the regeneration process, LiF and Al_2O_3 were deliberately introduced as additional impurities during the regeneration of S-NCM622. This approach enables a clearer understanding of how such impurities affect the local structure of the regenerated material, clarifies the specific inclusion mechanisms of Al and F, and highlights the effects of such inclusion on electrochemical properties, particularly when such inclusion accumulates over multiple regeneration processes.

Table 5.1. Calculated cell parameters and impurity phase fractions for F_3wt%, F_5wt%, F_7wt% and R-NCM622 from Rietveld refinement ("/" means that the corresponding content cannot be identified).

Samples		NCM-type *R-3m* phase		Impurity phases (wt%)		
		a (Å)	c (Å)	Li_3PO_4	Li_2CO_3	LiF
Unwashed	F_3wt%	2.86861(1)	14.22375(9)	0.38(0.10)	1.11(0.15)	1.48(0.36)
	F_5wt%	2.86860(1)	14.24364(10)	0.35(0.12)	1.08(0.17)	2.71(0.36)
	F_7wt%	2.86986(1)	14.22567(9)	0.39(0.13)	0.76(0.19)	3.66(0.28)
Washed	R-NCM622	2.86764(1)	14.21569(15)	0.19(0.12)	~0	/

The regeneration of such samples was performed by mixing unwashed S-NCM622 with $LiOH{\cdot}H_2O$ at a molar ratio of 1:0.3, followed by annealing at 750 °C, consistent with the process used to produce R-NCM622. At the same time, different proportions of LiF (3, 5, and 7 wt% relative to S-NCM622, denoted as F_3wt%, F_5wt% and F_7wt%, respectively) were introduced. To enable a clearer investigation of residual impurities, no subsequent aqueous washing was applied to any of the regenerated materials.

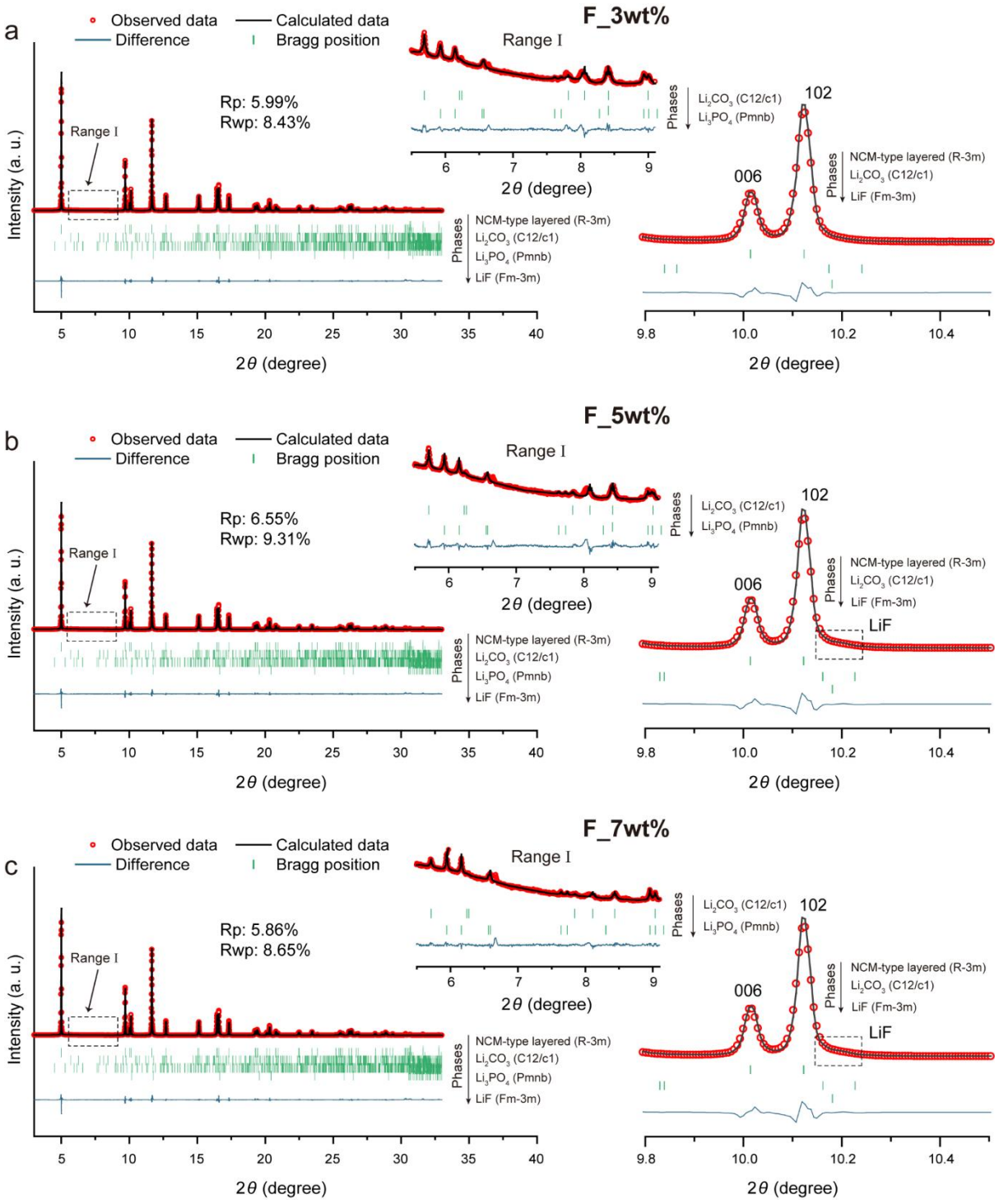

Fig. 5.7. SRD pattern (λ = 0.413820 Å) and corresponding Rietveld refinement results for (a) F_3wt%, (b) F_5wt%, and (c) F_7wt%.

Fig. 5.7a-c illustrates the corresponding SRD results of the regenerated materials. The impurities are primarily identified in range I. As shown in the enlarged views of this range, Li_3PO_4 and Li_2CO_3 are clearly observed as impurities for all regenerated samples. Rietveld refinement reveals Li_3PO_4 contents of approximately 0.38, 0.35, and 0.39 wt%, and Li_2CO_3 contents of approximately 1.11, 1.08, and 0.76 wt% in F_3wt%, F_5wt%, and F_7wt%,

respectively, as summarized in **Table 5.1**. In addition, a slight profile anomaly is found near the 102 reflection in F_5wt% and F_7wt%, which is most likely attributed to the presence of LiF. When the LiF phase is incorporated into the Rietveld refinement, its content is found to correlate strongly with the degree of this anomaly, increasing proportionally with the amount of LiF introduced during regeneration. This finding indicates that a portion of the added LiF does not participate in incorporation in the NCM structure. Structurally, all regenerated samples exhibit the characteristic rhombohedral structure with *R-3m* space group. However, compared to R-NCM622, the LiF-added samples exhibit noticeable increases in both lattice parameters *a* and *c*, which is most likely indicative of the F-inclusion.

To further understand the structural changes induced by F-inclusion, the XAS analysis was conducted. The corresponding XANES spectra at Ni, Co and Mn K-edges are presented in **Fig. 5.8a-c**. Compared to R-NCM622, the F-including samples exhibit edge shifts toward lower energies at both K-edges: Ni (max: ~0.3 eV) and Mn (max: ~0.2 eV), indicating a decrease in the average oxidation states of Ni and Mn. In contrast, no significant edge shift is observed at the Co K-edge. Given that F-inclusion typically involves substitution of oxygen atoms in the layered lattice, the resulting charge imbalance is compensated by a decrease in the oxidation states of nearby TMs [201]. Therefore, the observed edge shifts imply that the F-inclusion preferentially occurs in the Ni and Mn local environments.

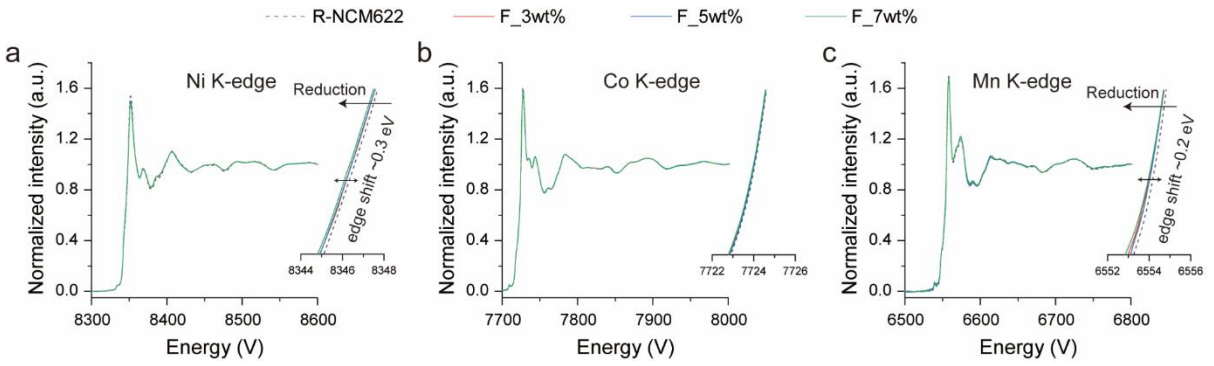

Fig. 5.8. Normalized XANES spectra of (a) Ni, (b) Co and (c) Mn K-edges for R-NCM622, F_3wt%, F_5wt%, and F_7wt%.

Fig. 5.9a illustrates the corresponding EXAFS of Ni K-edge, providing further insights into the local structural changes. All samples display two dominant peaks in the radial distribution function at ~1.8 and ~2.8 Å, corresponding to Ni-oxygen (Ni-O) and Ni-metal (Ni-M) coordination, respectively [68, 151]. Compared to R-NCM622, the F-including samples exhibit a decrease in magnitude of the Ni-O peak. This attenuation can be ascribed to the substitution of

oxygen by fluorine, resulting in the formation of Ni-$O_{6-x}F_x$ coordination environment. Due to the higher electronegativity of F^- compared with O^{2-}, such substitution could induce bond distortion and thereby reduce the symmetry of the NiO_6 octahedra.

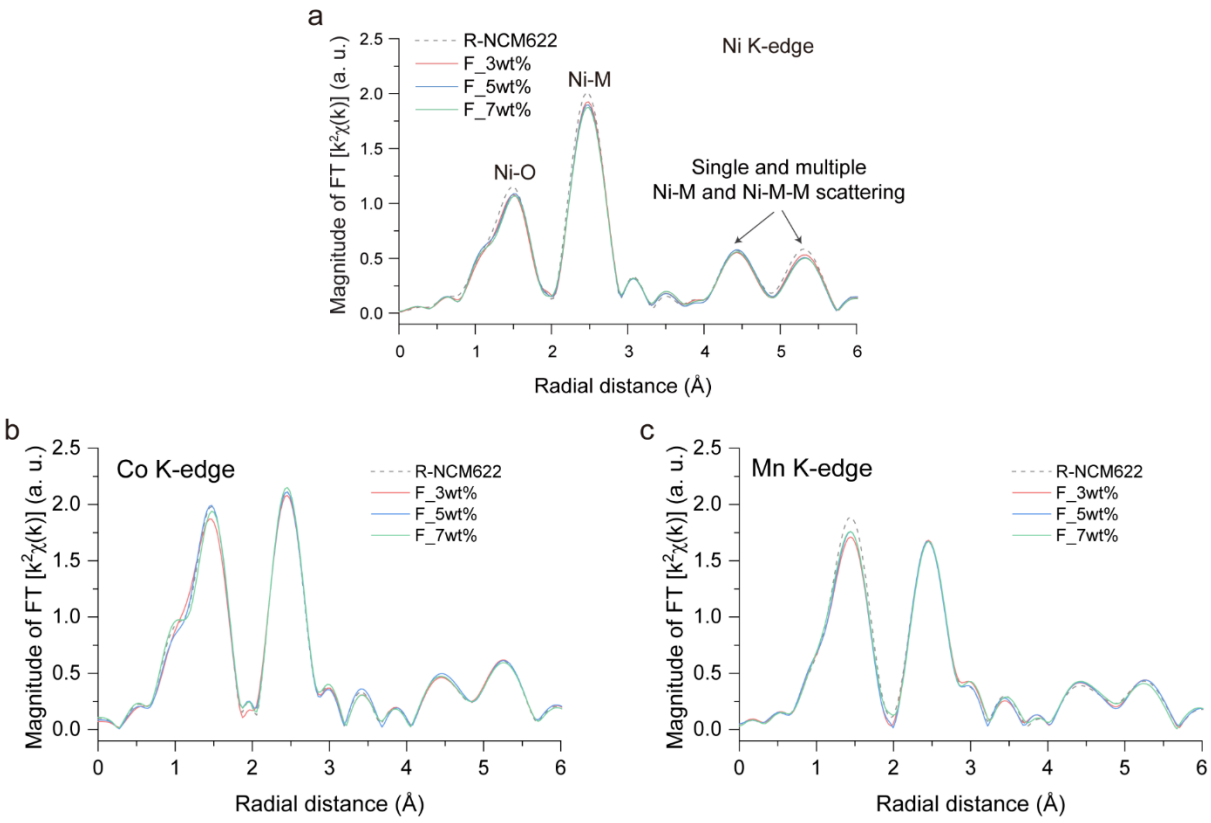

Fig. 5.9. EXAFS results of (a) Ni, (b) Co and (c) Mn K-edges for R-NCM622, F_3wt%, F_5wt%, and F_7wt%.

In addition, a decline in the Ni–M peak intensity is observed in the F-including samples, indicating that F-inclusion also affects the longer-range Ni–M_6 scattering environment. This implies that incorporation of F ions induces noticeable lattice distortions. The peak at around 5.5 Å, generally reflecting single and multiple scattering from Ni–M and Ni–M–M paths within the TM layer, also exhibits a decrease in magnitude. This further supports the presence of lattice distortion, which is likely oriented primarily along the *a*/*b* axis. Co and Mn K-edge EXAFS results (**Fig. 5.10b-c**) similarly reveal alterations in the local coordination environments of Co and Mn due to F-inclusion. Overall, these findings confirm the F-inclusion in the regenerated materials triggered by LiF impurity, and its induced lattice distortions.

Fig. 5.10 presents the initial discharge capacities of the F-including samples at 0.1 C (1 C = 160 mAh g^{-1}) with a cut-off voltage of 4.3 V. Prior to testing, all samples were water-washed and annealed at 650 °C to eliminate surface residual lithium and ensure accurate capacity tests.

A clear trend of decreasing discharge capacity with increasing LiF content is observed, while the charge capacities exhibit relatively minor differences. This likely suggests that excessive F incorporation into the lattice reduces the reversibility of the layered structure. This result underscores the detrimental effect of cumulative F incorporation in the lattice.

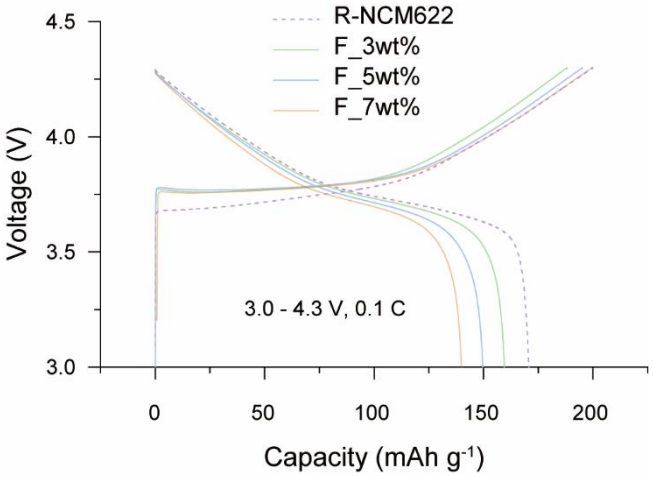

Fig. 5.10. Initial charge/discharge capacities at 0.1 C, over 3.0-4.3 V for R-NCM622, F_3wt%, F_5wt%, and F_7wt%.

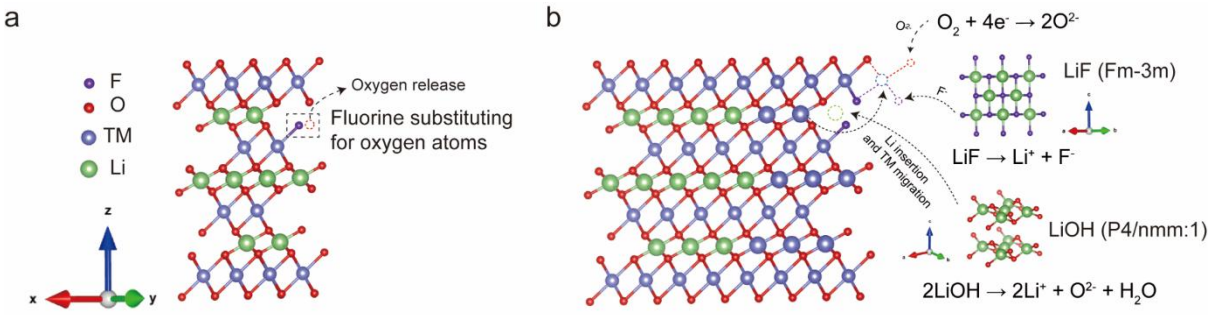

Fig. 5.11. (a) Schematic illustration for F-inclusion mechanism for pristine NCM materials. (b) Schematic illustration for a possible F-inclusion mechanism during regeneration.

It has been reported that the F-inclusion involves F^- substituting for O^{2-} within the octahedral coordination environment of TMs [201, 202]. In pristine NCM materials, such substitution results in the release of lattice oxygen and a respective reduction in the oxidation states of TMs, as schematically illustrated in **Fig. 5.11a**. However, in the context of direct regeneration, the F-inclusion likely proceeds via F^- substituting for O^{2-} during structural repair, thereby decreasing the overall demand for oxygen and mitigating lattice oxygen release. In general, the regeneration process involves the migration and oxidation of TM ions, accompanied by the reduction of O_2, which accepts electrons and facilitates the reconstruction of octahedral sites within the TM layer [203]. Under these conditions, F^- ions supplied by LiF can replace O^{2-},

becoming incorporated into the newly formed octahedral sites within the TM layer, followed by anion diffusion, as depicted in **Fig. 5.11b**. Moreover, the Li^+ released from LiF during incorporation are believed to serve as an additional lithium source, facilitating reconstruction of the Li layer in the layered structure.

5.3.4 Influence of Al impurity on structural repair

Fig. 5.12a-c presents the SRD results of the Al-including samples, where different Al_2O_3 contents were introduced during the regeneration process (3, 5, and 7 wt% relative to S-NCM622, denoted as Al_3wt%, Al_5wt% and Al_7wt%, respectively). The regeneration conditions were the same as those for the F-including samples, with no subsequent aqueous washing applied. It should be noted that, during Rietveld refinement, the LiF presence and content could not be reliably identified in the Al_2O_3-added samples, due to the absence of noticeable profile anomalies near the 102 reflection or other indications of such phase.

In the enlarged range I, impurities such as Li_3PO_4 and Li_2CO_3 are observed in all Al-including samples, similar to the F-including samples. The results of Rietveld refinement (**Table 5.2**) indicate relatively higher amounts of Li_3PO_4 and Li_2CO_3 in the Al-including samples compared to the F-including ones. Notably, γ-$LiAlO_2$ phase ($P4_12_12$) is identified, particularly in Al_5wt% and Al_7wt%, indicating that not all Al_2O_3 is incorporated into the NCM lattice as well. The unreacted Al_2O_3 merges with lithium salts to generate $LiAlO_2$, with its content increasing as the Al_2O_3 addition rises.

All regenerated samples exhibit the characteristic rhombohedral structure with *R-3m* space group. However, compared to R-NCM622, Al-including samples, unlike the F-including ones, show a decrease in *a* and a slight increase in *c* (**Table 5.3**). More importantly, most reflections, particularly the 104 reflection, exhibit asymmetry on the right side of their respective peak profiles, especially in range II (**Fig. 5.12a-c**). This observation suggests the formation of a secondary layered phase that retains rhombohedral symmetry but features a shorter TM–O bond distance. The formation of this phase is likely related to the Al-inclusion, and is thus referred to as $LiAlO_2$-type layered phase (*R-3m*) here. For comparison, the primary structure is denoted as the NCM-type layered phase (*R-3m*).

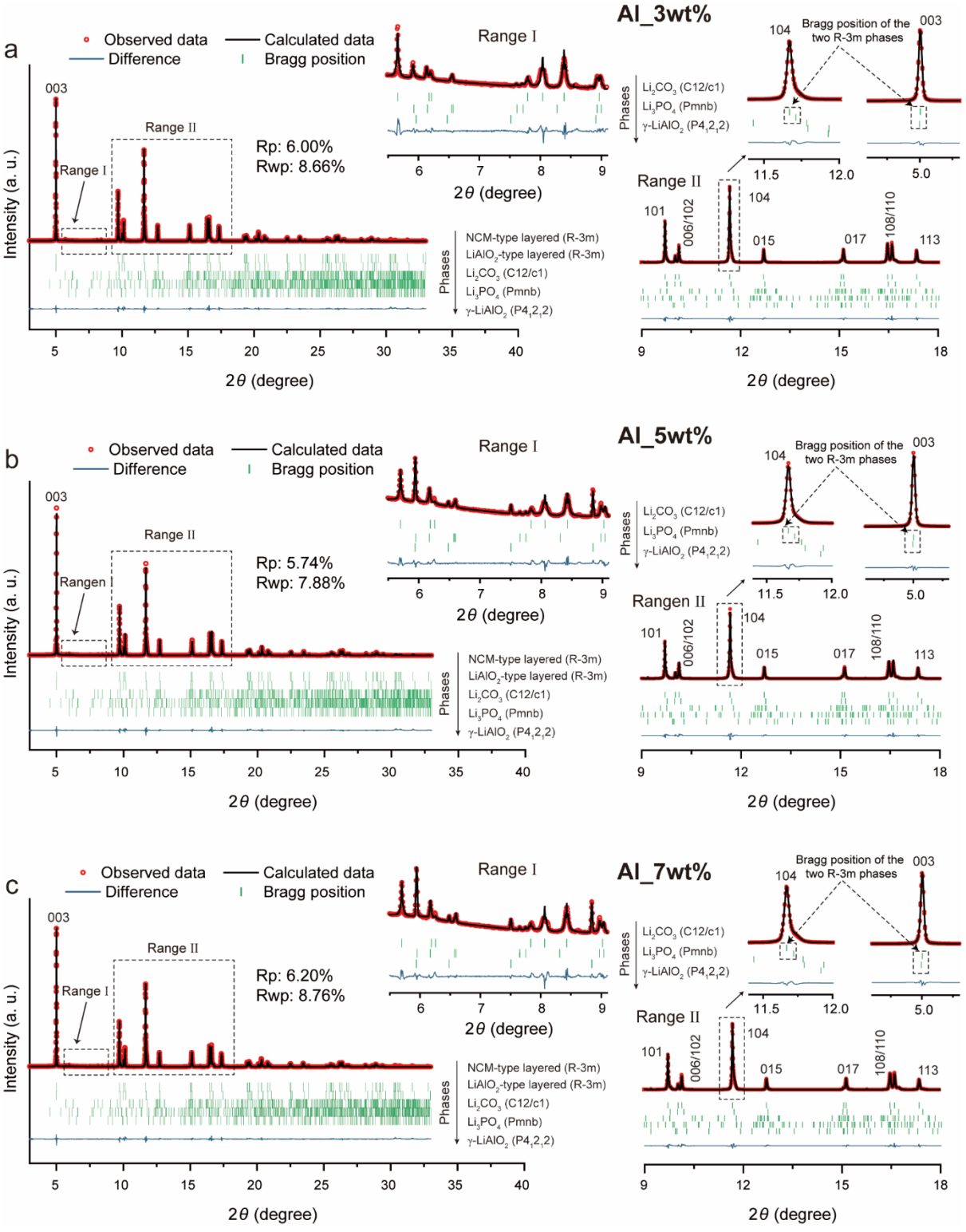

Fig. 5.12. SRD pattern (λ = 0.413820 Å) and corresponding Rietveld refinement results for (a) Al_3wt%, (b) Al_5wt%, and (c) Al_7wt%.

To further investigate this, Rietveld refinement including both layered phases was performed. The results reveal that the $LiAlO_2$-type layered phase fraction increases with higher Al_2O_3 addition (**Table 3**). In addition, the $LiAlO_2$-type layered structure exhibits a lower *a* value

compared to the NCM-type structure, reflecting a shorter TM-O bond distance. A continuous decrease in *a* value is observed with increasing Al_2O_3 content, while *c* value remains relatively unchanged, in line with the minimal asymmetry seen in the 003 reflection. The formation of the $LiAlO_2$-type layered phase is most likely due to limited Al diffusion into the bulk structure during regeneration. This leads to the development of Al-rich domains, which in turn cause noticeable contraction along the *a*/*b* plane of the TM layer. This behavior can be attributed to the higher bond dissociation energy of Al–O in octahedral coordination (~512 kJ mol^{-1}), compared to those of Ni-O (~391 kJ mol^{-1}), Co-O (~397 kJ mol^{-1}) and Mn-O (~402 kJ mol^{-1}) bonds [204, 205], thereby decreasing the average TM-O bond distance.

Table 5.2. Calculated impurity phase fractions for Al_3wt%, Al_5wt%, Al_7wt% and R-NCM622.

Samples		Impurity phases (wt%)		
		Li_3PO_4	Li_2CO_3	γ-$LiAlO_2$ ($P4_12_12$)
Unwashed	Al_3wt%	0.54(0.13)	5.09(0.16)	0.12(0.07)
	Al_5wt%	0.39(0.12)	2.54(0.15)	0.93(0.08)
	Al_7wt%	0.39(0.12)	2.84(0.20)	1.08(0.09)
Washed	R-NCM622	0.19(0.12)	~0	~0

Table 5.3. Calculated cell parameters for Al_3wt%, Al_5wt%, Al_7wt% and R-NCM622("/" means that the corresponding value cannot be identified).

Samples	NCM-type layered phase		$LiAlO_2$-type layered phase		$LiAlO_2$-type layered phase (wt%)
	a (Å)	c (Å)	a (Å)	c (Å)	
Al_3wt%	2.86637(1)	14.21796(10)	2.84946(18)	14.23471(154)	28.88(0.78)
Al_5wt%	2.86720(1)	14.21999(10)	2.84749(18)	14.24077(159)	30.11(0.72)
Al_7wt%	2.86651(1)	14.21845(11)	2.84604(16)	14.24144(131)	35.04(0.88)
R-NCM622	2.86764(1)	14.21569(15)	/	/	/

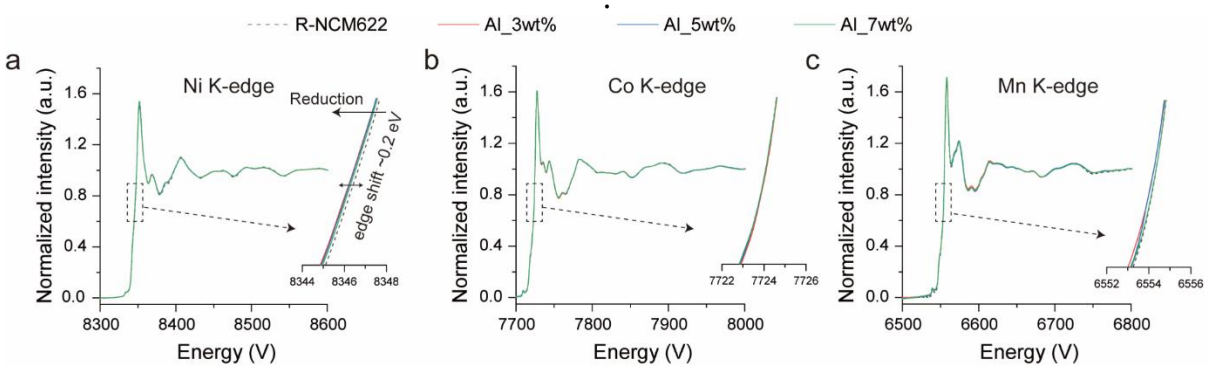

Fig. 5.13 Normalized XANES spectra of (a) Ni, (b) Co and (c) Mn K-edges for R-NCM622, Al_3wt%, Al_5wt%, and Al_7wt%.

The XAS analysis was conducted to further investigate the structural changes induced by Al-inclusion. As displayed in **Fig. 5.13a-c**, the XANES spectra at Co and Mn K-edges indicate that the oxidation states of Co and Mn remain largely unchanged. A slight edge shift (max: ~0.2 eV) toward lower energy in Ni K-edge is observed for Al-including samples, suggesting minimal decrease in its oxidation state. These results demonstrate that Al-inclusion has negligible effects on the oxidation states of TM.

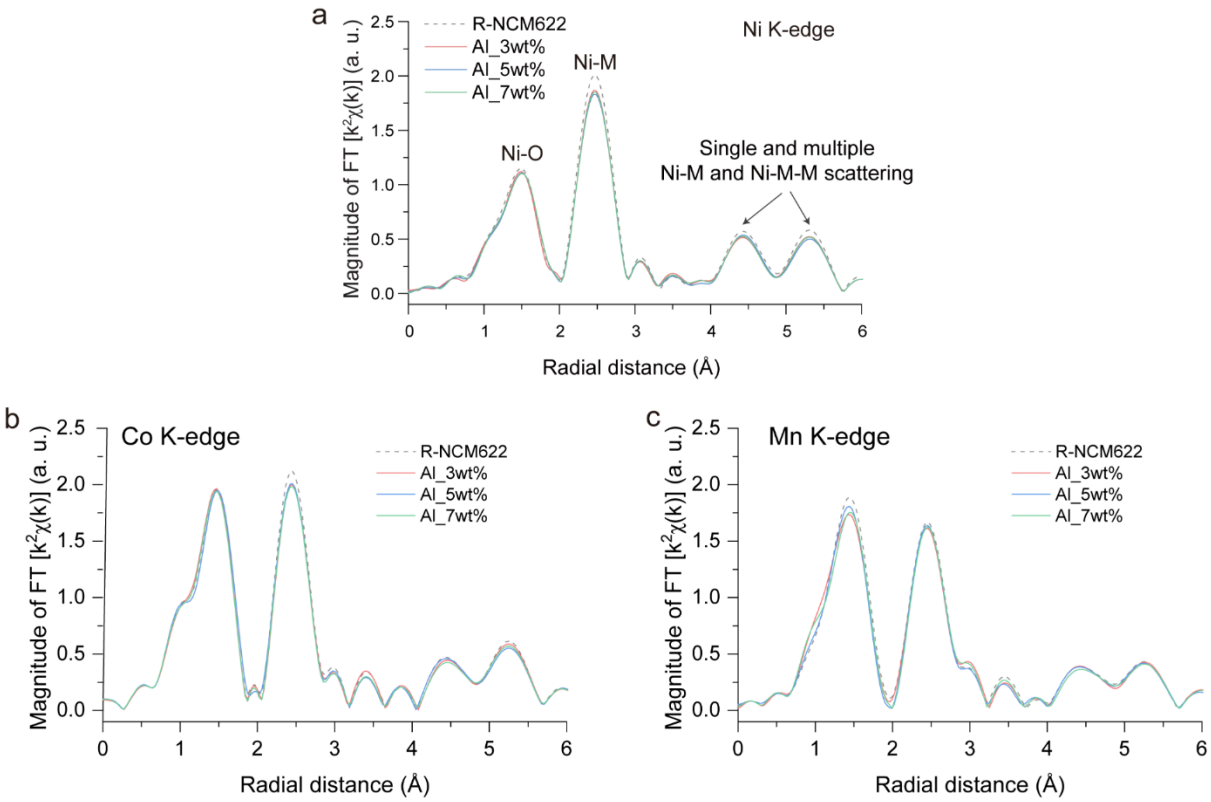

Fig. 5.14. EXAFS results of (a) Ni, (b) Co and (c) Mn K-edges for R-NCM622, Al_3wt%, Al_5wt%, and Al_7wt%.

Fig. 5.14-a-c presents the EXAFS results. No obvious differences are observed at the Ni-O peak between the Al-including samples and R-NCM622, nor at the Co-O peak (**Fig. 5.14a-b**). A small variation is noted in the Mn–O peak (**Fig. 5.14c**), but this could be related to the poorer data quality due to the low Mn concentration and its lower X-ray absorption edge energy (**Fig. A8**). Overall, these results suggest that Al-inclusion induces only minor changes in the TMO_6 octahedral coordination environment. Yet, the longer scattering paths associated with Ni-M and Ni-M-M interactions (~2.8, ~4.7 and ~5.5 Å) all show a decrease in magnitude in the Al-including samples compared to R-NCM622. Similar trends are observed in the Co K-edge EXAFS results. These changes are probably attributed to decreased backscattering from the TM lattice sites, resulting from the incorporation of Al, due to its lower atomic number.

Fig. 5.15 presents the initial discharge capacities of the Al-including samples at 0.1 C with a cut-off voltage of 4.3 V. Consistent with the F-including samples, these materials were subjected to water washing followed by annealing at 650 °C prior to testing, to remove the residual lithium compounds. A clear decrease in discharge capacity is observed with increasing Al_2O_3 content, likely due to the accumulation of electrochemically inactive Al within the lattice. This finding highlights the detrimental effect of excessive Al incorporation on electrochemical performance.

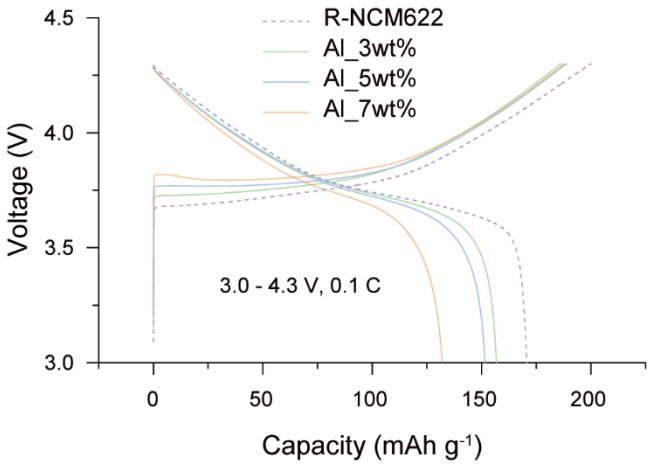

Fig. 5.15. Initial charge/discharge capacities at 0.1 C, over 3.0-4.3 V for R-NCM622, Al_3wt%, Al_5wt%, and Al_7wt%.

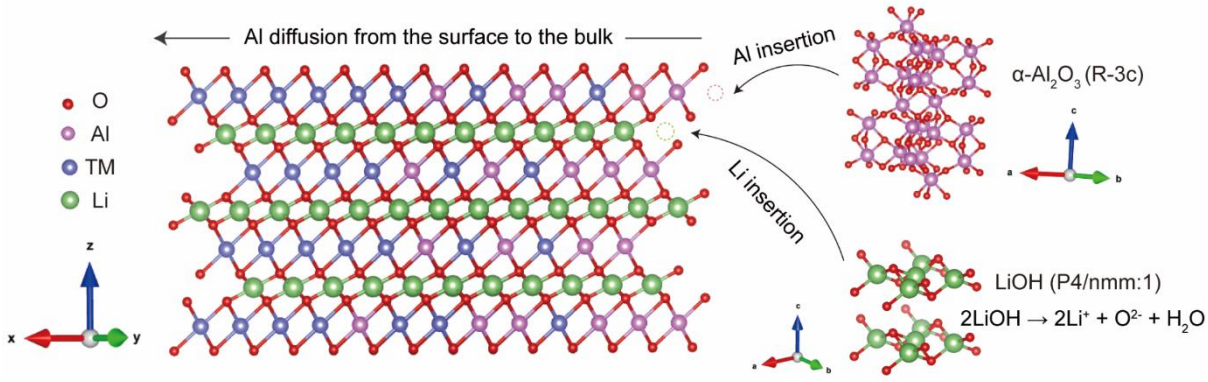

Fig. 5.16 Schematic illustration for a possible Al-inclusion mechanism during regeneration.

The mechanism of Al-inclusion is generally understood to involve the substitution of Al ions for TM ions within the lattice [205, 206]. This substitution typically implies that the incorporation of one Al ion necessitates the extraction of one TM ion, resulting in the formation of TM oxides. However, in this study, no indications of TM oxide formation are observed in either the SRD or XAS analyses. This absence suggests that an alternative mechanism of Al-inclusion may be at play. In other studies, about upcycling of cathode powder [54, 56], spent low- or mid-nickel

NCM materials are often mixed with nickel oxide or hydroxide and lithium salts, followed by high-temperature annealing. This process facilitates the transformation into high-nickel NCM materials. The underlying mechanism involves the extension of the TM and Li layers along certain crystallographic planes [55, 207]. By analogy, Al-inclusion in this study is proposed to follow a similar route. Owing to the excess of lithium salts used during regeneration, Al_2O_3 may be driven to dissolve into the lattice, promoting the crystallite growth and enabling Al incorporation into the crystal structure, as depicted in **Fig. 5.16**. However, due to the limited diffusion kinetics of Al in the lattice, its distribution is confined to surface-near regions, resulting in the generation of Al-rich domains.

Potential challenges for direct recycling

Based on the above observations, it can be concluded that the electrochemical capacity and local structure of the regenerated material show no significant difference from the pristine NCM622 during the first regeneration process, primarily due to the low concentration of impurities. Nevertheless, when impurity levels are deliberately increased, pronounced local structural distortions and capacity degradation are observed, driven by elemental inclusion in the regenerated materials. Such high-level inclusion may also accumulate over multiple cycles of direct regeneration if impurities are not effectively removed. Therefore, a purification step is essential to eliminate impurities for ensuring the long-term effectiveness of direct recycling.

Since most impurities present in the spent material are soluble in water or NaOH solution, an aqueous washing step prior to regeneration can be an effective method to reduce their concentrations. However, the limited solubility of certain species, such as Li_3PO_4 and LiF, along with the possible presence of impurities distributed within the intergranular spaces between primary particles, may hinder complete removal. Furthermore, due to the presence of both intragranular and intergranular cracks induced by prolonged cycling, the spent NCM material is especially vulnerable to further morphological damage during centrifugation-based aqueous washing (**Fig. 5.17a-b**), particularly under intensified treatments such as sonication aimed at improving impurity dissolution (**Fig. 5.17a and c**). Such damage can lead to severe particle aggregation during regeneration and result in heterogeneous morphology (**Fig. 5.18a**), which are generally detrimental to electrochemical performance. In contrast, samples regenerated prior to washing exhibit markedly improved morphological integrity (**Fig. 5.18b**). This is likely because the regeneration process can heal some intragranular and intergranular cracks, thereby preventing severe morphological damage during subsequent washing.

Overall, for spent polycrystalline NCM materials, it is crucial to develop practical and efficient purification strategies prior to regeneration for maintaining the structural and morphological integrity of the regenerated products.

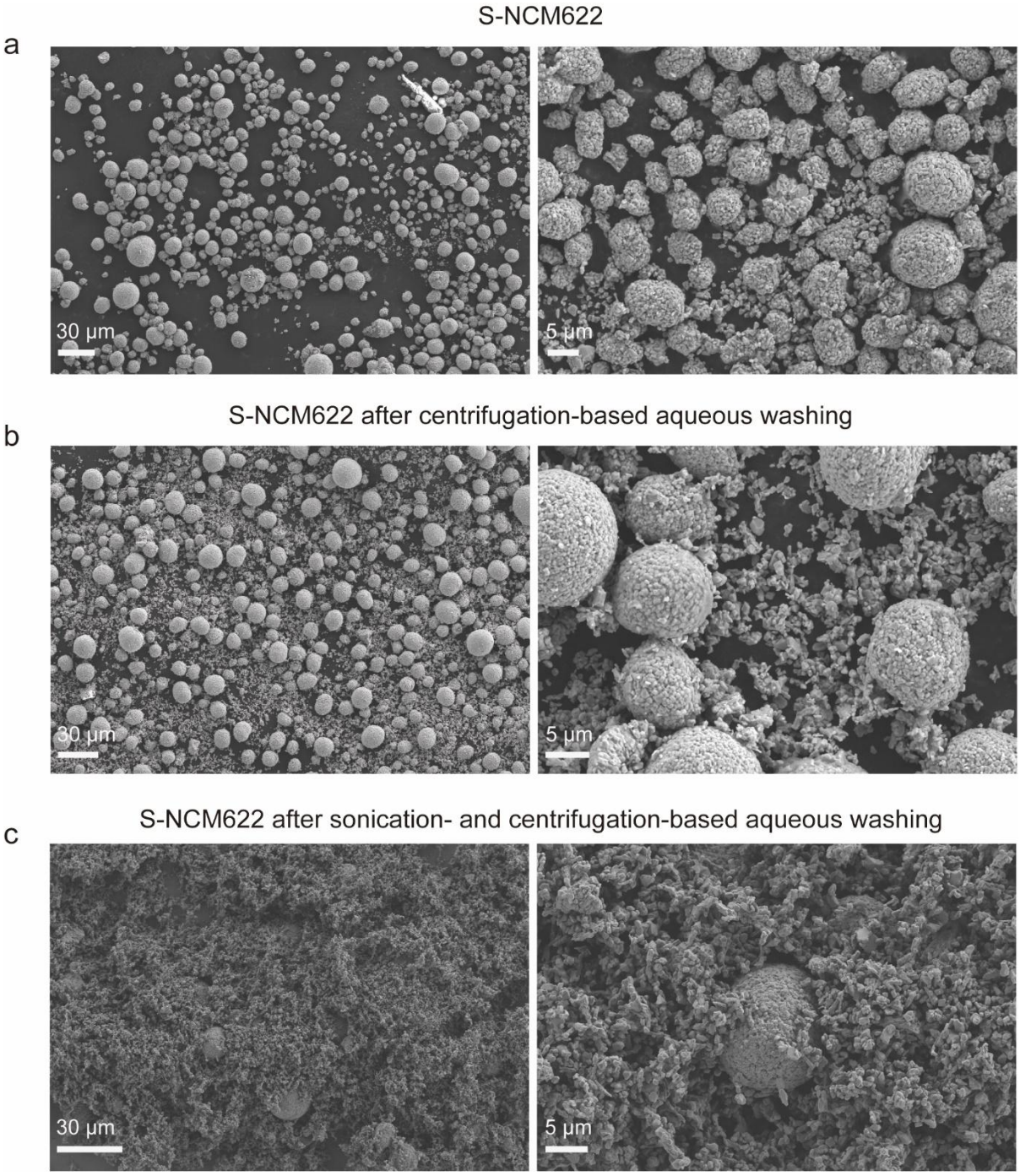

Fig. 5.17. SEM images for (a) S-NCM622, (b) S-NCM622 after centrifugation-based aqueous washing, and (c) after sonication- and centrifugation-based aqueous washing.

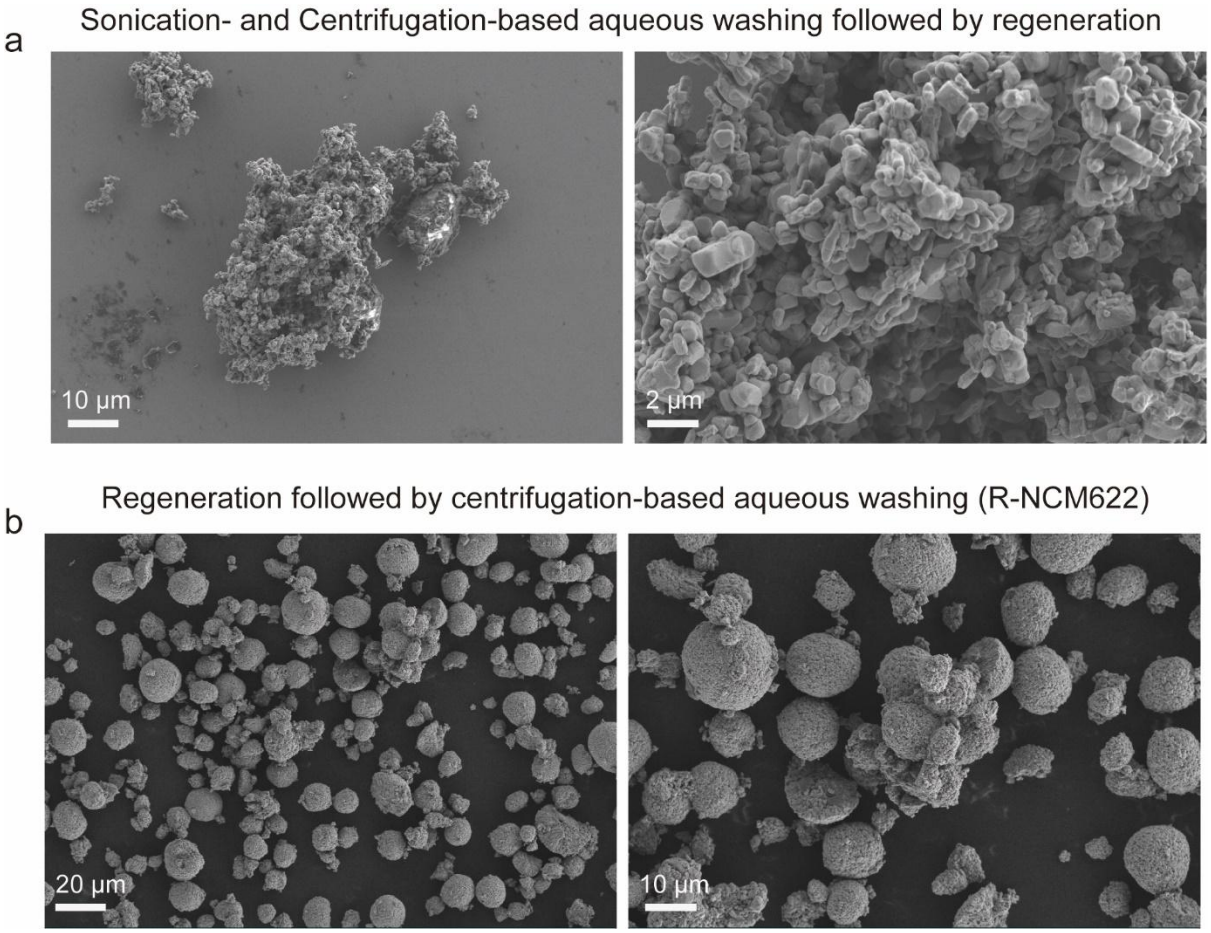

Fig. 5.18. SEM images for (a) material regenerated after sonication- and centrifugation-based aqueous washing followed by regeneration, and (b) material regenerated first followed by centrifugation-based aqueous washing.

5.4 Conclusion

In summary, this chapter systematically investigates the presence of potential impurities in spent NCM622 cathode materials and their influence on the regeneration process, using XPS, SRD, and XAS techniques. The impurities identified in the spent NCM622 include Al_2O_3, $AlPO_4$, AlF_3, Li_3PO_4, LiF, $Li_xPF_yO_4$, and Li_2CO_3, accompanied by Al-inclusion likely induced by thermal pretreatment. The regeneration process is primarily affected by Al- and F-containing impurities, which respectively lead to Al and F inclusion in the regenerated material. However, due to the relatively low impurity levels in the spent cathode material, the regenerated material shows negligible changes in local structure and electrochemical capacity when compared to the pristine material.

To comprehensively elucidate the effect of impurities on direct regeneration, LiF and Al_2O_3 were intentionally introduced during this process. The results show that the F-inclusion in regenerated material likely proceeds via F^- substituting for O^{2-} during structural repair, which

results in decreased oxidation states of transition metals (primarily Ni and Mn) and induces lattice distortions. In contrast, Al-inclusion does not appear to follow a simple substitution mechanism of Al for TM ions. Instead, the mechanism likely involves the extension of TM and Li layers along specific crystallographic planes, driven by excess lithium salts during regeneration. Meanwhile, due to the limited diffusion kinetics of Al, its incorporation is largely confined to near-surface regions, resulting in the formation of Al-rich domains and a noticeably localized lattice contraction along *a*/*b* axis. Both types of contaminants are found to adversely affect electrochemical performance when excessively incorporated. Therefore, the removal of corresponding impurities prior to regeneration is recommended to prevent cumulative incorporation of these elements into the crystal lattice over multiple recycling cycles, thereby ensuring the long-term viability of direct recycling.

6. Summary and outlook

Direct recycling has attracted considerable attention in both academia and industry due to its strong potential, yet its practical implementation still faces challenges. This work systematically clarifies the main material-level mechanisms underlying the direct recycling processes, identifies the critical factors governing the cathode regeneration, and demonstrates the feasibility of recycling spent LIBs through this approach. The findings not only deepen the fundamental understanding of thermal pretreatment, structural repair, and impurity effects but also provide practical insights for designing optimized recycling protocols.

In the first part (*Chapter 3*), the effects of thermal pretreatment under different atmospheres and temperatures on electrode separation and material degradation were systematically investigated. A treatment condition of 450 °C for 4 h under air for spent cathode was considered as a relatively suitable balance between separation efficiency and structural preservation, and the resulting NCM622 powders were used as the basis for subsequent regeneration studies.

In the second part (*Chapter 4*), advanced characterization techniques (XRD, XAS, and ^{6}Li solid-state NMR) revealed that structural degradation of spent NCM622 primarily originates from transition-metal migration into the Li layer, while successful regeneration is closely correlated with decreasing transition-metal occupancy. The optimized solid-state regeneration conditions (750 °C, 12 h, air; Li/TM = 0.3) yielded a repaired material with electrochemical capacity comparable to pristine NCM622, thus validating the effectiveness of the repair strategy.

In the third part (*Chapter 5*), the effect of impurities was systematically elucidated. Al- and F-containing species are found to significantly affect regeneration process, leading to Al- and F-inclusion in regenerated material. Both dopants are shown to impair the electrochemical performance and structural integrity when accumulated, underscoring the importance of impurity removal prior to regeneration to ensure the long-term viability of direct recycling.

Looking forward, future efforts should focus on impurity removal, optimization of regeneration conditions, and the development of efficient pretreatment strategies. These advances will be key to enhancing material recovery, preserving structural integrity, and accelerating the industrial implementation of direct recycling as a sustainable pathway for next-generation battery recycling technologies.

Reference

(1) Zubi, G.; Dufo-López, R.; Carvalho, M.; Pasaoglu, G. The lithium-ion battery: State of the art and future perspectives. *Renewable and Sustainable Energy Reviews* **2018**, *89*, 292-308.

(2) Tembo, P.; Dyer, C.; Subramanian, V. Lithium-ion battery recycling—a review of the material supply and policy infrastructure. *NPG Asia Materials* **2024**, *16* (1), 43.

(3) Padhi, A. K.; Nanjundaswamy, K. S.; Goodenough, J. B. Phospho-olivines as positive-electrode materials for rechargeable lithium batteries. *Journal of the electrochemical society* **1997**, *144* (4), 1188.

(4) Murugan, A. V.; Muraliganth, T.; Ferreira, P.; Manthiram, A. Dimensionally modulated, single-crystalline $LiMPO_4$ (M= Mn, Fe, Co, and Ni) with nano-thumblike shapes for high-power energy storage. *Inorganic chemistry* **2009**, *48* (3), 946-952.

(5) Gangulibabu; Bhuvaneswari, D.; Kalaiselvi, N.; Jayaprakash, N.; Periasamy, P. CAM sol–gel synthesized $LiMPO_4$ (M= Co, Ni) cathodes for rechargeable lithium batteries. *Journal of sol-gel science and technology* **2009**, *49*, 137-144.

(6) Muraliganth, T.; Manthiram, A. Understanding the Shifts in the Redox Potentials of Olivine $LiM_{1-y}M_yPO_4$ (M= Fe, Mn, Co, and Mg) Solid Solution Cathodes. *The Journal of Physical Chemistry C* **2010**, *114* (36), 15530-15540.

(7) Yamada, A.; Hosoya, M.; Chung, S.-C.; Kudo, Y.; Hinokuma, K.; Liu, K.-Y.; Nishi, Y. Olivine-type cathodes. *Journal of Power Sources* **2003**, *119-121*, 232-238.

(8) Kandhasamy, S.; Nallathamby, K.; Minakshi, M. Role of structural defects in olivine cathodes. *Progress in Solid State Chemistry* **2012**, *40* (1-2), 1-5.

(9) Chung, S.-Y.; Bloking, J. T.; Chiang, Y.-M. Electronically conductive phospho-olivines as lithium storage electrodes. *Nature materials* **2002**, *1* (2), 123-128.

(10) Kim, T.; Song, W.; Son, D.-Y.; Ono, L. K.; Qi, Y. Lithium-ion batteries: outlook on present, future, and hybridized technologies. *Journal of Materials Chemistry A* **2019**, *7* (7), 2942-2964.

(11) Rostami, H.; Valio, J.; Tynjala, P.; Lassi, U.; Suominen, P. Life Cycle of LiFePO(4) Batteries: Production, Recycling, and Market Trends. *Chemphyschem* **2024**, *25* (24), e202400459.

(12) Logan, E. R.; Eldesoky, A.; Liu, Y.; Lei, M.; Yang, X.; Hebecker, H.; Luscombe, A.; Johnson, M. B.; Dahn, J. R. The Effect of $LiFePO_4$ Particle Size and Surface Area on the Performance of LiFePO4/Graphite Cells. *Journal of The Electrochemical Society* **2022**, *169* (5), 050524.

(13) Liu, Y.; Liu, J.; Wang, J.; Banis, M. N.; Xiao, B.; Lushington, A.; Xiao, W.; Li, R.; Sham, T. K.; Liang, G.; et al. Formation of size-dependent and conductive phase on lithium iron phosphate during carbon coating. *Nat Commun* **2018**, *9* (1), 929.

(14) Wang, X.; Feng, Z.; Hou, X.; Liu, L.; He, M.; He, X.; Huang, J.; Wen, Z. Fluorine doped carbon coating of $LiFePO_4$ as a cathode material for lithium-ion batteries. *Chemical Engineering Journal* **2020**, *379*, 122371.

(15) Saravanan, K.; Balaya, P.; Reddy, M. V.; Chowdari, B. V. R.; Vittal, J. J. Morphology controlled synthesis of $LiFePO_4$/C nanoplates for Li-ion batteries. *Energy & Environmental Science* **2010**, *3* (4), 457.

(16) Yang, M.-R.; Ke, W.-H. The doping effect on the electrochemical properties of $LiFe_{0.95}M_{0.05}PO_4$ (M= Mg^{2+}, Ni^{2+}, Al^{3+}, or V^{3+}) as cathode materials for lithium-ion cells. *Journal of the Electrochemical Society* **2008**, *155* (10), A729.

(17) Kim, K. M.; Lee, Y.-G.; Kang, K.-Y.; Yang, Y. S.; Kim, J. A simple method for solving the voltage overshoots of $LiFePO_4$-based lithium-ion batteries with different capacity classes. *RSC Advances* **2012**, *2* (9), 3844-3849.

(18) Hou, X.; Liu, X.; Wang, H.; Zhang, X.; Zhou, J.; Wang, M. Specific countermeasures to intrinsic capacity decline issues and future direction of $LiMn_2O_4$ cathode. *Energy Storage Materials* **2023**, *57*, 577-606.

(19) Thackeray, M. M.; David, W. I.; Bruce, P. G.; Goodenough, J. B. Lithium insertion into manganese spinels. *Materials research bulletin* **1983**, *18* (4), 461-472.

(20) Kim, D. K.; Muralidharan, P.; Lee, H.-W.; Ruffo, R.; Yang, Y.; Chan, C. K.; Peng, H.; Huggins, R. A.; Cui, Y. Spinel $LiMn_2O_4$ nanorods as lithium ion battery cathodes. *Nano letters* **2008**, *8* (11), 3948-3952.

(21) Goodenough, J. B.; Park, K. S. The Li-ion rechargeable battery: a perspective. *Journal of the American Chemical Society* **2013**, *135* (4), 1167-1176.

(22) Michalska, M.; Ziółkowska, D. A.; Jasiński, J. B.; Lee, P. H.; Ławniczak, P.; Andrzejewski, B.; Ostrowski, A.; Bednarski, W.; Wu, S. H.; Lin, J. Y. Improved electrochemical performance of $LiMn_2O_4$ cathode material by Ce doping. *Electrochimica Acta* **2018**, *276*, 37-46.

(23) Baazizi, M.; Karbak, M.; Aqil, M.; Sayah, S.; Dahbi, M.; Ghamouss, F. High-Valence Surface-Modified LMO Cathode Materials for Lithium-Ion Batteries: Diffusion Kinetics and Operando Thermal Stability Investigation. *ACS Appl Mater Interfaces* **2023**, *15* (34), 40385-40396.

(24) Bi, Z.; Zhao, N.; Ma, L.; Shi, C.; Fu, Z.; Xu, F.; Guo, X. Surface coating of $LiMn_2O_4$

cathodes with garnet electrolytes for improving cycling stability of solid lithium batteries. *Journal of Materials Chemistry A* **2020**, *8* (8), 4252-4256.

(25) Huang, S.; Wu, H.; Chen, P.; Guo, Y.; Nie, B.; Chen, B.; Liu, H.; Zhang, Y. Facile pH-mediated synthesis of morphology-tunable $MnCO_3$ and their transformation to truncated octahedral spinel $LiMn_2O_4$ cathode materials for superior lithium storage. *Journal of Materials Chemistry A* **2015**, *3* (7), 3633-3640.

(26) Whittingham, M. S. Electrical energy storage and intercalation chemistry. *Science* **1976**, *192* (4244), 1126-1127.

(27) Whittingham, M. S. The role of ternary phases in cathode reactions. *Journal of The Electrochemical Society* **1976**, *123* (3), 315.

(28) Mizushima, K.; Jones, P. C.; Wiseman, P. J.; Goodenough, J. B. Li_xCoO_2 ($0< x< 1$): A new cathode material for batteries of high energy density. *Materials Research Bulletin* **1980**, *15* (6), 783-789.

(29) Ozawa, K. Lithium-ion rechargeable batteries with $LiCoO_2$ and carbon electrodes: the $LiCoO_2$/C system. *Solid State Ionics* **1994**, *69* (3-4), 212-221.

(30) Winter, M.; Besenhard, J. O.; Spahr, M. E.; Novak, P. Insertion electrode materials for rechargeable lithium batteries. *Advanced materials* **1998**, *10* (10), 725-763.

(31) Bruce, P. Solid-state chemistry of lithium power sources. *Chemical Communications* **1997**, (19), 1817-1824.

(32) Ohzuku, T.; Ueda, A. Solid-state redox reactions of $LiCoO_2$ (R-3m) for 4 volt secondary lithium cells. *Journal of The Electrochemical Society* **1994**, *141* (11), 2972.

(33) Mendiboure, A.; Delmas, C.; Hagenmuller, P. New layered structure obtained by electrochemical deintercalation of the metastable $LiCoO_2$ (O_2) variety. *Materials research bulletin* **1984**, *19* (10), 1383-1392.

(34) Bianchini, M.; Roca-Ayats, M.; Hartmann, P.; Brezesinski, T.; Janek, J. There and Back Again-The Journey of LiNiO(2) as a Cathode Active Material. *Angewandte Chemie International Edition* **2019**, *58* (31), 10434-10458.

(35) Dutta, G.; Manthiram, A.; Goodenough, J.; Grenier, J.-C. Chemical synthesis and properties of $Li_{1-\delta-x}Ni_{1+\delta}O_2$ and Li $[Ni_2]$ O_4. *Journal of Solid State Chemistry* **1992**, *96* (1), 123-131.

(36) Kalyani, P.; Kalaiselvi, N. Various aspects of $LiNiO_2$ chemistry: A review. *Science and technology of advanced materials* **2005**, *6* (6), 689.

(37) Nakai, I.; Takahashi, K.; Shiraishi, Y.; Nakagome, T.; Izumi, F.; Ishii, Y.; Nishikawa, F.; Konishi, T. X-ray absorption fine structure and neutron diffraction analyses of de-intercalation

behavior in the $LiCoO_2$ and $LiNiO_2$ systems. *Journal of power sources* **1997**, *68* (2), 536-539.
(38) Li, W.; Reimers, J.; Dahn, J. In situ x-ray diffraction and electrochemical studies of $Li_{1-x}NiO_2$. *Solid State Ionics* **1993**, *67* (1-2), 123-130.
(39) Shao-Horn, Y.; Hackney, S.; Armstrong, A.; Bruce, P. G.; Gitzendanner, R.; Johnson, C.; Thackeray, M. Structural characterization of layered $LiMnO_2$ electrodes by electron diffraction and lattice imaging. *Journal of the Electrochemical Society* **1999**, *146* (7), 2404.
(40) Reed, J.; Ceder, G.; Van Der Ven, A. Layered-to-spinel phase transition in Li_xMnO_2. *Electrochemical and Solid-State Letters* **2001**, *4* (6), A78.
(41) Liu, Z.; Yu, A.; Lee, J. Y. Synthesis and characterization of $LiNi_{1-x-y}Co_xMn_yO_2$ as the cathode materials of secondary lithium batteries. *Journal of Power Sources* **1999**, *81*, 416-419.
(42) Zeng, X.; Li, M.; Abd El-Hady, D.; Alshitari, W.; Al-Bogami, A. S.; Lu, J.; Amine, K. Commercialization of Lithium Battery Technologies for Electric Vehicles. *Advanced Energy Materials* **2019**, *9* (27), 1900161.
(43) Zeng, X.; Zhan, C.; Lu, J.; Amine, K. Stabilization of a High-Capacity and High-Power Nickel-Based Cathode for Li-Ion Batteries. *Chem* **2018**, *4* (4), 690-704.
(44) Purwanto, A.; Yudha, C. S.; Ubaidillah, U.; Widiyandari, H.; Ogi, T.; Haerudin, H. NCA cathode material: synthesis methods and performance enhancement efforts. *Materials Research Express* **2018**, *5* (12), 122001.
(45) Xu, J.; Cai, X.; Cai, S.; Shao, Y.; Hu, C.; Lu, S.; Ding, S. High-Energy Lithium-Ion Batteries: Recent Progress and a Promising Future in Applications. *Energy & Environmental Materials* **2023**, *6* (5), e12450.
(46) Mukherjee, P.; Faenza, N. V.; Pereira, N.; Ciston, J.; Piper, L. F. J.; Amatucci, G. G.; Cosandey, F. Surface Structural and Chemical Evolution of Layered $LiNi_{0.8}Co_{0.15}Al_{0.05}O_2$ (NCA) under High Voltage and Elevated Temperature Conditions. *Chemistry of Materials* **2018**, *30* (23), 8431-8445.
(47) Nitta, N.; Wu, F.; Lee, J. T.; Yushin, G. Li-ion battery materials: present and future. *Materials Today* **2015**, *18* (5), 252-264.
(48) Wu, Z.; Zeng, G.; Yin, J.; Chiang, C.-L.; Zhang, Q.; Zhang, B.; Chen, J.; Yan, Y.; Tang, Y.; Zhang, H.; et al. Unveiling the Evolution of $LiCoO_2$ beyond 4.6 V. *ACS Energy Letters* **2023**, *8* (11), 4806-4817.
(49) Bhandari, A.; Bhattacharya, J. Manganese Dissolution from Spinel Cathode: Few Unanswered Questions. *Journal of The Electrochemical Society* **2016**, *164* (2), A106-A127.
(50) *Global EV Outlook 2024*. IEA, 2024. https://www.iea.org/reports/global-ev-outlook-2024 (accessed.

(51) *Global EV Outlook 2025*. IEA, 2025. https://www.iea.org/reports/global-ev-outlook-2025 (accessed.

(52) Park, G.-T.; Ryu, J.-H.; Kim, J.-H.; Sun, H. H.; Suh, D. E.; Han, S.-M.; Park, N.-Y.; Sun, Y.-K. Aluminum-distribution-dependent microstructural evolution of NCA cathodes: Is aluminum homogeneity really favorable? *Energy Storage Materials* **2024**, *70*, 103496.

(53) Li, W.; Liu, X.; Xie, Q.; You, Y.; Chi, M.; Manthiram, A. Long-Term Cyclability of NCM-811 at High Voltages in Lithium-Ion Batteries: an In-Depth Diagnostic Study. *Chemistry of Materials* **2020**, *32* (18), 7796-7804.

(54) Ma, X.; Hou, J.; Vanaphuti, P.; Yao, Z.; Fu, J.; Azhari, L.; Liu, Y.; Wang, Y. Direct upcycling of mixed Ni-lean polycrystals to single-crystal Ni-rich cathode materials. *Chem* **2022**, *8* (7), 1944-1955.

(55) Nisbet, M. L.; Luong, D.; Allen, E.; Park, S.; Kinnibrugh, T. L.; Stubbs, J. E.; Eng, P. J.; Vaughey, J. T.; Fister, T. T. In Situ Diffraction and Ex Situ Transmission X-Ray Microscopy Studies of Solid-State Upcycling for NMC Cathodes. *Advanced Energy Materials* **2025**, 2500698.

(56) Qian, G.; Li, Z.; Wang, Y.; Xie, X.; He, Y.; Li, J.; Zhu, Y.; Xie, S.; Cheng, Z.; Che, H.; et al. Value-creating upcycling of retired electric vehicle battery cathodes. *Cell Reports Physical Science* **2022**, *3* (2), 100741.

(57) Jiang, M.; Danilov, D. L.; Eichel, R. A.; Notten, P. H. L. A Review of Degradation Mechanisms and Recent Achievements for Ni-Rich Cathode-Based Li-Ion Batteries. *Advanced Energy Materials* **2021**, *11* (48), 2103005.

(58) de Biasi, L.; Schwarz, B.; Brezesinski, T.; Hartmann, P.; Janek, J.; Ehrenberg, H. Chemical, Structural, and Electronic Aspects of Formation and Degradation Behavior on Different Length Scales of Ni-Rich NCM and Li-Rich HE-NCM Cathode Materials in Li-Ion Batteries. *Advanced Materials* **2019**, *31* (26), e1900985.

(59) Lee, S.; Jin, W.; Kim, S. H.; Joo, S. H.; Nam, G.; Oh, P.; Kim, Y. K.; Kwak, S. K.; Cho, J. Oxygen Vacancy Diffusion and Condensation in Lithium-Ion Battery Cathode Materials. *Angewandte Chemie International Edition* **2019**, *58* (31), 10478-10485.

(60) Yan, P.; Zheng, J.; Chen, T.; Luo, L.; Jiang, Y.; Wang, K.; Sui, M.; Zhang, J. G.; Zhang, S.; Wang, C. Coupling of electrochemically triggered thermal and mechanical effects to aggravate failure in a layered cathode. *Nature Communnications* **2018**, *9* (1), 2437.

(61) Yan, P.; Zheng, J.; Gu, M.; Xiao, J.; Zhang, J. G.; Wang, C. M. Intragranular cracking as a critical barrier for high-voltage usage of layer-structured cathode for lithium-ion batteries. *Nature Communications* **2017**, *8* (1), 14101. From NLM PubMed-not-MEDLINE.

(62) Lin, Q.; Guan, W.; Zhou, J.; Meng, J.; Huang, W.; Chen, T.; Gao, Q.; Wei, X.; Zeng, Y.; Li, J.; et al. Ni–Li anti-site defect induced intragranular cracking in Ni-rich layer-structured cathode. *Nano Energy* **2020**, *76*, 105021.

(63) Lim, J. M.; Hwang, T.; Kim, D.; Park, M. S.; Cho, K.; Cho, M. Intrinsic Origins of Crack Generation in Ni-rich LiNi(0.8)Co(0.1)Mn(0.1)O(2) Layered Oxide Cathode Material. *Scientific reports* **2017**, *7*, 39669.

(64) Mu, L.; Lin, R.; Xu, R.; Han, L.; Xia, S.; Sokaras, D.; Steiner, J. D.; Weng, T. C.; Nordlund, D.; Doeff, M. M.; et al. Oxygen Release Induced Chemomechanical Breakdown of Layered Cathode Materials. *Nano letters* **2018**, *18* (5), 3241-3249.

(65) Zhang, H.; Omenya, F.; Yan, P.; Luo, L.; Whittingham, M. S.; Wang, C.; Zhou, G. Rock-Salt Growth-Induced (003) Cracking in a Layered Positive Electrode for Li-Ion Batteries. *ACS Energy Letters* **2017**, *2* (11), 2607-2615.

(66) Lin, F.; Markus, I. M.; Nordlund, D.; Weng, T. C.; Asta, M. D.; Xin, H. L.; Doeff, M. M. Surface reconstruction and chemical evolution of stoichiometric layered cathode materials for lithium-ion batteries. *Nature Communications* **2014**, *5* (1), 3529.

(67) Zhang, H.; Liu, H.; Piper, L. F. J.; Whittingham, M. S.; Zhou, G. Oxygen Loss in Layered Oxide Cathodes for Li-Ion Batteries: Mechanisms, Effects, and Mitigation. *Chem Rev* **2022**, *122* (6), 5641-5681.

(68) Nam, K. W.; Bak, S. M.; Hu, E.; Yu, X.; Zhou, Y.; Wang, X.; Wu, L.; Zhu, Y.; Chung, K. Y.; Yang, X. Q. Combining In Situ Synchrotron X-Ray Diffraction and Absorption Techniques with Transmission Electron Microscopy to Study the Origin of Thermal Instability in Overcharged Cathode Materials for Lithium-Ion Batteries. *Advanced Functional Materials* **2012**, *23* (8), 1047-1063.

(69) Konishi, H.; Yoshikawa, M.; Hirano, T.; Hidaka, K. Evaluation of thermal stability in $Li_{0.2}Ni_xMn_{(1-x)/2}Co_{(1-x)/2}O_2$ (x = 1/3, 0.6, and 0.8) through X-ray absorption fine structure. *Journal of Power Sources* **2014**, *254*, 338-344.

(70) Wang, L.; Maxisch, T.; Ceder, G. A first-principles approach to studying the thermal stability of oxide cathode materials. *Chemistry of materials* **2007**, *19* (3), 543-552.

(71) Sharifi-Asl, S.; Lu, J.; Amine, K.; Shahbazian-Yassar, R. Oxygen Release Degradation in Li-Ion Battery Cathode Materials: Mechanisms and Mitigating Approaches. *Advanced Energy Materials* **2019**, *9* (22), 1900551.

(72) Reed, J.; Ceder, G. Role of electronic structure in the susceptibility of metastable transition-metal oxide structures to transformation. *Chemical reviews* **2004**, *104* (10), 4513-4534.

(73) Xu, P.; Tan, D. H. S.; Jiao, B.; Gao, H.; Yu, X.; Chen, Z. A Materials Perspective on Direct Recycling of Lithium-Ion Batteries: Principles, Challenges and Opportunities. *Advanced Functional Materials* **2023**, *33* (14), 2213168.
(74) Harper, G.; Sommerville, R.; Kendrick, E.; Driscoll, L.; Slater, P.; Stolkin, R.; Walton, A.; Christensen, P.; Heidrich, O.; Lambert, S.; et al. Recycling lithium-ion batteries from electric vehicles. *Nature* **2019**, *575* (7781), 75-86.
(75) Spiewak, M.; Piątek, J.; Rodrigues, B. V. M.; Slabon, A. Sustainable recycling of lithium-ion batteries: Pipe dream or realistic solution. *Cell Reports Sustainability* **2025**, *2* (7), 100429.
(76) Chen, M.; Ma, X.; Chen, B.; Arsenault, R.; Karlson, P.; Simon, N.; Wang, Y. Recycling End-of-Life Electric Vehicle Lithium-Ion Batteries. *Joule* **2019**, *3* (11), 2622-2646.
(77) Yao, Y.; Zhu, M.; Zhao, Z.; Tong, B.; Fan, Y.; Hua, Z. Hydrometallurgical Processes for Recycling Spent Lithium-Ion Batteries: A Critical Review. *ACS Sustainable Chemistry & Engineering* **2018**, *6* (11), 13611-13627.
(78) Lin, X.; Wang, X.; Liu, G.; Zhang, G. *Recycling of Power Lithium-Ion Batteries: Technology, Equipment, and Policies*; John Wiley & Sons, 2022.
(79) He, B.; Zheng, H.; Tang, K.; Xi, P.; Li, M.; Wei, L.; Guan, Q. A Comprehensive Review of Lithium-Ion Battery (LiB) Recycling Technologies and Industrial Market Trend Insights. *Recycling* **2024**, *9* (1), 9.
(80) Fang, Z.; Wu, Z.; Zeng, W.; Bontempi, E.; Duan, Q.; Sun, J.; Wang, Q. Exploring the viability of cryogenic freezing for safe pretreatment in lithium-ion battery recycling. *Renewable Energy* **2025**, *252*, 123481.
(81) Ni, Y.; Nie, C.-c.; Shi, S.-x.; Zhu, X.-n. Effect of mechanical force on dissociation characteristics of cathode materials in spent lithium-ion batteries. *Process Safety and Environmental Protection* **2022**, *161*, 374-383.
(82) Diekmann, J.; Hanisch, C.; Froböse, L.; Schälicke, G.; Loellhoeffel, T.; Fölster, A.-S.; Kwade, A. Ecological Recycling of Lithium-Ion Batteries from Electric Vehicles with Focus on Mechanical Processes. *Journal of The Electrochemical Society* **2016**, *164* (1), A6184-A6191.
(83) Xiao, J.; Li, J.; Xu, Z. Challenges to Future Development of Spent Lithium Ion Batteries Recovery from Environmental and Technological Perspectives. *Environ Sci Technol* **2020**, *54* (1), 9-25.
(84) Hagelüken, C. Recycling of electronic scrap at Umicore precious metals refining. *Acta Metallurgica Slovaca* **2006**, *12* (2006), 111-120.
(85) Harvey, J. P.; Courchesne, W.; Vo, M. D.; Oishi, K.; Robelin, C.; Mahue, U.; Leclerc, P.;

Al-Haiek, A. Greener reactants, renewable energies and environmental impact mitigation strategies in pyrometallurgical processes: A review. *MRS Energy Sustain* **2022**, *9* (2), 212-247.
(86) Pinegar, H.; Smith, Y. R. Recycling of End-of-Life Lithium Ion Batteries, Part I: Commercial Processes. *Journal of Sustainable Metallurgy* **2019**, *5* (3), 402-416.
(87) Magdalena, R.; Valero, A.; Calvo, G. Limit of recovery: How future evolution of ore grades could influence energy consumption and prices for Nickel, Cobalt, and PGMs. *Minerals Engineering* **2023**, *200*, 108150.
(88) Röntgen, W. C. Uber eine neue Art von Strahlen. *Sitzung Physikal-Medicin Gesellschaft* **1895**, *137*, 132-141.
(89) Friedrich, W.; Knipping, P.; Laue, M. Interferenzerscheinungen bei roentgenstrahlen. *Annalen der Physik* **1913**, *346* (10), 971-988.
(90) Spieß, L.; Behnken, H.; Genzel, C.; Schwarzer, R.; Teichert, G. *Moderne röntgenbeugung*; Springer, 2009.
(91) Noyan, I. C.; Cohen, J. B. *Residual stress: measurement by diffraction and interpretation*; Springer, 2013.
(92) Epp, J. X-ray diffraction (XRD) techniques for materials characterization. In *Materials Characterization Using Nondestructive Evaluation (NDE) Methods*, 2016; pp 81-124.
(93) Fitzpatrick, M. E.; Lodini, A. *Analysis of residual stress by diffraction using neutron and synchrotron radiation*; CRC Press, 2003.
(94) Hauk, V. *Structural and residual stress analysis by nondestructive methods: Evaluation-Application-Assessment*; 1997.
(95) Hölzer, G.; Fritsch, M.; Deutsch, M.; Härtwig, J.; Förster, E. $K_{\alpha 1,\,2}$ and $K_{\beta 1,\,3}$ X-ray emission lines of the 3d transition metals. *Physical Review A* **1997**, *56* (6), 4554.
(96) Bragg, W. L. The diffraction of short electromagnetic waves by a crystal. *Scientia* **1929**, *23* (45).
(97) Will, G. *Powder diffraction: The Rietveld method and the two stage method to determine and refine crystal structures from powder diffraction data*; Springer Science & Business Media, 2006.
(98) Guinebretière, R. *Diffraction des rayons X sur échantillons polycristallins*; Hermès, 2002.
(99) Yano, J.; Yachandra, V. K. X-ray absorption spectroscopy. *Photosynthesis research* **2009**, *102*, 241-254.
(100) Shulman, G.; Yafet, Y.; Eisenberger, P.; Blumberg, W. Observations and interpretation of x-ray absorption edges in iron compounds and proteins. *Proceedings of the National Academy of Sciences* **1976**, *73* (5), 1384-1388.

(101) Iglesias-Juez, A.; Chiarello, G. L.; Patience, G. S.; Guerrero-Pérez, M. O. Experimental methods in chemical engineering: X-ray absorption spectroscopy—XAS, XANES, EXAFS. *The Canadian Journal of Chemical Engineering* **2021**, *100* (1), 3-22.
(102) Ketenoglu, D. A general overview and comparative interpretation on element-specific X-ray spectroscopy techniques: XPS, XAS,and XRS. *X-Ray Spectrometry* **2022**, *51* (5-6), 422-443.
(103) Aziz, M.; Ismail, A. X-ray photoelectron spectroscopy (XPS). In *Membrane Characterization*, Elsevier, 2017; pp 81-93.
(104) Krishna, D. N. G.; Philip, J. Review on surface-characterization applications of X-ray photoelectron spectroscopy (XPS): Recent developments and challenges. *Applied Surface Science Advances* **2022**, *12*, 100332.
(105) Sommerville, R.; Shaw-Stewart, J.; Goodship, V.; Rowson, N.; Kendrick, E. A review of physical processes used in the safe recycling of lithium ion batteries. *Sustainable Materials and Technologies* **2020**, *25*, e00197.
(106) He, L. P.; Sun, S. Y.; Song, X. F.; Yu, J. G. Recovery of cathode materials and Al from spent lithium-ion batteries by ultrasonic cleaning. *Waste management* **2015**, *46*, 523-528.
(107) Zhou, X.; He, W. z.; Li, G. m.; Zhang, X. j.; Huang, J. w.; Zhu, S. g. Recycling of Electrode Materials from Spent Lithium-Ion Batteries. In *2010 4th International Conference on Bioinformatics and Biomedical Engineering*, 18-20 June 2010, 2010; IEEE: pp 1-4.
(108) Song, X.; Hu, T.; Liang, C.; Long, H. L.; Zhou, L.; Song, W.; You, L.; Wu, Z. S.; Liu, J. W. Direct regeneration of cathode materials from spent lithium iron phosphate batteries using a solid phase sintering method. *RSC Advances* **2017**, *7* (8), 4783-4790.
(109) Tokoro, C.; Kurihara, T.; Narita, A.; Koita, T. Localized degradation influences the separation of cathode active materials from aluminum foil by direct electrical pulsed discharge. *Journal of Material Cycles and Waste Management* **2025**, *27*, 2723–2735.
(110) Chen, Y.; Liu, N.; Jie, Y.; Hu, F.; Li, Y.; Wilson, B. P.; Xi, Y.; Lai, Y.; Yang, S. Toxicity Identification and Evolution Mechanism of Thermolysis-Driven Gas Emissions from Cathodes of Spent Lithium-Ion Batteries. *ACS Sustainable Chemistry & Engineering* **2019**, *7* (22), 18228-18235.
(111) Yang, Y.; Huang, G.; Xu, S.; He, Y.; Liu, X. Thermal treatment process for the recovery of valuable metals from spent lithium-ion batteries. *Hydrometallurgy* **2016**, *165*, 390-396.
(112) Smith, A.; Stüble, P.; Leuthner, L.; Hofmann, A.; Jeschull, F.; Mereacre, L. Potential and Limitations of Research Battery Cell Types for Electrochemical Data Acquisition. *Batteries & Supercaps* **2023**, *6* (6), e20230008.

(113) Rodríquez-Carvajal, J.; Roisnel, T. Line broadening analysis using FullProf*: determination of microstructural properties. In *Materials Science Forum*, 2004; Trans Tech Publ: Vol. 443, pp 123-126.

(114) Li, X.; Huang, C.; Yang, H.; Li, Y.; Cheng, Y. Thermal reaction properties of aluminum/copper (II) oxide/poly(vinylidene fluoride) nanocomposite. *Journal of Thermal Analysis and Calorimetry* **2015**, *124* (2), 899-907.

(115) Rehwoldt, M. C.; Wang, Y.; Xu, F.; Ghildiyal, P.; Zachariah, M. R. High-Temperature Interactions of Metal Oxides and a PVDF Binder. *ACS Applied Materials & Interfaces* **2022**, *14* (7), 8938-8946.

(116) Liu, S.; Yang, J.; Hao, S.; Jiang, S.; Li, X.; Dolotko, O.; Wu, F.; Li, Y.; He, Z. J. C. E. J. Paving the way for electrochemical recycling of spent lithium-ion batteries: Targeting the direct regeneration of de-lithiated materials. *chemical Engineering Journal* **2024**, *479*, 147607.

(117) DeLisio, J. B.; Hu, X.; Wu, T.; Egan, G. C.; Young, G.; Zachariah, M. R. Probing the Reaction Mechanism of Aluminum/Poly(vinylidene fluoride) Composites. *The Journal of Physical Chemistry B* **2016**, *120* (24), 5534-5542.

(118) Leanza, D.; Vaz, C. A. F.; Novák, P.; El Kazzi, M. Instability of PVDF Binder in the $LiFePO_4$ versus $Li_4Ti_5O_{12}$ Li-Ion Battery Cell. *Helvetica Chimica Acta* **2020**, *104* (1), e2000183.

(119) Papp, J. K.; Forster, J. D.; Burke, C. M.; Kim, H. W.; Luntz, A. C.; Shelby, R. M.; Urban, J. J.; McCloskey, B. D. Poly(vinylidene fluoride) (PVDF) Binder Degradation in Li-O(2) Batteries: A Consideration for the Characterization of Lithium Superoxide. *J Phys Chem Lett* **2017**, *8* (6), 1169-1174.

(120) Saxena, P.; Shukla, P. A comprehensive review on fundamental properties and applications of poly(vinylidene fluoride) (PVDF). *Advanced Composites and Hybrid Materials* **2021**, *4* (1), 8-26.

(121) Lovinger, A.; Reed, D. Inhomogeneous Thermal Degradation of Poly(vinylidene fluoride) Crystallized from the Melt. *Macromolecules* **1980**, *13* (4), 989-994.

(122) Sungjemmenla; S. K, V.; Soni, C. B.; Kumar, V.; Seh, Z. W. Understanding the Cathode–Electrolyte Interphase in Lithium-Ion Batteries. *Energy Technology* **2022**, *10* (9), 2200421.

(123) El-Sakhawy, M.; Tohamy, H.-A. S.; Salama, A.; Kamel, S. Thermal properties of carboxymethyl cellulose acetate butyrate. *Cellulose Chemistry and Technology* **2019**, *53* (7-8), 667-675.

(124) Zhang, Y.; Liu, Q.; Xiang, J.; Frost, R. L. Thermal stability and decomposition kinetics of styrene-butadiene rubber nanocomposites filled with different particle sized kaolinites.

Applied Clay Science **2014**, *95*, 159-166.

(125) An, S. J.; Li, J.; Daniel, C.; Mohanty, D.; Nagpure, S.; Wood, D. L. The state of understanding of the lithium-ion-battery graphite solid electrolyte interphase (SEI) and its relationship to formation cycling. *Carbon* **2016**, *105*, 52-76.

(126) Qin, Z.; Li, J.; Zhang, T.; Wen, Z.; Zheng, Z.; Zhang, Y.; Zhang, N.; Jia, C.; Liu, X.; Chen, G. Effective separation of $LiNi_{0.5}Co_{0.2}Mn_{0.3}O_2$ cathode material and Al foil via digestion of PVDF enabling a closed-loop recycle. *Journal of Materials Chemistry A* **2022**, *10* (44), 23905-23914.

(127) Wang, M.; Liu, K.; Yu, J.; Zhang, Q.; Zhang, Y.; Valix, M.; Tsang, D. C. W. Challenges in Recycling Spent Lithium-Ion Batteries: Spotlight on Polyvinylidene Fluoride Removal. *Glob Chall* **2023**, *7* (3), 2200237.

(128) Wang, H.; Liu, C.; Qu, G.; Zhou, S.; Li, B.; Wei, Y. Study on Pyrolysis Pretreatment Characteristics of Spent Lithium-Ion Batteries. *Separations* **2023**, *10* (4). DOI: 10.3390/separations10040259.

(129) Wang, S.; Hua, W.; Missyul, A.; Darma, M. S. D.; Tayal, A.; Indris, S.; Ehrenberg, H.; Liu, L.; Knapp, M. Kinetic Control of Long-Range Cationic Ordering in the Synthesis of Layered Ni-Rich Oxides. *Advanced Functional Materials* **2021**, *31* (19), 2009949.

(130) Zhang, G.; Yuan, X.; He, Y.; Wang, H.; Xie, W.; Zhang, T. Organics removal combined with in situ thermal-reduction for enhancing the liberation and metallurgy efficiency of LiCoO(2) derived from spent lithium-ion batteries. *Waste Management* **2020**, *115*, 113-120.

(131) Zhang, G.; Yuan, X.; Tay, C. Y.; He, Y.; Wang, H.; Duan, C. Selective recycling of lithium from spent lithium-ion batteries by carbothermal reduction combined with multistage leaching. *Separation and Purification Technology* **2023**, *314*, 123555.

(132) Zhao, J.; Zhang, W.; Huq, A.; Misture, S. T.; Zhang, B.; Guo, S.; Wu, L.; Zhu, Y.; Chen, Z.; Amine, K.; et al. In Situ Probing and Synthetic Control of Cationic Ordering in Ni-Rich Layered Oxide Cathodes. *Advanced Energy Materials* **2016**, *7* (3), 1601266.

(133) Bai, J.; Sun, W.; Zhao, J.; Wang, D.; Xiao, P.; Ko, J. Y. P.; Huq, A.; Ceder, G.; Wang, F. Kinetic Pathways Templated by Low-Temperature Intermediates during Solid-State Synthesis of Layered Oxides. *Chemistry of Materials* **2020**, *32* (23), 9906-9913.

(134) Shi, Y.; Chen, G.; Liu, F.; Yue, X.; Chen, Z. Resolving the Compositional and Structural Defects of Degraded $LiNi_xCo_yMn_zO_2$ Particles to Directly Regenerate High-Performance Lithium-Ion Battery Cathodes. *ACS Energy Letters* **2018**, *3* (7), 1683-1692.

(135) Gao, H.; Yan, Q.; Tran, D.; Yu, X.; Liu, H.; Li, M.; Li, W.; Wu, J.; Tang, W.; Gupta, V.; et al. Upcycling of Spent $LiNi_{0.33}Co_{0.33}Mn_{0.33}O_2$ to Single-Crystal Ni-Rich Cathodes Using

Lean Precursors. *ACS Energy Letters* **2023**, *8* (10), 4136-4144.
(136) Mancini, M.; Hoffmann, M. F.; Martin, J.; Weirather-Köstner, D.; Axmann, P.; Wohlfahrt-Mehrens, M. A proof-of-concept of direct recycling of anode and cathode active materials: From spent batteries to performance in new Li-ion cells. *Journal of Power Sources* **2024**, *595*, 233997.
(137) Gupta, V.; Yu, X.; Gao, H.; Brooks, C.; Li, W.; Chen, Z. Scalable Direct Recycling of Cathode Black Mass from Spent Lithium-Ion Batteries. *Advanced Energy Materials* **2022**, *13* (6), 2203093.
(138) Gnutzmann, M. M.; Makvandi, A.; Ying, B.; Buchmann, J.; Lüther, M. J.; Helm, B.; Nagel, P.; Peterlechner, M.; Wilde, G.; Gomez-Martin, A.; et al. Direct Recycling at the Material Level: Unravelling Challenges and Opportunities through a Case Study on Spent Ni-Rich Layered Oxide-Based Cathodes. *Advanced Energy Materials* **2024**, *14* (36), 2400840.
(139) Rodríguez-Carvajal, J. FullProf. *CEA/Saclay, France* **2001**, *1045*, 132-146.
(140) Ravel, B.; Newville, M. ATHENA, ARTEMIS, HEPHAESTUS: data analysis for X-ray absorption spectroscopy using IFEFFIT. *Journal of synchrotron radiation* **2005**, *12* (4), 537-541.
(141) Li, H.; Hua, W.; Liu-Théato, X.; Fu, Q.; Desmau, M.; Missyul, A.; Knapp, M.; Ehrenberg, H.; Indris, S. New Insights into Lithium Hopping and Ordering in $LiNiO_2$ Cathodes during Li (De)intercalation. *Chemistry of Materials* **2021**, *33* (24), 9546-9559.
(142) Bielecki, A.; Burum, D. P. Temperature dependence of ^{207}Pb MAS spectra of solid lead nitrate. an accurate, sensitive thermometer for variable-temperature MAS. *Journal of Magnetic Resonance, Series A* **1995**, *116* (2), 215-220.
(143) Heenan, T. M. M.; Wade, A.; Tan, C.; Parker, J. E.; Matras, D.; Leach, A. S.; Robinson, J. B.; Llewellyn, A.; Dimitrijevic, A.; Jervis, R.; et al. Identifying the Origins of Microstructural Defects Such as Cracking within Ni-Rich NMC811 Cathode Particles for Lithium-Ion Batteries. *Advanced Energy Materials* **2020**, *10* (47), 2002655.
(144) Yan, P.; Zheng, J.; Gu, M.; Xiao, J.; Zhang, J.-G.; Wang, C.-M. Intragranular cracking as a critical barrier for high-voltage usage of layer-structured cathode for lithium-ion batteries. *Nature Communications* **2017**, *8* (1), 14101.
(145) Liu, T.; Yu, L.; Liu, J.; Dai, A.; Zhou, T.; Wang, J.; Huang, W.; Li, L.; Li, M.; Li, T.; et al. Ultrastable cathodes enabled by compositional and structural dual-gradient design. *Nature Energy* **2024**, *9* (10), 1252-1263.
(146) Shah, N. A.; Páez Fajardo, G. J.; Banerjee, H.; Pandey, G. C.; Menon, A. S.; Ans, M.; Majherova, V.; Bree, G.; Bolloju, S.; Grinter, D. C.; et al. Nature of the Oxygen-Loss-Induced

Rocksalt Layer and Its Impact on Capacity Fade in Ni-Rich Layered Oxide Cathodes. *ACS Energy Letters* **2025**, *10* (3), 1313-1320.

(147) Zhang, S.; Yang, Z.; Lu, Y.; Xie, W.; Yan, Z.; Chen, J. Insights into Cation Migration and Intermixing in Advanced Cathode Materials for Lithium-Ion Batteries. *Advanced Energy Materials* **2024**, *14* (36), 2402068.

(148) Genreith-Schriever, A. R.; Coates, C. S.; Marker, K.; Seymour, I. D.; Bassey, E. N.; Grey, C. P. Probing Jahn-Teller Distortions and Antisite Defects in LiNiO(2) with (7)Li NMR Spectroscopy and Density Functional Theory. *Chemistry of Materials* **2024**, *36* (9), 4226-4239.

(149) Shen, J.; Zhou, M.; Tang, W.; Huang, Q.; Pi, H.; Liu, W.; Liu, R.; Li, L. Surface reconstruction strategy enables rapid upcycling highly degraded layered cathode. *Nano Energy* **2025**, *136*, 110741.

(150) Ren, X.; Wang, J.; Lin, Y.; Wang, Y.; Xie, H.; Huang, H.; Yang, B.; Yan, Y.; Gao, Y.; He, J.; et al. Mobile iodides capture for highly photolysis- and reverse-bias-stable perovskite solar cells. *Nature materials* **2024**, *23* (6), 810-817.

(151) Tallman, K. R.; Wheeler, G. P.; Kern, C. J.; Stavitski, E.; Tong, X.; Takeuchi, K. J.; Marschilok, A. C.; Bock, D. C.; Takeuchi, E. S. Nickel-rich Nickel Manganese Cobalt (NMC622) Cathode Lithiation Mechanism and Extended Cycling Effects Using Operando X-ray Absorption Spectroscopy. *The Journal of Physical Chemistry C* **2020**, *125* (1), 58-73.

(152) Tsai, Y.; Hwang, B.; Ceder, G.; Sheu, H.; Liu, D.; Lee, J. In-situ X-ray absorption spectroscopic study on variation of electronic transitions and local structure of $LiNi_{1/3}Co_{1/3}Mn_{1/3}O_2$ cathode material during electrochemical cycling. *Chemistry of materials* **2005**, *17* (12), 3191-3199.

(153) Pickering, I. J.; George, G. N.; Lewandowski, J. T.; Jacobson, A. J. Nickel K-edge X-ray absorption fine structure of lithium nickel oxides. *Journal of the American chemical society* **1993**, *115* (10), 4137-4144.

(154) Li, Y.; Bettge, M.; Polzin, B.; Zhu, Y.; Balasubramanian, M.; Abraham, D. P. Understanding Long-Term Cycling Performance of $Li_{1.2}Ni_{0.15}Mn_{0.55}Co_{0.1}O_2$–Graphite Lithium-Ion Cells. *Journal of The Electrochemical Society* **2013**, *160* (5), A3006-A3019.

(155) Croy, J. R.; Balasubramanian, M.; Kim, D.; Kang, S.-H.; Thackeray, M. M. Designing High-Capacity, Lithium-Ion Cathodes Using X-ray Absorption Spectroscopy. *Chemistry of Materials* **2011**, *23* (24), 5415-5424.

(156) Xing, C.; Gan, M.; Ying, Y.; Zhang, B.; Liu, L.; Ye, J.; Liu, Y.; Zhang, Y.; Huang, H.; Fei, L. Multiscale observations on mechanisms for direct regeneration of degraded NCM cathode materials. *Energy Storage Materials* **2024**, *65*, 103182.

(157) Wang, J.; Ma, J.; Jia, K.; Liang, Z.; Ji, G.; Zhao, Y.; Li, B.; Zhou, G.; Cheng, H.-M. Efficient Extraction of Lithium from Anode for Direct Regeneration of Cathode Materials of Spent Li-Ion Batteries. *ACS Energy Letters* **2022**, *7* (8), 2816-2824.

(158) Wang, J.; Ji, H.; Li, J.; Liang, Z.; Chen, W.; Zhu, Y.; Ji, G.; Shi, R.; Zhou, G.; Cheng, H.-M. Direct recycling of spent cathode material at ambient conditions via spontaneous lithiation. *Nature Sustainability* **2024**, *7* (10), 1283-1293.

(159) Wang, J.; Jia, K.; Ma, J.; Liang, Z.; Zhuang, Z.; Zhao, Y.; Li, B.; Zhou, G.; Cheng, H.-M. Sustainable upcycling of spent $LiCoO_2$ to an ultra-stable battery cathode at high voltage. *Nature Sustainability* **2023**, *6* (7), 797-805.

(160) Yabuuchi, N.; Kim, Y.-T.; Li, H. H.; Shao-Horn, Y. Thermal instability of cycled $Li_xNi_{0.5}Mn_{0.5}O_2$ electrodes: an in situ synchrotron X-ray powder diffraction study. *Chemistry of Materials* **2008**, *20* (15), 4936-4951.

(161) Goonetilleke, D.; Sharma, N.; Pang, W. K.; Peterson, V. K.; Petibon, R.; Li, J.; Dahn, J. R. Structural Evolution and High-Voltage Structural Stability of $Li(Ni_xMn_yCo_z)O_2$ Electrodes. *Chemistry of Materials* **2018**, *31* (2), 376-386.

(162) Wang, Y. Y.; Gao, M. Y.; Liu, S.; Li, G. R.; Gao, X. P. Yttrium Surface Gradient Doping for Enhancing Structure and Thermal Stability of High-Ni Layered Oxide as Cathode for Li-Ion Batteries. *ACS Applied Materials & Interfaces* **2021**, *13* (6), 7343-7354.

(163) Zeng, D.; Cabana, J.; Bréger, J.; Yoon, W.-S.; Grey, C. P. Cation Ordering in Li $[Ni_xMn_xCo_{(1-2x)}]O_2$-Layered Cathode Materials: A Nuclear Magnetic Resonance (NMR), Pair Distribution Function, X-ray Absorption Spectroscopy, and Electrochemical Study. *Chemistry of Materials* **2007**, *19* (25), 6277-6289.

(164) Pan, C.; Lee, Y. J.; Ammundsen, B.; Grey, C. P. ^{6}Li MAS NMR studies of the local structure and electrochemical properties of Cr-doped lithium manganese and lithium cobalt oxide cathode materials for lithium-ion batteries. *Chemistry of materials* **2002**, *14* (5), 2289-2299.

(165) Qi, H. P.; Taylor, P.; Berglund, M.; De Bièvre, P. Calibrated measurements of the isotopic composition and atomic weight of the natural Li isotopic reference material IRMM-016. *International journal of mass spectrometry and ion processes* **1997**, *171* (1-3), 263-268.

(166) Hua, W.; Wang, K.; Knapp, M.; Schwarz, B.; Wang, S.; Liu, H.; Lai, J.; Müller, M.; Schökel, A.; Missyul, A.; et al. Chemical and Structural Evolution during the Synthesis of Layered $Li(Ni,Co,Mn)O_2$ Oxides. *Chemistry of Materials* **2020**, *32* (12), 4984-4997.

(167) Todd, P. K.; Neilson, J. R. Selective formation of yttrium manganese oxides through kinetically competent assisted metathesis reactions. *Journal of the American Chemical Society*

2019, *141* (3), 1191-1195.

(168) Zhang, M. J.; Teng, G.; Chen-Wiegart, Y. K.; Duan, Y.; Ko, J. Y. P.; Zheng, J.; Thieme, J.; Dooryhee, E.; Chen, Z.; Bai, J.; et al. Cationic Ordering Coupled to Reconstruction of Basic Building Units during Synthesis of High-Ni Layered Oxides. *Journal of the American Chemical Society* **2018**, *140* (39), 12484-12492.

(169) Stich, M.; Göttlinger, M.; Kurniawan, M.; Schmidt, U.; Bund, A. Hydrolysis of $LiPF_6$ in Carbonate-Based Electrolytes for Lithium-Ion Batteries and in Aqueous Media. *The Journal of Physical Chemistry C* **2018**, *122* (16), 8836-8842.

(170) Gupta, V.; Potts, C.; Tran, D.; Gao, H.; Li, M.; Lin, J.; Chen, Z. Streamlining Ni-Rich $LiNi_xMn_yCo_zO_2$ Cathode Black Mass Purification for Direct Recycling and Upcycling through the Alkoxythermal Process. *Advanced Energy Materials* **2025**, 2406083.

(171) Wang, M.; Liu, K.; Yu, J.; Zhang, Q.; Zhang, Y.; Valix, M.; Tsang, D. C. W. Challenges in Recycling Spent Lithium-Ion Batteries: Spotlight on Polyvinylidene Fluoride Removal. *Global Challenges* **2023**, *7* (3), 2200237.

(172) Zheng, Y.; Zhang, R.; Vanaphuti, P.; Fu, J.; Yang, Z.; Wang, Y. Unveiling the Influence of Carbon Impurity on Recovered NCM622 Cathode Material. *ACS Sustainable Chemistry & Engineering* **2021**, *9* (17), 6087-6096.

(173) Xing, C.; Da, H.; Yang, P.; Huang, J.; Gan, M.; Zhou, J.; Li, Y.; Zhang, H.; Ge, B.; Fei, L. Aluminum Impurity from Current Collectors Reactivates Degraded NCM Cathode Materials toward Superior Electrochemical Performance. *ACS Nano* **2023**, *17* (3), 3194-3203.

(174) Xiang, Y.; Li, J.; Lei, J.; Liu, D.; Xie, Z.; Qu, D.; Li, K.; Deng, T.; Tang, H. Advanced Separators for Lithium-Ion and Lithium-Sulfur Batteries: A Review of Recent Progress. *ChemSusChem* **2016**, *9* (21), 3023-3039.

(175) Wang, T.; Wang, L.; Yi, C.; Sun, W.; Wu, M.; Yang, Y. Towards beneficial transformation of aluminum impurity for cathode material regeneration from spent lithium-ion batteries: In-situ Al doping for high-performance $LiNi_{0.9}Co_{0.05}Mn_{0.05}O_2$. *Chemical Engineering Journal* **2024**, *492*, 152298.

(176) Zheng, Y.; Zhang, R.; Vanaphuti, P.; Liu, Y.; Yang, Z.; Wang, Y. Positive Role of Fluorine Impurity in Recovered LiNi(0.6)Co(0.2)Mn(0.2)O(2) Cathode Materials. *ACS Applied Materials & Interfaces* **2021**, *13* (48), 57171-57181.

(177) Wu, T.; Wang, G.; Liu, B.; Huang, Q.; Su, Y.; Wu, F.; Kelly, R. M. The role of Cu impurity on the structure and electrochemical performance of Ni-rich cathode material for lithium-ion batteries. *Journal of Power Sources* **2021**, *494*, 229774.

(178) Zhang, R.; Meng, Z.; Ma, X.; Chen, M.; Chen, B.; Zheng, Y.; Yao, Z.; Vanaphuti, P.;

Bong, S.; Yang, Z.; et al. Understanding fundamental effects of Cu impurity in different forms for recovered $LiNi_{0.6}Co_{0.2}Mn_{0.2}O_2$ cathode materials. *Nano Energy* **2020**, *78*, 105214.
(179) Lei, H.; Cui, X.; Zeng, Z.; Zhu, C.; Sun, W.; Yang, Y.; Ge, P. Directly Regenerating of Spent $LiCoO_2$ with Gradient F-Doped Subsurface towards Ultra-Stable Storage Properties. *Angewandte Chemie International Edition* **2025**, *64* (2), e202414918.
(180) Scofield, J. H. Hartree-Slater subshell photoionization cross-sections at 1254 and 1487 eV. *Journal of electron spectroscopy and related phenomena* **1976**, *8* (2), 129-137.
(181) Liu, S.; Liu, H.; Bokov, A.; Jaleh, M.; Li, H.; Indris, S.; Dolotko, O.; Kalinko, A.; Villalobos-Postillo, E. E.; Marini, C.; et al. Insights into the Mechanisms Behind Structural Repair of Spent Layered Cathode Materials for Lithium-Ion Batteries. *Angewandte Chemie International Edition* **2025**, *137* (32), e202504382.
(182) Spotte-Smith, E. W. C.; Petrocelli, T. B.; Patel, H. D.; Blau, S. M.; Persson, K. A. Elementary Decomposition Mechanisms of Lithium Hexafluorophosphate in Battery Electrolytes and Interphases. *ACS Energy Letters* **2022**, *8* (1), 347-355.
(183) Rotole, J. A.; Sherwood, P. M. A. Corrundum (α-Al_2O_3) by XPS. *Surface Science Spectra* **1998**, *5* (1), 11-17.
(184) Talari, M.; Sarapulova, A.; Zemlyanushin, E.; Sabi, N.; Hofmann, A.; Trouillet, V.; Dsoke, S. Exploring the Possibility of Aluminum Plating/Stripping from a Non-Corrosive $Al(OTf)_3$-Based Electrolyte. *Batteries & Supercaps* **2024**, *8* (1), e202400317.
(185) Rotole, J. A.; Sherwood, P. M. A. Aluminum Phosphate by XPS. *Surface Science Spectra* **1998**, *5* (1), 60-66.
(186) Lindblad, T.; Rebenstorf, B.; Yan, Z.-G.; Andersson, S. L. T. Characterization of vanadia supported on amorphous $AlPO_4$ and its properties for oxidative dehydrogenation of propane. *Applied Catalysis A: General* **1994**, *112* (2), 187-208.
(187) Verdier, S.; El Ouatani, L.; Dedryvère, R.; Bonhomme, F.; Biensan, P.; Gonbeau, D. XPS study on Al_2O_3-and $AlPO_4$-coated $LiCoO_2$ cathode material for high-capacity Li ion batteries. *Journal of The Electrochemical Society* **2007**, *154* (12), A1088.
(188) Jones, A. H.; Gaskins, J. T.; Hopkins, P. E.; Walton, S. G.; Boris, D. R.; Murphy, J. P.; Rodriguez de Marcos, L. V.; Del Hoyo, J.; Quijada, M. A. Characterization of AlF_3-passivated aluminum mirrors using non-contact thermal metrology. *Review of Scientific Instruments* **2025**, *96* (2), 024901.
(189) Limcharoen, A.; Pakpum, C.; Limsuwan, P. An X-ray Photoelectron Spectroscopy Investigation of Redeposition from Fluorine-based Plasma Etch on Magnetic Recording Slider Head Substrate. *Procedia Engineering* **2012**, *32*, 1043-1049.

(190) König, R.; Scholz, G.; Scheurell, K.; Heidemann, D.; Buchem, I.; Unger, W. E. S.; Kemnitz, E. Spectroscopic characterization of crystalline AlF3 phases. *Journal of Fluorine Chemistry* **2010**, *131* (1), 91-97.
(191) Azmi, R.; Lindgren, F.; Stokes-Rodriguez, K.; Buga, M.; Ungureanu, C.; Gouveia, T.; Christensen, I.; Pal, S.; Vlad, A.; Ladam, A.; et al. An XPS Study of Electrolytes for Li-Ion Batteries in Full Cell LNMO vs Si/Graphite. *ACS Applied Materials & Interfaces* **2024**, *16* (26), 34266-34280.
(192) Makarowicz, A.; Bailey, C. L.; Weiher, N.; Kemnitz, E.; Schroeder, S. L. M.; Mukhopadhyay, S.; Wander, A.; Searle, B. G.; Harrison, N. M. Electronic structure of Lewis acid sites on high surface area aluminium fluorides: a combined XPS and ab initio investigation. *Physical Chemistry Chemical Physics* **2009**, *11* (27), 5664-5673.
(193) Su, Y.; Falgenhauer, J.; Leichtweiß, T.; Geiß, M.; Lupó, C.; Polity, A.; Zhou, S.; Obel, J.; Schlettwein, D.; Janek, J.; et al. Electrochemical properties and optical transmission of high Li+ conducting LiSiPON electrolyte films. *physica status solidi (b)* **2016**, *254* (2), 1600088.
(194) Nikam, R. D.; Kwak, M.; Lee, J.; Rajput, K. G.; Banerjee, W.; Hwang, H. Near ideal synaptic functionalities in Li ion synaptic transistor using Li(3)PO(x)Se(x) electrolyte with high ionic conductivity. *Sci Rep* **2019**, *9* (1), 18883.
(195) Philippe, B.; Dedryvère, R.; Allouche, J.; Lindgren, F.; Gorgoi, M.; Rensmo, H. k.; Gonbeau, D.; Edström, K. Nanosilicon electrodes for lithium-ion batteries: interfacial mechanisms studied by hard and soft X-ray photoelectron spectroscopy. *Chemistry of Materials* **2012**, *24* (6), 1107-1115.
(196) Østli, E. R.; Mathew, A.; Tolchard, J. R.; Brandell, D.; Svensson, A. M.; Selbach, S. M.; Wagner, N. P. Stabilizing the Cathode Interphase of LNMO using an Ionic-liquid based Electrolyte. *Batteries & Supercaps* **2023**, *6* (7), e202300085.
(197) Murai, K.-i.; Suzuki, Y.; Moriga, T.; Yoshiasa, A. EXAFS and XPS Study of Rutile-Type Difluorides of First-Row Transition Metals. In AIP Conference Proceedings, 2007.
(198) Tasaka, A.; Kawagoe, T.; Takuwa, A.; Yamanaka, M.; Tojo, T.; Aritsuka, M. Effect of anode materials on NF_3 formation. *Journal of the Electrochemical Society* **1998**, *145* (4), 1160.
(199) Barin, I.; Platzki, G. *Thermochemical data of pure substances*; VCh Weinheim, 1989.
(200) Xu, G.-L.; Liu, Q.; Lau, K. K. S.; Liu, Y.; Liu, X.; Gao, H.; Zhou, X.; Zhuang, M.; Ren, Y.; Li, J.; et al. Building ultraconformal protective layers on both secondary and primary particles of layered lithium transition metal oxide cathodes. *Nature Energy* **2019**, *4* (6), 484-494.
(201) Binder, J. O.; Culver, S. P.; Pinedo, R.; Weber, D. A.; Friedrich, M. S.; Gries, K. I.; Volz,

K.; Zeier, W. G.; Janek, J. Investigation of Fluorine and Nitrogen as Anionic Dopants in Nickel-Rich Cathode Materials for Lithium-Ion Batteries. *ACS Applied Materials & Interfaces* **2018**, *10* (51), 44452-44462.

(202) Zhang, N.; Stark, J.; Li, H.; Liu, A.; Li, Y.; Hamam, I.; Dahn, J. R. Effects of Fluorine Doping on Nickel-Rich Positive Electrode Materials for Lithium-Ion Batteries. *Journal of The Electrochemical Society* **2020**, *167* (8), 080518.

(203) Wolfman, M.; Wang, X.; Garcia, J. C.; Barai, P.; Stubbs, J. E.; Eng, P. J.; Kahvecioglu, O.; Kinnibrugh, T. L.; Madsen, K. E.; Iddir, H.; et al. The Importance of Surface Oxygen for Lithiation and Morphology Evolution during Calcination of High-Nickel NMC Cathodes. *Advanced Energy Materials* **2022**, *12* (16), 2102951.

(204) Zhao, W.; Zou, L.; Jia, H.; Zheng, J.; Wang, D.; Song, J.; Hong, C.; Liu, R.; Xu, W.; Yang, Y.; et al. Optimized Al Doping Improves Both Interphase Stability and Bulk Structural Integrity of Ni-Rich NMC Cathode Materials. *ACS Applied Energy Materials* **2020**, *3* (4), 3369-3377.

(205) Liu, K.; Zhang, Y.; Wang, M.; Zhu, X.; Maboudian, R.; Tsang, D. C. W. Dissolution of Spent Lithium-Ion Battery Cathode Materials: Overlooked Significance of Aluminum Impurities. *Advanced Science* **2025**, *12* (21), e2417737.

(206) Dixit, M.; Markovsky, B.; Aurbach, D.; Major, D. T. Unraveling the Effects of Al Doping on the Electrochemical Properties of $LiNi_{0.5}Co_{0.2}Mn_{0.3}O_2$ Using First Principles. *Journal of The Electrochemical Society* **2017**, *164* (1), A6359-A6365.

(207) Zhang, N.; Li, H.; Ye, C.; Qiao, S. Z. Mechanical Homogenization Promoting Dual-Directional Upcycling of Layered Oxide Cathodes. *Advanced Materials* **2025**, *37* (29), e2504380.

Appendix

Anlage 5b

Versicherung gemäß § 13 Absatz 2 Satz 2 Ziffer 5 der Promotionsordnung des Karlsruher Instituts für Technologie (KIT) für die KIT-Fakultät für Chemie und Biowissenschaften

1. Einen erheblichen Verstoß gegen die Grundsätze guter wissenschaftlicher Praxis habe ich bislang nicht begangen.

2. Es gab bisher keine Promotionseignungsprüfung oder gleichwertige Prüfung an einer Universität oder dieser gleichgestellten Hochschule, an der ich erfolglos teilgenommen habe.

3. Diesem Promotionsverfahren gingen keine anderen Promotionsverfahren voran und ich bin in keinen weiteren Promotionsverfahren Kandidat/-in.

5. Ein entgeltliches Vertragsverhältnis, das eine gewerbliche Promotionsberatung zum Gegen stand hat und zur Unselbstständigkeit zumindest einer Promotionsleistung führen kann, besteht bzw. bestand nicht.

6. Die „Regeln zur Sicherung guter wissenschaftlicher Praxis am Karlsruher Institut für Technologie (KIT)“ habe ich beachtet.

7. In die Dissertation wurden Vorveröffentlichungen einbezogen, bei denen ich im Rahmen einer Mitautorenschaft jeweils einen signifikanten Teil selbstständig erbracht habe. Eine Aufstellung mit den Angaben:

Autoren/Autorinnen:

Titel der Vorveröffentlichung:

Veröffentlicht in:

Ausführliche Darlegung des selbstständig erbrachten, signifikanten Beitrages der Vorveröffentlichung oder der zur Veröffentlichung eingereichten Arbeit:

ist dieser Erklärung beigefügt. Die Aufstellung ist Bestandteil dieser Erklärung.

8. Die Dissertation oder Teile davon wurden nicht bei einer anderen Fakultät als Dissertation eingereicht.

9. Die Richtigkeit der vorstehenden Erklärungen bestätige ich.

Ort und Datum Unterschrift

Supporting Information for Chapter 4

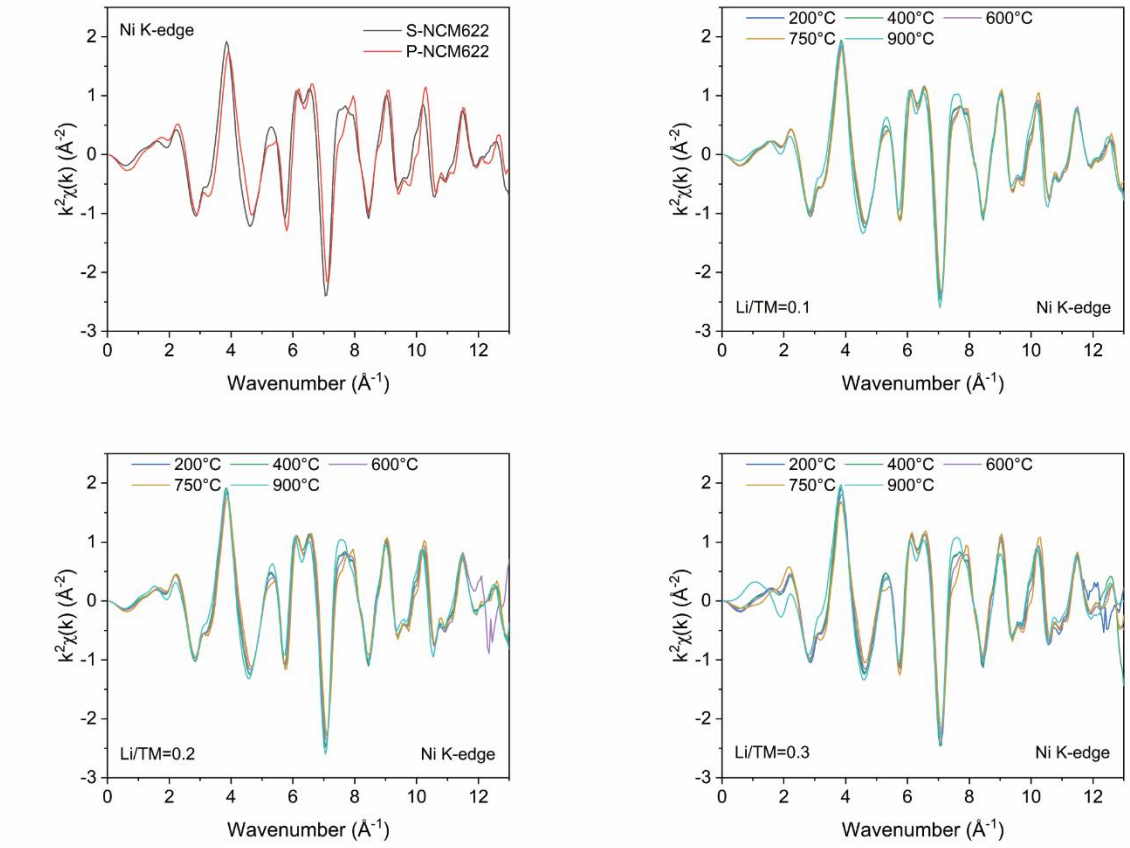

Fig. A1. Corresponding $k^2\chi(k)$ data of Ni K-edge with a spline range from 0 to 13.0 $Å^{-1}$.

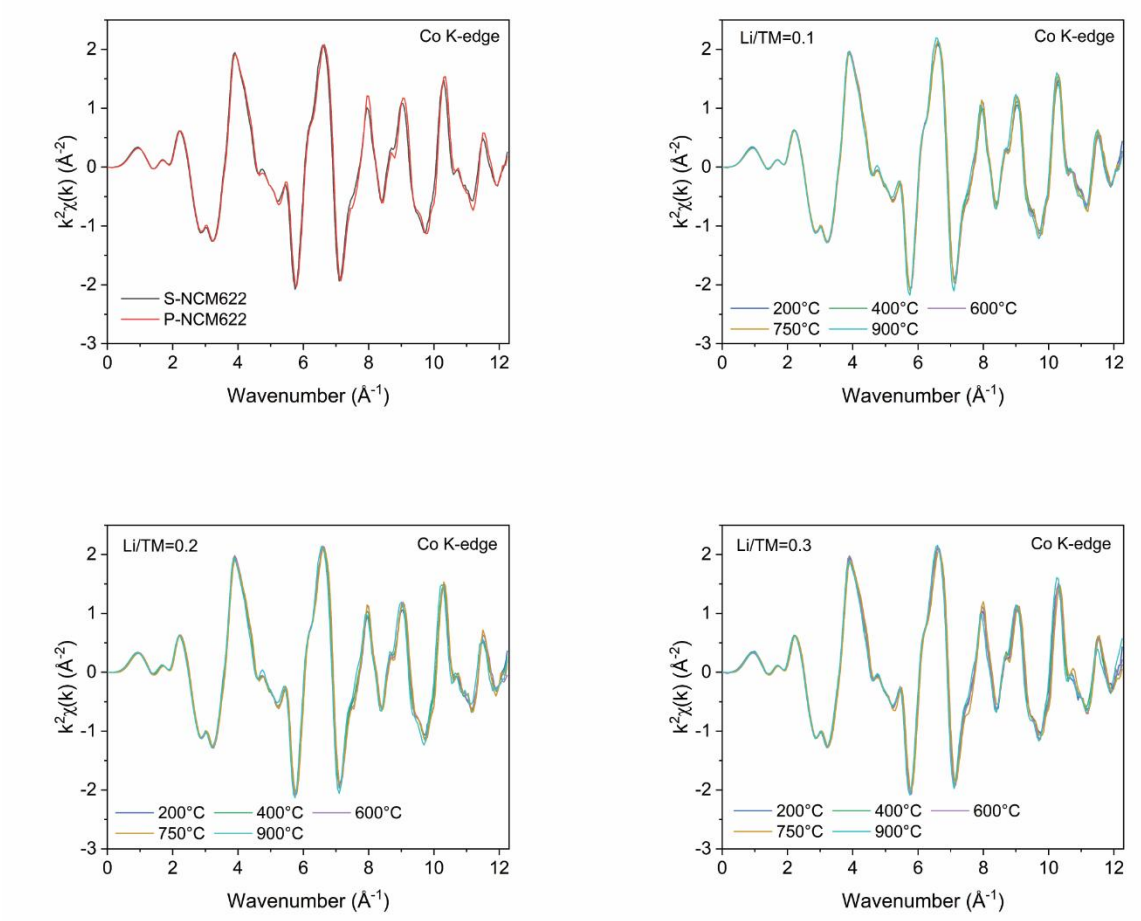

Fig. A2. Corresponding $k^2\chi(k)$ data of Co K-edge with a spline range from 0 to 12.3 Å^{-1}.

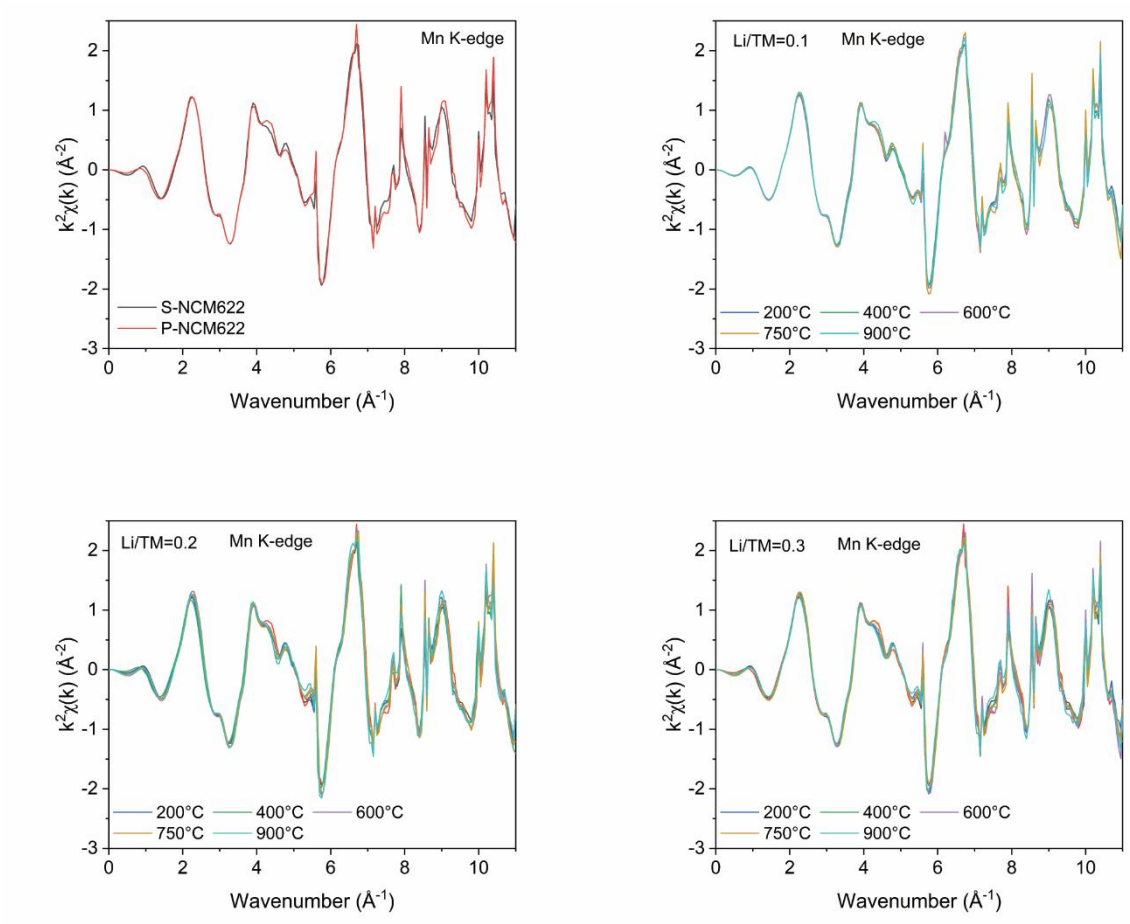

Fig. A3. Corresponding $k^2\chi(k)$ data of Mn K-edge with a spline range from 0 to 11.0 Å^{-1}

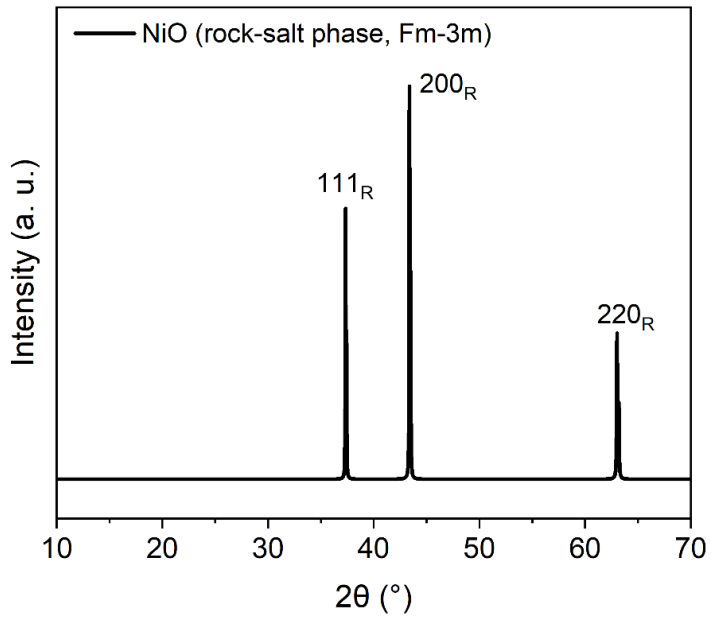

Fig. A4. Bragg reflections of standard NiO (rock-salt phase, *Fm-3m*).

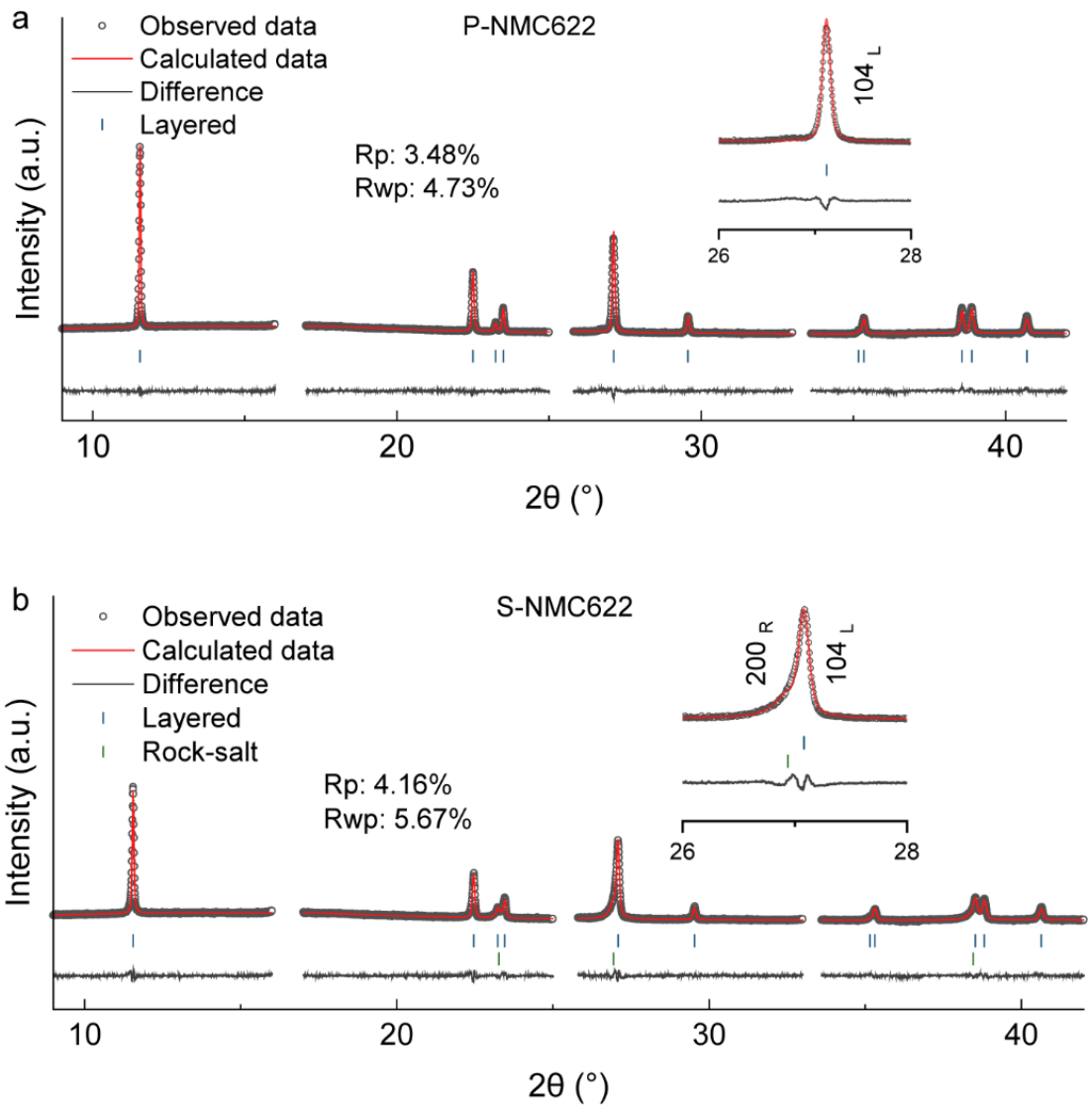

Fig. A5. Synchrotron Radiation Diffraction (SRD) patterns (λ = 0.9542 Å) and corresponding refinement results for (a) pristine NCM622 (P-NCM622) and (b) spent NCM622 (S-NCM622).

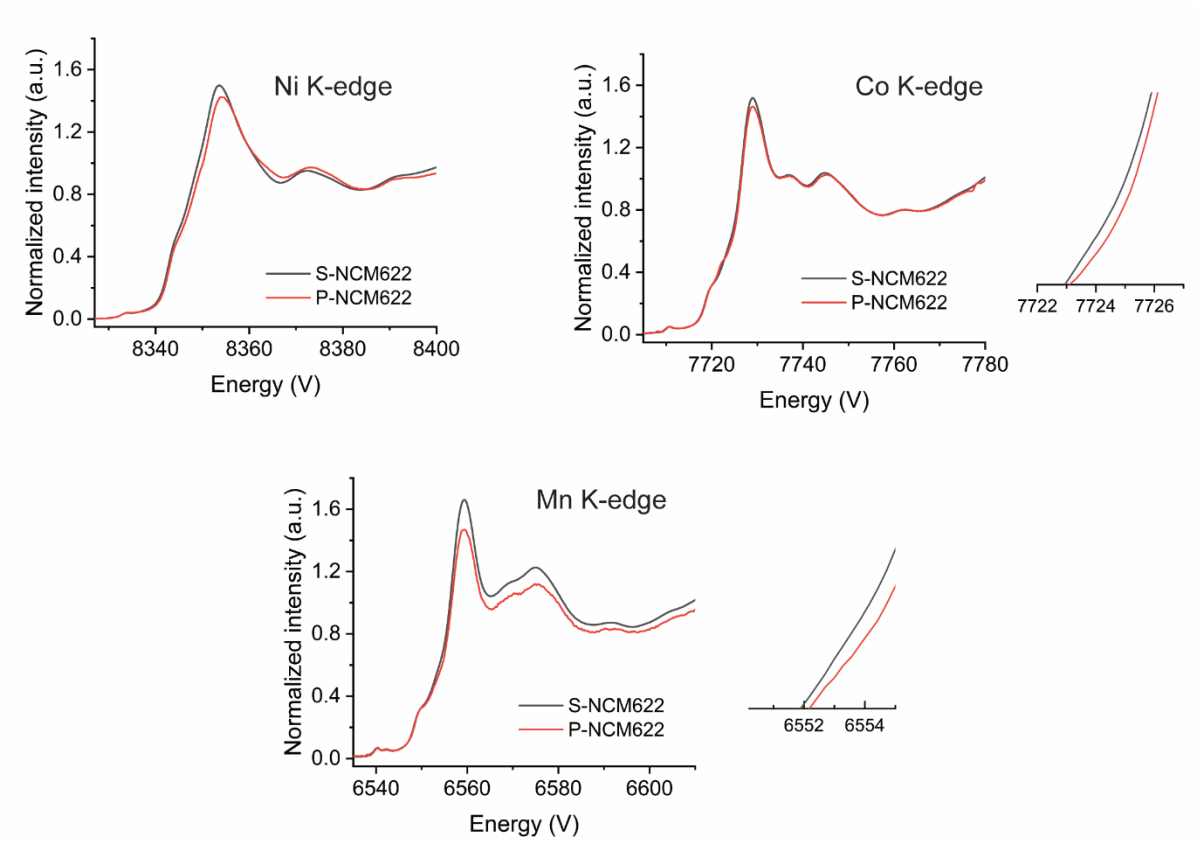

Fig. A6. Normalized XANES spectra of Ni, Co, and Mn K-edges for P-NCM622 and S-NCM622, measured at ALBA.

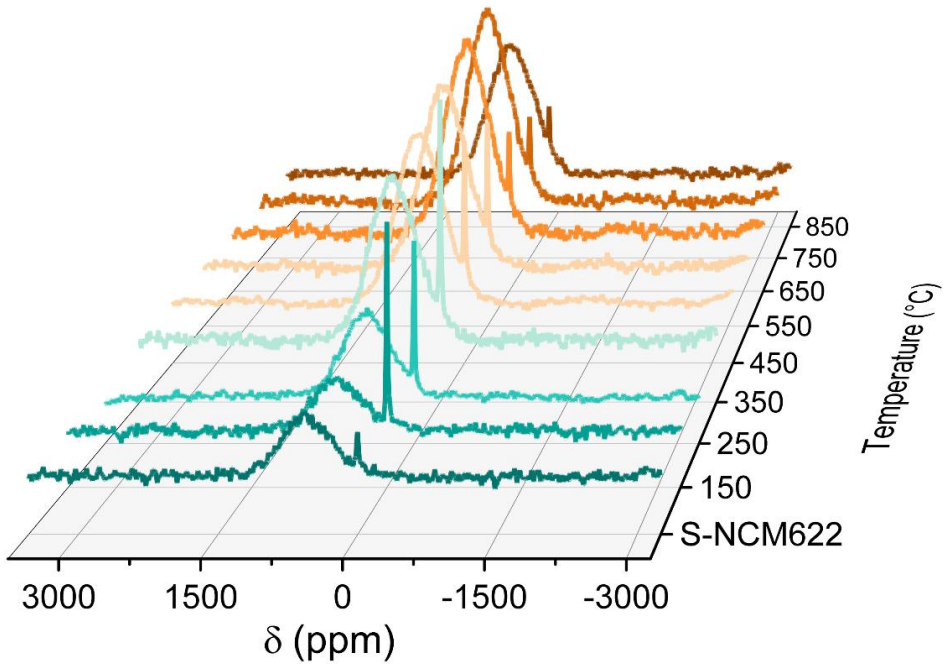

Fig. A7. ^{6}Li solid-state NMR waterfall spectra for materials regenerated under different temperatures (150-850 °C, per 100 °C) with a Li/TM ratio of 0.3.

Supporting Information for Chapter 5

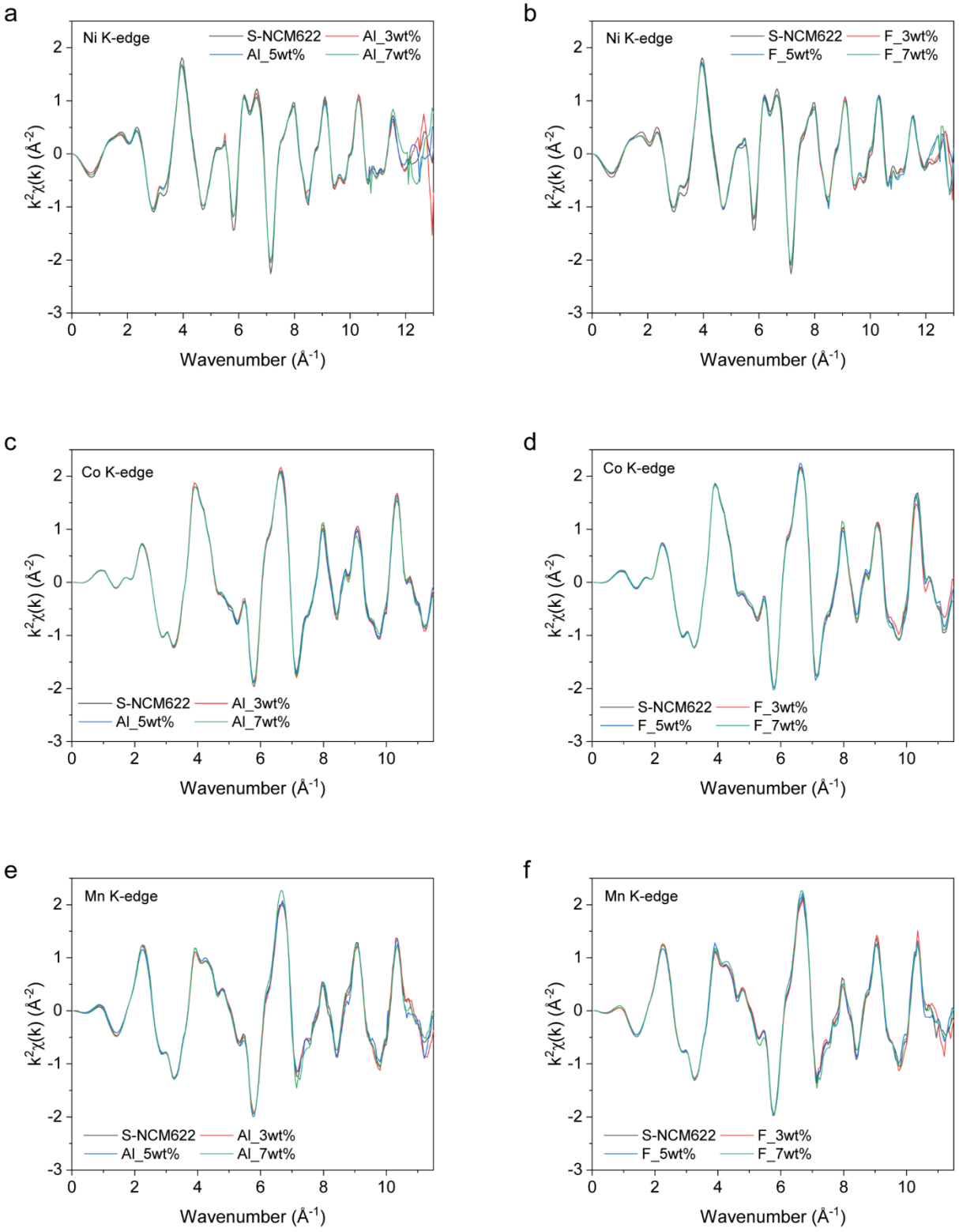

Fig. A8. Corresponding $k^2\chi(k)$ data of (a-b) Ni K-edge with a spline range from 0 to 13.0 $Å^{-1}$, (c-d) Co K-edge with a spline range from 0 to 11.5 $Å^{-1}$, and (e-f) Mn K-edge with a spline range from 0 to 11.5 $Å^{-1}$.

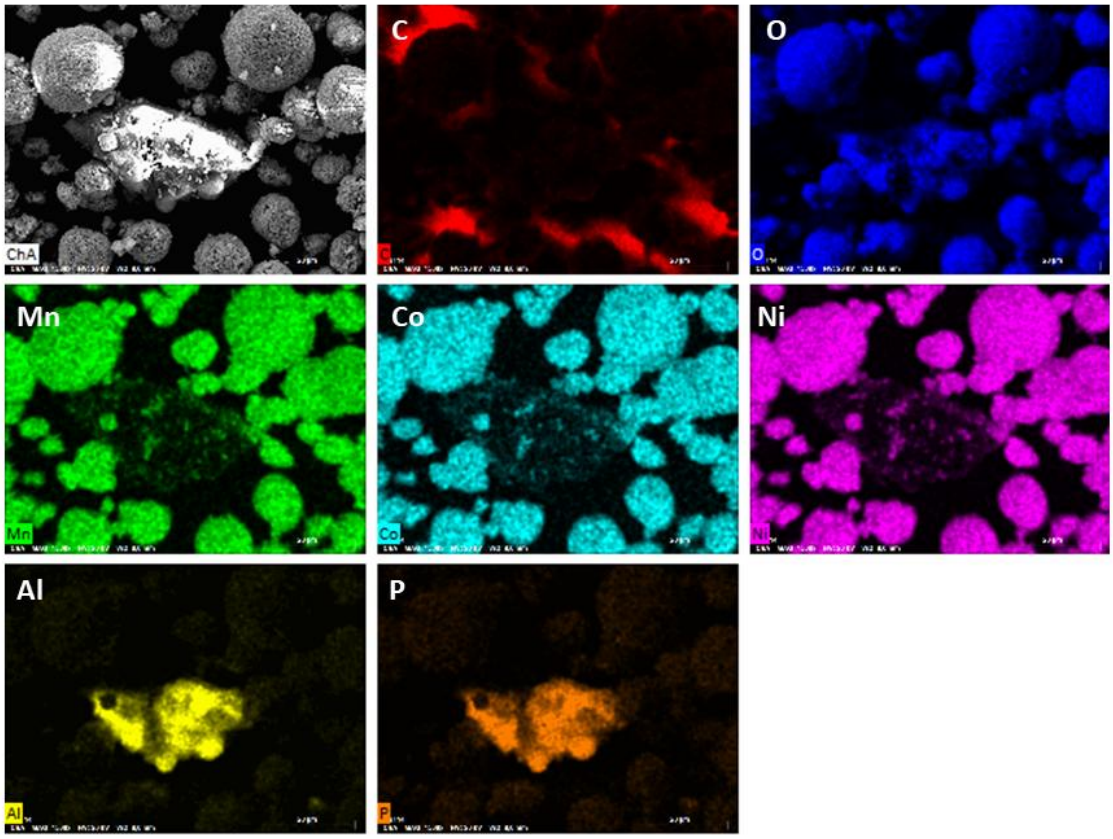

Fig. A9**.** SEM-EDX images of S-NCM622.

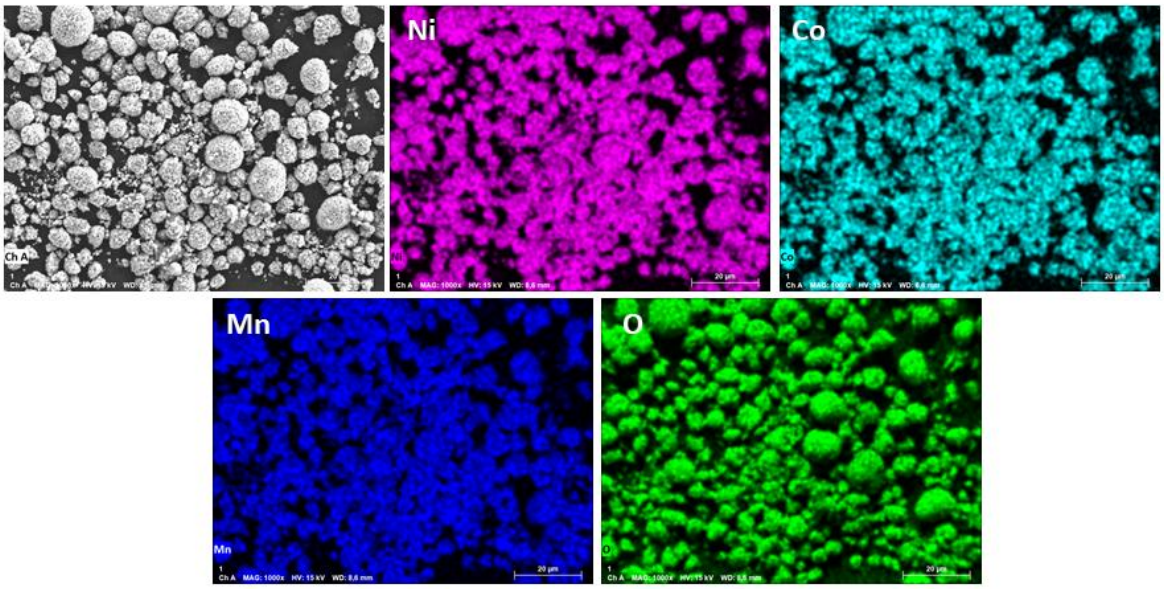

Fig. A10. SEM-EDX images of S-NCM622 in a different region compared to Fig. A9.

Table A1. Corresponding Gibbs free energy of formation ($\Delta G_f{}^0$, adapted from NIST Chemistry Webbook and reference [199]).

Substances	$\Delta G_f{}^0$ (kJ mol^{-1})
$AlPO_4$ (s)	-1860
AlF_3 (s)	-1512
LiOH (s)	-380
Li_3PO_4 (s)	-1876
Al_2O_3 (s)	-1582
LiF (s)	-617
H_2O (g)	-229

Manuscript 1 (Results and Discussion in Chapter 3)

Authors: Shuaiwei Liu, Oleksandr Dolotko, Thomas Bergfeldt, Michael Knapp and Helmut Ehrenberg

Publication title: Towards Sustainable Direct Recycling: Unraveling Structural Degradation Induced by Thermal Pretreatment of Lithium-Ion Battery Electrodes

Published in: ChemSusChem

The co-authors listed in Table 1 were involved in the implementation and evaluation of some measurements.

Table 1: Statement of co-author contributions

Co-authors	Contributions
Oleksandr Dolotko	Supervise the work, XRD measurement and Rietveld refinement
Thomas Bergfeldt	ICP-OES and CGHE measurements
Michael Knapp	Supervise the work, XRD Rietveld refinement
Helmut Ehrenberg	Supervise the work

Description of the contribution made independently:

Practical work:
This publication addresses the separation of active materials from current collectors via thermal pretreatment and the resulting structural changes in the active materials. All separation experiments were independently carried out by me. The pouch cell assembly, electrochemical cycling, deep discharging, and post-mortem electrode extraction were performed at the KIT Battery Technology Center (KIT-BATEC) by Olivia Wiegand, Steffen Jokisch, Dr. Robert Löwe, and Dr. Anna Smith.

Measurements:
Most XRD measurements were conducted by me, with additional support from Oleksandr Dolotko for some measurements. Michael Knapp and Oleksandr Dolotko provided guidance for the Rietveld refinement, of which the majority was independently completed by me.

Thomas Bergfeldt carried out the ICP-OES and CGHE measurements.

Creating the manuscript:
The idea for the publication was developed in discussion with Oleksandr Dolotko. I wrote the manuscript, which was subsequently revised by Oleksandr Dolotko, Michael Knapp, and Helmut Ehrenberg.

Manuscript 2 (Results and Discussion in Chapter 4)

Authors: Shuaiwei Liu, Hao Liu, Arseniy Bokov, Mohammad Jaleh, Hang Li, Sylvio Indris, Oleksandr Dolotko, Aleksandr Kalinko, Edgar Eduardo Villalobos Portillo, Carlo Marini, Thomas Bergfeldt, Michael Knapp and Helmut Ehrenberg

Publication title: Insights into the Mechanisms Behind Structural Repair of Spent Layered Cathode Materials for Lithium-Ion Batteries

Published in: Angewandte Chemie

The co-authors listed in Table 2 were involved in the implementation and evaluation of some measurements.

Table 2: Statement of co-author contributions

Co-authors	Contributions
Hao Liu	XAS and XRD analysis
Arseniy Bokov	Supervise the work, in/ex-situ XRD measurements
Mohammad Jaleh	Part of experiments
Hang Li & Sylvio Indris	NMR measurement
Oleksandr Dolotko	XRD Rietveld refinement
Aleksandr Kalinko	XAS measurement in DESY
Edgar Eduardo Villalobos Portillo & Carlo Marini	XAS and SRD measurements in ALBA
Thomas Bergfeldt	ICP-OES and CGHE measurements
Michael Knapp	Supervise the work, XRD Rietveld refinement
Helmut Ehrenberg	Supervise the work

Description of the contribution made independently:

Practical work:

This publication focuses on understanding the underlying mechanisms of structural repair. Most of the experiments, including material synthesis, battery assembly, and electrochemical testing, were independently carried out by me, with additional support from Mohammad Jaleh

for certain measurements. As in Manuscript 1, the pouch cell assembly, electrochemical cycling, deep discharging, and post-mortem electrode extraction were performed at the KIT Battery Technology Center (KIT-BATEC) by Olivia Wiegand, Steffen Jokisch, Dr. Robert Löwe, and Dr. Anna Smith.

Measurements:
The in situ and ex situ XRD measurements were performed with assistance from Arseniy Bokov. Hang Li and Sylvio Indris carried out the NMR spectroscopy measurements and supported their interpretation. Oleksandr Dolotko provided guidance with the Rietveld refinement. Synchrotron XAS measurements at DESY were conducted with the help of Aleksandr Kalinko. While synchrotron SRD and XAS measurements at ALBA were supported by Edgar Eduardo Villalobos Portillo and Carlo Marin, with extensive assistance from Sylvio Indris and Michael Knapp. ICP-OES and CGHE measurements were performed by Thomas Bergfeldt. SEM measurement was conducted by Bijian Deng and Liuda Mereacre. Hao Liu provided significant support during the interpretation of both XAS and XRD data.

Creating the manuscript:
I primarily conceived the idea and wrote the manuscript. It was subsequently revised by Oleksandr Dolotko, Arseniy Bokov, Michael Knapp, and Helmut Ehrenberg. Other co-authors listed in Table 2 contributed through data interpretation, discussion of results, and manuscript revision as well.

Manuscript 3 (Results and Discussion in Chapter 5)

Authors: Shuaiwei Liu, Arseniy Bokov, Vanessa Trouillet, Ramon Zimmermanns, Sylvio Indris, Subhajit Nandy, Liuda Mereacre, Alexander Missyul, Thomas Bergfeldt, Michael Knapp and Helmut Ehrenberg

Publication title: Effect of impurities on Direct Recycling of Spent $LiNi_xCo_yMn_zO_2$ Cathode Material for Lithium-ion Batteries

Published in: To submit

The co-authors listed in Table 3 were involved in the implementation and evaluation of some measurements.

Table 3: Statement of co-author contributions

Co-authors	Contributions
Arseniy Bokov	Supervise the work, XRD measurements
Vanessa Trouillet	XPS measurement and analysis
Ramon Zimmermanns & Sylvio Indris & Subhajit Nandy	XAS measurement in DESY
Liuda Mereacre	SEM and SRD measurements
Alexander Missyul	SRD measurement
Thomas Bergfeldt	ICP-OES and CGHE measurements
Michael Knapp	Supervise the work, SRD measurement
Helmut Ehrenberg	Supervise the work

Description of the contribution made independently:

Practical work:
This publication focuses on understanding the effect of impurity on the regeneration process. All the experiments, including material synthesis, battery assembly, and electrochemical testing, were independently carried out by me. As in Manuscript 1 and 2, the pouch cell assembly, electrochemical cycling, deep discharging, and post-mortem electrode extraction were performed at the KIT Battery Technology Center (KIT-BATEC) by Olivia Wiegand, Steffen Jokisch, Dr. Robert Löwe, and Dr. Anna Smith.

Measurements:

The in situ and ex situ XRD measurements were performed with assistance from Arseniy Bokov. The XPS measurement was carried out by Vanessa Trouillet. Synchrotron XAS measurements at DESY were conducted with the help of Ramon Zimmermanns, Sylvio Indris and Subhajit Nandy. SRD measurement at ALBA was performed with the help of Liuda Mereacre, Alexander Missyul and Michael Knapp. ICP-OES and CGHE measurements were performed by Thomas Bergfeldt. SEM measurement was conducted by Liuda Mereacre.

Creating the manuscript:

I primarily conceived the idea and wrote the manuscript. It was subsequently revised by Arseniy Bokov, Michael Knapp, and Helmut Ehrenberg. Other co-authors listed in Table 3 contributed through data interpretation, discussion of results, and manuscript revision as well.

Publications during PhD

1. **Shuaiwei Liu**, Hao Liu, Arseniy Bokov, Mohammad Jaleh, Hang Li, Sylvio Indris, Oleksandr Dolotko, Oleksandr Dolotko, Edgar Eduardo Villalobos Portillo, Carlo Marini, Thomas Bergfeldt, Michael Knapp, Helmut Ehrenberg. Insights into the Mechanisms Behind Structural Repair of Spent Layered Cathode Materials for Lithium-Ion Batteries. ***Angewandte Chemie***, 2025, 137(32), e202504382.

2. **Shuaiwei Liu**, Oleksandr Dolotko, Thomas Bergfeldt, Michael Knapp, Helmut Ehrenberg. Towards Sustainable Direct Recycling: Unraveling Structural Degradation Induced by Thermal Pretreatment of Lithium-Ion Battery Electrodes. ***ChemSusChem***, 2025, 18(1), e202400727.

3. **Shuaiwei Liu**, Jiachao Yang, Shuaipeng Hao, Shijie Jiang, Xiaohui Li, Oleksandr Dolotko, Feixiang Wu, Yunjiao Li, Zhenjiang He. Paving the way for electrochemical recycling of spent lithium-ion batteries: Targeting the direct regeneration of de-lithiated materials. ***Chemical Engineering Journal***, 2024, 479, 147607.

4. **Shuaiwei Liu**, Arseniy Bokov, Vanessa Trouillet, Ramon Zimmermanns, Sylvio Indris, Subhajit Nandy, Liuda Mereacre, Alexander Missyul, Thomas Bergfeldt, Michael Knapp and Helmut Ehrenberg. Effect of impurities on Direct Recycling of Spent $LiNi_xCo_yMn_zO_2$ Cathode Material for Lithium-ion Batteries. (in peer review under ***Angewandte Chemie***)

5. Jianpeng Peng, Jiachao Yang, Shuaipeng Hao, Yunjiao Li, **Shuaiwei Liu**, Shijie Jiang, Shuhui Sun, Zhenjiang He. Enhanced mechanical property promote high stability of single-crystal Ni-rich cathode at 4.5 V. **Energy Storage Materials**, 2025, 77, 104199.

5. Shuaipeng Hao, Jiachao Yang, Yunjiao Li, **Shuaiwei Liu**, Shijie Jiang, Zhenjiang He. Utilizing Oxygen-Vacancy-Rich Violet Tungsten Oxide Enabling Ultralong Cycling of Nickel-Rich Cathodes at High Voltage. **ACS Nano**, 2025, 19(7), 7263-7272.

6. Shuaipeng Hao, Yuelin Lv, Yi Zhang, **Shuaiwei Liu**, Zhouliang Tan, Wei Liu, Yuanguang Xia, Wen Yin, Yaqi Liao, Haijin Ji, Yuelin Kong, Yudi Shao, Yunhui Huang, Lixia Yuan. Restoration of Li^+ pathways in the [010] direction during direct regeneration for spent $LiFePO_4$. **Energy & Environmental Science**, 2025, 18(8), 3750-3760.

Acknowledgement

I officially began my PhD work in November 2022 at the Department of Chemistry and Biosciences, Karlsruhe Institute of Technology (KIT), within the Institute for Applied Materials – Energy Storage Systems (IAM-ESS). I would like to sincerely thank the China Scholarship Council (CSC, No. 202206370052) for their financial support. I am also deeply grateful to all those who have offered guidance, encouragement, and assistance throughout this journey.

First and foremost, I wish to express my heartfelt gratitude to my supervisor, Prof. Dr. Helmut Ehrenberg, for giving me the opportunity to conduct my research at IAM-ESS and for his continuous support, valuable guidance, and insightful comments.

I am also deeply thankful to my co-supervisor, Dr. Michael Knapp, for his understanding, encouragement, and unwavering support throughout my studies at KIT. His guidance allowed me to fully explore my research interests and engage deeply with the topics I am most passionate about. My sincere thanks also go to Dr. Arseniy Bokov, for his assistance with XRD measurements, constructive suggestions during experiments, and valuable advice on scientific writing, which significantly enhanced the quality of my work. I would also like to thank Dr. Oleksandr Dolotko, who guided me through experimental work during the early stages of my doctoral program, provided insightful suggestions, and engaged in fruitful discussions that laid a solid foundation for my research.

I am further grateful to many colleagues for their expertise and support: Dr. Sylvio Indris, for assistance with NMR measurements and synchrotron experiments; M. Sc. Liuda Mereacre, for training in laboratory techniques and support with SEM measurements; Dr. Hao Liu, for help with interpreting experimental results; Dr. Hang Li, for support with NMR measurements and analysis; Dr. Vanessa Trouillet, for help with XPS measurements and analysis; Dr. Ramon Zimmermanns, for assistance with XAS measurements and analysis; Dr. Anna Smith's group, for providing end-of-life batteries; Dr. Thomas Bergfeldt, for help with ICP-OES and CGHE measurements; and Dr. Edgar Eduardo Villalobos Portillo, Dr. Carlo Marini (both beamline scientists at ALBA, Barcelona), Dr. Subhajit Nandy and Dr. Aleksandr Kalinko (both beamline scientists at DESY, Hamburg), for their kind support with synchrotron experiments.

My sincere appreciation also goes to my colleagues at IAM-ESS: Dr. Xinyang Liu-Theato, Dr. Liqun Sun, Dr. Jiali Peng, Dr. Bijian Deng, Dr. Anhao Zuo, Kun Tang, Xinyue Zhang, Liwen Yang, Ying Li, Hongyuan Yu, Jilu Zhang, Raphael Sieweck, Alexander Maximilian, Felix Bauer, and Marius Ast. I am also grateful to all colleagues working on the recycling topic at IAM-ESS for their support and helpful collaboration throughout this research. In addition, I would like to acknowledge the indispensable support of Mrs. Almut Kriese (administrative support), Mr. Heinz-Robert Goebel (equipment support), Mr. Luis Martin Sanchez Neudeck (IT support), and Mr. Philip Richter (procurement support).

Finally, I would like to express my deep gratitude to my parents for their consistent support and understanding during my years of study abroad. Their selfless and endless love give me courage and confidence to challenge and overcome all difficulties. They gave me the support and understanding to pursue my dreams.

Looking back, my three years at IAM-ESS have been truly unforgettable, filled with invaluable experiences, inspiring guidance, and lasting friendships that I will always cherish.

Declaration

Ich versichere hiermit, dass ich die vorliegende Dissertation selbständig und ohne unzulässige fremde Hilfe erbracht habe. Ich habe keine anderen als die angegeben Quellen und Hilfsmittel benutzt, sowie wörtliche und sinngemäße Zitate kenntlich gemacht. Die Dissertation wurde bisher an keiner anderen Hochschule oder Universität eingereicht.

Karlsruhe, den 03.11.2025
M. Sc. Shuaiwei Liu

I hereby declare that I have made this work independently and used no other than the specified sources and tools, as well as, whether verbatim or with regards to content, indicated all citations as such and I have paid attention to the statute of the Karlsruhe Institute of Technology (KIT) in the current version to ensure good scientific practice.

Karlsruhe, 03.11.2025
M. Sc. Shuaiwei Liu